Title

Nanotubes from first principle and data-driven methods: real and reimagined

Author

Yu, Hsuan Ming

Publication Date

2024

Peer reviewed|Thesis/dissertation

UNIVERSITY OF CALIFORNIA
Los Angeles

Nanotubes from first principle and data-driven methods: real and reimagined

A dissertation submitted in partial satisfaction
of the requirements for the degree
Doctor of Philosophy in Material Science and Engineering

by

Hsuan Ming Yu

2024

ABSTRACT OF THE DISSERTATION

Nanotubes from first principle and data-driven methods: real and reimagined

by

Hsuan Ming Yu
Doctor of Philosophy in Material Science and Engineering
University of California, Los Angeles, 2024
Professor Amartya Sankar Banerjee, Chair

First principle methods and data-driven approach were employed to investigate the intricate mechanical and electrical behaviors and properties of various nanotubes, both real and reimagined. A real space, helical and cyclic symmetry adapted, Kohn Sham DFT code—HelicalDFT was utilized to explore the torsional, extensional and electronic properties of group-IV nanotubes, unveiling unique mechanical and electronic responses. The study further delves into Carbon Kagome Nanotubes (CKNTs) and novel P_2C_3 nanotubes, highlighting their potential in material science due to distinctive electronic characteristics. A data-driven approach using machine learning predicts the electronic structure of nanotubes even under deformation, enhancing the understanding of nanomaterial behavior. Additionally, the integration of ellipsoidal coordinate systems within the current computational framework to advance in future evaluation of Gaussian curvature effects, opening new avenues for the design of nanomaterials with customized properties. This comprehensive research provides valuable insights into nanotube properties, offering a robust framework for future material science explorations and technological applications.

The dissertation of Hsuan Ming Yu is approved.

Ya-Hong Xie

Jaime Marian

Xiangfeng Duan

Amartya Sankar Banerjee, Committee Chair

University of California, Los Angeles

2024

Dedicated to my family

TABLE OF CONTENTS

LIST OF FIGURES

LIST OF TABLES

ACKNOWLEDGMENTS

I am sincerely grateful to everyone who has supported and motivated me throughout my academic journey. Special thanks to my advisor, Prof. Amartya S. Banerjee, for his invaluable guidance and the opportunity to delve into intriguing challenges in computational Material Science. I am also thankful to my committee members, Prof. Xiangfeng Duan, Prof. Jaime Marian, and Prof. Ya-Hong Xie, whose insightful suggestions and discussions have enriched my understanding of Material Science.

I acknowledge the support from MURI project grant (FA9550-18-1-0095), DOE funding (DE-SC0023432) and NERSC (BES- ERCAP0025205 and BES-ERCAP0025168)

The contents of Chapter 2 and 3 are published in the following journal article:

H. M. Yu and A.S. Banerjee (2022): Density functional theory method for twisted geometries with application to torsional deformations in group-IV nanotubes; Journal of Computational Physics; Volume 456, 111023 DOI:10.1016/j.jcp.2022.111023.

The contents of Chapter 4 are published in the following journal article:

H. M. Yu, S. Sharma, S. Agarwal, O. Liebman and A.S. Banerjee (2023): Carbon Kagome Nanotubes — quasi-one-dimensional nanostructures with flat bands; RSC Advances, 2024, 14, 963-981 DOI:10.1039/D3RA06988E.

The contents of Chapter 5 are in preperation for publication:

Structural and electronic phase transition in double kagome P2C3 nanotubes.

The contents of Chapter 6 are published in the following journal article:

S. Pathrudkar, H. M. Yu, S. Ghosh and A.S. Banerjee (2022): Machine learning based prediction of the electronic structure of quasi-one-dimensional materials under strain; Physical Review B; Volume 105 (No. 19), 195141.DOI:10.1103/PhysRevB.105.195141

The works are reprinted with permissions from all the coauthors above.

VITA

Hsuan Ming Yu

EDUCATION

Bachelor of Science in Physics **2015**
University of California, Los Angeles *Los Angeles, CA*

RESEARCH EXPERIENCE

Graduate Student Researcher **2019–2024**
University of California, Los Angeles *Los Angeles, CA*

TEACHING EXPERIENCE

Teaching Assistant **2019–2024**
University of California, Los Angeles *Los Angeles, CA*

REFEREED JOURNAL PUBLICATIONS

Density functional theory method for twisted geometries with application to torsional deformations in group-IV nanotubes **2022**
Journal of Computational Physics

Machine learning based prediction of the electronic structure of quasi-one-dimensional materials under strain **2022**
Physical Review B

Carbon Kagome nanotubes—quasi-one-dimensional nanostructures with flat bands **2024**
RSC Advances

AWARDS

USNCCM16 Conference Award
Conference Award from USACM in 2021.

CHAPTER 1

Introduction

Over the past few decades, the synthesis and characterization of novel nanomaterials and nanostructures has blossomed into a major scientific and technological endeavor (10; 11; 12; 13). Such materials are usually associated with shapes and structures that are quite different from crystalline materials, and they often display properties that are radically distinct from the bulk phase. Consequently, a variety of computational techniques employing different physical theories have been developed over the years, to aid in their design and discovery (14; 15; 16; 17; 18).

A defining feature of the aforementioned class of materials is that they are of limited spatial extent along one or more dimensions. This often makes it possible to sustain unusual and/or large modes of deformation in such systems, without incurring material failure. Since a variety of material properties of nanostructures, including, e.g., optical, electronic and transport behavior are often strongly coupled to distortions in the material's structure, engineering the response of these systems through the application of mechanical strains constitutes an active and important area of scientific research today (19; 20; 21; 22; 23; 24). In particular, inhomogeneous strain fields — such as those associated with overall torsion (i.e., twisting) or flexure (i.e., bending) of the nanostructure, as well as those arising from localized deformations such as wrinkles or corrugations, have often been used to elicit fascinating electro-mechanical responses in such systems (25; 26; 27; 28). A persistent issue however, is that there appears to be a paucity of systematic and efficient computational techniques that can model these systems as they are undergoing such deformations, especially from first

principles. We view the current contribution as an important step in addressing this gap in the literature and present a real-space formulation and implementation of Kohn-Sham Density Functional Theory (KS-DFT) that is suited to twisted geometries.

Systems associated with intrinsic twist are quite common among nanomaterials, with chiral carbon nanotubes (29), nanocoils (30) and inorganic nanoassemblies (31) constituting well known examples. Twisting is particularly relevant as a mode of deformation for quasi-one-dimensional systems such as nanotubes, nanoribbons, nanowires and nanorods (32), and can be an important route to engineering the properties of these materials through the imposition of strain. In particular, imposition of twist naturally gives rise to so-called *helical potentials* in achiral nanostructures, which can then cause these materials to display unusual transport properties and fascinating light-matter interactions (33). Twisted geometries also have found relevance recently in the context of quasi-two-dimensional systems such as graphene bilayers (34; 35; 36; 37), which are associated with strong electronic correlations and superconductivity, as well as the use of screw dislocations to engineer growth processes (38; 39; 40). We anticipate that the simulation technique discussed in this work will have broad relevance to most of the materials systems described above, while being particularly consequential for the computational study of quasi-one-dimensional systems and their deformations, from first principles.

The vast majority of first principles calculations being carried out today use KS-DFT, as implemented using the pseudopotential plane-wave method (41; 42; 43; 44). While this is a powerful computational technique for the study of periodic systems (such as crystals) and their homogeneous deformations, it is fundamentally unsuitable for modeling systems subjected to inhomogeneous strain fields (such as those associated with bending or torsion), that break periodic symmetry. Indeed, modeling such systems by use of the plane-wave method can result in the use of uncontrolled approximations and/or performance and convergence (with respect to discretization parameters) issues that can render the calculations infeasible. For example, plane-wave calculations of a quasi-one-dimensional system that is undergoing

twisting (Figure 1.1) will usually involve making the system artificially periodic along the direction of the twist axis — thus resulting in a supercell containing a very large number of atoms, as well as the inclusion of a substantial amount of vacuum padding in the directions orthogonal to the twist axis, so as to minimize interactions between periodic images. Together, these conditions can make such calculations extremely challenging even on high performance computing platforms, if not altogether impractical. It has been pointed out in

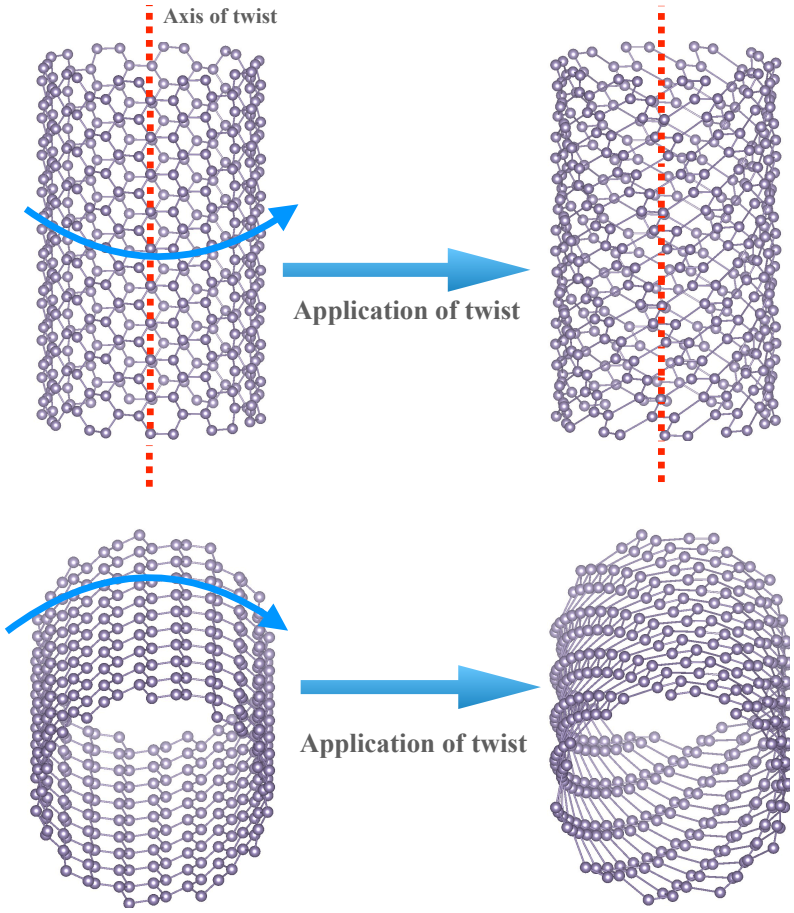

Figure 1.1: Depiction of a prototypical twisted geometry — a nanotube being subjected to torsional deformation. Two views are shown.

the literature however, that the aforementioned computational issues related to the study of twisted or bent nanostructures can be avoided by making use of the connections of such inhomogeneous strain states with non-periodic symmetries (32; 45; 46; 47; 48; 49; 50; 51; 52; 53).

Specifically, as long as edge effects are unimportant in a system under study, cyclic symmetries can be used to simulate bent nanostructures, while helical symmetries can be used to simulate systems with twist. A key ingredient for such an approach is the availability of efficient computational methods that can adequately handle such non-periodic symmetries. Following this line of thought, we have been developing systematic first principles simulation techniques suited to the study of systems with non-periodic symmetries (54). In particular, we have developed *ab initio* methods that explicitly incorporate cyclic symmetries, and used this methodology to simulate bending in nanoribbons (55) and sheets of two-dimensional materials (7). More recently, we have rigorously formulated and implemented a novel first principles computational technique that explicitly accounts for helical symmetries (4). We view the present contribution as a follow up of this most recent development, and focus on the computational and application aspects of the simulation technique in this work, in contrast to our earlier contribution, which was largely concerned with the mathematical aspects. In particular, salient features of the current contribution are as follows. We present in this work a self-contained, intuitive derivation of the governing equations for systems associated with twisted geometries and make connections with helical symmetries, while also allowing for the possibility that such systems may have inherent cyclic symmetries. We describe the details of our computational strategy, including discretization choices in real and reciprocal space, numerical linear algebra issues and choice of eigensolvers. We touch upon specific aspects of our MATLAB based numerical implementation. We then discuss various features of the simulation method, including its convergence, accuracy, consistency, computational efficiency and parallel scaling properties. Finally, we apply the method to the study of torsional deformations of an important class of nanomaterials (i.e., nanotubes from Group IV of the periodic table[1]) and investigate the electro-mechanical response of these systems. Notably, the present contribution subsumes our earlier work on KS-DFT for cylindrical geometries

[1]In modern IUPAC convention this group is also referred to as Group 14. Elsewhere, this group is also referred to as Group IVa or the Carbon group.

(7), and many of the results in that former contribution can be derived as special cases of the results presented here for twisted geometries (by considering simulations with zero twist). Together, the present contribution, and our earlier body of work extends symmetry adapted molecular dynamics and tight-binding based computational methods developed in the literature for studying bent and/or twisted nanomaterials, to the realm of first principles calculations.

The numerical technique described here employs finite difference discretization in helical coordinates[2] which allows us to set up a computational domain in an annular region of space. In turn, this enables us to carry out simulations of systems associated with twisted geometries, while employing small unit cells containing just a few atoms. With this setup in hand, we were able to carry out an extensive series of simulations involving various nanotubes of Group IV elements and even compound based nanotubes. This enabled us to compare and contrast the properties of these different materials, and also allowed us to extend some well-known qualitative and quantitative features of the electro-mechanical properties of carbon nanotubes, to the broader class of Group IV nanotubes and beyond— including nanotubes reimagined from novel two-dimensional materials. We would like to point out that these studies would not have been possible without the use of a specialized computational method such as the one presented here. Moreover, a machine learning approach was employed to develop efficient, accurate, and interpretable models based on the rich repository of simulation data produced by our method. Additionally, we have extended this real space finite difference density functional theory approach to investigate gaussian curvature effects on nanotubes and other nanomaterials, further broadening the scope of our research. This extension allows us to explore how anisotropic curvatures influence the structural, electronic, and mechanical properties of these nanostructures. By investigating Gaussian curvature effects, we aim to

[2]We are aware of chemistry literature based on Linear Combination of Atomic Orbitals (LCAO) methods (56; 57; 58; 59; 60; 61), which have explored the use of helical and cyclic symmetries for studying nanostructures of interest. The connection of such symmetries with deformation modes in nanostructures does not appear to have been explored by these authors, as far as we can tell, and at any rate, these methods are quite distinct from the real space technique presented here.

uncover new insights into the behavior of nanotubes and other nanomaterials, shedding light on their unique characteristics and potential applications. This expansion of our research not only deepens our understanding of nanoscale phenomena but also opens up exciting avenues for the design and engineering of novel materials with tailored properties and functionalities. This dissertation is an adaptation of previously published papers (5; 62; 63) and other ongoing research projects. By consolidating these papers into a single document, this dissertation aims to present a cohesive and comprehensive overview of the research conducted and its contributions to the field.

CHAPTER 2

Helical DFT: Helical symmetry adapted density functional theory

2.1 Formulation

In this section, we describe our formulation of Kohn-Sham density functional theory for twisted geometries. We first lay out the notation used in the rest of the paper. In what follows, $\mathbf{e_X}, \mathbf{e_Y}, \mathbf{e_Z}$ will denote the standard orthonormal basis of $\mathbb{R}^3$. The Cartesian coordinates of a point $\mathbf{p} \in \mathbb{R}^3$ will be denoted as $(x_\mathbf{p}, y_\mathbf{p}, z_\mathbf{p})$, i.e., $\mathbf{X} = x_\mathbf{p}\,\mathbf{e_X} + y_\mathbf{p}\,\mathbf{e_Y} + z_\mathbf{p}\,\mathbf{e_Z}$. The corresponding helical coordinates (introduced later in Section 2.2.1) and cylindrical coordinates of the point will be denoted as $(r_\mathbf{p}, \theta_{1\,\mathbf{p}}, \theta_{2\,\mathbf{p}})$ and $(r_\mathbf{p}, \vartheta_\mathbf{p}, z_\mathbf{p})$ respectively. The coordinates of a generic point will be denoted as (x, y, z), (r, θ_1, θ_2) and (r, ϑ, z) in Cartesian, helical and cylindrical coordinates respectively. Vectors and matrices will be denoted in boldface, with vectors typically denoted using lower case letters (e.g., $\mathbf{p}$) and matrices using uppercase (e.g. $\mathbf{q}$). The symbol $\cdot$ will be often used as a generic placeholder instead of specifying a variable explicitly (e.g. $f(\cdot)$ instead of $f(x)$ or $f(y)$). The notation $\mathsf{L}^2(\Omega)$ will be used to denote the space of square integrable functions over a domain Ω. The inner product over such a space will be denoted as $\langle \cdot, \cdot \rangle_{\mathsf{L}^2(\Omega)}$. An overbar will be used to denote complex conjugation (e.g. $\overline{f(\mathbf{X})}$). Finally, $|\cdot|$ will be used to denote the absolute value of a scalar, and $\|\cdot\|$ will be used to denote the norm of a vector or function.

2.1.1 System specification: Computational domain, atomic configuration and symmetries

We consider a nanostructure aligned along $\mathbf{e_Z}$, the axis of twist, as the prototypical system of interest. In order to avoid quantum finite-size effects and/or mechanical constraints at the edges due to the imposition of twist (64; 49) , we will assume that the structure is infinite in extent along $\mathbf{e_Z}$. For the sake of simplicity, we will also assume that the structure is of limited spatial extent along $\mathbf{e_X}$ and $\mathbf{e_Y}$, i.e., it is a quasi-one-dimensional system. The large majority of nanomaterials for which twisted geometries might be relevant as deformation modes, are included within the scope of the above set of assumptions. These conditions imply that the system can be embedded in a cylinder with axis $\mathbf{e_Z}$ (or annular cylinder, if the system is tubular), of infinite height and finite radius, and we will refer to this region of space as the *global simulation domain*.

For most quasi-one-dimensional systems of interest, the infinite extent along $\mathbf{e_Z}$ is related to periodicity along this axis. Additionally, for many such systems, including for example, the tubular structures considered in this work, there may be rotational symmetries about the same axis. Let the atoms of the untwisted structure have positions:

$$\mathcal{S}_{\text{untwisted}} = \{\mathbf{p}_1, \mathbf{p}_2, \mathbf{p}_3, \ldots\}\,. \tag{2.1}$$

The above assumptions on periodicity and rotational symmetry imply that there is a periodic group consisting of translations along $\mathbf{e_Z}$:

$$\mathcal{G}_{\text{periodic}} = \left\{ \left(\mathbf{I} \,|\, m\tau\, \mathbf{e_Z} \right) : m \in \mathbb{Z} \right\}, \tag{2.2}$$

a cyclic group of order $\mathfrak{N}$ about $\mathbf{e_Z}$ (consisting of rotations through multiples of the angle $\Theta = \dfrac{2\pi}{\mathfrak{N}}$):

$$\mathcal{G}_{\text{cyclic}} = \left\{ \left(\mathbf{R}_{n\Theta} \,|\, \mathbf{0} \right) : n = 0, 1, \ldots, \mathfrak{N} - 1 \right\}, \tag{2.3}$$

and a finite collection of points:

$$\mathcal{P} = \left\{ \mathbf{r}_k \in \mathbb{R}^3 : k = 1, 2, \ldots, M \right\}, \tag{2.4}$$

such that the entire structure $\mathcal{S}_{\text{untwisted}}$ can be described as the action of the composite group:

$$\mathcal{G}_{\text{untwisted}} = \left\{ \left(\mathbf{R}_{n\Theta} \,|\, m\tau\, \mathbf{e_Z} \right) : m \in \mathbb{Z}, n = 0, 1, \ldots, \mathfrak{N} - 1 \right\}, \tag{2.5}$$

on the points in $\mathcal{P}$, i.e.,

$$\mathcal{S}_{\text{untwisted}} = \bigcup_{\substack{\Upsilon \in \mathcal{G}_{\text{untwisted}}, \\ k=1,2,\ldots,M}} \Upsilon \circ \mathbf{r}_k \;=\; \bigcup_{\substack{m \in \mathbb{Z}, \\ n=0,1,\ldots,\mathfrak{N}-1 \\ k=1,2,\ldots,M}} \mathbf{R}_{n\Theta}\, \mathbf{r}_k + m\tau\, \mathbf{e_Z}\,. \tag{2.6}$$

In the above equations, a symbol of the form $\left(\mathbf{q} \,|\, \mathbf{t} \right)$ denotes an isometry with rotation $\mathbf{q} \in \mathrm{SO}(3)$ and translation $\mathbf{t} \in \mathbb{R}^3$. Its action on a point $\mathbf{X} \in \mathbb{R}^3$ can be written as:

$$\left(\mathbf{q} \,|\, \mathbf{t} \right) \circ \mathbf{X} = \mathbf{q}\, \mathbf{X} + \mathbf{t}\,. \tag{2.7}$$

Additionally, $\mathbf{R}_{n\Theta}$ denotes the following rotation matrix with axis $\mathbf{e_Z}$:

$$\mathbf{R}_{n\Theta} = \begin{pmatrix} \cos(n\Theta) & -\sin(n\Theta) & 0 \\ \sin(n\Theta) & \cos(n\Theta) & 0 \\ 0 & 0 & 1 \end{pmatrix}, \Theta = \frac{2\pi}{\mathfrak{N}}\,, \tag{2.8}$$

$\mathbf{I}$ denotes the identity matrix and $\mathbf{0}$ denotes the zero vector. The scalar $0 < \tau < \infty$ is the fundamental period of the group $\mathcal{G}_{\text{periodic}}$. We will refer to the points in $\mathcal{P}$ as the *simulated atoms*. We will use Z_k to denote the valence nuclear charge of the simulated atom located at position $\mathbf{r}_k$.

Now let us suppose that the structure $\mathcal{S}_{\text{untwisted}}$ is subjected to a uniform twist of $2\pi\alpha$ radians per τ bohr along the axis $\mathbf{e_Z}$, so as to result in the structure $\mathcal{S}_{\text{twisted}}$ with the atomic positions:

$$\mathcal{S}_{\text{twisted}} = \{ \mathbf{q}_1, \mathbf{q}_2, \mathbf{q}_3, \ldots \}\,. \tag{2.9}$$

Since we are dealing with structures that extend to infinity along $\mathbf{e_Z}$, we may obtain the deformed (twisted) configuration by prescribing a mapping of the form $\mathbf{q} = \mathbf{R}_{\frac{2\pi\alpha z_\mathbf{p}}{\tau}}\mathbf{p}$, to the undeformed one. Here, $\alpha \in [0, 1)$ is a scalar twist parameter, τ can be re-identified as the *pitch of the twist*, and $\beta = \frac{2\pi\alpha}{\tau}$, is the *rate of twist*. Furthermore,

$$\mathbf{R}_{\frac{2\pi\alpha z_\mathbf{p}}{\tau}} = \begin{pmatrix} \cos(\frac{2\pi\alpha z_\mathbf{p}}{\tau}) & -\sin(\frac{2\pi\alpha z_\mathbf{p}}{\tau}) & 0 \\ \sin(\frac{2\pi\alpha z_\mathbf{p}}{\tau}) & \cos(\frac{2\pi\alpha z_\mathbf{p}}{\tau}) & 0 \\ 0 & 0 & 1 \end{pmatrix} = \begin{pmatrix} \cos(\beta z_\mathbf{p}) & -\sin(\beta z_\mathbf{p}) & 0 \\ \sin(\beta z_\mathbf{p}) & \cos(\beta z_\mathbf{p}) & 0 \\ 0 & 0 & 1 \end{pmatrix}, \tag{2.10}$$

denotes a rotation matrix with axis $\mathbf{e_Z}$ for which the (twist) angle depends on the coordinate along $\mathbf{e_Z}$. At the atomic level, this implies (32; 45; 4) that the deformed structure may be obtained from the undeformed one by replacing the group of translations $\mathcal{G}_{\text{periodic}}$ used to generate $\mathcal{S}_{\text{untwisted}}$, by a group of screw transformations (or helical isometries), i.e.:

$$\mathcal{G}_{\text{helical}} = \left\{ \left(\mathbf{R}_{2\pi m\alpha} \,|\, m\tau\,\mathbf{e_Z} \right) : m \in \mathbb{Z} \right\}. \tag{2.11}$$

Here $\mathbf{R}_{2\pi m\alpha}$ denotes the following rotation matrix with axis $\mathbf{e_Z}$:

$$\mathbf{R}_{2\pi m\alpha} = \begin{pmatrix} \cos(2\pi m\alpha) & -\sin(2\pi m\alpha) & 0 \\ \sin(2\pi m\alpha) & \cos(2\pi m\alpha) & 0 \\ 0 & 0 & 1 \end{pmatrix}. \tag{2.12}$$

In other words, by replacing the composite group $\mathcal{G}_{\text{untwisted}}$ with:

$$\mathcal{G}_{\text{twisted}} = \left\{ \left(\mathbf{R}_{(2\pi m\alpha + n\Theta)} \,|\, m\tau\,\mathbf{e_Z} \right) : m \in \mathbb{Z}, n = 0, 1, \ldots, \mathfrak{N} - 1 \right\}, \tag{2.13}$$

we may generate the structure with the prescribed amount of twist as:

$$\mathcal{S}_{\text{twisted}} = \bigcup_{\substack{\Upsilon \in \mathcal{G}_{\text{twisted}}, \\ k=1,2,\ldots,M}} \Upsilon \circ \mathbf{r}_k = \bigcup_{\substack{m\in\mathbb{Z}, \\ n=0,1,\ldots,\mathfrak{N}-1 \\ k=1,2,\ldots,M}} \mathbf{R}_{(2\pi m\alpha+n\Theta)}\,\mathbf{r}_k + m\tau\,\mathbf{e_Z}\,. \tag{2.14}$$

In the above equations, $\mathbf{R}_{(2\pi m\alpha+n\Theta)}$ denotes the following rotation matrix with axis $\mathbf{e_Z}$:

$$\mathbf{R}_{(2\pi m\alpha+n\Theta)} = \begin{pmatrix} \cos(2\pi m\alpha + n\Theta) & -\sin(2\pi m\alpha + n\Theta) & 0 \\ \sin(2\pi m\alpha + n\Theta) & \cos(2\pi m\alpha + n\Theta) & 0 \\ 0 & 0 & 1 \end{pmatrix}. \tag{2.15}$$

Note that in this formulation, the structure continues to maintain its cyclic symmetries even after twisting. Also note that the formula in eq. 2.14 (and similarly, eq. 2.6) is meant to be species preserving in the sense that an atom in the simulated set $\mathcal{P}$ has the same atomic number as its images under the isometries in $\mathcal{G}_{\text{untwisted}}$ (or $\mathcal{G}_{\text{untwisted}}$).[1] Also note that by virtue of the above definitions, the group $\mathcal{G}_{\text{twisted}}$ serves as a physical symmetry group for the structure $\mathcal{S}_{\text{twisted}}$ in the sense that the action of any $\Upsilon \in \mathcal{G}_{\text{twisted}}$ on all the points in $\mathcal{S}_{\text{twisted}}$ leaves it invariant (and similarly for $\mathcal{G}_{\text{untwisted}}$ and $\mathcal{S}_{\text{untwisted}}$).

The group $\mathcal{G}_{\text{twisted}}$ will play a central role in the rest of this work. Note that this group subsumes the group $\mathcal{G}_{\text{untwisted}}$ in the sense that the latter can be recovered by simply setting $\alpha = 0$ in the former. In what follows, we will simplify notation a bit and simply use $\mathcal{G}$ to denote this group. Further, we will use the notation:

$$\Upsilon_{m,n} = \left(\mathbf{R}_{(2\pi m\alpha + n\Theta)} \,|\, m\tau\, \mathbf{e_Z} \right), \tag{2.16}$$

to denote group elements from $\mathcal{G}$. The action of $\Upsilon_{m,n}$ on a generic point in space is to rotate it about axis $\mathbf{e_Z}$ by angle $2\pi m\alpha + n\Theta$ while also translating it by $m\tau$ along the same axis.

In subsequent sections, we will describe how the Kohn-Sham problem for the entire twisted structure as posed on the global simulation domain, can be appropriately reformulated as a problem over a *fundamental domain* (or *symmetry adapted unit cell*), such that only the simulated atoms and the symmetry group $\mathcal{G}$ are involved in the resulting equations. This symmetry adapted computational domain has to be a regular region of space with sufficiently smooth boundaries that encompasses the simulated atoms and can be used to tile the global simulation domain by the action of the group $\mathcal{G}$. Furthermore, this region should be minimal in the sense that the above tiling operation should not produce intersecting volumes. In the context of the twisted tubular structures considered in this work, if the simulated atoms have radial coordinates lying between R_{in} and R_{out}, the following region

[1] More specifically, if the atom at $\mathbf{q}_k \in \mathcal{S}_{\text{twisted}}$ has atomic number Z, then the simulated atom at $\mathbf{r}_{k'}$ which satisfies $\mathbf{q}_k = \Upsilon \circ \mathbf{r}_{k'}$ for some $\Upsilon \in \mathcal{G}_{\text{twisted}}$ also has atomic number Z. Similarly also for $\mathcal{S}_{\text{untwisted}}$ and $\mathcal{G}_{\text{untwisted}}$.

serves as an appropriate fundamental domain (expressed using cylindrical coordinates):

$$\mathcal{D} = \left\{(r, \vartheta, z) \in \mathbb{R}^3 : R_{\text{in}} \leq r \leq R_{\text{out}}, \frac{2\pi\alpha z}{\tau} \leq \vartheta \leq \frac{2\pi\alpha z}{\tau} + \Theta, 0 \leq z \leq \tau\right\}. \tag{2.17}$$

The boundaries of the fundamental domain defined above can be expressed as:

$$\partial\mathcal{D} = \partial R_{\text{in}} \bigcup \partial R_{\text{out}} \bigcup \partial\vartheta_0 \bigcup \partial\vartheta_\Theta \bigcup \partial\mathcal{Z}_0 \bigcup \partial\mathcal{Z}_\tau \,. \tag{2.18}$$

Here ∂R_{in} and ∂R_{out} denote boundaries related to the radial direction (i.e., the surfaces $r = R_{\text{in}}$ and $r = R_{\text{out}}$ respectively), $\partial\vartheta_0$ and $\partial\vartheta_\Theta$ denote (z-dependent) bounding surfaces related to the angular direction (i.e., $\vartheta = \frac{2\pi\alpha z}{\tau}$ and $\vartheta = \frac{2\pi\alpha z}{\tau} + \Theta$ respectively), and finally, $\partial\mathcal{Z}_0$ and $\partial\mathcal{Z}_\tau$ denote boundaries related to the $\mathbf{e_Z}$ direction (i.e., the surfaces $z = 0$ and $z = \tau$ respectively). Note that for no applied twist, the region $\mathcal{D}$ is simply an annular cylindrical sector, i.e.,

$$\mathcal{D}^{\alpha=0} = \left\{(r, \vartheta, z) \in \mathbb{R}^3 : R_{\text{in}} \leq r \leq R_{\text{out}}, 0 \leq \vartheta \leq \Theta, 0 \leq z \leq \tau\right\}, \tag{2.19}$$

and the boundaries $\partial\vartheta_0$ and $\partial\vartheta_\Theta$ are then vertical surfaces perpendicular to the $\mathbf{e_Y}-\mathbf{e_Z}$ plane. Figure 2.1 shows two views of the fundamental domain used for the simulations used in this work and also highlights the boundaries described above. In what follows, we will formulate suitable versions of the equations of Kohn-Sham theory as posed on the simulation cell $\mathcal{D}$ and also elaborate on the conditions that have to be applied on the bounding surfaces that make up ∂D. Our derivation of the governing equations presented here is largely heuristic, and a more nuanced, mathematically rigorous discussion is available in (4).

2.1.2 Governing equations

2.1.2.1 Helical Bloch theorem and block-diagonalization of Hamiltonian

As described above (eq. 2.14), the atomic positions of the twisted structure can be described as the orbit of a discrete group of isometries (i.e., the group $\mathcal{G}$). Due to the presence of such symmetries in the system, it follows under fairly general hypotheses (54; 55; 7; 4) that the

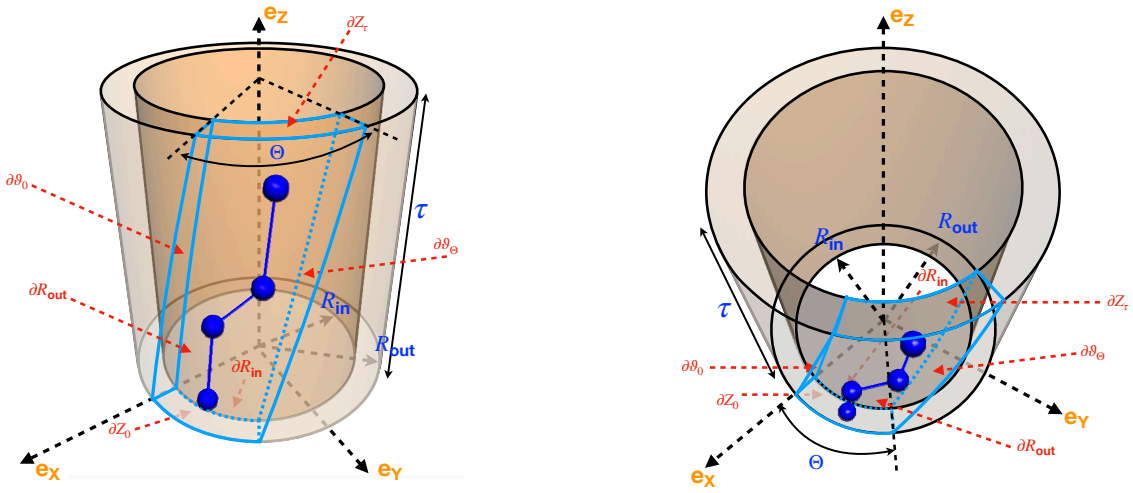

(a) Front view

(b) Top view

Figure 2.1: Illustration of the symmetry adapted unit cell or fundamental domain $\mathcal{D}$ (domain boundary lines in blue) of the twisted structure. The region $\mathcal{D}$ also serves as the computational domain for the calculations presented in this work. A few contained atoms as well as various bounding surfaces of the domain are also shown. For a tubular structure, the parameter $\Theta = 2\pi/\mathfrak{N}$ relates to the cyclic symmetry of the structure. The parameter τ is related to the pitch of the applied twist.

ground state electron density for such a system is invariant under the same symmetry group. Furthermore, the Kohn-Sham Hamiltonian for the system commutes with the symmetry operations of the group (65; 66). Consequently, the eigenstates of the Hamiltonian can be labeled using irreducible representations of the group $\mathcal{G}$, and they transform under action of the group in the same manner as the irreducible representations themselves do (54; 66; 65; 4). Since the group $\mathcal{G}$ is Abelian, results from group representation theory(67; 68) imply that the complex irreducible representations are one dimensional. These are the so called *complex characters* of $\mathcal{G}$, which, keeping in mind that $\mathcal{G}$ is the direct product of the groups $\mathcal{G}_{\text{helical}}$ and $\mathcal{G}_{\text{cyclic}}$, can be expressed as (for $m \in \mathbb{Z}, n \in \{0, 1, 2, \ldots, \mathfrak{N}-1\}$):

$$\widehat{\mathcal{G}} = \left\{ e^{2\pi i \left(m\eta + \frac{n\nu}{\mathfrak{N}}\right)} : \eta \in \left[-\frac{1}{2}, \frac{1}{2}\right); \nu \in \{0, 1, 2, \ldots, \mathfrak{N}-1\} \right\}. \tag{2.20}$$

In other words, for each value of $\eta \in$ and ν as defined above, the character $\hat{\zeta} \in \widehat{\mathcal{G}}$ is a complex valued map on the group[2], that assigns the value $e^{2\pi i\left(m\eta+\frac{n\nu}{\mathfrak{N}}\right)}$ to the group element $\Upsilon_{m,n} \in \mathcal{G}$. Since any character $\hat{\zeta} \in \widehat{\mathcal{G}}$ can be labeled using the pair (η, ν), these can be also used to label the eigenstates of the Kohn-Sham Hamiltonian, and other quantities related to its spectrum. Accordingly, we will use $\lambda_j(\eta,\nu)$, $\psi_j(\mathbf{x};\eta,\nu)$ and $g_j(\eta,\nu)$ to explicitly indicate the labels for the eigenvalues, the eigenvectors, and the electronic occupations, respectively. Collections of the eigenvalues, eigenvectors and electronic occupations will be denoted using Λ, Ψ and $\mathfrak{G}$ respectively, i.e.:

$$\begin{aligned}
\Lambda &= \left\{ \lambda_j(\eta,\nu) : \eta \in \big[-\frac{1}{2},\frac{1}{2}\big); \nu \in \{0,1,2,\ldots,\mathfrak{N}-1\}; j = 1,2,\ldots,\infty \right\}, \\
\Psi &= \left\{ \psi_j(\cdot;\eta,\nu) : \eta \in \big[-\frac{1}{2},\frac{1}{2}\big); \nu \in \{0,1,2,\ldots,\mathfrak{N}-1\}; j = 1,2,\ldots,\infty \right\}, \\
\mathfrak{G} &= \left\{ g_j(\eta,\nu) : \eta \in \big[-\frac{1}{2},\frac{1}{2}\big); \nu \in \{0,1,2,\ldots,\mathfrak{N}-1\}; j = 1,2,\ldots,\infty \right\}.
\end{aligned} \tag{2.21}$$

Mathematical properties of the characters and the above discussion lead to a number of important considerations that are worth mentioning at this point. First, as a consequence of the orthogonality relations obeyed by the characters (67; 68) the eigenstates associated with distinct characters are orthogonal to each other. This can be used to cast the Hamiltonian (which commutes with the symmetry operations in $\mathcal{G}$) in a symmetry adapted basis (66), such that it appears *block-diagonal* (54; 4). Since the blocks associated with distinct characters can be dealt with independently of each other and are of reduced dimension compared to the full Hamiltonian (within any finite dimensional approximation, e.g.), this implies that the problem of diagonalizing the Hamiltonian is greatly simplified. Second, the fact that the eigenstates of the Hamiltonian transform under symmetry operations in the same manner as the characters, implies that they obey a *Helical Bloch theorem* (54; 4; 64; 1), i.e., for any $\Upsilon_{m,n} \in \mathcal{G}$:

$$\psi_j(\Upsilon_{m,n}^{-1} \circ \mathbf{x};\eta,\nu) = e^{2\pi i\left(m\eta+\frac{n\nu}{\mathfrak{N}}\right)}\psi_j(\mathbf{x};\eta,\nu)\,, \tag{2.22}$$

[2] $\widehat{\mathcal{G}}$ is often referred to as the *dual group* of $\mathcal{G}$ in the mathematics literature (67; 68).

or equivalently:

$$\psi_j(\Upsilon_{m,n} \circ \mathbf{x}; \eta, \nu) = e^{-2\pi i\left(m\eta + \frac{n\nu}{\mathfrak{N}}\right)} \psi_j(\mathbf{x}; \eta, \nu)\,. \tag{2.23}$$

These relations can be used to deduce the conditions that need to be applied to the boundary surfaces of the fundamental domain while formulating the Kohn-Sham problem. Finally, in order to write down quantities that depend on all eigenstates cumulatively, we need to account for contributions from each $\zeta \in \widehat{\mathcal{G}}$. This amounts to integrating the eigenstate dependent quantities against a suitable integration measure over $\widehat{\mathcal{G}}$, i.e., by forming sums of the form $\frac{1}{\mathfrak{N}} \sum_{\nu=0}^{\mathfrak{N}-1}$, along with integrals in η. As an example, if we intend to compute the sum of the occupation numbers over all the electronic states in the system, we need to evaluate:

$$s = \int_{\mathfrak{I}} \frac{1}{\mathfrak{N}} \sum_{\nu=0}^{\mathfrak{N}-1} \sum_{j=1}^{\infty} g_j(\eta, \nu)\,. \tag{2.24}$$

Here and henceforth, $\mathfrak{I}$ is used to denote the set $\left[-\frac{1}{2}, \frac{1}{2}\right)$.

2.1.2.2 Electronic free energy functional and Kohn-Sham equations for twisted structure

In what follows, we will consider the (twisted) system of interest to be one in which the effects of spin can be ignored, and for which the electronic temperature is set at T_{e}. This implies that the electronic occupations can be expressed in terms of the Kohn-Sham eigenvalues as:

$$g_j(\eta, \nu) = f_{T_{\mathrm{e}}}\big(\lambda_j(\eta, \nu)\big)\,, \tag{2.25}$$

with $f_{T_{\mathrm{e}}}(\cdot)$ denoting the Fermi-Dirac function, i.e.,

$$f_{T_e}(y) = \frac{1}{1 + \exp\left(\frac{y - \lambda_{\mathrm{F}}}{k_{\mathrm{B}} T_{\mathrm{e}}}\right)}\,. \tag{2.26}$$

Here λ_{F} and k_{B} denote the system's Fermi level and the Boltzmann constant respectively. In order to motivate the correct form of the various terms of the governing equations for the twisted structure, we will often refer to the simpler, more well known expressions of

these quantities for finite (or isolated) systems. We will denote these finite system relevant quantities (scalar fields, energies, etc.) with a $^\circ$ superscript.

For a finite system (7; 69), the electron density can be expressed in terms of the Kohn-Sham eigenvectors and the electronic occupations as:

$$\rho^\circ(\mathbf{x}) = 2\sum_{j=1}^{\infty} g_j^\circ \, |\psi_j^\circ(\mathbf{x})|^2 \,. \tag{2.27}$$

Following the discussion above, this expression has to be modified for our case as:

$$\rho(\mathbf{x}) = 2\int_{\mathfrak{I}} \frac{1}{\mathfrak{N}} \sum_{\nu=0}^{\mathfrak{N}-1} \sum_{j=1}^{\infty} g_j(\eta,\nu) \, |\psi_j(\mathbf{x};\eta,\nu)|^2 \, d\eta \,. \tag{2.28}$$

Note that the factor of 2 in the expressions above is due to ignoring electronic spin. Further note that due to the Helical Bloch conditions obeyed by the Kohn-Sham eigenvectors (eq. 2.23), the expression above is invariant under the symmetry operations in $\mathcal{G}$, as is required of the ground state electron density.

- Electronic free energy: To derive the governing equations of Kohn-Sham theory for our system, we take recourse to an energy minimization approach (4; 7; 70). The relevant quantity in this case, since the system is of an extended nature, is the *ground state electronic free energy per unit fundamental domain*. We denote this quantity here as $\mathcal{F}(\mathfrak{G},\Psi,\mathcal{P},\mathcal{D},\mathcal{G})$ to emphasize its dependence on the electronic occupation numbers, the eigenstates, the positions of the simulated atoms, the fundamental domain and the symmetry group $\mathcal{G}$. Within the pseudopotential (71; 17) and Local Density Approximations (72), we may express it as:

$$\begin{aligned}\mathcal{F}(\mathfrak{G},\Psi,\mathcal{P},\mathcal{D},\mathcal{G}) = T_{\text{kin}}(\mathfrak{G},\Psi,\mathcal{P},\mathcal{D},\mathcal{G}) \, + \, E_{\text{xc}}(\rho,\mathcal{D}) \, + \, K(\mathfrak{G},\Psi,\mathcal{P},\mathcal{D},\mathcal{G}) \\ + \, E_{\text{el}}(\rho,\mathcal{P},\mathcal{D},\mathcal{G}) \, - \, T_{\text{e}} \, S(\mathfrak{G}) \,.\end{aligned} \tag{2.29}$$

The terms on the right-hand side of the above expression represent (per unit fundamental domain) the kinetic energy of the electrons, the exchange correlation energy, the nonlocal pseudopotential energy, the electrostatic energy and the electronic entropy contribution, respectively. We now elaborate on each of these quantities.

• Kinetic energy: The first term on the right hand side of the expression above is the electronic kinetic energy per unit fundamental domain. For an isolated system (placed in $\mathbb{R}^3$), this term can be expressed (69; 7) in terms of the Kohn-Sham eigenstates and the occupations as:

$$T^{\circ}_{\text{kin}} = \sum_{j=1}^{\infty} 2\, g^{\circ}_j \, \langle -\frac{1}{2}\Delta\psi^{\circ}_j, \psi^{\circ}_j \rangle_{\mathsf{L}^2(\mathbb{R}^3)} = \sum_{j=1}^{\infty} 2\, g^{\circ}_j \int_{\mathbb{R}^3} -\frac{1}{2}\Delta\psi^{\circ}_j(\mathbf{x})\, \overline{\psi^{\circ}_j(\mathbf{x})}\, d\mathbf{x}\,. \tag{2.30}$$

For the system at hand, this is modified to read:

$$T_{\text{kin}}(\mathfrak{G}, \Psi, \mathcal{P}, \mathcal{D}, \mathcal{G}) = \int_{\mathfrak{I}} \frac{1}{\mathfrak{N}} \sum_{\nu=0}^{\mathfrak{N}-1} \left(\sum_{j=1}^{\infty} 2\, g_j(\eta,\nu) \big\langle -\frac{1}{2}\Delta\psi_j(\cdot;\eta,\nu), \psi_j(\cdot;\eta,\nu) \big\rangle_{\mathsf{L}^2(D)} \right) d\eta\,. \tag{2.31}$$

• Exchange-correlation energy: The second term represents the exchange correlation energy per unit fundamental domain and is expressible using the Local Density Approximation (LDA) (72) as:

$$E_{\text{xc}}(\rho, \mathcal{D}) = \int_{\mathcal{D}} \varepsilon_{\text{xc}}[\rho(\mathbf{x})]\, \rho(\mathbf{x})\, d\mathbf{x}\,. \tag{2.32}$$

Note that the above formulation does not preclude the use of more sophisticated exchange correlation functionals such as the Generalized Gradient Approximation (73). Since the use of such functionals has little bearing on the subsequent discussion, we do not consider them further in this work.

• Nonlocal pseudopotential energy: The third term on the right hand side of eq. 2.29 represents the nonlocal pseudopotential energy per unit fundamental domain. For a finite system consisting of M° atoms located at the points $\{\mathbf{r}^{\circ}_k \in \mathbb{R}^3\}_{k=1}^{M^{\circ}}$, the non-local pseudopotential operator in Kleinman-Bylander form (74) can be written as:

$$\mathcal{V}^{\circ}_{\text{nl}} = \sum_{k=1}^{M^{\circ}} \sum_{p \in \mathcal{N}_k} \gamma_{k,p}\, \chi_{k,p}(\cdot;\mathbf{r}^{\circ}_k)\, \overline{\chi_{k,p}(\cdot;\mathbf{r}^{\circ}_k)}\,, \tag{2.33}$$

in terms of the projection functions $\{\chi_{k,p}(\cdot;\mathbf{r}_k)\}_{p=1}^{\mathcal{N}_k}$ and the corresponding normalization constants $\{\gamma_{k,p}\}_{p=1}^{\mathcal{N}_k}$ associated with the k^{th} atom (located at $\mathbf{y}_k$). The nonlocal pseudopotential

energy in that case has the form:

$$K^{\circ} = 2 \sum_{k=1}^{M^{\circ}} \sum_{p \in \mathcal{N}_k} \gamma_{k,p} \sum_{j=1}^{\infty} g_j \left| \langle \chi_{k,p}(\cdot; \mathbf{r}_k), \psi_j^{\circ}(\cdot) \rangle_{\mathsf{L}^2(\mathbb{R}^3)} \right|^2 \tag{2.34}$$

To obtain the analogous expression for the twisted structure, we consider the contributions from the atoms located within the fundamental domain and all the electronic states in the system (4) to get the nonlocal pseudopotential energy per unit fundamental domain as:

$$\begin{aligned} &K(\mathfrak{G}, \Psi, \mathcal{P}, \mathcal{D}, \mathcal{G}) \\ &= 2 \sum_{k=1}^{M} \sum_{p \in \mathcal{N}_k} \gamma_{k,p} \sum_{j=1}^{\infty} \int_{\mathfrak{I}} \frac{1}{\mathfrak{N}} \sum_{\nu=0}^{\mathfrak{N}-1} \left(g_j(\eta, \nu) \left| \left\langle \chi_{k,p}(\cdot; \eta, \nu; \mathbf{r}_k), \psi_j(\cdot; \eta, \nu) \right\rangle_{\mathsf{L}^2(\mathcal{C})} \right|^2 \right) d\eta \,. \end{aligned} \tag{2.35}$$

Here, the overlaps of the orbitals with the atom centered projectors are carried out over the global simulation domain $\mathcal{C}$, since the latter can have support extending beyond the fundamental domain. With the aid of the Helical Bloch Theorem (eq. 2.23) and by using the properties of the projection functions $\chi_{k,p}$, the integral implicit in the above expression can be reduced to the fundamental domain (7; 4), so that a more computationally convenient expression for the nonlocal pseudopotential energy per unit fundamental domain reads as:

$$\begin{aligned} &K(\mathfrak{G}, \Psi, \mathcal{P}, \mathcal{D}, \mathcal{G}) \\ &= 2 \sum_{k=1}^{M} \sum_{p \in \mathcal{N}_k} \gamma_{k,p} \sum_{j=1}^{\infty} \int_{\mathfrak{I}} \frac{1}{\mathfrak{N}} \sum_{\nu=0}^{\mathfrak{N}-1} \left(g_j(\eta, \nu) \left| \left\langle \hat{\chi}_{k,p}(\cdot; \eta, \nu; \mathbf{r}_k), \psi_j(\cdot; \eta, \nu) \right\rangle_{\mathsf{L}^2(\mathcal{D})} \right|^2 \right) d\eta \,. \end{aligned} \tag{2.36}$$

The functions $\hat{\chi}_{k,p}$ in the equation above can be expressed as:

$$\hat{\chi}_{k,p}(\mathbf{x}; \eta, \nu; \mathbf{r}_k) = \sum_{m \in \mathbb{Z}} \sum_{n=0}^{\mathfrak{N}-1} \chi_{k;p}\big(\Upsilon_{m,n} \circ \mathbf{x}; \mathbf{r}_k\big)\, e^{i2\pi(m\eta + \frac{n\nu}{\mathfrak{N}})} \,. \tag{2.37}$$

• Electrostatic interaction energy: The fourth term on the right hand side of eq. 2.29 represents the electrostatic interaction energy per unit fundamental domain. This includes the Coulombic attraction between the electrons and the nuclei, as well as the mutual repulsion between the electrons themselves. To express this term, it is useful to introduce the net electrostatic potential Φ, which also appears in the Kohn-Sham equations (as part of the

effective potential). To see how this can be done, we consider first a finite system placed in $\mathbb{R}^3$, with nuclei located at the points $\{\mathbf{r}_k^\circ \in \mathbb{R}^3\}_{k=1}^{M^\circ}$. For this example system, the net electrostatic potential Φ°, can be expressed in terms of the total charge of the (finite) system as:

$$\Phi^\circ(\mathbf{x}) = \int_{\mathbb{R}^3} \frac{\rho^\circ(\mathbf{y}) + b^\circ(\mathbf{y})}{\|\mathbf{x}-\mathbf{y}\|_{\mathbb{R}^3}}\, d\mathbf{y}\,. \tag{2.38}$$

Here, ρ° represents the electron density and b^{finite} represents the total nuclear pseudocharge. The latter can be expressed in terms of the individual nuclear pseudocharges $\left\{b_k(\mathbf{x};\mathbf{r}_k^\circ)\right\}_{k=1}^{M^\circ}$ as:

$$b^\circ(\mathbf{x}) = \sum_{k=1}^{M^\circ} b_k(\mathbf{x};\mathbf{r}_k^\circ)\,, \tag{2.39}$$

Note that for each atom, the pseudocharge (typically a smooth, radially symmetric, compactly supported function) integrates to its valence nuclear charge, i.e.,

$$\int_{\mathbb{R}^3} b_k(\mathbf{x};\mathbf{r}_k^\circ)\, d\mathbf{x} = Z_k\,. \tag{2.40}$$

The connection between the potential Φ° and the electrostatic interaction energy is that we may express the latter as:

$$\begin{aligned} E_{\text{el}}^\circ = \max_{\widetilde{\Phi}^\circ}\Big\{ -\frac{1}{8\pi}\int_{\mathbb{R}^3} |\nabla\widetilde{\Phi}^\circ|^2\, d\mathbf{x} + \int_{\mathbb{R}^3} (\rho^\circ + b^\circ)\,\widetilde{\Phi}^\circ\, d\mathbf{x}\Big\} \\ + E_{\text{sc}}^\circ(\mathbf{r}_1^\circ, \mathbf{r}_2^\circ, \ldots, \mathbf{r}_k^\circ)\,, \end{aligned} \tag{2.41}$$

and the scalar field $\widetilde{\Phi}^\circ$ which attains the maximum in the above problem is precisely the one presecribed using eq. 2.38. Note that the constant term $E_{\text{sc}}^\circ(\mathbf{r}_1^\circ, \mathbf{r}_2^\circ, \ldots, \mathbf{r}_k^\circ)$ is added as a correction for self-interactions and possible overlaps of the nuclear pseudocharges (75). It is independent of $\widetilde{\Phi}^\circ$ and does not play a role in the above optimization problem.

With the above discussion in mind, we may now introduce the net electrostatic potential for the twisted structure using the electron density (eq. 2.28) and the net nuclear pseudocharge associated with the system, in a manner that is analogous to eq. 2.38, i.e.,

$$\Phi(\mathbf{x}) = \int_{\mathcal{C}} \frac{\rho(\mathbf{y}) + b(\mathbf{y},\mathcal{P},\mathcal{G})}{\|\mathbf{x}-\mathbf{y}\|_{\mathbb{R}^3}}\, d\mathbf{y}\,, \tag{2.42}$$

The net nuclear pseudocharge at any point in the global simulation domain can be expressed using the pseudocharges of the atoms in the fundamental domain as:

$$b(\mathbf{x},\mathcal{P},\mathcal{G}) = \sum_{m\in\mathbb{Z}}\sum_{n=0}^{\mathfrak{N}-1}\sum_{k=1}^{M} b_k(\mathbf{x};\Upsilon_{m,n}\circ\mathbf{r}_k)\,, \tag{2.43}$$

Note that since the electron density is group invariant, as is the net nuclear pseudocharge (by construction), the total electrostatic potential for the twisted structure is group invariant as well. Thus, it suffices to compute this quantity over the fundamental domain, in addition to specifying boundary conditions that are consistent with the group invariance of the function. Following eq. 2.41, we now write the electrostatic interaction energy per unit fundamental domain as:

$$\begin{aligned} E_{\mathrm{el}}(\rho,\mathcal{P},\mathcal{D},\mathcal{G}) = \max_{\widetilde{\Phi}}\Bigg\{ -\frac{1}{8\pi}\int_{\mathcal{D}} |\nabla\widetilde{\Phi}|^2\,d\mathbf{x} + \int_{\mathcal{D}}\Big(\rho(\mathbf{x}) + b(\mathbf{x},\mathcal{P},\mathcal{G})\Big)\widetilde{\Phi}(\mathbf{x})\,d\mathbf{x}\Bigg\} \\ + E_{\mathrm{sc}}(\mathcal{P},\mathcal{G},\mathcal{D})\,. \end{aligned} \tag{2.44}$$

The scalar field $\widetilde{\Phi}$ which attains the maximum in the above problem, is the same one specified in eq. 2.42. The constant (i.e., $\widetilde{\Phi}$-independent) term $E_{\mathrm{sc}}(\mathcal{P},\mathcal{G},\mathcal{D})$ accounts for self-interaction corrections and possible overlaps between pseudocharges. We omit the details of this term here for the sake of brevity, and cite references (55; 69; 75) for relevant details.

- Electronic entropy: Finally, the last term on the right hand side of eq. 2.29 deals with the contribution of the electronic entropy to the free energy. Using Fermi-Dirac smearing, for a finite system at electronic temperature T_{e}, the electronic entropy can be represented :

$$S^{\circ} = -2\,k_{\mathrm{B}}\sum_{j=1}^{\infty} g_j^{\circ}\log(g_j^{\circ}) + (1-g_j^{\circ})\,\log(1-g_j^{\circ})\,. \tag{2.45}$$

Analogously, the corresponding term for the twisted structure reads as:

$$S(\mathfrak{G}) = -2\,k_{\mathrm{B}}\int_{\mathfrak{I}}\left[\frac{1}{\mathfrak{N}}\sum_{\nu=0}^{\mathfrak{N}-1}\sum_{j=1}^{\infty} g_j(\eta,\nu)\log\big(g_j(\eta,\nu)\big) + \big(1-g_j(\eta,\nu)\big)\,\log\big(1-g_j(\eta,\nu)\big)\right]d\eta\,. \tag{2.46}$$

• Kohn-Sham Equations: With the expressions for the various energy terms in place, we write the electronic ground-state energy for the twisted structure as the following minimization problem:

$$\mathcal{F}_{\substack{\text{Ground}\\\text{State}}}(\mathcal{P},\mathcal{D},\mathcal{G}) = \inf._{\Psi,\mathfrak{G}}\, \mathcal{F}(\mathfrak{G},\Psi,\mathcal{P},\mathcal{D},\mathcal{G})\,, \tag{2.47}$$

with the added constraints that:

1. the orbitals in Ψ are helical Bloch states, namely, they obey eq. 2.23 and are orthonormal over the fundamental domain for each $\zeta \in \widehat{\mathcal{G}}$, i.e.:

$$\langle \psi_j(\cdot;\eta,\nu), \psi_{j'}(\cdot;\eta,\nu)\rangle_{\mathsf{L}^2(\mathcal{D})} = \delta_{j,j'}\,, \tag{2.48}$$

   and,

2. the number of electrons per unit fundamental domain is a fixed number, i.e.,

$$\int_{\mathcal{D}} \rho(\mathbf{x})\, d\mathbf{x} = \frac{2}{\mathfrak{N}} \sum_{\nu=0}^{\mathfrak{N}-1} \int_{\mathfrak{I}} \sum_{j=1}^{\infty} g_j(\eta,\nu) = N_{\mathrm{e}}\,. \tag{2.49}$$

The Euler-Lagrange equations corresponding to the above variational problem are the Kohn-Sham equations for the twisted structure, as posed on the fundamental domain. For $j \in \mathbb{N}$, $\eta \in \mathfrak{I}$ and $\nu = 0, 1, \ldots \mathfrak{N}-1$, we may express them as:

$$\mathfrak{H}^{\mathrm{KS}}\, \psi_j(\cdot;\eta,\nu) = \lambda_j(\eta,\nu)\, \psi_j(\cdot;\eta,\nu)\,, \tag{2.50}$$

with $\mathfrak{H}^{\mathrm{KS}}$ denoting the Kohn-Sham operator, i.e.:

$$\mathfrak{H}^{\mathrm{KS}} \equiv -\frac{1}{2}\Delta + V_{\mathrm{xc}} + \Phi + \mathcal{V}_{\mathrm{nl}}\,. \tag{2.51}$$

Here, V_{xc} denotes the exchange correlation potential:

$$V_{\mathrm{xc}} = \frac{\delta E_{\mathrm{xc}}(\rho,\mathcal{D})}{\delta\rho} = \varepsilon_{\mathrm{xc}} + \rho\,\frac{d\varepsilon_{\mathrm{xc}}}{d\rho}\,, \tag{2.52}$$

Φ (as introduced in eq. 2.42) denotes the net electrostatic potential arising from the electrons and the nuclear pseudocharges, and obeys the Poisson equation:

$$-\Delta\Phi = 4\pi\left(\rho + b(\cdot, \mathcal{P}, \mathcal{G})\right), \tag{2.53}$$

while $\mathcal{V}_{\text{nl}}$ denotes the non-local pseudoptential operator (specifically, its (η, ν) component), and can be expressed in terms of the functions $\hat{\chi}_{k,p}$ (introduced in eq. 2.37) as:

$$\mathcal{V}_{\text{nl}} = \sum_{k=1}^{M} \sum_{p \in \mathcal{N}_k} \gamma_{k,p}\, \hat{\chi}_{k,p}(\cdot; \eta, \nu; \mathbf{x}_k)\, \overline{\hat{\chi}_{k,p}(\cdot; \eta, \nu; \mathbf{x}_k)} \tag{2.54}$$

Note that the use of eq. 2.53 in lieu of eq. 2.42 is preferable for practical calculations since computationally inconvenient non-local integrals that appear in the latter equation are avoided (76; 75; 77; 7). Together, eqs. 2.50 - 2.54, along with eq. 2.48 and 2.49 form the governing equations for our system and need to be solved self-consistently.

2.1.3 Boundary Conditions

The unknown fields in the governing equations above are the orbitals $\psi_j(\cdot; \eta, \nu) \in \Psi$ and the electrostatic potential Φ. Since these fields are posed on the fundamental domain $\mathcal{D}$, we need to augment the governing equations with boundary conditions on the surfaces that make up $\partial\mathcal{D}$. By using the conditions in eq. 2.23 on the orbitals, and observing that the symmetry operation $\Upsilon_{1,0} = \left(\mathbf{R}_{2\pi\alpha} \,|\, \tau\, \mathbf{e_Z}\right)$ maps $\partial\mathcal{Z}_0$ to $\partial\mathcal{Z}_\tau$, while the operation $\Upsilon_{0,1} = \left(\mathbf{R}_\Theta \,|\, \mathbf{0}\right)$ maps $\partial\vartheta_0$ to $\partial\vartheta_\Theta$, we arrive at:

$$\psi_j(\mathbf{x} \in \partial\mathcal{Z}_\tau, \eta, \nu) = e^{-2\pi i \eta} \psi_j(\mathbf{x} \in \partial\mathcal{Z}_0, \eta, \nu)\,, \tag{2.55}$$

$$\psi_j(\mathbf{x} \in \partial\vartheta_\Theta, \eta, \nu) = e^{-2\pi i \frac{\nu}{\mathfrak{N}}} \psi_j(\mathbf{x} \in \partial\vartheta_0, \eta, \nu)\,. \tag{2.56}$$

Concurrently, since the net electrostatic potential is invariant under all symmetry operations in $\mathcal{G}$, it obeys the boundary conditions:

$$\Phi(\mathbf{x} \in \partial\mathcal{Z}_\tau) = \Phi(\mathbf{x} \in \partial\mathcal{Z}_0)\,, \tag{2.57}$$

$$\Phi(\mathbf{x} \in \partial\vartheta_\Theta) = \Phi(\mathbf{x} \in \partial\vartheta_0)\,. \tag{2.58}$$

The above equations leave the boundary conditions on the surfaces ∂R_{in} and ∂R_{out} unspecified. As far as the wavefunctions are concerned, we may enforce Dirichlet boundary conditions on these surfaces, by appealing to the decay of the electron density along the radial direction (4; 7). This gives us:

$$\psi_j(\mathbf{x} \in \partial R_{\text{in}}, \eta, \nu) = \psi_j(\mathbf{x} \in \partial R_{\text{out}}, \eta, \nu) = 0\,. \tag{2.59}$$

On the other hand, the electrostatic potential Φ may not decay to zero quickly along the radial direction. Therefore, it is more prudent to set $\Phi(\mathbf{x} \in \partial R_{\text{in}})$ and $\Phi(\mathbf{x} \in \partial R_{\text{out}})$ by direct evaluation of eq. 2.42 by using a modified version of the Ewald summation technique (78). In practical calculations however, this correction may be sometimes ignored (4) in favor of Dirichlet boundary conditions on those surfaces.

2.1.4 Other quantities of interest at self-consistency

At the end of the self consistent field iterations, a number of other quantities may be computed from the converged electronic states. For instance, we may obtain a more accurate estimate (i.e., one that is less sensitive to self-consistency errors) of the Kohn-Sham ground state electronic free energy (per unit fundamental domain) by using the Harris-Foulkes functional (79; 80) instead of eq. 2.29. This can be written for the twisted structure, using quantities expressed over the fundamental domain as:

$$\begin{aligned}\mathcal{F}^{\text{HF}}(\Lambda, \Psi, \mathcal{P}, \mathcal{D}, \mathcal{G}) = 2 \int_{\mathfrak{I}} \frac{1}{\mathfrak{N}} \sum_{\nu=0}^{\mathfrak{N}-1} \sum_{j=1}^{\infty} \lambda_j(\eta, \nu)\, g_j(\eta, \nu)\, d\eta + E_{\text{xc}}(\rho, \mathcal{D}) \\ - \int_{\mathcal{D}} V_{\text{xc}}(\rho(\mathbf{x}))\rho(\mathbf{x})\, d\mathbf{x} + \frac{1}{2} \int_{\mathcal{D}} \Big(b(\mathbf{x}, \mathcal{P}, \mathcal{G}) - \rho(\mathbf{x}) \Big) \Phi(\mathbf{x})\, d\mathbf{x} \\ + E_{\text{sc}}(\mathcal{P}, \mathcal{G}, \mathcal{D}) - T_{\text{e}}\, S(\Lambda)\,.\end{aligned} \tag{2.60}$$

Note that the first term on the right hand side of the above equation is the electronic band energy.

For ab initio molecular dynamics or structural relaxation calculations, atomic forces need to be calculated. The Hellmann-Feynman forces on the atom located at $\mathbf{r}_k$ in the fundamental

domain can be computed about the ground-state as:

$$\begin{aligned}\mathbf{f}_k &= -\frac{\partial \mathcal{F}(\mathfrak{G},\Psi,\mathcal{P},\mathcal{D},\mathcal{G})}{\partial \mathbf{r}_k}\bigg|_{\substack{\text{Ground}\\ \text{State}}} \\ &= \sum_{m\in\mathbb{Z}}\sum_{n=0}^{\mathfrak{N}-1}(\mathbf{R}_{2\pi m\alpha+n\Theta})^{-1}\int_{\mathcal{D}}\nabla b_k\big(\mathbf{x};(\Upsilon_{m,n}\circ\mathbf{x}_k\big)\Phi(\mathbf{x})\,d\mathbf{x} - \frac{\partial E_{\text{sc}}(\mathcal{P},\mathcal{G},\mathcal{D})}{\partial \mathbf{r}_k} \\ &\quad - 4\sum_{j=1}^{\infty}\Bigg(\int_{\mathfrak{I}}\frac{1}{\mathfrak{N}}\sum_{\nu=0}^{\mathfrak{N}-1}g_j(\eta,\nu)\sum_{p\in\mathcal{N}_k}\gamma_{k;p}\,\text{Re.}\Bigg\{\Bigg[\int_{\mathcal{D}}\hat{\chi}_{k,p}(\mathbf{x};\eta,\nu;\mathbf{r}_k)\,\overline{\psi_j(\mathbf{x};\eta,\nu)}\,d\mathbf{x}\Bigg] \\ &\qquad\qquad \times\Bigg[\int_{\mathcal{D}}\psi_j(\mathbf{x};\eta,\nu)\,\overline{\frac{\partial\hat{\chi}_{k,p}(\mathbf{x};\eta,\nu;\mathbf{r}_k)}{\partial\mathbf{r}_k}}\,d\mathbf{x}\Bigg]\Bigg\}\Bigg)\,d\eta\,.\end{aligned} \tag{2.61}$$

Note that since the forces are derivatives of a free energy which is invariant with respect to the symmetry operations in $\mathcal{G}$, it follows that the force on an atom $\Upsilon_{m,n}\circ\mathbf{r}_k$ located outside the fundamental domain can be evaluated in terms of the force on its counterpart in the fundamental domain as $(\mathbf{R}_{2\pi m\alpha+n\Theta})^{-1}\mathbf{f}_k$ (45). Thus, to perform structural relaxations on the twisted structure, it suffices to concentrate on the atoms in the fundamental domain and drive their forces to zero.

Finally, the electronic density of states which often offers useful information about the electronic properties of a material under study, can be computed at an electronic temperature T_{e} as (81):

$$\aleph_{T_{\text{e}}}(E) = 2\int_{\mathfrak{I}}\frac{1}{\mathfrak{N}}\sum_{\nu=0}^{\mathfrak{N}-1}\Bigg(\sum_{j=1}^{\infty}f'_{T_{\text{e}}}\big(E-\lambda_j(\eta,\nu)\big)\Bigg)\,d\eta\,, \tag{2.62}$$

with $f'_{T_{\text{e}}}(\cdot)$ denoting the derivative of the Fermi-Dirac function.

2.1.5 Comments on first principle simulations of torsional and extensional deformation applied to the nanotubes

Here we would like to comment on how the torsional and extensional deformations are simulated using Helical DFT. The approach taken is similar to that of linear elastic deformation

of a crystal (82; 83). To elaborate, let us consider the torsional deformation. Within the HelicalDFT framework, the rate of twist is controlled by the parameter α (which can be prescribed by the user independently) that introduce a twist to the fundamental domain. Given the prescribed twist, within the deformed fundamental domain, the positions of the atoms are allowed to relax under the influence of external forces or constraints mimicking a torque applied at the two ends of the infinite nanotube during relaxation. Note that utilizing Born-Oppenheimer approximation, the atomic relaxation process is separated from the electronic structure calculations, allowing for a optimization of the atomic positions, while assuming that the electronic configuration remains in its ground state for every given atomic configuration(82). Therefore, under the Born-Oppenheimer approximation, we assume that the electronic structure adjusts rapidly to changes in nuclear positions, effectively reaching its ground state configuration instantaneously compared to the much slower motion of the nuclei (or fictitious atomic motion during the relaxation process). Note that, due to the very large difference in masses of the electrons and the nuclei, the time scale associated with their motions differ by orders of magnitude. Thus, for a given arrangement of nuclei, the electronic configuration is assumed to be in its ground state, allowing us to solve the Kohn-Sham equations independently of the nuclear motions. This decoupling simplifies the overall problem, as it allows us to treat the electronic and nuclear motions as separate problems with the nuclear coordinates feeding into the electronic structure problem and the Hellman-Feynman forces from the electronic structure problem feeding back into the atomic motion/structural relaxation problem. The adaptation of helical symmetry constraints in Helical DFT ensures that atomic positions evolve in a manner consistent with the nanotube's symmetry and deformation under the external stress, controlled by α or τ, thereby preventing the atoms from reverting to their original untwisted positions. Instead, the relaxation process converges to a new equilibrium configuration that reflects the deformed state of the nanotube. If the value of α is too high, it is possible that the nanotube will develop instability, as a result, the original fundamental domain may be incapable of capturing this instability. Therefore, we

limit the range of deformation to be within linear elastic response. However, if desired, a larger fundamental domain can be used with a larger α to explore responses far away from equilibrium.

2.2 Implementation

We now discuss different numerical and computational aspects of the implementation of the above methodology.

2.2.1 Use of helical coordinates

The equations in Section 2.1 above are expressed in a manner that do not make any explicit reference to a coordinate system. For numerical implementation purposes however, it is useful to introduce a coordinate system that is commensurate with the geometry of the twisted structure and the symmetries of the system. The helical coordinate system, introduced in (54; 4) is well suited for these purposes. If a point $\mathbf{p}$ in the global simulation domain $\mathcal{C}$ has Cartesian coordinates $(x_{\mathbf{p}}, y_{\mathbf{p}}, z_{\mathbf{p}})$ and cylindrical coordinates $(r_{\mathbf{p}}, \vartheta_{\mathbf{p}}, z_{\mathbf{p}})$, then the corresponding helical coordinates $(r_{\mathbf{p}}, \theta_{1\,\mathbf{p}}, \theta_{2\,\mathbf{p}})$ are defined as:

$$\begin{aligned} r_{\mathbf{p}} &= \sqrt{x_{\mathbf{p}}^2 + y_{\mathbf{p}}^2}\,,\ \theta_{1\,\mathbf{p}} = \frac{z_{\mathbf{p}}}{\tau}\,, \\ \theta_{2\,\mathbf{p}} &= \frac{1}{2\pi}\arctan2(y_{\mathbf{p}}, x_{\mathbf{p}}) - \alpha\frac{z_{\mathbf{p}}}{\tau} = \frac{\vartheta_{\mathbf{p}}}{2\pi} - \alpha\frac{z_{\mathbf{p}}}{\tau}\,. \end{aligned} \tag{2.63}$$

The helical coordinates reduce to the usual cylindrical coordinates when the twist parameter of the system is 0 and the pitch τ is set to unity. The inverse relations:

$$x_{\mathbf{p}} = r_{\mathbf{p}}\cos\big(2\pi(\alpha\theta_{1\,\mathbf{p}} + \theta_{2\,\mathbf{p}})\big)\,,\ y_{\mathbf{p}} = r_{\mathbf{p}}\sin\big(2\pi(\alpha\theta_{1\,\mathbf{p}} + \theta_{2\,\mathbf{p}})\big)\,,\ z_{\mathbf{p}} = \tau\,\theta_{1\,\mathbf{p}}\,, \tag{2.64}$$

map the helical coordinates of $\mathbf{p}$ to their Cartesian counterparts.

The coordinate transformations introduced above can be used to map the curvilinear coordinate system associated with the twisted structure, to a rectilinear one in which com-

putations are simpler to set up. Specifically, the relations in eq. 2.64 above map the cuboid $(R_{\text{in}}, R_{\text{out}}) \times (0,1) \times (0, 1/\mathfrak{N})$ to the fundamental domain $\mathcal{D}$. In particular, the bounding surfaces of the fundamental domain can be described in helical coordinates as $r = R_{\text{in}}$ (for ∂R_{in}), $r = R_{\text{out}}$ (for ∂R_{out}), $\theta_1 = 0$ (for $\partial \mathcal{Z}_0$), $\theta_1 = 1$ (for $\partial \mathcal{Z}_\tau$), $\theta_2 = 0$ (for $\partial \vartheta_0$) and $\theta_2 = 1/\mathfrak{N}$ (for $\partial \vartheta_\Theta$). Furthermore, the symmetry operation $\Upsilon_{m,n}$ maps the helical coordinates of a point $\mathbf{p}$ from $(r_{\mathbf{p}}, \theta_{1\,\mathbf{p}}, \theta_{2\,\mathbf{p}})$ to $(r_{\mathbf{p}}, \theta_{1\,\mathbf{p}} + m, \theta_{2\,\mathbf{p}} + \frac{n}{\mathfrak{N}})$.

In order to express the equations in Section 2.1.2 in helical coordinates, we need the the Laplacian operator, the Cartesian gradient and the integral of a function (over the fundamental domain) expressed in helical coordinates. For a function $f(r, \theta_1, \theta_2)$ these take the form (4):

$$\Delta f = \frac{\partial^2 f}{\partial r^2} + \frac{1}{r}\frac{\partial f}{\partial r} + \frac{1}{\tau^2}\frac{\partial^2 f}{\partial \theta_1^2} - \frac{2\alpha}{\tau^2}\frac{\partial^2 f}{\partial \theta_1 \partial \theta_2} + \frac{1}{4\pi^2}\left(\frac{1}{r^2} + \frac{4\pi^2\alpha^2}{\tau^2}\right)\frac{\partial^2 f}{\partial \theta_2^2}\,, \tag{2.65}$$

$$\begin{aligned}\nabla f = &\left(\frac{\partial f}{\partial r}\cos\big(2\pi(\alpha\theta_1 + \theta_2)\big) - \frac{\partial f}{\partial \theta_2}\frac{\sin\big(2\pi(\alpha\theta_1 + \theta_2)\big)}{2\pi r}\right)\mathbf{e_X} \\ &+ \left(\frac{\partial f}{\partial r}\sin\big(2\pi(\alpha\theta_1 + \theta_2)\big) - \frac{\partial f}{\partial \theta_2}\frac{\cos\big(2\pi(\alpha\theta_1 + \theta_2)\big)}{2\pi r}\right)\mathbf{e_Y} \\ &+ \left(\frac{1}{\tau}\Big(\frac{\partial f}{\partial \theta_1} - \alpha\frac{\partial f}{\partial \theta_2}\Big)\right)\mathbf{e_Z}\end{aligned} \tag{2.66}$$

$$\int_{\mathbf{x}\in\mathcal{D}} f(\mathbf{x})\, d\mathbf{x} = \int_{r=R_{\text{in}}}^{r=R_{\text{out}}}\int_{\theta_1=0}^{\theta_1=1}\int_{\theta_2=0}^{\theta_2=\frac{1}{\mathfrak{N}}} f(r,\theta_1,\theta_2)\, 2\pi\tau r\, dr\, d\theta_1\, d\theta_2\,. \tag{2.67}$$

Upon expressing the Kohn-Sham orbitals as $\psi_j(r, \theta_1, \theta_2; \eta, \nu)$, the above expressions allow the governing equations and boundary conditions to be expressed in helical coordinates exclusively. For numerical implementation purposes however, it is convenient to work with functions that are completely invariant under symmetry operations instead of being invariant upto a Bloch phase, as the orbitals are. To this end, we write:

$$\psi_j(r, \theta_1, \theta_2; \eta, \nu) = e^{-2\pi i(\eta\theta_1 + \nu\theta_2)}\, u_j(r, \theta_1, \theta_2; \eta, \nu)\,, \tag{2.68}$$

where the functions $u_j(r, \theta_1, \theta_2; \eta, \nu)$ are group invariant. In terms of these auxiliary func-

tions, the governing equations over the fundamental domain are:

$$
\begin{aligned}
&-\frac{1}{2}\Delta u_j(r,\theta_1,\theta_2;\eta,\nu) - \frac{2i\pi}{\tau^2}\left(\nu\alpha-\eta\right)\frac{\partial u_j(r,\theta_1,\theta_2;\eta,\nu)}{\partial\theta_1}\\
&-2i\pi\left(\frac{\alpha}{\tau^2}\left(\eta-\nu\alpha\right)-\frac{\nu}{4\pi^2r^2}\right)\frac{\partial u_j(r,\theta_1,\theta_2;\eta,\nu)}{\partial\theta_2}\\
&+\left(\frac{\nu^2}{2r^2}-\frac{2\pi^2}{\tau^2}\left\{\nu\alpha\left(2\eta-\nu\alpha\right)-\eta^2\right\}+V_{\mathrm{xc}}(r,\theta_1,\theta_2)+\Phi(r,\theta_1,\theta_2)\right)u_j(r,\theta_1,\theta_2;\eta,\nu)\\
&+e^{2\pi i\left(\eta\theta_1+\nu\theta_2\right)}\,\mathcal{V}_{\mathrm{nl}}\,e^{-2\pi i\left(\eta\theta_1+\nu\theta_2\right)}u_j(r,\theta_1,\theta_2;\eta,\nu)=\lambda_j(\eta,\nu)\,u_j(r,\theta_1,\theta_2;\eta,\nu)\,,
\end{aligned}
\tag{2.69}
$$

$$
-\frac{1}{2}\Delta\Phi(r,\theta_1,\theta_2)=\rho(r,\theta_1,\theta_2)+b(r,\theta_1,\theta_2;\mathcal{P},\mathcal{G})
\tag{2.70}
$$

$$
\rho(r,\theta_1,\theta_2)=2\int_{\mathfrak{I}}\frac{1}{\mathfrak{N}}\sum_{\nu=0}^{\mathfrak{N}-1}\sum_{j=1}^{\infty}g_j(\eta,\nu)\left|u_j(r,\theta_1,\theta_2;\eta,\nu)\right|^2d\eta\,,
\tag{2.71}
$$

$$
g_j(\eta,\nu)=f_{T_{\mathrm{e}}}\left(\lambda_j(\eta,\nu)\right),\ \frac{2}{\mathfrak{N}}\sum_{\nu=0}^{\mathfrak{N}-1}\int_{\mathfrak{I}}\sum_{j=1}^{\infty}g_j(\eta,\nu)=N_{\mathrm{e}}
\tag{2.72}
$$

The boundary conditions[3] are:

$$
\begin{aligned}
u_j(r=R_{\mathrm{out}},\theta_1,\theta_2;\eta,\nu)&=u_j(r=R_{\mathrm{out}},\theta_1,\theta_2;\eta,\nu)=0\,,\\
u_j(r,\theta_1=0,\theta_2;\eta,\nu)&=u_j(r,\theta_1=1,\theta_2;\eta,\nu)\,,\\
u_j(r,\theta_1,\theta_2=0;\eta,\nu)&=u_j(r,\theta_1,\theta_2=\frac{1}{\mathfrak{N}};\eta,\nu)\,.
\end{aligned}
\tag{2.73}
$$

$$
\begin{aligned}
\Phi(r=R_{\mathrm{out}},\theta_1,\theta_2)=\phi_{R_{\mathrm{out}}}\,,\ \Phi(r=R_{\mathrm{in}},\theta_1,\theta_2)=\phi_{R_{\mathrm{in}}}\,,\\
\Phi(r,\theta_1=0,\theta_2)=\Phi(r,\theta_1=1,\theta_2)\,,\\
\Phi(r,\theta_1,\theta_2=0)=\Phi(r,\theta_1,\theta_2=\frac{1}{\mathfrak{N}})\,.
\end{aligned}
\tag{2.74}
$$

2.2.2 Approximation of infinite series in governing equations

The governing equations as posed above, contain series sums over infinite numbers of terms which need to be truncated for the purposes of numerical implementation. Such infinite

[3]The use of $R_{\mathrm{in}}>0$ is well justified for tubes with large enough radii (based on wavefunction decay effects or the nearsightedness principle (84), for example), such as the ones considered in this work. This has the added benefit of being able to computationally avoid the coordinate singularities in the Laplacian at the origin, without incurring any performance or accuracy issues.

sums not only appear explicitly while summing over an infinite number of electronic states (eqs. 2.71, 2.72), but also implicitly in the calculation of quantities such as the net pseudocharge (eqs. 2.70, 2.43) and the nonlocal pseudopotential operator (eqs. 2.69, 2.54, 2.37). We now describe our strategies for dealing with such quantities.

In order to truncate sums involving an infinite number of electronic states, we may assume — as is commonly done in the literature (85; 86), that the electronic occupation numbers decay to zero beyond the lowest N_{s} electronic states. In effect, this implies that sums over the index j in equations 2.71 - 2.72 run from 1 to N_{s} (instead of 1 to ∞), and that a set of N_{s} eigenvalue problems for each value of η and ν, as posed in eq. 2.69, have to be considered. In practical calculations when the electronic temperature is less than a few thousand Kelvin, the number of states N_{s} can be related to the number of electrons per unit cell N_{e} as $N_{\mathrm{s}} = \lceil c_{\mathrm{s}} \times \frac{N_{\mathrm{e}}}{2} \rceil$, with the constant c_{s} chosen to be between 1.05 and 1.20 (86).

The infinite sums involved in calculation of the net pseudocharge and the non-local pseudopotential operator both arise due to summations over individual atoms in the fundamental domain, as well as their repeated images under the group $\mathcal{G}$ (eqs. 2.43, 2.54, 2.37). However, we observe that the functions being summed in these cases are always centered about the atoms in question, and they have the property of being compactly supported in a small spherical region of space around the atom (i.e., the functions $b_k(\cdot)$ in eq. 2.43 and $\chi_{k;p}(\cdot)$ in eq. 2.37 all have this property). Thus, the contribution of such terms to the fundamental domain is zero beyond a few terms of the series expressed in eqs. 2.43 and 2.37, and the infinite summations in these expressions can be reduced to a set of values of m and n that are near zero.[4]

[4]This typically involves $m = \pm 1, \pm 2, \pm 3$, etc., from the helical symmetry operations, and $n = 1, 2, 3, \mathfrak{N} - 1, \mathfrak{N} - 2, \mathfrak{N} - 3$, etc. from the cyclic symmetry operations.

2.2.3 Discretization Strategy

The equations above need to be discretized in real space (i.e., over the fundamental domain $\mathcal{D}$) as well as in reciprocal space (i.e., over the set $\widehat{\mathcal{G}}$). We now describe our strategies for addressing each of these issues.

2.2.3.1 Real space discretization of the fundamental domain

We use a higher order finite difference scheme (87; 88; 89; 90; 69; 70; 7; 4) for real space discretization. Since helical coordinates have the property of "unwrapping" the fundamental domain $\mathcal{D}$ to a cuboid, a convenient meshing of the computational domain can be attained by choosing equispaced points in the r, θ_1 and θ_2 directions. Accordingly, we choose $\mathscr{N}_r$, $\mathscr{N}_{\theta_1}$ and $\mathscr{N}_{\theta_2}$ grid points along these directions (respectively), and observe that the corresponding mesh spacings $h_r, h_{\theta_1}, h_{\theta_2}$ satisfy:

$$\mathscr{N}_r \, h_r = R_{\text{out}} - R_{\text{in}} \, , \; \mathscr{N}_{\theta_1} \, h_{\theta_1} = 1 \, , \; \mathscr{N}_{\theta_2} \, h_{\theta_2} = \frac{1}{\mathfrak{N}} \, . \tag{2.75}$$

We will often refer to the quantity $h = \text{Max.}\Big(h_r, \tau h_{\theta_1}, 2\pi\big(\frac{R_{\text{in}}+R_{\text{out}}}{2}\big) h_{\theta_2} \Big)$ as the overall mesh spacing for a particular level of discretization. We index each finite difference node using a triplet of natural numbers:

$$(\mathsf{i},\mathsf{j},\mathsf{k}) \in \{1,2,\ldots,\mathscr{N}_r\} \times \{1,2,\ldots,\mathscr{N}_{\theta_1}\} \times \{1,2,\ldots,\mathscr{N}_{\theta_2}\} \, , \tag{2.76}$$

and we use $f^{(\mathsf{i},\mathsf{j},\mathsf{k})}$ to denote the value a function f at the grid point $\mathsf{i},\mathsf{j},\mathsf{k}$. The grid point with indices $(\mathsf{i},\mathsf{j},\mathsf{k})$ is associated with the radial coordinate $r_{\mathsf{i}} = R_{\text{in}} + (\mathsf{i}-1) * h_r$, θ_1 coordinate $\theta_{1_{\mathsf{j}}} = (\mathsf{j}-1) * h_{\theta_1}$ and θ_2 coordinate $\theta_{2_{\mathsf{k}}} = (\mathsf{k}-1) * h_{\theta_2}$. The total number of real space grid points is $N_{\mathcal{D}} = \mathscr{N}_r \times \mathscr{N}_{\theta_1} \times \mathscr{N}_{\theta_2}$.

To discretize equations 2.69 - 2.72 using the finite difference scheme, we require expressions for first and second order derivatives, as well as a quadrature rule to compute integrals over the fundamental domain (e.g., to evaluate the action of $\mathcal{V}_{\text{nl}}$ on a given function). The

expressions for the first order derivatives are:

$$\begin{aligned}
\left.\frac{\partial f}{\partial r}\right|^{(\mathsf{i},\mathsf{j},\mathsf{k})} &\approx \sum_{p=1}^{n_o} \left(w_{p,r}^{\text{first}} \left(f^{(\mathsf{i}+p,\mathsf{j},\mathsf{k})} - f^{(\mathsf{i}-p,\mathsf{j},\mathsf{k})} \right) \right), \\
\left.\frac{\partial f}{\partial \theta_1}\right|^{(\mathsf{i},\mathsf{j},\mathsf{k})} &\approx \sum_{p=1}^{n_o} \left(w_{p,\theta_1}^{\text{first}} \left(f^{(\mathsf{i},\mathsf{j}+p,\mathsf{k})} - f^{(\mathsf{i},\mathsf{j}-p,\mathsf{k})} \right) \right), \\
\left.\frac{\partial f}{\partial \theta_2}\right|^{(\mathsf{i},\mathsf{j},\mathsf{k})} &\approx \sum_{p=1}^{n_o} \left(w_{p,\theta_2}^{\text{first}} \left(f^{(\mathsf{i},\mathsf{j},\mathsf{k}+p)} - f^{(\mathsf{i},\mathsf{j},\mathsf{k}-p)} \right) \right).
\end{aligned} \tag{2.77}$$

The expressions for the second order derivatives are:

$$\begin{aligned}
\left.\frac{\partial^2 f}{\partial r^2}\right|^{(\mathsf{i},\mathsf{j},\mathsf{k})} &\approx \sum_{p=0}^{n_o} \left(w_{p,r}^{\text{second}} \left(f^{(\mathsf{i}+p,\mathsf{j},\mathsf{k})} + f^{(\mathsf{i}-p,\mathsf{j},\mathsf{k})} \right) \right), \\
\left.\frac{\partial^2 f}{\partial \theta_1^2}\right|^{(\mathsf{i},\mathsf{j},\mathsf{k})} &\approx \sum_{p=0}^{n_o} \left(w_{p,\theta_1}^{\text{second}} \left(f^{(\mathsf{i},\mathsf{j}+p,\mathsf{k})} + f^{(\mathsf{i},\mathsf{j}-p,\mathsf{k})} \right) \right), \\
\left.\frac{\partial^2 f}{\partial \theta_2^2}\right|^{(\mathsf{i},\mathsf{j},\mathsf{k})} &\approx \sum_{p=0}^{n_o} \left(w_{p,\theta_2}^{\text{second}} \left(f^{(\mathsf{i},\mathsf{j},\mathsf{k}+p)} + f^{(\mathsf{i},\mathsf{j},\mathsf{k}-p)} \right) \right), \\
\left.\frac{\partial^2 f}{\partial \theta_1 \partial \theta_2}\right|^{(\mathsf{i},\mathsf{j},\mathsf{k})} &\approx \sum_{p=1}^{n_o} w_{p,\theta_2}^{\text{first}} \left[\left\{ \sum_{p'=1}^{n_o} w_{p',\theta_1}^{\text{first}} \left(f^{(\mathsf{i},\mathsf{j}+p',\mathsf{k}+p)} - f^{(\mathsf{i},\mathsf{j}-p',\mathsf{k}+p)} \right) \right\} \right. \\
&\qquad \left. - \left\{ \sum_{p'=1}^{n_o} w_{p',\theta_1}^{\text{first}} \left(f^{(\mathsf{i},\mathsf{j}+p',\mathsf{k}-p)} - f^{(\mathsf{i},\mathsf{j}-p',\mathsf{k}-p)} \right) \right\} \right].
\end{aligned} \tag{2.78}$$

In the above expressions, n_o denotes half the finite difference order, s denotes r, θ_1 or θ_2, and the finite difference weights $w_{p,s}^{\text{second}}$ and $w_{p,s}^{\text{first}}$ can be expressed as (91):

$$\begin{aligned}
w_{0,s}^{\text{second}} &= -\frac{1}{h_s^2} \sum_{q=1}^{n_o} \frac{1}{q^2}, \\
w_{p,s}^{\text{second}} &= \frac{2(-1)^{p+1}}{h_s^2\, p^2} \frac{(n_o!)^2}{(n_o-p)!(n_o+p)!} \quad \text{for } p = 1, 2, \ldots, n_o, \\
w_{p,s}^{\text{first}} &= \frac{(-1)^{p+1}}{h_s\, p} \frac{(n_o!)^2}{(n_o-p)!(n_o+p)!} \quad \text{for } p = 1, 2, \ldots, n_o.
\end{aligned} \tag{2.79}$$

Finally, the expression for evaluating integrals over the fundamental domain is:

$$\int_{\mathbf{x}\in\mathcal{D}} f(\mathbf{x})\, d\mathbf{x} \approx h_r h_{\theta_1} h_{\theta_2} \sum_{\mathsf{i}=1}^{\mathscr{N}_r} \sum_{\mathsf{j}=1}^{\mathscr{N}_{\theta_1}} \sum_{\mathsf{k}=1}^{\mathscr{N}_{\theta_2}} 2\pi\tau r_{\mathsf{i}}\, f^{(\mathsf{i},\mathsf{j},\mathsf{k})}. \tag{2.80}$$

2.2.3.2 Reciprocal space discretization

As is evident from the governing equations, many quantities of interest (including the electron density, for example) involve accumulating sums from each of the characters $\zeta \in \widehat{\mathcal{G}}$. Since this is equivalent to computing sums of the form $\frac{1}{\mathfrak{N}} \sum_{\nu=0}^{\mathfrak{N}-1}$ and integrals over the set $\mathfrak{I}$, we need a suitable scheme for discretizing the set $\widehat{\mathcal{G}}$. Accordingly, we perform quadratures over the set $\widehat{\mathcal{G}}$ using:

$$\frac{1}{\mathfrak{N}} \sum_{\nu=0}^{\mathfrak{N}-1} \int_{\mathfrak{I}} f(\eta, \nu)\, d\eta \approx \frac{1}{\mathfrak{N}} \sum_{\nu=0}^{\mathfrak{N}-1} \sum_{b=1}^{\mathcal{N}_\eta} w_b\, f(\eta_b, \nu)\,. \tag{2.81}$$

In the above expression, in accordance with the Monkhorst-Pack scheme (92), the quadrature nodes η_b are equi-spaced, while the corresponding quadrature weights w_b are uniform. Effectively, the above scheme discretizes the set $\mathcal{G}$ using $N_{\mathcal{K}} = \mathcal{N}_\eta \times \mathfrak{N}$ representative reciprocal space points. By use of time reversal symmetry (93; 7; 4), it is possible to reduce the number $N_{\mathcal{K}}$ by a factor of 2, which helps in cutting down computational wall time in practical calculations.

2.2.4 Solution strategies for the discretized equations and MATLAB implementation

The governing equations for the twisted structure represent a set of coupled nonlinear eigenvalue problems. We use self consistent field (SCF) iterations accelerated via Periodic-Pulay extrapolation (94) to solve them in this work. The total effective potential (i.e., $V_{\text{xc}} + \Phi$) is used as the mixing variable. Solution of the Poisson equation associated with the electrostatic field (eq. 2.70) is carried out using the Generalized Minimal Residual method (GMRES) (95), and an incomplete LU factorization based preconditioner (96) is used to accelerate convergence of the GMRES iterations. Solution to eq. 2.72 is carried out using a nonlinear equation root finder (97).

As a consequence of the discretization choices and other simplifications outlined previ-

ously, there are $N_{\mathcal{K}}$ linear eigenvalue problems, each of dimension $N_{\mathcal{D}}$, that have to be solved on each SCF iteration step. Furthermore, for each of these eigenvalue problems, the lowest N_{s} eigenstates have to be determined via a suitable diagonalization process. Due to our use of finite differences, the discretized Hamiltonian operators (at each value of η and ν) are non-Hermitian, even though the original infinite dimensional operators they represent are not. This is a well known issue that arises while approximating differential operators such as the Laplacian in curvilinear coordinates using finite differences (98; 55; 7). In practice, this issue is mitigated by a combination of factors. First, as the mesh spacing h is made finer, and/or the degree of the finite difference discretization n_o is made larger, the discretized operators approximate their infinite dimensional counterparts more closely. Consequently, the discretized operators become more Hermitian (i.e., the norm of the difference between the operator and its Hermitian conjugate goes to zero), the eigenvalues have small imaginary components, and conventional iterative methods for obtaining the spectrum of a sparse symmetric Hamiltonian (99; 100; 101) can be employed for diagonalization. Indeed, for the discretization parameters used to produce the results in this work, the imaginary parts of the Hamiltonian eigenvalues are small enough that they can be ignored without any deleterious effects on the stability or quality of the simulations. Second, by choosing eigensolvers that can handle non-Hermitian problems in a robust manner, even calculations involving relatively coarse meshes (i.e., for which the Hamiltonian is well conditioned, but might have some eigenvalues with non-vanishing imaginary parts), or problems with poorly conditioned Hamiltonian matrices (which can arise if a system with a large amount of prescribed twist is being studied) can be performed.

Keeping the above factors in mind, our implementation employs a combination of the Generalized Preconditioned Locally Harmonic Residual (GPLHR) method (102), as well as iterative diagonalization based on Chebyshev polynomial filtered subspace iterations (CheFSI) (99; 103; 104). Due to the ability of GPLHR to employ preconditioners (based on incomplete LU factorization, e.g.), the method can be particularly effective in handling

poorly conditioned Hamiltonian matrices — i.e., for problems in which the CheFSI method tends to use relatively large polynomial filter orders. For such problems, we have also observed that GPLHR generally requires fewer iterations to reach SCF convergence, when compared to CheFSI, and between 5 to 8 iterations of the method are sufficient per SCF step. Nevertheless, for the systems considered in this work, we found that Chebyshev polynomial filter orders in the range 60 to 80 were adequate in guaranteeing stable, well converged simulations, and in this scenario the CheFSI method generally required shorter wall-times-to-solution overall. Thus, for the bulk of the simulations presented in this work, CheFSI was the method of choice. We show examples of the SCF convergence behavior for two example systems using CheFSI and GPLHR in Figure 2.2.

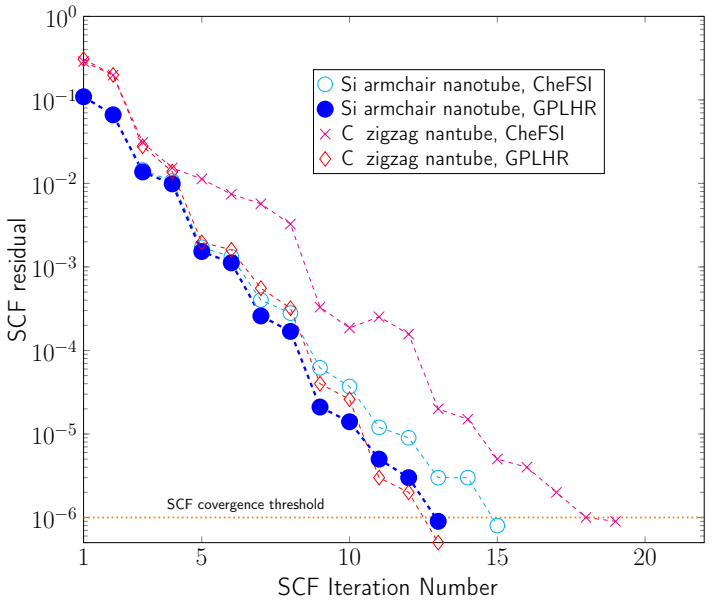

Figure 2.2: Examples of SCF convergence using CheFSI and GPLHR methods in Helical DFT. The armchair silicon nanotube has radius 0.96 nm, and was subjected to a twist of 5.67 degrees/nm. The zigzag carbon nanotube has radius 0.70 nm, and was subjected to a twist of 4.27 degrees/nm.

We have implemented the above methods and algorithms in a computational package called Helical DFT. The current version of the code is largely written in MATLAB (105),

with certain key routines (including Hamiltonian matrix-vector products, sections containing multiple nested loops, etc.) written in C to alleviate speed and/or memory footprint issues. The code makes use of MATLAB's vectorization capabilities, and achieves parallelization by performing diagonalization of the Hamiltonian for different values of η and ν simultaneously over multiple computational cores. Helical DFT is capable of performing structural relaxation by use of the Fast Intertial Relaxation Engine (FIRE) algorithm (106) as well as *ab initio* molecular dynamics simulations by use of a velocity Verlet integrator (107).

CHAPTER 3

Application of Helical DFT to torsional deformation in group-IV nanotubes

3.1 Simulations and Results

3.1.1 Computational Platform

All simulations involving Helical DFT were run using a dedicated desktop workstation (Dell Precision 7920 Tower) or single nodes of the Hoffman2 cluster at UCLA's Institute for Digital Research and Education (IDRE). The desktop workstation has an 18-core Intel Xeon Gold 5220 processor (24.75 MB cache, running at 2.2 GHz), 256 GB of RAM and a 1 TB SATA Class 20 Solid State Drive (SSD). Each compute node of the Hoffman2 cluster has two 18-core Intel Xeon Gold 6140 processors (with 24.75 MB cache, running at 2.3 GHz), 192 GB of RAM and local SSD storage. MATLAB version 9.7.0 (R2019b) was used for the simulations. Compilation of C language routines was carried out using MinGW (on the workstation) and GCC (on the Hoffman2 nodes) software suites. Interfacing between MATLAB and C language routines was carried out by means of MATLAB's MEX and Coder frameworks, while parallelization was achieved by use of using MATLAB's Parallel Computing Toolbox.

3.1.2 Simulation Parameters

We used an SCF iteration convergence tolerance of 10^{-6} in the total effective potential (relative residual). The Periodic Pulay mixing scheme (94) used a history of 7 iterations, the

mixing parameter was set at 0.2, and Pulay extrapolation was performed on every alternate SCF step. GMRES iterations for the Poisson problem was carried out till the residual dropped below 10^{-9} on every SCF step. We employed an electronic temperature of T_e = 315.77 Kelvin in the Fermi-Dirac function (this corresponds to about 1 milli-Hartree of smearing), and included 2 extra states at each value of η and ν to accommodate fractional occupancies. We used Troullier-Martins norm conserving pseudopotentials (71) and Perdew-Wang parametrization (108) of the Local Density Approximation (72). We used a 12^{th} order finite difference discretization scheme (i.e., $n_o = 6$ in eqs. 2.77, 2.78, 2.79) and diagonalization via CheFSI used filters of order 60 to 80. Determination of spectral bounds within the CheFSI method used MATLAB's eigs function (109) with a relatively loose tolerance of 10^{-2}. For the nanotube simulations described here, we ensured a gap of 10 to 11 Bohrs between the atoms located within the fundamental domain, and the boundary surfaces ∂R_{in} and ∂R_{out}, in order for the electron density and the wavefunctions to decay sufficiently in the radial direction[1]. Real space and reciprocal space discretization parameters were chosen on a case by case basis, as described later.

3.1.3 Materials Systems: Group IV Nanotubes

Nanotubes and other similar systems are particularly well suited for study using the methods described in this work. We choose single walled nanotubes of carbon, silicon, germanium, and tin as materials systems for investigation here. These systems are used for carrying out numerical validation studies, and due to their technological importance, also for gaining insights into their properties by the use of our method. Such one-dimensional nanostructures from Group IV of the periodic table can be described in terms of a "roll-up" procedure (110),

[1]We have carried out tests regarding the effect of the amount of vacuum padding (i.e., distance between R_{in} or R_{out} and the atoms of the structure) on the energies and forces, and have observed the deviations in these quantities drop to 10^{-5} or so (in atomic units) at a vacuum padding of about 8 Bohr, for the systems considered here. In our actual simulations, we use a somewhat larger vacuum padding of $10 - 11$ Bohrs and the tube radii are also chosen accordingly.

starting from their two-dimensional sheet counterparts (i.e., graphene, silicene, germanene and stanene). We collectively refer to these one- and two-dimensional materials as X (X = C, Si, Ge, Sn) nanotubes, and Xenes, respectively. Both these classes of materials have been intensely studied in recent years through both experimental and computational methods, due to their association with fascinating materials properties (111; 112; 113; 114; 115; 116; 117; 118; 119; 120; 121; 122; 123; 124; 125; 126; 127; 128; 129; 130; 131; 132; 133; 134; 135; 136; 137; 138; 139; 140; 141; 142; 143; 144; 145; 146; 147; 148; 149; 117; 115; 150). In particular, the electronic properties of deformed carbon nanotubes have received extensive treatment in the literature through theoretical and computational means (143; 151; 3; 152; 153; 1; 154; 155; 156; 157). Although a few computational studies on the electronic structure of the larger class of Group IV nanotubes are also available (140; 7; 158; 159; 160), as far as we can tell, this work is the first to investigate from first principles, the behavior of these materials under torsional deformations, and to extend some well known results for carbon nanotubes to the broader class of Group IV nanotubes.

By using the roll up construction on the Xene sheets (see Figure 3.1), we can represent untwisted tubes using just four atoms in the fundamental domain (7; 32; 45), and a twist can be prescribed on the system by choosing a non-zero value of α. Depending on the direction of rolling, the untwisted tubes can be classified as armchair or zigzag, and the fundamental period τ of the untwisted tubes in these cases are $\sqrt{3}\,a$ and $3\,a$, respectively, with a denoting the (planar) interatomic distance among the X atoms. Furthermore, the cyclic group order $\mathfrak{N}$ can be expressed in terms of the nanotube radius via the relation $\mathfrak{N}\,L = 2\pi R_{\text{avg.}}$. Here $L = \sqrt{3}\,a$ and $3\,a$, for armchair and zigzag cases, respectively, and $R_{\text{avg.}}$ denotes the average radial coordinate of the atoms in the fundamental domain. For subsequent simulations, we adopted the values of the parameter a, as well as the out of plane buckling parameter δ, as reported in (7). We include the values of the parameters in Table 3.1 for the sake of having a self contained presentation here.[2]

[2]To compute these parameters, the relaxed ground state structure of the Xene sheets (single layer)

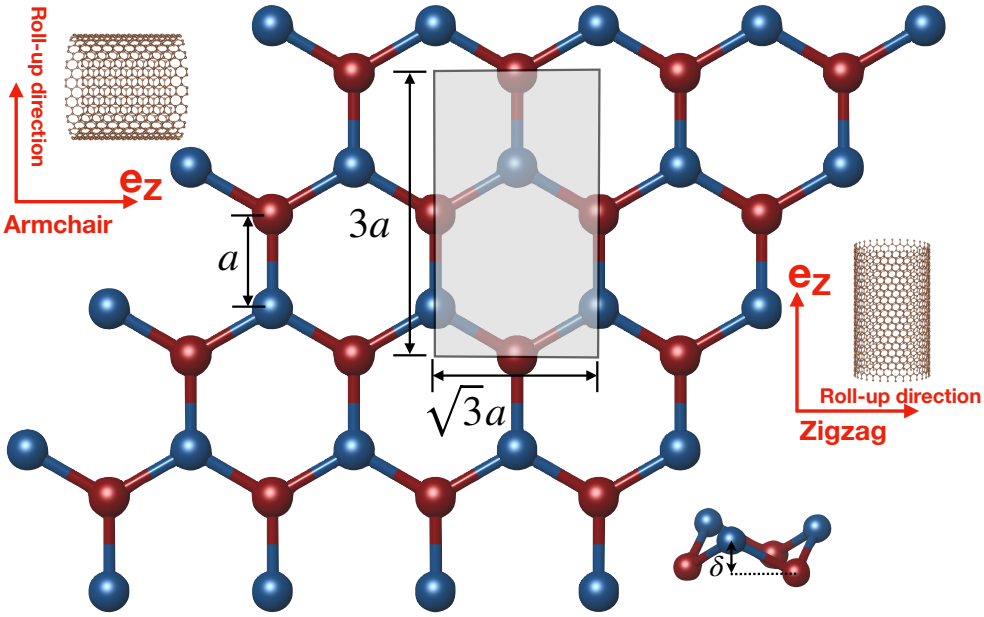

Figure 3.1: Roll-up construction of untwisted X nanotube, starting from Xene sheet. Atoms in the fundamental domain are shaded and are the same ones conventionally used for carrying out simulations of (planar) Xenes using orthogonal unit cells. The parameter a represents the planar interatomic distance, δ represents the out of plane buckling parameter, and in-plane and out-of-plane atoms are shown in alternate colors.

3.1.4 Convergence, accuracy and efficiency studies

We begin with a discussion of the convergence properties of our numerical implementation with respect to discretization parameters. We choose armchair nanotubes of carbon (radius = 1.07 nm, $\mathfrak{N} = 16$), silicon (radius = 0.97 nm, $\mathfrak{N} = 9$), germanium (radius = 1.73 nm, $\mathfrak{N} = 16$) and tin (radius = 0.99 nm, $\mathfrak{N} = 8$), as example systems. We apply a twist to

was computed using the plane-wave DFT code ABINIT (42; 161). The same pseudopotentials, exchange correlation functional and electronic temperature were used between ABINIT and Helical DFT. Energy cutoffs between 40 and 60 Ha, $30 \times 30 \times 1$ k-points, and a cell vacuum of 25 Bohr in the direction orthogonal to the sheets, were employed. At the end of the geometry relaxation procedure, the atomic forces and the cell stress were of the order of 10^{-5} Ha/Bohr and 10^{-8} Ha/Bohr^3, respectively. The agreement of these parameters with existing literature is quite good (7), thus lending confidence to the physical properties of the X nanotubes as revealed via our simulations.

Material	a (Angstrom)	δ (Angstrom)
Graphene	1.407	-
Silicene	2.200	0.404
Germanene	2.232	0.566
Stanene	2.522	0.699

Table 3.1: Equilibrium lattice parameters of Xene sheets, as obtained from (7), and used in subsequent Helical DFT simulations.

each of these systems by setting α between 0.003 and 0.006 (this corresponded to between 2.47 and 8.86 degrees/nm of imposed rate of twist). With all the other parameters of the computational method fixed to values described earlier, the only remaining quantities that can dictate the accuracy of the numerical solutions are fineness of the real and reciprocal space discretizations. Accordingly, we study the convergence behavior of the ground state energy and the atomic forces as a function of the mesh spacing h, and the number of reciprocal space points N_η used in the calculations. The results are shown in Figure 3.2. For the mesh convergence study, we used $h = 0.15$ Bohr to evaluate the reference value while computing errors, while for studies involving convergence with respect to reciprocal space discretization, we used $N_\eta = 21$ as reference.

From the figures, we see that the numerical method converges systematically in each of the cases under study. By fitting straight lines to the convergence data with respect to h, we observed slopes between 5.5 and 6.5 which are somewhat lower than values observed for finite difference calculations using (untwisted) cylindrical coordinates (7). We are also able to estimate that a mesh spacing of about $h = 0.3$ Bohr, and a value of $N_\eta = 15$ are more than sufficient to reach chemical accuracy thresholds in all cases (i.e., 10^{-3} Ha/atom in the energies and 10^{-3} Ha/Bohr in the atomic forces), and we used these discretization choices in structural relaxation calculations in subsequent sections. Figure 3.3 shows the consistency of the forces and the energies as computed by Helical DFT at this level of discretization

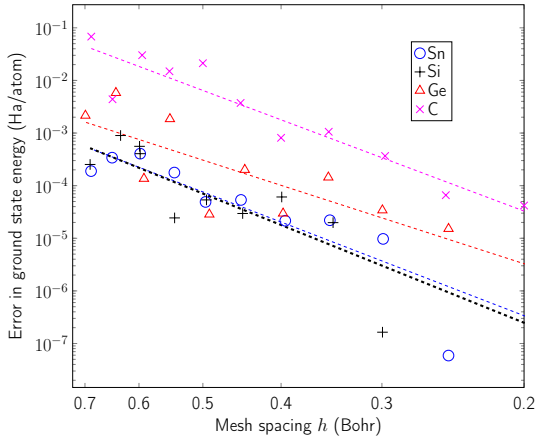

(a) Convergence of ground state energy w.r.t. real space discretization

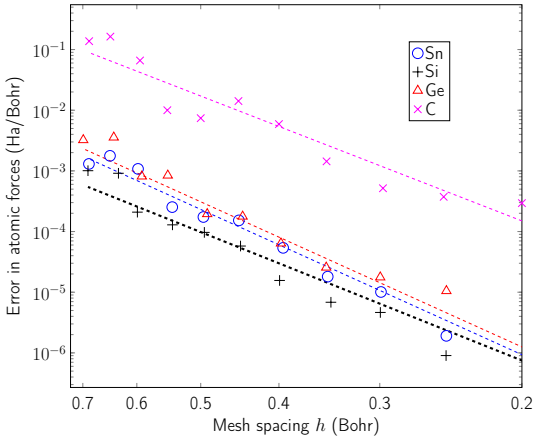

(b) Convergence of atomic forces w.r.t. real space discretization

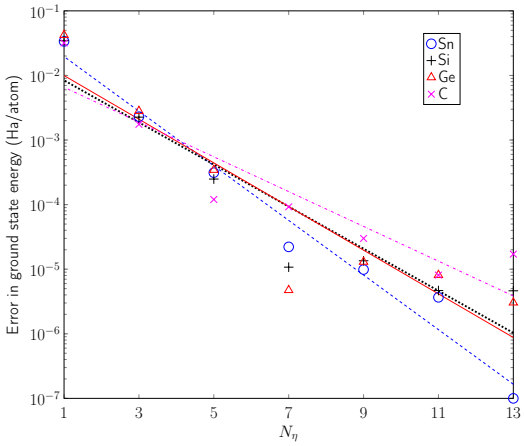

(c) Convergence of ground state energy w.r.t. reciprocal space discretization

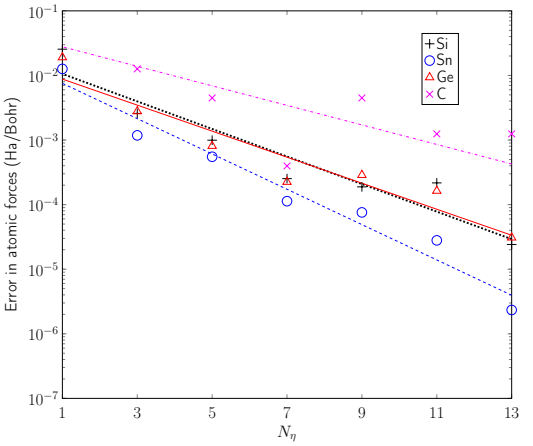

(d) Convergence of atomic forces w.r.t. reciprocal space discretization

Figure 3.2: Convergence behavior of the numerical method for X nanotubes, with respect to real space and reciprocal space discretization parameters. The error in the forces is the magnitude of the maximum difference in all the force components on all the atoms. Dotted lines indicate straight line fits.

(i.e., numerical derivatives of the free energy per unit cell as computed via eq. 2.29, yield the atomic force as computed via eq. 2.61). To compute the energies and band structures of relaxed structures, we employed the finest discretization parameters that we could reliably afford within computational resource constraints. This corresponded to the choices $h = 0.25$ Bohr and $N_\eta = 21$.

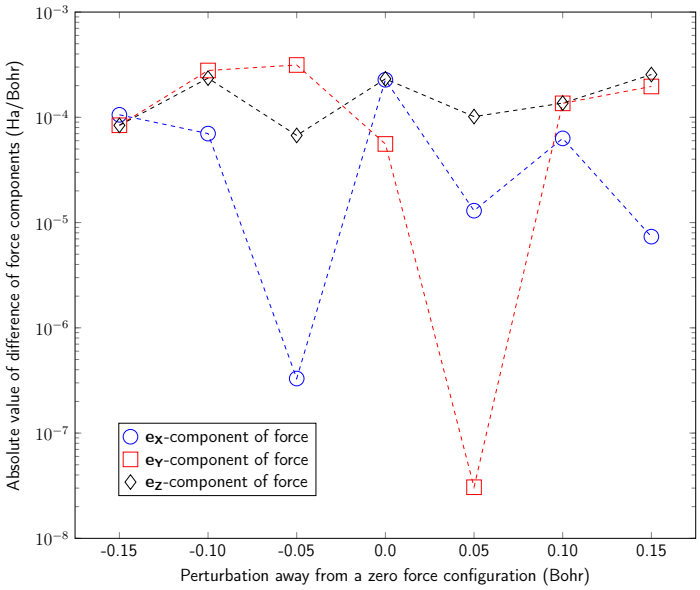

Figure 3.3: Consistency of the energies and forces as calculated by the Helical DFT code. For this test, a relaxed configuration of an armchair silicon nanotube (radius = 0.96 nm) subjected to a rate of twist = 5.67 degree/nm was chosen. One atom in particular was then translated along $\mathbf{e_X}, \mathbf{e_Y}$ and $\mathbf{e_Z}$ directions (one direction at a time). The force components on the atom were obtained both via computing the derivative of a spline fit of the energy at each configuration, and direct evaluation of eq. 2.61. The absolute value of the difference is shown in each case. The agreement is $\mathcal{O}(10^{-4})$ Ha/Bohr or better in all configurations, giving us confidence the results produced by the code.

Next, we come to a discussion of verification of the numerical method against results produced by standard, widely used plane-wave codes such as ABINIT (42; 161). As described earlier, this can be an arduous endeavor since such codes may require a very large number of

atoms to be included in the periodic unit cell, in order to mimic the systems being simulated via Helical DFT. Moreover, in order to accurately accommodate the boundary conditions implemented in Helical DFT, a large amount of vacuum padding has to be often employed in the plane-wave code unit cell, and nanotube-like structures tend to encase a large amount of vacuum as it is. These factors together can result in slow convergence of the electrostatics problem, as well as, poor conditioning of the systems of equations being solved by the plane-wave code. The latter issue, in turn, leads to SCF convergence problems which tend to worsen if calculations at high accuracies are required (i.e., upon using a large value of E_{cut} for the plane-wave code). With these factors in mind, we chose the armchair carbon and silicon nanotube systems described above for comparison against ABINIT. For the former, we did not prescribe any twist and use a 64 atom unit cell. For the latter, we prescribed a twist of $\alpha = 0.1$, and used a 360 atom unit cell. While dealing with these systems in ABINIT, periodicity was naturally enforced along the Z axis, Dirichlet boundary conditions were enforced along the X and Y axes by padding with a large amount of vacuum, and an SCF preconditioner (diemac option in ABINIT) was used to deal with instabilities associated with spatial inhomogeneities in the periodic unit cell. Helical DFT was made to use four atom unit cells for both examples. For each of these model systems, we observed that the energies (in Ha/atom) and the forces (in Ha/Bohr), from ABINIT and Helical DFT agreed with each other to $\mathcal{O}(10^{-4})$, thus giving us confidence in the accuracy of the results produced by our method.[3]

Based on the above tests, we were also able to observe that even a well optimized plane-wave code like ABINIT can take up to orders of magnitude more in simulation time (measured in c.p.u. hours) compared to Helical DFT, when simulations of nanotube structures

[3]Convergence and accuracy properties of the Helical DFT code have also been discussed in our earlier contribution (4). However, the materials systems considered in this work are different from (4), and so, we include this discussion here for the sake of a self-contained presentation. In particular, carbon is known to be associated with somewhat hard pseudopotentials and these studies helped us determine the appropriate discretization parameters for this element, so that numerically accurate predictions of electromechanical properties of carbon nanotubes could be made.

(particularly, ones with imposed twist) are desired. This makes our computational method a particularly attractive choice in the first principles characterization of such systems. The relative efficiency of our method stems from the use of a coordinate system and a computational domain that are well adapted to the geometry of the twisted structure, and also from the appropriate use of symmetry. To highlight the latter aspect, we considered again the silicon nanotube system subjected to a twist of $\alpha = 0.1$. We used Helical DFT to calculate the ground state electronic structure of this system by considering the following four equivalent scenarios:

(a) No helical or cyclic symmetries (360 atom unit cell with $\alpha = 0$ and periodicity along $\mathbf{e_Z}$, $N_\eta = 1$ and only $\nu = 0$ considered).

(b) Only cyclic symmetries (40 atom unit cell with $\alpha = 0$ and periodicity along $\mathbf{e_Z}$, $N_\eta = 1$ and $\nu = 0, 1, \ldots, 8$ considered).

(c) Only helical symmetries (36 atom unit cell with $\alpha = 0.1$, $N_\eta = 10$, and only $\nu = 0$ considered).

(d) Both cyclic and helical symmetries considered (4 atom unit cell with $\alpha = 0.1$, $N_\eta = 10$ and $\nu = 0, 1, \ldots, 8$ considered).

The single core wall times required for each SCF step, and computation of the atomic forces at the end of the SCF iterations are compared in Figure 3.4.

From these plots, it is clear that the SCF wall time is approximately 20 times lower for the case with full symmetry adaptation, when compared to the case in which no cyclic or helical symmetries were used. Even more drastically, the computational wall time for the calculation of the force is about 3 orders of magnitude lower for the former case, when compared to the latter. These computational advantages tend to be even more dramatic for simulations in which the angle of twist is relatively low (e.g. $\alpha = 0.0005$ to 0.005), and such

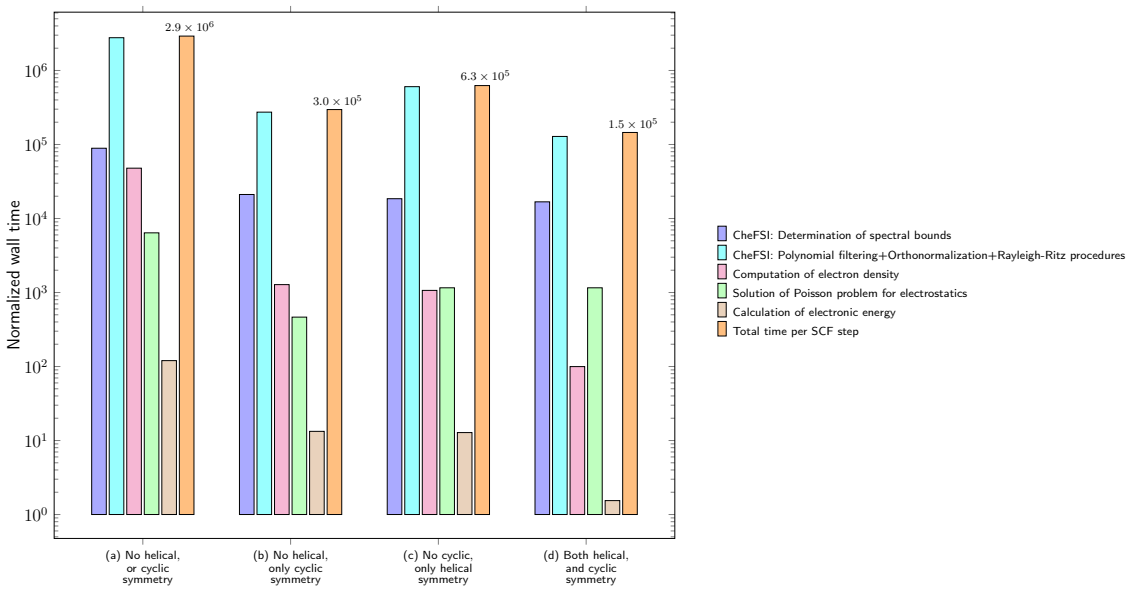

(a) SCF iteration wall times (normalized). Y-axis is logarithmic.

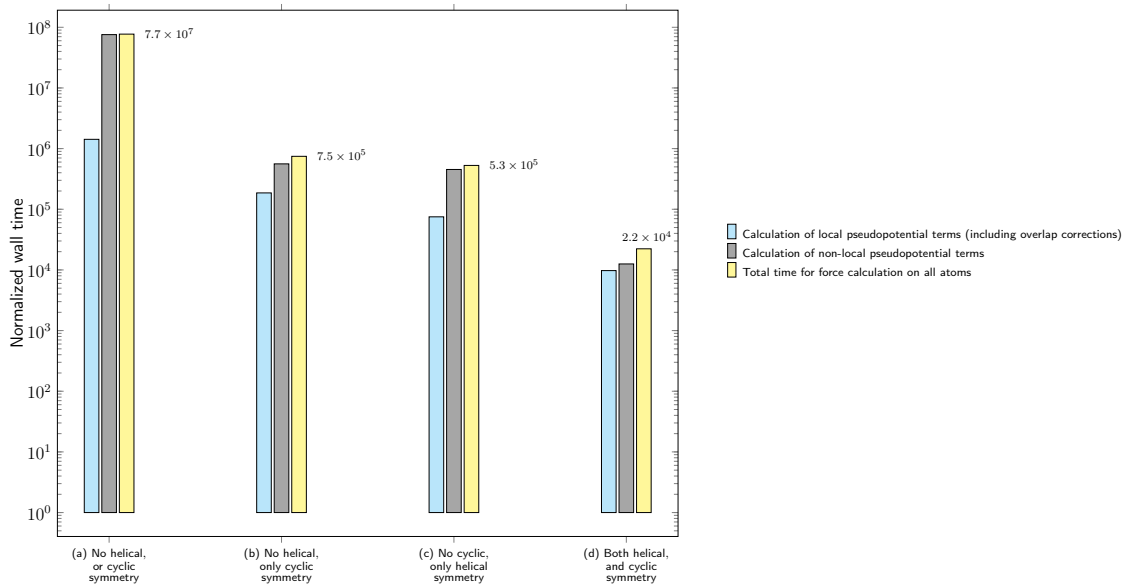

(b) Force calculation wall times (normalized). Y-axis is logarithmic.

Figure 3.4: Influence of symmetry adaptation on computational wall times (single core). Numbers appearing in the plots above indicate the total time per SCF step and the total time for computation of the forces (both quantities normalized).

cases tend to arise routinely while probing the torsional response of the nanotubes in the linear elastic regime, as described in the next section.

Finally, we show in Figure 3.5 the strong scaling behavior of the numerical implementation. We use case (d) described above for this study. We see that up to 16 computational cores, the code has a strong scaling efficiency of about 60 %. This follows the strong scaling efficiency of the CheFSI step closely, since this forms the dominant computational cost in every SCF step (see Figure 3.4(a)). The scaling of the force computation step is far worse, dropping to about 10 % at 16 cores. In general, the scaling behavior is expected to improve for problems with a larger number of η and ν points (e.g. for simulations of nanotubes of large diameter) since the current version of the code only uses parallelization over different values of η and ν. Improvement of the scaling behavior of the code, particularly by use of domain decomposition and band parallelization techniques in conjunction with the MATLAB Parallel Server framework (to enable deployment over distributed memory computers) is the scope of future work.[4]

3.1.5 Computation of torsional stiffness from first principles

We now turn to demonstrations of the use of our computational method for evaluation of materials properties from first principles. We first concentrate on the mechanical response and evaluate the torsional stiffness of the X nanotubes in the linear elastic regime, *ab initio*. We choose 9 to 10 nanotubes of each material, about half of which are of zigzag type and

[4]As pointed out to us by an anonymous reviewer, these scaling performance figures suggest that the Helical DFT code is heavily memory bound in the regime in which the data was collected, and therefore, perhaps a better metric might be to estimate the percentage of total peak performance. However, estimating this number involves calculation of the number of floating point operations performed during the operation of the code, and this can be somewhat challenging due to the use of both MATLAB and C source code. Furthermore, due to the lack of internal MATLAB routines for estimating flops, only tools developed by the MATLAB user community can be employed. We ran tests using the Lightspeed suite (162) and we focused only on one the core routines of the code, i.e., the matrix vector-product implementation. Our tests suggest that on the 18-core Intel Xeon Gold 5220 processor, the core routines reached about 10.7 % of the peak performance (peak performance data obtained from the Intel website (163)), which is not entirely unexpected due to the large amount of data movement operations associated with the calculation (164).

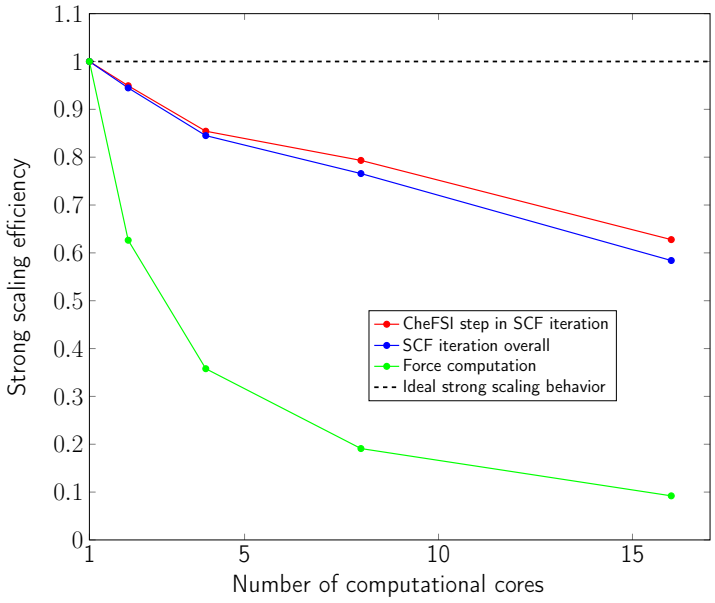

Figure 3.5: Strong scaling behavior of the Helical DFT code.

the other half armchair. The nanotubes all had radii in the range 1 to 3 nm, approximately. To carry out these simulations, we choose a four atom unit cell for the untwisted nanotube in each case, and perform structural relaxation using the FIRE algorithm (106) till all force components on all the atoms in the simulation cell dropped below 10^{-3} Ha/Bohr. We then successively increase α to impose twist, and in each case re-perform structural relaxation (see Figure 3.6 for some examples of the relaxation procedure).

To avoid the appearance of torsional instabilities, we ensured that the prescribed rate of twist on the system was less than about 4.5 degrees per nanometer (45), and this corresponded to choosing α between 0.0005 and 0.005. We express the amount of applied twist per unit length of the tube (i.e., the *rate of twist*) as $\beta = \dfrac{2\pi\alpha}{\tau}$, and compute the twisting energy per unit length of the structure as the difference in the ground state free energy per unit fundamental domain between the twisted and untwisted configurations (after atomic relaxation is carried out in both cases), i.e.:

$$U_{\text{twist}}(\beta) = \frac{\mathfrak{N}}{\tau}\left(\mathcal{F}_{\substack{\text{Ground}\\\text{State}}}(\mathcal{P}^{**},\mathcal{D},\mathcal{G}|_{\beta}) - \mathcal{F}_{\substack{\text{Ground}\\\text{State}}}(\mathcal{P}^{*},\mathcal{D},\mathcal{G}|_{\beta=0})\right). \tag{3.1}$$

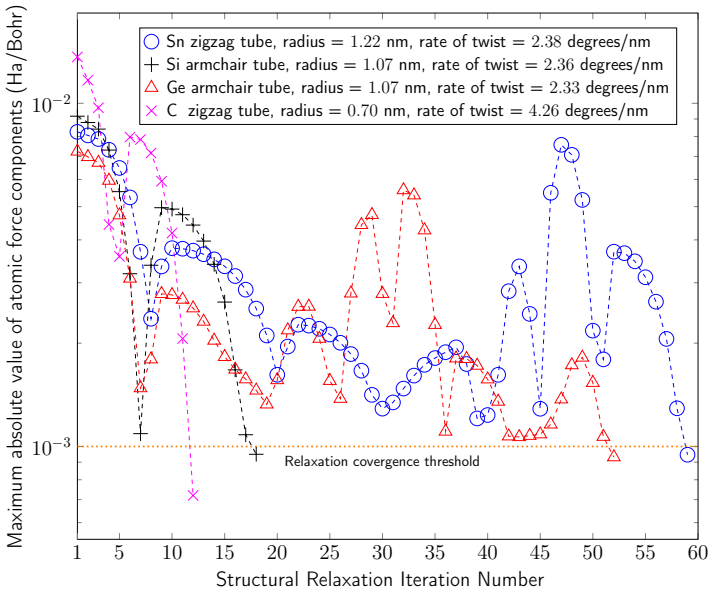

Figure 3.6: Examples of *ab initio* structural relaxation of twisted structures using Helical DFT.

Here, $\mathcal{G}|_{\beta}$ and $\mathcal{G}|_{\beta=0}$ denote the symmetry groups associated with the twisted and untwisted structures, respectively. Also, $\mathcal{P}^{**}$ and $\mathcal{P}^{*}$ denote the collections of positions of the atoms in the fundamental domain, after relaxation in each case. For each of the nanotubes, we verified that mechanical response was in the linear regime, by fitting $U_{\text{twist}}(\beta)$ to a function of the form $U_{\text{twist}}(\beta) = c \times \beta^q$ and observing that $q \approx 2.0$ holds. We show a few examples in Figure 3.7.

Next, using the above data, we estimated the twisting stiffness of each nanotube, defined as:

$$k_{\text{twist}} = \left. \frac{\partial^2 U_{\text{twist}}(\beta)}{\partial \beta^2} \right|_{\beta=0} . \tag{3.2}$$

For each category of nanotube (i.e., armchair or zigzag, and type of material), we then studied the variation of k_{twist} with the nanotube radius (computed as the average of the radial coordinates of all atoms in the fundamental domain), by using a fit of the form:

$$k_{\text{twist}} = \kappa \times R_{\text{tube}}^{p} . \tag{3.3}$$

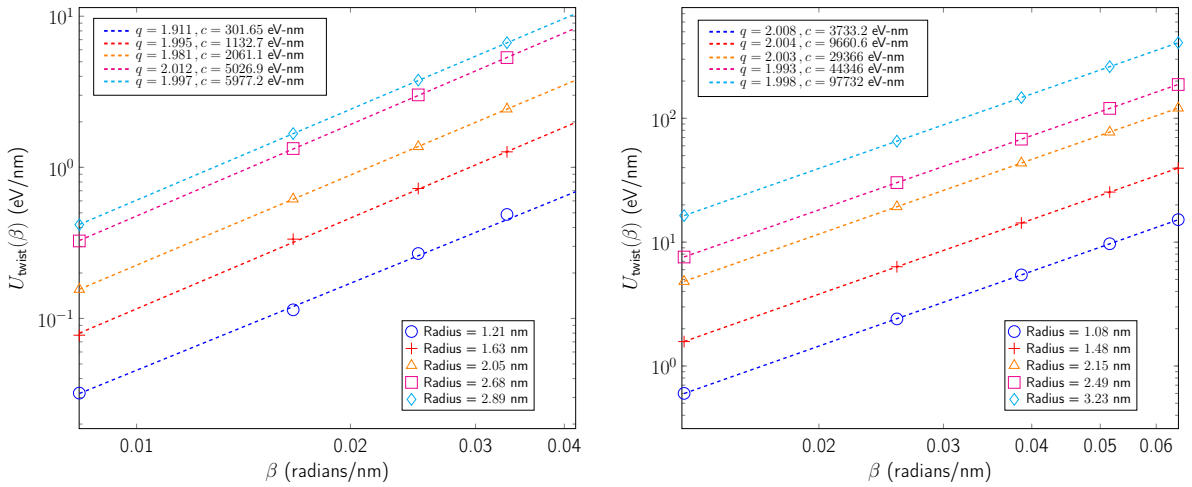

(a) Zigzag Sn nanotubes

(b) Armchair C nanotubes

Figure 3.7: Dependence of twist energy per unit length on angle of twist per unit length (i.e., rate of twist) for two representative classes of nanotubes. Dotted lines indicate straight line fits of the data to an ansatz of the form $U_{\text{twist}}(\beta) = c \times \beta^q$.

The results from this procedure are shown in Figure 3.8 and the values of κ and p obtained in each case are displayed in Table 3.2. Note that generation of this torsional response data required hundreds of individual simulations, which would not have been possible without the use of a specialized computational method such as the one presented here.

A few comments are in order at this stage. First, we observe that the value of the exponent p is nearly 3 in every case. This suggests that the torsional response of the tubes is consistent with linear elasticity theory, in which k_{twist} for a thin elastic tube with unit length, radius R_{tube}, thickness t, and shear modulus G can be expressed as $Gt\pi R_{\text{tube}}^3$ (165). From this, it is possible to estimate the thickness-normalized shear modulus (i.e., Gt) of the Xene sheets as κ/π. Second, by comparing the different values of κ, we see that they span an order of magnitude across the different elements. In particular, for a given radius, k_{twist} is the highest for carbon nanotubes and the lowest for those of tin, while nanotubes of silicon and germanium have intermediate values of this quantity close to each other. Third, for each material, the torsional response is quite similar in the armchair and zigzag directions

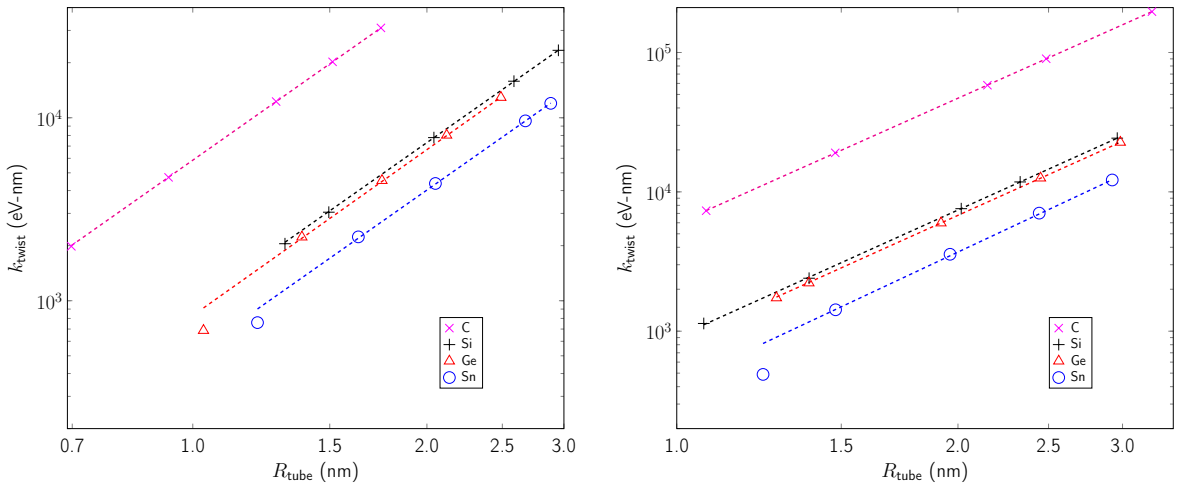

(a) Zigzag nanotubes

(b) Armchair nanotubes

Figure 3.8: Variation of torsional stiffness k_{twist} (eV-nm) with tube radius R_{tube} (nm). Both axes are logarithmic. Dotted lines correspond to $k_{\text{twist}} = \kappa \times R_{\text{tube}}^{p}$ with fitted parameters for κ (eV/nm^2) and p (Table 3.2).

with variations less than about 1.5%, except for the case of tin, in which case the variation is more substantial. This largely isotropic torsional response for the Xene nanotubes is quite distinct from the bending response of their sheet counterparts, which show strong anisotropic behavior that is correlated with the value of the normalized buckling parameter (i.e., δ/a) for each material (7). Our findings on the mechanical response of carbon nanotubes under torsion are broadly consistent with earlier studies for this material that used empirical potentials or tight-binding calculations (45; 47), although the value of κ reported here is lower from (45), where Tersoff potentials were used (166).

Finally, we mention in passing, the effects of atomic relaxation. In general, if relaxation is not performed after the imposition of twist, the value of k_{twist} for the system tends to be higher. The degree of variation can be quite different depending on the material involved. For carbon nanotube systems, we observed that k_{twist} for an unrelaxed system was typically higher by a factor of about 1.08, whereas for silicon nanotubes, this factor had the higher value of about 1.38. Generally, these higher values of k_{twist} also imply higher values of κ by

X	Type	κ (eV/nm^{p-1})	p
C	Armchair	5905.76	2.992
C	Zigzag	5859.81	2.990
Si	Armchair	909.34	3.026
Si	Zigzag	923.78	2.986
Ge	Armchair	837.12	3.018
Ge	Zigzag	829.57	3.012
Sn	Armchair	418.23	3.144
Sn	Zigzag	508.83	2.984

Table 3.2: Torsional stiffness parameters for the X nanotubes, with $k_{\text{twist}} = \kappa \times R_{\text{tube}}^{p}$

the same factors, although the value of the exponent p continues to be about 3, when the fitting in eq. 3.3 is used.

3.1.6 Investigation of electronic properties of nanotubes undergoing torsional deformation

We now discuss the variation in electronic properties of nanotubes as they are subject to twisting. Due to the ability of our computational method to use symmetries connected with the system, electronic band-diagrams along both η and ν can be obtained from Helical DFT. Moreover, the eigenvalues $\lambda_j(\eta, \nu)$ as j is held constant and η, ν are varied, can be plotted as a two-dimensional surface. Since η and ν serve to label the set of characters, and are natural quantum numbers for twisted structures, they serve to provide a clean and intuitive interpretation of the electronic states of the system, and allow easy identification of the size and type of band-gaps. In contrast, the traditional band diagram for a quasi-one-dimensional system using a periodic method can be far more complicated, even for an untwisted structure. We show some examples of this contrast in Figures 3.9 and 3.10.

Armed with the above tools, we study the variation in the bandgaps of nanotubes as

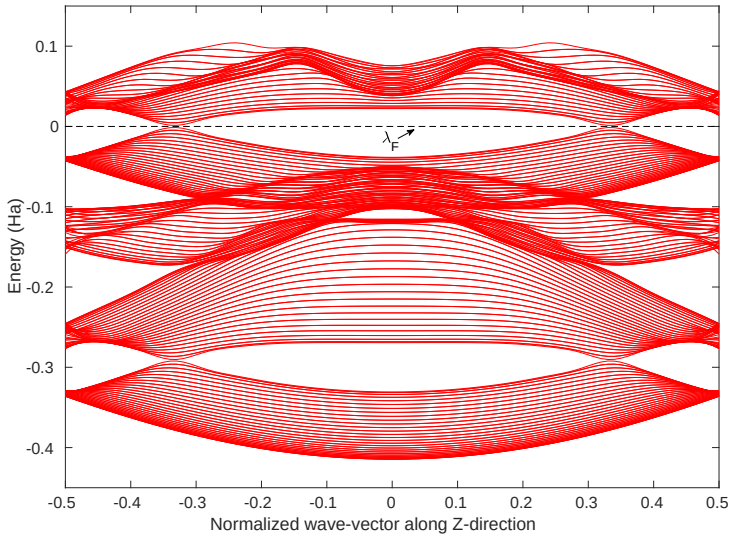

Figure 3.9: Conventional band diagram for an untwisted armchair Si nanotube of radius 2.96 nm.

they are subjected to twisting. For reasons explained later, we mainly concentrate on investigations related to armchair X nanotubes, although we also briefly comment on our findings related to zigzag X nanotubes subsequently. The behavior of carbon armchair nanotubes in particular, has received much attention in the literature (143; 151; 3; 1), and serves as an important benchmark against which our results can be validated. Such nanotubes are known to be metallic (3; 167; 151) although in practical calculations, a vanishingly small bandgap at the location $\eta = \frac{1}{3}, \nu = 0$ (or equivalently, $\eta = -\frac{1}{3}, \nu = 0$) may be observed (7). Upon twisting, armchair carbon nanotubes undergo a metal-to-semiconductor transition, with the characteristic feature that the bandgap-versus-rate-of-twist plot has a slope of $3\,t_0\,R_{\text{tube}}$ in the linear regime (i.e., in the neighborhood of zero twist). Here t_0 is the tight-binding hopping parameter for carbon (1). Here, the metal-to-semiconductor transition is referring to the opening of the energy bandgap, which in DFT calculation is defined as the difference between the highest occupied state (HOMO) and lowest unoccupied state (LUMO). Using armchair carbon nanotubes of radii 1.08, 1.48 and 1.88 nm as examples, we used Helical DFT to compute the slope of the bandgap-versus-rate-of-twist plot in the linear

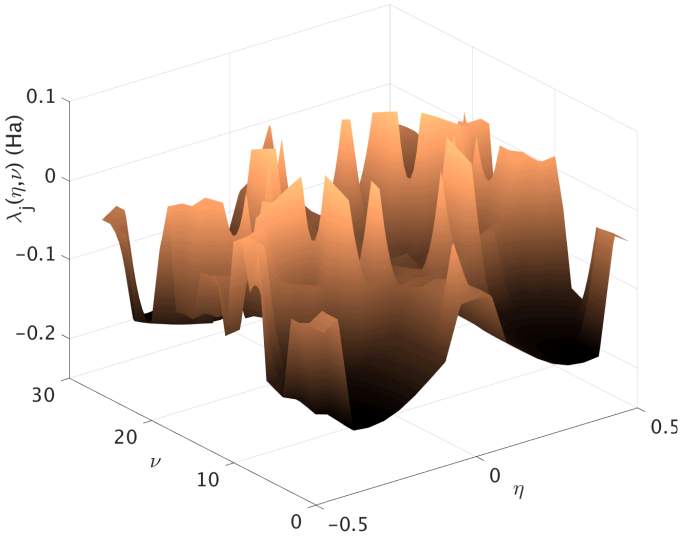

(a) 2D surface plot of the eigenvalues $\lambda_j(\eta, \nu)$, for $j = 8$.

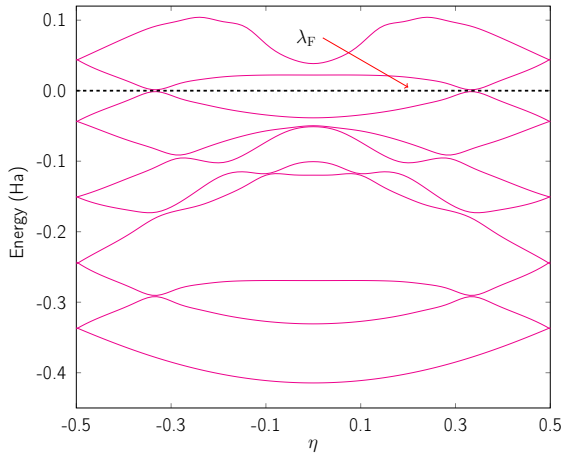

(b) Symmetry adapted band diagram in η, along $\nu = 0$. Plot is symmetric about $\eta = 0$ due to time reversal symmetry.

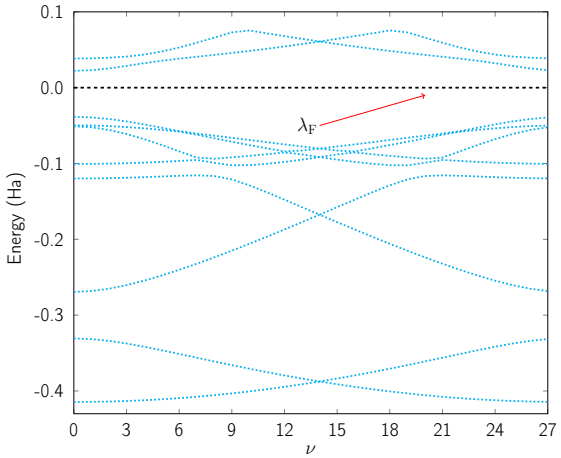

(c) Symmetry adapted band diagram in ν, along $\eta = 0$. Plot is symmetric about $\nu = 14$ due to time reversal symmetry.

Figure 3.10: Visualization of electronic states for the untwisted armchair Si nanotube (radius 2.96 nm) using results from Helical DFT. Compare this to Figure 3.9.

regime and obtained values of t_0 between 2.6 and 3.0 eV (see Figure 3.11). These agree well with the literature (1; 2; 3), giving us confidence in the quality of our subsequent simulations. Upon twisting these nanotubes further, the band gap is known to further increase and then decrease, as the tube alternates between metallic and semiconducting states, and the period of oscillation (of the band gap versus rate of twist plot) is theoretically known to be (143; 151; 3; 1):

$$\xi_{\text{period}}^{\text{theory}} = \frac{a}{R_{\text{tube}}^2}\,. \tag{3.4}$$

Here a denotes the carbon-carbon bond length (see Table 3.1). Using Helical DFT, we were able to compute the electronic density of states near the Fermi level and qualitatively verify the metal-to-semiconductor transitions in the armchair carbon nanotubes as they are twisted (see Figure 3.13(a)). To verify that Helical DFT also reproduces the quantitative aspects of the variation, we fit the band gap data from Helical DFT, to a general sine curve of the form:

$$\text{band gap} = s_1 \sin\left(\frac{2\pi\alpha}{s_2} + \frac{2\pi}{s_3}\right) + s_4\,, \tag{3.5}$$

from which, the period of oscillation may be computed as:

$$\xi_{\text{period}}^{\text{fit}} = \frac{2\pi s_2}{\tau} = \frac{2\pi s_2}{\sqrt{3}a}\,. \tag{3.6}$$

We verified that $\xi_{\text{period}}^{\text{fit}}$ and $\xi_{\text{period}}^{\text{theory}}$ are in close agreement in all cases under study (see Figure 3.11 for a specific example). An alternate means of quantifying this agreement, following (1), is to equate $\xi_{\text{period}}^{\text{fit}}$ and $\xi_{\text{period}}^{\text{theory}}$, and estimate the bond length a, from this instead. In other words, by writing:

$$s_2 = \frac{\sqrt{3}\,a^2}{2\pi R_{\text{tube}}^2}\,, \tag{3.7}$$

or more generally,

$$s_2 = \sigma \times R_{\text{tube}}^{\mu}\,, \tag{3.8}$$

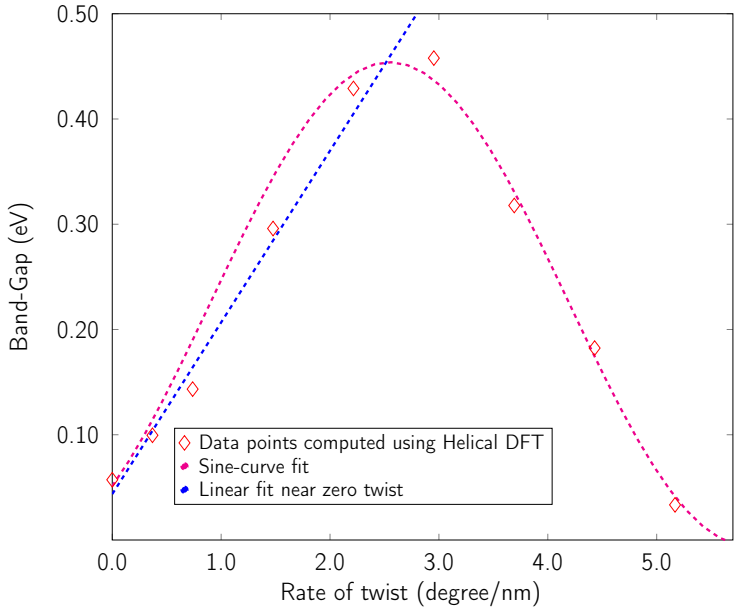

Figure 3.11: Analysis of the variation of band-gap with applied twist, using an armchair carbon nanotube example (Radius = 1.07 nm). The straight line fit near zero enables the evaluation of the tight-binding hopping parameter t_0, which comes out to be 2.897 eV, in close agreement with (1; 2; 3). The sine curve fit (in the non-linear response region) enables evaluation of the periodicity in the band gap variation and yields $\xi^{\rm fit}_{\rm period} = 0.1154$ rad/nm. The theoretical value from eq. 3.4 is $\xi^{\rm theory}_{\rm period} = 0.1217$ rad/nm, in close agreement.

we may evaluate the exponent μ and the constant σ from a plot of s_2 versus $R_{\rm tube}$, and from this, we may further estimate the bond length as:

$$a_{\rm fit} = \frac{\sqrt{2\pi\sigma}}{3^{\frac{1}{4}}}\,. \tag{3.9}$$

Using this procedure, we arrived at $\mu = -1.98$, and $a_{\rm fit} = 1.37$ angstrom, both of which are very close to the expected values of -2.00 and 1.40 angstrom, respectively. These results give us further confidence in the quantitative results obtained using Helical DFT.

Turning to the broader class of armchair group IV nanotubes (i.e., X = Si, Ge, Sn) we make the following observations using the data obtained from Helical DFT. In general, these nanotubes are semiconducting, with a direct band gap located at the same position

as the armchair carbon nanotubes, i.e., $\eta = \frac{1}{3}, \nu = 0$ (or equivalently, $\eta = -\frac{1}{3}, \nu = 0$) for untwisted tubes. Upon twisting, these tubes also undergo periodic oscillations in their band gaps,[5] although the amplitudes of the oscillations are generally more muted than the case of armchair carbon nanotubes, and we did not observe metal-to-semiconductor type transitions for most tubes. For tubes with larger radii however, the untwisted states can be associated with vanishingly small band gaps to begin with — owing to the decay relations obeyed by the band gaps (7; 140), and these tubes are likely to be practically metallic at room temperature. Therefore, changes to the band gap upon application of twist can be more easily discerned (See Figures 3.10 and 3.12 for an example involving an armchair silicon nanotube). To quantify the periodic changes in the band gaps, we obtained the period of oscillation in each case using the sine curve fitting procedure outlined above (eq. 3.5), and computed the power law dependence of the period on the tube radius by means of eq. 3.8 (see Figure 3.14). The values of c and μ so obtained are shown in Table 3.3.

The results are clearly suggestive of the fact that the period of variation of the band gap scales in an inverse quadratic manner with the tube radius for all armchair X nanotubes. We also observed that evaluation of eq. 3.9 using the values of σ shown in Table 3.3 leads to quantities that are fairly close to the values of a shown in Table 3.1, for each armchair X nanotube, suggesting that the theoretical relation in eq. 3.4 is generally valid for this entire class of nanotubes.

Finally, we touch upon our investigations related to zigzag X nanotubes. These can be of different "types" (7; 151), i.e., Type I, II or III, depending on whether $\mathrm{mod}(\mathfrak{N}, 3) = 1, 2$ or 0. In general, zigzag X nanotubes, barring Type III carbon variants, are semiconducting (7; 168), and the untwisted tubes have direct bandgaps located at the following values of η

[5]The location of the band gap initially continues to be the same as that of the untwisted tube, but then it transitions to small values in ν (i.e. $\nu = 1, 2$, etc.), while remaining at the same location in η (i.e., $\eta = \frac{1}{3}$). Thus, for relatively small twists, the band gap continues to be a direct one. Upon further application of twist however, the band gap becomes indirect and the eigenvalue just above the Fermi level is associated with a different value of ν as compared to the eigenvalue just below the Fermi level, although the value of η associated with these eigenvalues continues to be $\frac{1}{3}$.

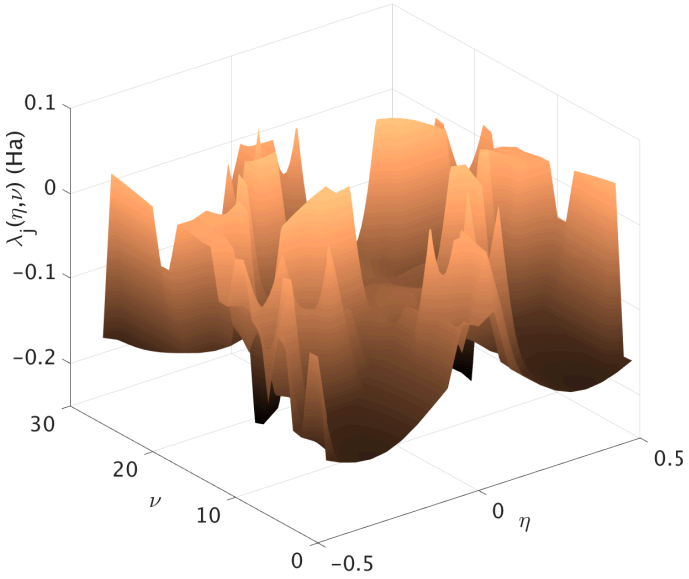

(a) 2D surface plot of the eigenvalues $\lambda_j(\eta, \nu)$, for $j = 8$.

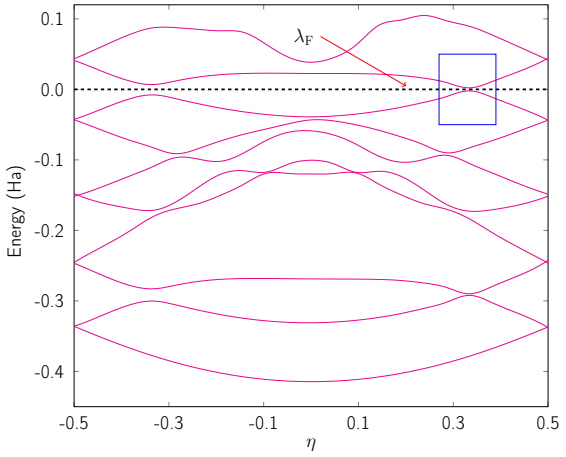

(b) Symmetry adapted band diagram in η, along $\nu = 1$. Location of band gap highlighted by blue rectangle.

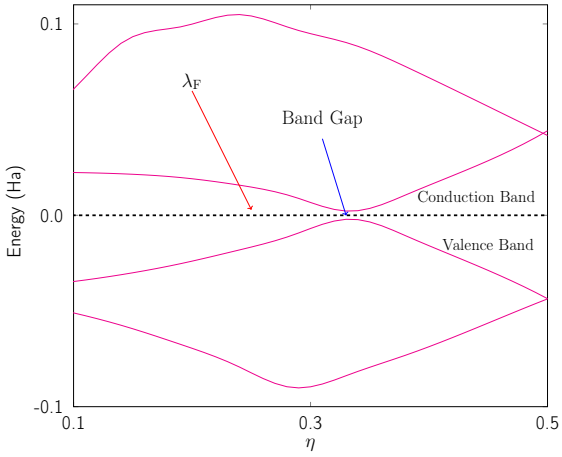

(c) Zoomed in view of band gap and its location.

Figure 3.12: Visualization of electronic states for twisted armchair Si nanotube (radius = 2.96 nm), for 0.94 degree per nanometer of applied twist. A small bandgap of about 0.11 eV opens up in this case. Location of band gap ($\eta = 1/3, \nu = 1$) has been highlighted by blue rectangle in sub-figure (b) and a zoomed in view is available in sub-figure (c). The surface plot in sub-figure (a) also looks noticeably different from Figure 3.10 (a).

Material	σ ($\text{Å}^{-\mu}$)	μ
Carbon	0.52	-1.98
Silicon	1.86	-2.10
Germanium	1.91	-2.09
Tin	1.34	-1.91

Table 3.3: Parameters for the scaling law $s_2 = \sigma \times R_{\text{tube}}^{\mu}$ for armchair X nanotubes. Here, s_2 is the bandgap oscillation parameter as defined in eq. 3.5. The value of μ in each case is close to -2.00, suggesting that the period of variation of the band gap scales in an inverse quadratic manner with the nanotube radius for these tubes.

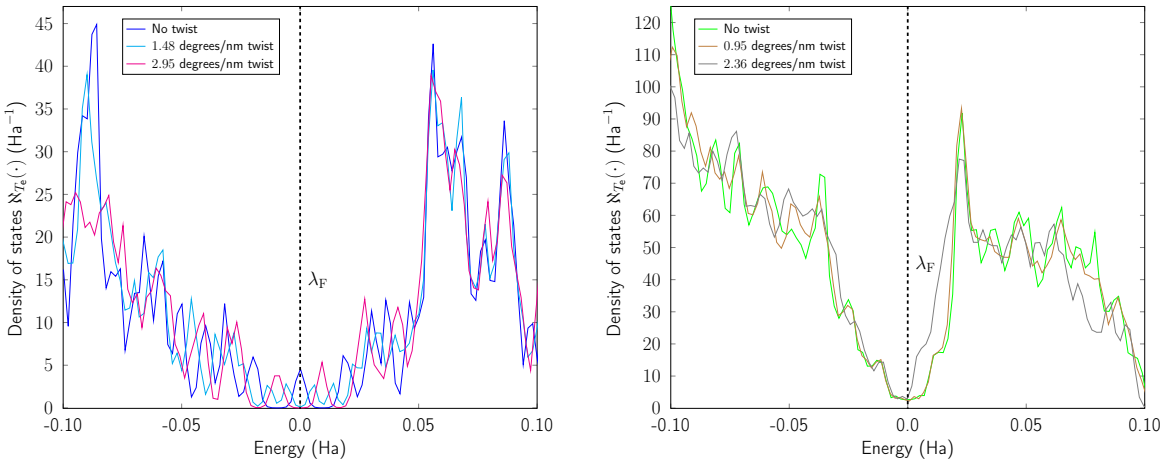

(a) Carbon nanotube, radius = 1.07 nm

(b) Silicon nanotube, radius = 2.96 nm

Figure 3.13: Variation in the electronic density of states near the Fermi level, for some armchair X nanotubes, when subjected to twist. The carbon nanotube undergoes a clear metal-to-semiconductor type transition upon twisting, as evidenced by the value of $\aleph_{T_e}(\cdot)$ falling to zero at the Fermi level. Other armchair Xene nanotubes (including the silicon nanotube shown here) do not show such stark variations, although changes in the electronic structure are clearly induced by the application of twist.

and ν – Type I carbon nanotubes: $\eta = 0, \nu = \frac{\mathfrak{N}-1}{3}$; other Type I nanotubes: $\eta = 0, \nu = \frac{\mathfrak{N}+2}{3}$; Type II nanotubes: $\eta = 0, \nu = \frac{\mathfrak{N}+1}{3}$; Type III nanotubes: $\eta = 0, \nu = \frac{\mathfrak{N}}{3}$. We found that

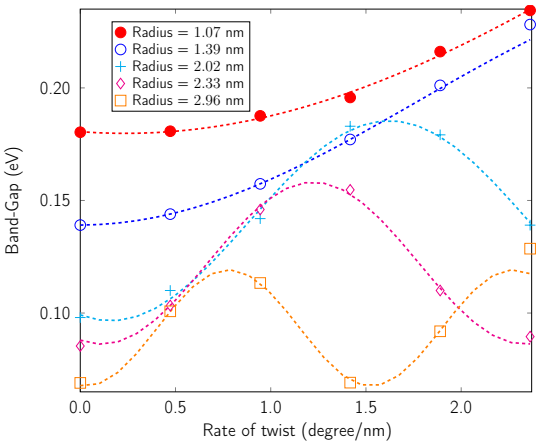

(a) Silicon nanotubes

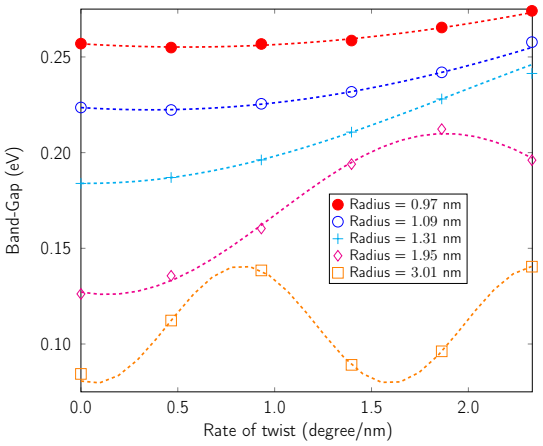

(b) Germanium nanotubes

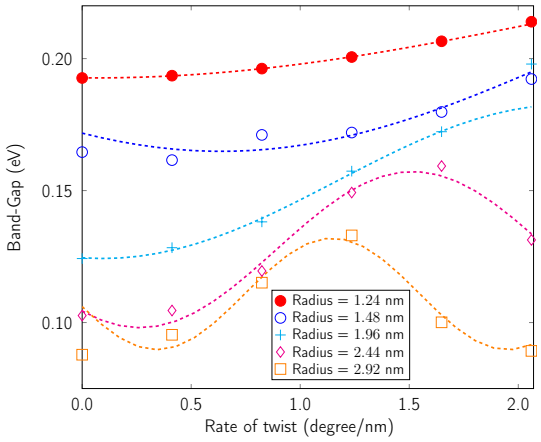

(c) Tin nanotubes

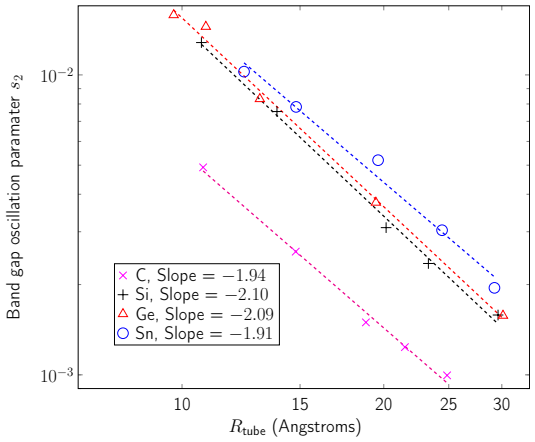

(d) Investigation of scaling laws in periodicity of band gap variation

Figure 3.14: Variation of band gap with applied twist for armchair X (= Si, Ge, Sn) nanotubes. Sub-figures (a), (b) and (c) include data from Helical DFT, as well as sine curve fits (dotted lines) used to determine the band gap oscillation parameter s_2 (eq. 3.5). Sub-figure (d) explores the variation of this parameter with the tube radius (eq. 3.8). The slope of each of the straight line fits is close to -2.00, suggesting that the period of variation of the band gap scales in an inverse quadratic manner with the nanotube radius.

the band gaps of Type I and II zigzag X nanotubes tend to have a rather limited response to torsional deformations, consistent with earlier observations made regarding zigzag carbon nanotubes specifically (143; 151; 3). For most of these types of materials, the band gaps are non vanishing at zero twist for even relatively large radii tubes and the subsequent changes to their band gaps due to twisting are fairly small at the levels of torsional deformation we considered. This tends to cause issues in discriminating between actual changes to the band gaps due to deformation, and the numerical noise associated with the simulations. Therefore, although we did observe oscillatory patterns in the band gap versus rate of twist plots (see Figure 3.15 for an example) we found it difficult to extract scaling laws from this data unambiguously. Out of all the different zigzag X nanotubes however, the Type III variants of carbon are metallic, especially at larger radii (i.e., when curvature effects are minimal) (7; 169), and we observed such tubes to be quite sensitive to torsional deformations. Similar to the case of armchair nanotubes, we observed these tubes to show oscillatory behavior between metallic and semiconducting states (see Figure 3.15), and an analysis of the period of variation of the band gap (using eq. 3.5 and 3.8) yielded $\mu = -1.98$, thus suggesting an inverse quadratic dependence on the radius. A thorough re-investigation of scaling laws in the electronic response of zigzag X nanotubes, by making use of more accurate numerical techniques (based on spectral methods (170; 171), for instance) remains the scope of future work.

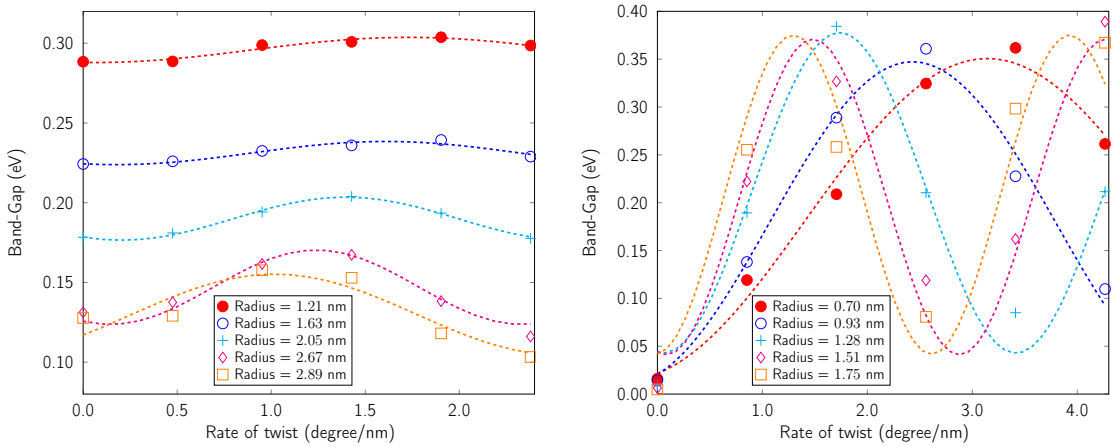

(a) Type II zigzag tin nanotubes

(b) Type III zigzag carbon nanotubes

Figure 3.15: Variation of band gap with applied twist for some zigzag nanotubes. Data from Helical DFT, as well as sine curve fits (dotted lines) are included. For most zigzag X nanotubes, particularly of Types I and II, the band gap changes little with twist. Sub-figure (a) shows examples of this using Type II tin nanotubes. In contrast, Type III zizag carbon nanotubes (sub-figure (b)) are metallic in the absence of twist and show more pronounced oscillatory changes between metallic and semiconducting states upon being twisted.

CHAPTER 4

Nanotubes reimagined: Carbon Kagome nanotubes

4.1 Introduction

Over the past two decades, the design, discovery and characterization of nanomaterials and nanostructures with special features in their electronic band structure has gained prominence. Exemplified famously by the case of linear dispersive relations in graphene (associated with massless Dirac fermions (135; 172)), such features often point to the existence of exotic electronic states, and the possibility of realizing unconventional electromagnetic, transport and optical properties in real systems. In recent years, materials and structures featuring dispersionless electronic states or *flat bands* have been heavily investigated due to the fact that electrons associated with such states have quenched kinetic energies[1] (are spatially localized), and interact in the strong correlation regime(173; 174; 175; 176). This manner of interaction leads to a variety of fascinating materials phenomena, including superconductivity (173; 177), ferromagnetism (178), Wigner crystallization (179; 180), and the fractional quantum Hall effect (181; 182; 183; 184).

Along these lines, moiré superlattices in twisted bilayers (185; 186; 35; 178; 187; 36) and materials with tailored atomic lattices (188; 189; 190; 191) have received much attention since they feature flat bands and rich electron physics. In order to observe and maintain desirable electronic properties, such systems usually involve some degree of engineering, and more often, a fine control over important system parameters (e.g. bilayer twists at

[1]While linearly dispersive states are associated with extremely high charge carrier mobilities, flat band electrons are massive and effectively have zero group velocity.

specific *magic angles* (192), or a critical magnetic field strength in quasi-two-dimensional (2D) network structures (193; 194)). Therefore, a strand of recent investigations has focused on the synthesis and characterization of materials which feature electronic flat bands due to their natural atomic arrangements (195; 196; 197; 198; 199; 200; 201; 202; 203). Exotic electronic states hosted by such materials can be stable with respect to perturbations such as changes in temperature or applied strains, and they can often display such states without external fields — features which make them suitable for device applications. Alongside these experimental studies, computational investigations have also probed elemental versions of such materials, i.e., stable bulk or 2D nanomaterials made of a single species of atom that can feature unusual electronic states by virtue of their atomic arrangements alone (204; 205; 206; 8; 9; 207; 8). The present study extends this particular line of work to the important case of quasi-one-dimensional (1D) nanomaterials featuring flat bands, which have generally received far less attention in the literature.[2]

The possibility of realizing flat band physics and exotic states of electronic matter in wire-like geometries is particularly exciting. While well known theoretical considerations (211; 212) appear to preclude the existence of long range order in low dimensional systems (necessary, e.g. in realizing superconducting states), such restrictions do not necessarily apply to the quasi-one-dimensional structures considered here (213). In fact, there are reasons to expect that the screw transformation symmetries and quantum confinement effects often associated with such systems can actually result in enhancement of collective or correlated electronic properties (214; 32; 215), and that such properties are likely to be manifested in manners that are quite different from bulk phase materials. In particular, materials such as the ones considered in this chapter can be *chiral* — due to intrinsic or applied twists — and therefore, feature anomalous transport (the Chiral Induced Spin Selectivity, or CISS

[2]There has been recent work (see e.g. (208; 176; 209; 210)) on quasi-two-dimensional systems and heterostructures, featuring one-dimensional flat bands, or flat bands along specific directions of a two-dimensional Brillouin zone. In contrast, the systems studied here are all elemental quasi-one-dimensional (1D) nanostructures that feature flat bands throughout the entirety of their (one-dimensional) Brillouin zone.

effect (216; 217)). The exploration of simultaneous manifestations of such effects along with correlated electron physics has begun fairly recently (218; 219; 220; 221). We posit that the carbon nanostructures explored here are likely to emerge as a possible material platform for such studies in the future.

Due to its unique allotrope forming features and versatility (222; 223; 224), carbon is particularly attractive as a building block of novel materials. A large number of computational studies have recently been devoted to 2D and bulk allotropes of carbon displaying Dirac cones, flat bands and non-trivial topological states (225; 226; 205; 227; 228; 229; 230; 231; 232). On the other hand, although several 1D allotropes of carbon are well known (29; 137; 233; 234; 235; 236; 237; 238; 239; 240; 241; 242), none of these systems are usually associated with flat band physics. As far as we can tell, there have been only a few earlier attempts at producing and investigating flat bands in realistic 1D nanomaterials of carbon: partially flat bands in zigzag graphene nanoribbons (243), spin polarized flat bands in hydrogenated carbon nanotubes (244), and moiré type flat bands in chiral carbon nanotubes with collapsed structures (245; 246) or incommensurate double wall geometries (247). Our contribution aims to address this particular gap in the literature by studying a family of realistic 1D carbon nanostructures that naturally feature flat bands throughout their Brillouin zone. The flat bands in the structures presented here arise out of geometric and orbital frustration and without the aid of dopant or major structural instability effects, as employed in the aforementioned studies. Moreover, as we demonstrate, these dispersionless electronic states show fascinating transitions as the structures are subjected to strains, while also proving to be robust and retaining many desirable characteristics in some respects.

To obtain a 1D carbon nanostructure with flat bands, our starting point is a planar sheet of Kagome graphene. We then "roll up" this 2D material along different directions to obtain Carbon Kagome Nanotubes (CKNTs). Kagome graphene and related bulk structures have recently received much attention in the materials literature (9; 8; 207; 204; 206; 248; 249), and also in the physics literature, where the material is often identified as a "decorated

honeycomb" or "star lattice" structure (250; 251; 252; 253; 254; 255; 191). Although Kagome graphene remains to be experimentally synthesized, successful synthesis of a variant of this material, i.e., nitrogen-doped graphene on a silver substrate — a 2D material with a Kagome pattern, has been carried out recently (256; 257). Moreover, synthesis of novel complex nanotube structures in general (see e.g. (258)) and through the roll-up of 2D sheets in particular, is fairly common (see e.g. (259)), thus suggesting that CKNTs can be synthesized in the near future.

In this chapter, we introduce CKNTs, and carry out a thorough and systematic first principles characterization of this material in terms of its structural, mechanical and electromechanical properties. Wherever relevant, we provide comparisons of the properties of CKNTs against those of conventional carbon nanotubes (CNTs). All CKNTs studied here are metallic and feature flat bands (throughout their Brillouin zone) near the Fermi level, along with an associated singular peak in the electronic density of states. We show in particular that CKNTs appear to be more mechanically compliant when compared against CNTs, and that their electronic properties undergo significant electronic transitions — with emergent partial flat bands and Dirac points — when subjected to torsional strains. Our studies are made possible largely due to a suite of recently developed symmetry adapted electronic structure calculation techniques (54; 4; 5; 7; 55; 62; 260), that allow ab initio calculations of 1D materials and their deformed states to be carried out accurately and efficiently. We also develop a π-electron based tight binding model that includes up to next-nearest-neighbor interactions, which is able to capture many of the electronic properties of CKNTs, as revealed via first principles data.

4.2 Material and Methodology

In this section, we introduce the geometry of Carbon Kagome nanotubes (CKNTs) and their construction from Kagome graphene through the "roll up" procedure commonly employed

in other similar types of nanomaterials (261; 45). We also provide an outline of the various computational and theoretical methods used in our study.

4.2.1 From Kagome Graphene to Carbon Kagome Nanotubes

Several recent studies have explored the structure of Kagome graphene sheets and related bulk structures (206; 8; 248; 207; 204; 191). As a starting point, we first consider the geometry of Kagome graphene. The hexagonal unit cell of this 2D material consists of 6 carbon atoms that form a pair of equilateral triangles, as shown in Fig. 4.1. We used the planewave

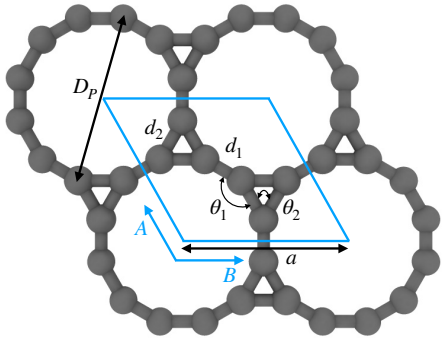

Figure 4.1: Unit cell of Kagome Graphene with various structural parameters indicated. The angle θ_1 is 150°, while θ_2 is 60°. The other parameters can be found in Table 4.1.

code ABINIT (42; 262; 161) to optimize the geometry of this structure. Our calculations employed norm conserving Troullier Martins pseudopotentials (263), an energy cutoff of 50 Ha, $21 \times 21 \times 1$ k-point sampling and Fermi-Dirac smearing of 0.001 Ha. These parameters were sufficient to produce accurate energies, forces and cell stresses for the pseudopotentials chosen (5). We employed both Perdew-Wang (108) local density approximation (LDA) and Perdew-Burke-Ernzerhof (PBE)(264) generalized gradient approximation (GGA) exchange correlation functionals. At the end of the relaxation procedure, the atomic forces were typically of the order of 10^{-5} Ha/Bohr, while the cell stresses were of the order of 10^{-8} Ha/Bohr^3.

Table 4.1 shows that the optimized structural parameters obtained by us are in very

good agreement with the literature. As expected (265), the LDA bond lengths are somewhat shorter than those obtained through functionals involving gradient corrections, although the variations observed are quite minor overall. Notably, the intertriangle C-C bond length was found to be slightly smaller than the bond length corresponding to the triangle sides. Additionally, the calculated bond angles were found to be 60° (in-triangle) and 150° (inter-triangle) almost perfectly, consistent with the literature. Next, following the construction

Parameters	Current work	Literature
a (Å)	$5.1370^a (5.1662)^b$	$5.2085^c, 5.2087^d, 4.46^e$
d_1 (Å)	$1.3402^a (1.3400)^b$	$1.3559^c, 1.3567^d, 1.50^e$
d_2 (Å)	$1.4078^a (1.4206)^b$	$1.4305^c, 1.4299^d, 1.53^e$
D_p (Å)	$5.3090^a (5.3331)^b$	$5.3817^c, 5.3829^d$

Table 4.1: Optimized structural parameters of Kagome graphene. Superscripts denote parameters obtained using: (a) LDA functional (this work), (b) GGA functional (this work), (c) SGGA-PBE functional (reference (8)), (d) SGGA-PBE functional with Grimme D3 correction (reference (8)), and (e) GGA functional using the bulk structure (reference (9)).

of carbon nanotubes from graphene (266; 267; 261), we rolled up the optmized flat Kagome graphene structures into seamless cylinders and arrived at carbon Kagome nanotubes (see Fig. 4.2). Depending on the direction of rolling, the tubes maybe armchair, zigzag or chiral, with non-negative integers (n, m) denoting the chirality indices. In this work, we focus exclusively on armchair (i.e., (n, n)) and zigzag (i.e., $(n, 0)$) nanotubes (illustrated in Fig. 4.3). The index n for such achiral tubes indicates the degree of cyclic symmetry about the tube axis. An investigation of chiral CKNTs is the scope of future work. Notably, the replacement of hexagons in conventional CNTs, by dodecagonal rings in CKNTs, results in a structure with more porous sidewalls, and suggests the use of this material in filtration (268), desalination (269) and electrochemical storage aplications (270; 271; 272).

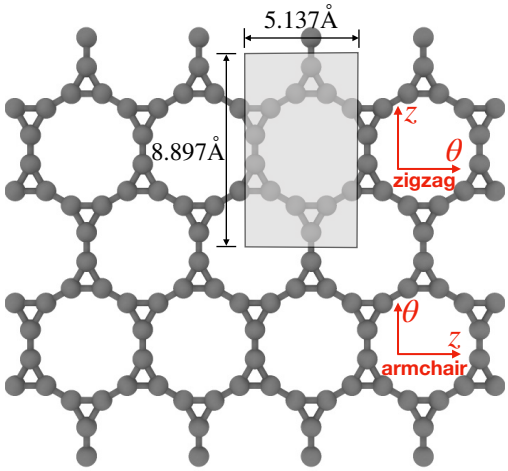

Figure 4.2: Roll-up construction of CKNTs, starting from a sheet of Kagome graphene. θ denotes the direction of roll up, while z denotes the tube axis direction. The 12 atoms shown in the shaded region are the representative atoms in the fundamental domain used for Helical DFT (4; 5) calculations. The domain size parameters illustrated above correspond to calculations based on LDA exchange-correlation.

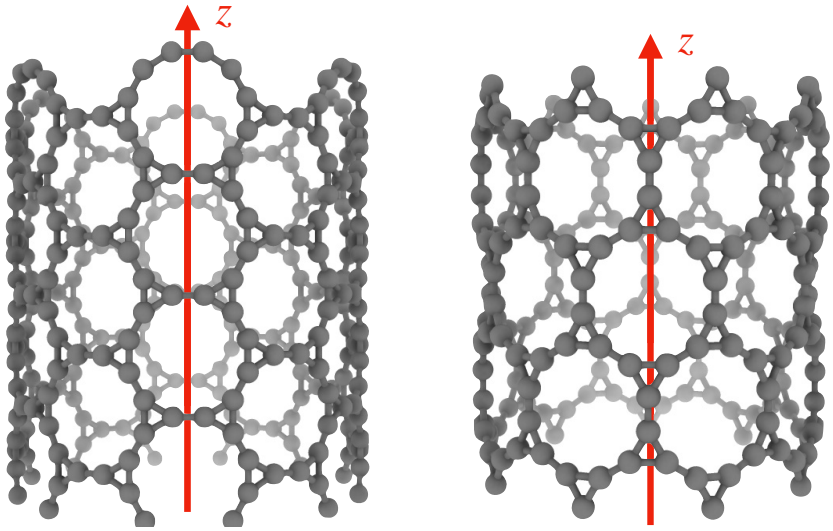

(a) Armchair (6,6) CKNT (b) Zigzag (9,0) CKNT

Figure 4.3: Two varieties of CKNTs investigated in this work: (a) Armchair (n, n) and (b) Zigzag $(n, 0)$ tubes. The tube radii are 0.85 nm and 0.74 nm, respectively for the above examples. n is the cyclic symmetry group order about the tube axis.

4.2.2 Plane-wave DFT calculations

While the majority of the first principles calculations in this work have been carried out using Helical DFT, we used plane-wave DFT (16; 273) for carrying out a few additional first principles calculations of CKNTs. Specifically, we investigated the dynamic stability of undistorted CKNTs by performing *ab inito* molecular dynamics (AIMD) simulations. The highly scalable PWDFT code (274; 275; 276; 277) was used for this purpose. We investigated two generic CKNTs — one each of the zigzag and armchair varieties — with radii of 0.75 and 0.85 nm for our simulations. In order to capture long range deformation modes, we considered atoms beyond the minimal periodic unit cell and chose multiple layers of the tubular structures along the axial direction. This resulted in supercells containing 144 and 216 atoms for the armchair and zigzag variety tubes respectively. Periodic boundary conditions were enforced along the axial direction and a large amount of vacuum padding (~ 35 Bohr) was included in the other two directions to prevent interactions between periodic images. Optimized Norm Conserving (ONCV) pseudopotentials (278; 279), and LDA exchange correlation were employed. An energy cutoff of 40 Ha was employed and only the gamma point of the Brillouin zone was sampled. The structures were first relaxed using the Broyden–Fletcher–Goldfarb–Shanno (BFGS) algorithm (280) following which AIMD simulations were performed at temperatures of 315.77 K, 631.55 K and 947.31 K using the Nosé–Hoover thermostat (281; 282). Time steps of 1.0 fs were employed for integration and $5.0 - 7.0$ ps of trajectory data were collected for analysis.

Finally, we used the Quantum Espresso code (43; 283; 284) for computing the projected density of states (PDOS) of undistorted armchair and zigzag CKNTs. Pseudopotentials from the Standard Solid State Pseudopotentials (SSSP) library (285; 286), along with an energy cutoff of 40 Ha, LDA exchange correlation and Gaussian smearing (corresponding to an electronic temperature of 315.77 K) were employed. Keeping in mind the geometry of the nanotube, the PDOS were calculated in the local atomic coordinate frame, i.e., the projections were taken on atomic orbitals that had been rotated to a basis in which the

occupation matrix appears diagonal.

4.3 Properties of CKNTs

In this section, we discuss the structural, mechanical and electronic properties of CKNTs as revealed by our simulations.

4.3.1 Structural properties: Cohesive energy, sheet bending modulus and dynamic stability

Fig. 4.4 shows the cohesive energy of armchair and zigzag CKNTs as the tube radius varies in the range 1 to 3 nm (approximately). Owing to the contribution from the elastic sheet bending energy, the cohesive energy of both types of tubes decrease monotonically as the tube radius increases, i.e., the tubes are energetically more favorable with decreasing sheet curvature. In our calculations, the energy of an atom in Kagome graphene, as calculated in terms of the large radius limit of the energies of CKNTs, agrees with direct calculations of the sheet to better than 1 milli-eV, thus ensuring overall consistency of the results. For a given radius, the zigzag and armchair CKNTs appear nearly identical energetically, similar to the behavior of conventional CNTs, also shown in Fig. 4.4. Assuming a quadratic dependence of the bending energy on curvature, i.e., Euler-Bernoulli behavior, we evaluated the area-normalized sheet bending modulus of Kagome graphene to be 0.506 eV and 0.502 eV in the armchair and zigzag directions, respectively (also see Fig. 4.2). This is about a third of the sheet bending modulus of conventional graphene, estimated to be about 1.5 eV through similar first principles calculations (7).

From Fig. 4.4, it is also evident that for a similar value of the radius, CNTs are energetically more favorable compared to CKNTs (i.e., CNTs have larger cohesive energies). We remark however that this observation in of itself does not preclude the synthesis of CKNTs. Indeed, fullerenes can be readily produced, although they have long been known to

have cohesive energies that are somewhat lower than other common allotropes of carbon (261; 287; 288; 289). More recently γ-graphyne, which has a significantly lower cohesive energy compared to graphene (290) has also been chemically synthesized (291; 292; 293). Notably, there has also been success in synthesis of other unusual quasi-one-dimensional allotropes of carbon starting from conventional carbon nanotubes (236), which may be adopted for producing CKNTs. The phonon stability of Kagome graphene sheets has been investi-

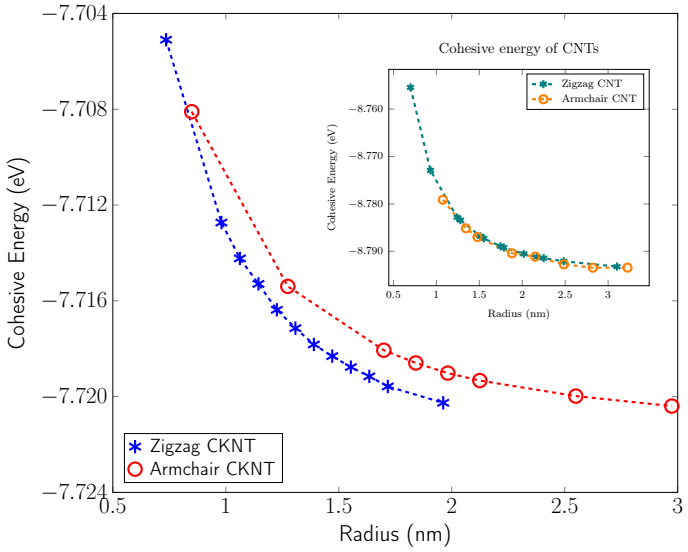

Figure 4.4: Cohesive energy of zigzag and armchair CKNTs. Inset: Cohesive energy of conventional zigzag and armchair carbon nanotubes (CNTs) presented for comparison.

gated earlier (207). Based on band-folding considerations (294; 295; 296), such calculations are also likely to be indicative of the stability of CKNTs at zero temperature. To investigate the finite temperature structural stability of CKNTs, we carried out AIMD simulations at three different temperatures — 315.77 K, 631.54 K and 947.31 K. The system energy is observed to be stable throughout each of these simulations (Fig.4.7). We conclude that CKNTs are able to maintain their overall structural integrity at room temperature, and beyond, thus making them physically realistic nanostructures. Notably, during the course of the simulations, the structures appear to undergo dynamic distortions similar to conventional CNTs (297; 45; 298), and show a propensity for developing transitory ellipsoidal cross sections,

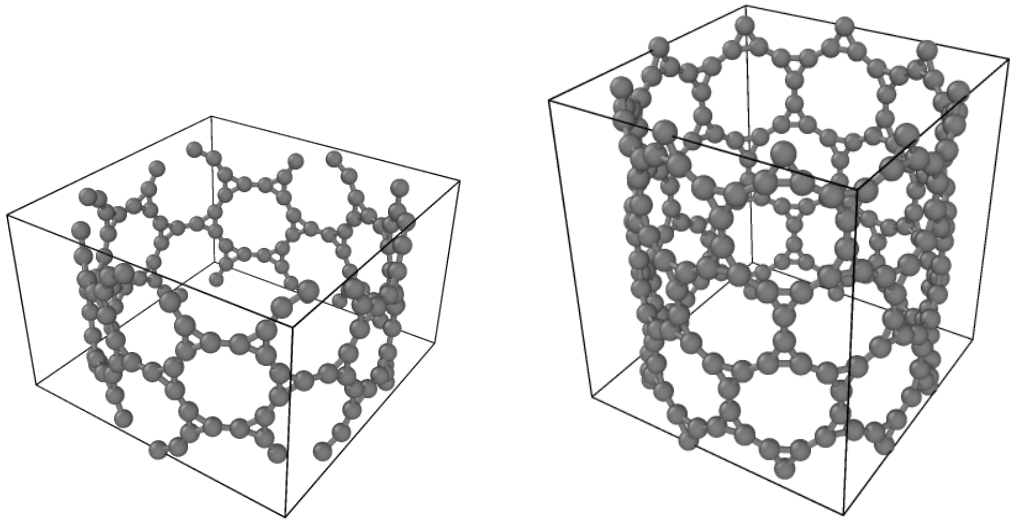

(a) Armchair CKNT (Unit cell with 144 atoms)

(b) Zigzag CKNT (Unit cell with 216 atoms)

Figure 4.5: Snapshot of AIMD simulations at 315.77 K for both types of CKNTs.

especially at elevated temperature (Fig. 4.6 (a)). Nevertheless, the dodecagonal rings which make up CKNTs and which are crucially related to their fascinating electronic properties (discussed in Section 4.3.3), continue to be maintained (Fig. 4.6 (b)). Given the relatively low sheet bending stiffness of Kagome graphene (as compared to conventional graphene, e.g.), it is quite possible that large diameter CKNTs, like their CNT counterparts (299; 300; 301) have a tendency to collapse. From this perspective, the distorted cross sections described above are possible indicators of this kind of structural transition, and warrant further investigation in the future. Snapshots of the AIMD simulations is provided in Figs. 4.5 and 4.6, and the entire simulation trajectories at 315.77 K are available as Supplementary Materials.

4.3.2 Mechanical properties: Torsional and extensional stiffness

We focus on mechanical properties of CKNTs, namely their torsional and extensional responses in the linear elastic regime. As described earlier, Helical DFT allow such calculations to be carried out by introducing changes in the nanotube symmetry group parameters.

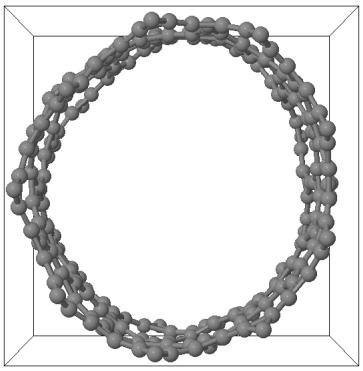

(a) Transitory ellipsoidal cross section of Zigzag CKNT at elevated temperature

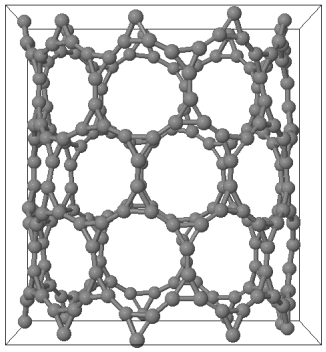

(b) Side view of the same structure showing overall structural integrity and persistence of dodecagonal rings

Figure 4.6: Snapshot of AIMD simulations of a Zigzag CKNT at an elevated temperature of 631.554 K. The cross-section shows a propensity for developing transitory distortions (left image). However, the overall structural integrity and the 12-fold rings continue to be maintained (right image).

We consider $(12, 12)$ armchair (radius 1.7 nm) and $(12, 0)$ zigzag (radius 0.98 nm) CKNTs as representative examples. For both these tubes, we start from the undistorted, relaxed configurations.

For simulations involving torsion, we increment the parameter α in regular intervals, imposing up to about $\beta = 4.5^\circ$ of twist per nanometer, the limit of linear response for conventional CNTs (45). For each twisted configuration, we relax the atomic forces and compute the twisting energy per unit length of the nanotubes as the difference in the ground state free energy (per fundamental domain) of the twisted and untwisted structures, i.e.:

$$U_{\text{twist}}(\beta) = \frac{\mathfrak{N}}{\tau}\left(\mathcal{F}_{\substack{\text{Ground}\\\text{State}}}(\mathcal{P}^{**}, \mathcal{D}, \mathcal{G}|_\beta) - \mathcal{F}_{\substack{\text{Ground}\\\text{State}}}(\mathcal{P}^{*}, \mathcal{D}, \mathcal{G}|_{\beta=0})\right). \tag{4.1}$$

In the equation above, $\mathcal{G}|_\beta$ and $\mathcal{G}|_{\beta=0}$ denote the symmetry groups associated with the twisted and untwisted structures, respectively and (as before) $\mathfrak{N}$ denotes the cyclic group order. Additionally, $\mathcal{P}^{**}$ and $\mathcal{P}^{*}$ denote the collections of relaxed positions of the atoms in

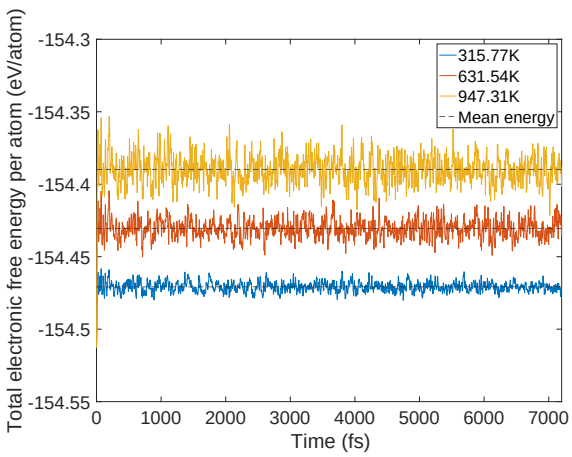

(a) Energy variation over ab-initio molecular dynamics trajectories over 7 ps of simulation time at 315.77 K (blue), 631.54 K (red) and 947.31 K (yellow) of an armchair CKNT. Black broken line represent the mean energy.

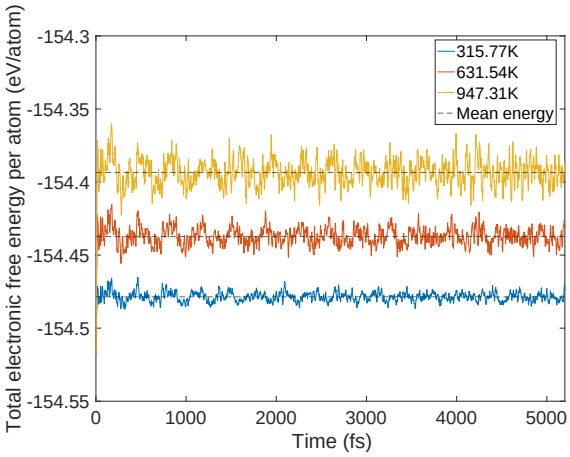

(b) Energy variation over ab-initio molecular dynamics trajectories over 5 ps of simulation time, at 315.77 K (blue), 631.54 K (red) and 947.31 K (yellow), of a zigzag CKNT. Black broken line represent the mean energy.

Figure 4.7: System energy variation over ab-initio molecular dynamics (AIMD) trajectories at three different temperatures for (a) an Armchair CKNT and (b) a Zigzag CKNT. The AIMD simulations reveal that the nanotubes maintains their overall structural integrity far above room temperature.

the fundamental domain in each case. Thereafter, the torsional stiffness is computed as:

$$k_{\text{twist}} = \left.\frac{\partial^2 U_{\text{twist}}(\beta)}{\partial \beta^2}\right|_{\beta=0}. \tag{4.2}$$

We observed that for the range of torsional deformations considered here, the behavior of $U_{\text{twist}}(\beta)$ is almost perfectly quadratic with respect to β, consistent with linear elastic response (see Fig. 4.8). Moreover, the value of k_{twist} is estimated to be 3156.1 eV-nm and 979.51 eV-nm for the armchair and zigzag tubes, respectively. In the linear elastic regime, the torsional behavior of nanotubes is well approximated by continuum models which suggest that k_{twist} should vary with the tube radius in a cubic manner (5; 45; 165). By use of this scaling law, we were able to estimate that conventional CNTs with radii comparable to the CKNTs considered above are expected to be significantly more rigid with respect to twisting

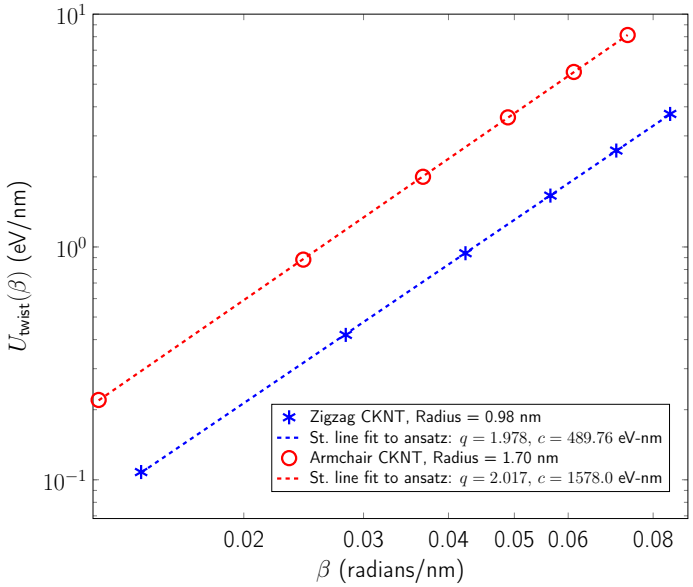

Figure 4.8: Twist energy per unit length as a function of angle of twist per unit length for two representative nanotubes (both axes logarithmic). Dotted lines indicate straight line fits of the data to an ansatz of the form $U_{\text{twist}}(\beta) = c \times \beta^q$. The exponent q is nearly 2 in both cases, suggesting linear elastic behavior.

(with k_{twist} values equal 2.8977×10^4 eV-nm and 5525.0 eV-nm for 1.7 nm and 0.98 nm radius conventional CNTs, respectively).

Next, for simulations involving axial stretch and compression, we proceed in a manner similar to the torsion simulations. For a given value of axial strain ϵ, we modify the pitch of the helical symmetry group as $\tau = \tau_0(1+\epsilon)$, with τ_0 denoting the equilibrium, undistorted values. Subsequent to this kinematic prescription, we relax the atomic forces, and compute the extensional energy per unit length of the nanotubes as the difference in the ground state free energy per fundamental domain, between stretched and unstretched structures, i.e.:

$$U_{\text{stretch}}(\epsilon) = \frac{\mathfrak{N}}{\tau_0}\Bigg(\underset{\text{State}}{\mathcal{F}_{\text{Ground}}}(\mathcal{P}^{**}, \mathcal{D}, \mathcal{G}|_{\tau=\tau_0(1+\epsilon)}) - \underset{\text{State}}{\mathcal{F}_{\text{Ground}}}(\mathcal{P}^{*}, \mathcal{D}, \mathcal{G}|_{\tau=\tau_0})\Bigg). \tag{4.3}$$

In the equation above, $\mathcal{G}|_{\tau=\tau_0(1+\epsilon)}$ and $\mathcal{G}|_{\tau=\tau_0}$ denote the symmetry groups associated with

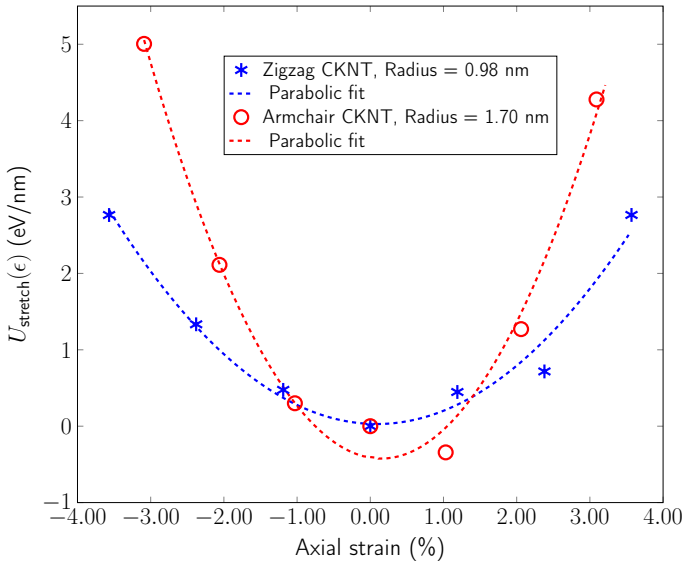

Figure 4.9: Extensional energy per unit length as a function of axial strain for two representative CKNTs. Dotted curves indicate parabolic fits of the data to an ansatz of the form $U_{\text{stretch}}(\epsilon) = c \times \epsilon^2$.

the stretched and unstretched structures, respectively. Additionally, $\mathcal{P}^{**}$ and $\mathcal{P}^{*}$ denote the collections of relaxed positions of the atoms in the fundamental domain in each case. The stretching stiffness of the nanotubes may be then calculated as:

$$k_{\text{stretch}} = \left. \frac{\partial^2 U_{\text{stretch}}(\epsilon)}{\partial \epsilon^2} \right|_{\epsilon=0}. \tag{4.4}$$

In our simulations, we restricted ϵ to be between $+3.6\%$ and -3.6%. In this range, $U_{\text{stretched}}(\epsilon)$ is found to depend in a quadratic manner on ϵ, consistent with linear elastic behavior (see Fig. 4.9). We also observed a small Poisson effect, which we have ignored in subsequent analyses. For armchair $(12, 12)$ and zigzag $(12, 0)$ CKNTs, we estimated k_{stretch} to be 5220.9 eV/nm and 2093.4 eV/nm respectively. Based on scaling laws arising from continuum theory (165), we also estimated that conventional armchair CNTs with the same radii as the CKNTs considered above would be noticeably stiffer to axial deformations (k_{stretch} values equal to 1.2213×10^4 eV/nm and 7048.2 ev/nm for 1.7 nm and 0.98 nm radius

conventional CNTs, respectively).

Overall, these results suggest that CKNTs are significantly more pliable with respect to torsional and axial deformations, as compared to their conventional CNT counterparts. Coupled with the lower bending stiffness of Kagome graphene as compared to conventional graphene, they are indicative of the fact that Kagome graphene has a lower value of in-plane (thickness normalized) Young's modulus and shear modulus.

4.3.3 Electronic properties

We discuss the electronic properties of CKNTs as revealed by first principles simulations. We start from a discussion of the properties of undistorted tubes, following which we discuss the electronic response of the tubes when subjected to torsional and axial strains. Conventional CNTs can be metallic or semiconducting depending on whether they are armchair (all tubes metallic) or zigzag (tubes with cyclic group order $\mathfrak{N}$ divisible by 3 are metallic), and the electronic band diagrams of these materials prominently feature Dirac points near the Fermi level (7; 5; 302; 261; 151). In contrast, our simulations reveal *all CKNTs* to be metallic, with their electronic band diagrams prominently featuring dispersionless electronic states, or *flat bands*, close to the Fermi level. Figs. 4.10a and 4.12a show complete band diagrams of undistorted CKNTs (i.e., all electronic states corresponding to allowable values of reciprocal space parameters η, ν are plotted), while Fig. 4.11 and 4.13 show symmetry adapted versions of these plots (i.e., band diagrams with chosen reciprocal space parameters along cyclic or helical directions). Notably, a CKNT of cyclic group order $\mathfrak{N}$ is found to feature $2\mathfrak{N}$ nearly degenerate flat bands near the Fermi level. An associated singular peak in the electronic density of states (Figs. 4.10b, 4.12b) is also observed[3], and both zigzag and armchair tubes are found to feature quadratic band crossing (QBC) points at $\eta = 0$ (corresponding to the gamma

[3]Our simulations suggest that the singular peak in the DOS of CKNTs occurs very close to the Fermi level — about 0.006 Ha away for the examples discussed here. In experimental situations, the peak in the DOS can be brought to the Fermi level exactly, by application of an external electric field or by doping (207), thus making the associated electronic states more readily accessible.

point of the flat sheet). These features make CKNTs striking examples of realistic quasi-one-dimensional materials that are likely to exhibit strongly correlated electronic states. The detailed investigation of exotic materials phenomenon in CKNTs resulting from such strong electronic correlations — including e.g., Wigner crystallization, flat-band ferromagnetism and the emergence of superconducting, nematic or topological phases (303; 207; 304) — is the scope of future work. Considering that such phenomena have been studied primarily in bulk and two dimensional materials, the role that the quasi-one-dimensional morphology of CKNTs might play in them makes these investigations particularly interesting.

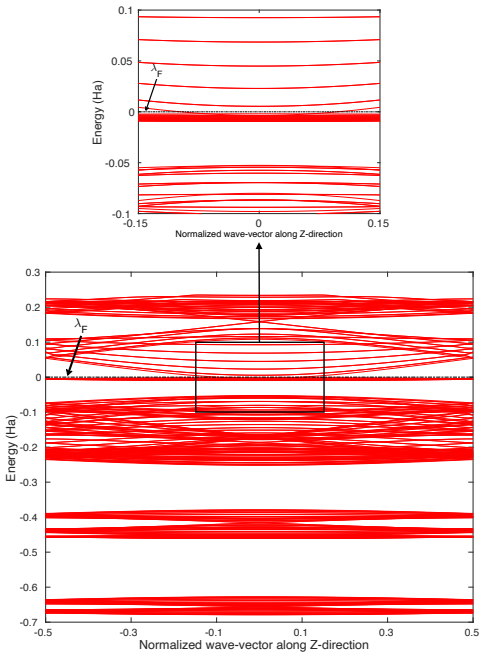

(a) Complete band diagram for an undistorted zigzag CKNT of radius 0.98 nm with a zoomed-in view of flat bands and quadratic band crossing point.

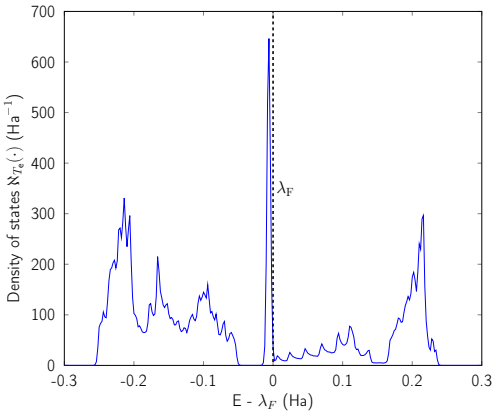

(b) Electronic density of states of the same material.

Figure 4.10: (a) Complete band diagram and (b) Electronic density of states near the Fermi level of an undistorted zigzag CKNT (radius 0.98 nm). λ_F denotes the Fermi level.

The dispersionless states in CKNTs are caused by destructive interference, resulting from geometric and orbital frustration, as has also been shown to occur in other Kagome lattice

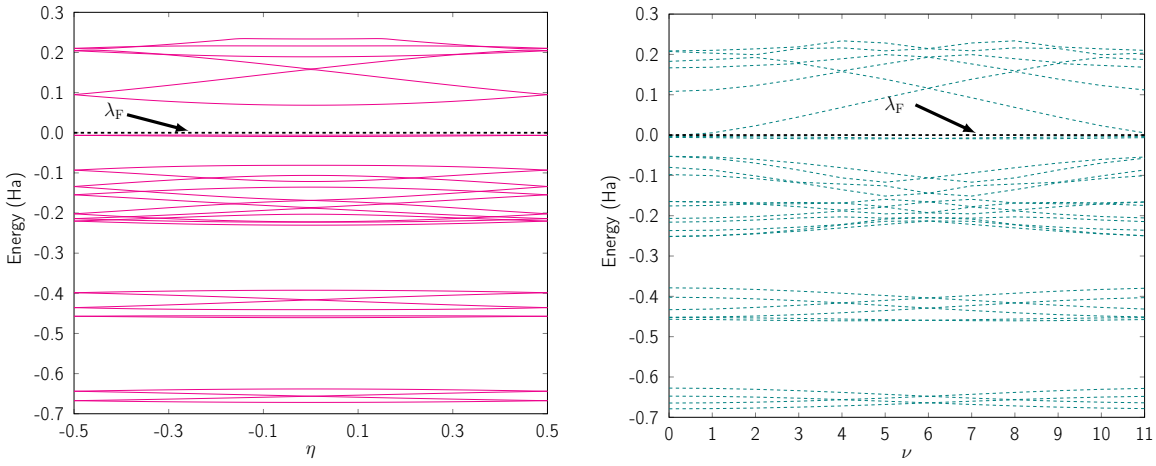

(a) Symmetry adapted band diagram in η, along $\nu = 4$.

(b) Symmetry adapted band diagram in ν, along $\eta = 0$. Quadratic band crossing at $\nu = 0$ can be observed.

Figure 4.11: Symmetry adapted band diagrams of an undistorted zigzag CKNT (radius 0.98 nm) obtained using Helical DFT (4; 5). λ_F denotes the Fermi level.

systems (305; 306; 307). The electron effective mass is arbitrarily large at the flat band and the diminished electronic kinetic energy allows the Columbic interactions to dominate, resulting in strong electronic correlation. In turn, this causes electron localization[4] and the emergence of a sharp peak (i.e., van Hove singularity (310)) in the electronic density of states (DOS) near the Fermi level (as shown in Figs. 4.10b and 4.12b). The localized states corresponding to an undistorted armchair CKNT are shown in Fig. 4.14a. A plot of the electron density distribution for that system is also shown (Fig. 4.14b).

At this point, it is worth mentioning some similarities of the electronic properties of CKNTs with their conventional counterparts. Like conventional CNTs, the fascinating electronic properties of CKNTs are largely connected to π electrons formed from radially oriented p_z orbitals, while the p_x and p_y orbitals form in-plane σ bonds and are largely electronically inactive (207). This is supported by projected density of states (PDOS) calculations for CK-

[4]The localization mechanism described above is different from Anderson localization, where electronic waves become diffusionless due to disorder/impurities in the system (308; 309).

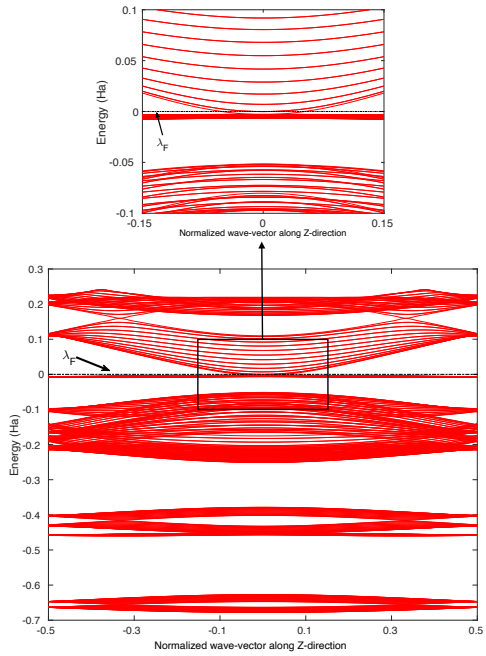

(a) Complete band diagram for an undistorted armchair CKNT of radius 1.70 nm, with zoomed-in view of flat bands and quadratic band crossing point.

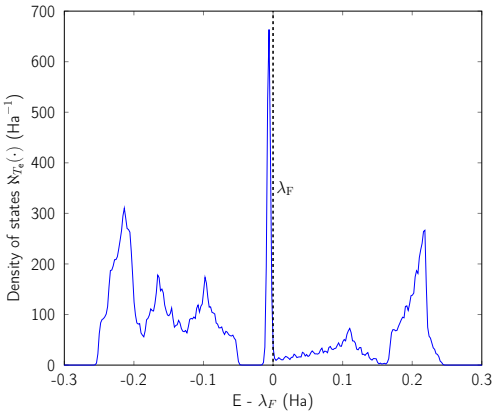

(b) Electronic density of states of the same material.

Figure 4.12: (a) Complete band diagram and (b) Electronic density of states near the Fermi level for the undistorted armchair CKNT (radius 1.70 nm). λ_{F} denotes the Fermi level.

NTs (Fig. 4.15), which show that the singular peak in the (total) electronic density of states near the Fermi level is largely attributable to the contributions of the individual (radially oriented) $\mathrm{p_z}$ ($l = 1, m_l = 0$) orbitals, while p_{x} and p_{y} orbital contributions lie well below the Fermi level. Moreover, the band diagrams of CKNTs have some similarities in appearance with those of conventional CNTS, e.g., the presence of Dirac points at $\eta = 0$ for zigzag tubes and at $\eta = \pm\frac{1}{3}$ for armchair ones (Figs. 4.10a, 4.12a). However, unlike conventional CNTs, these Dirac points do not appear at the Fermi level in undistorted CKNTs, but are prominently featured as a part of the excited states of the system.

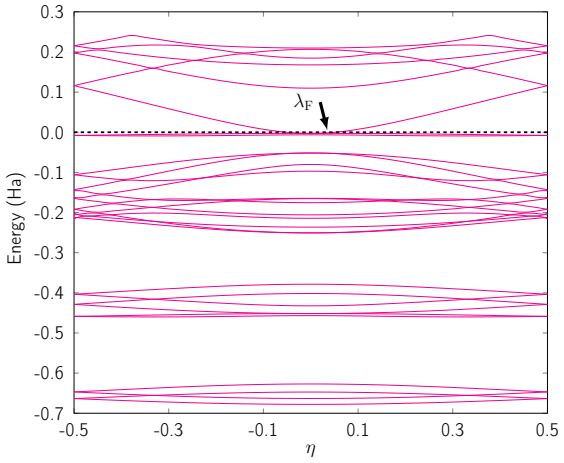

(a) Symmetry adapted band diagram in η, along $\nu = 0$. Quadratic band crossing at $\eta = 0$ can be observed.

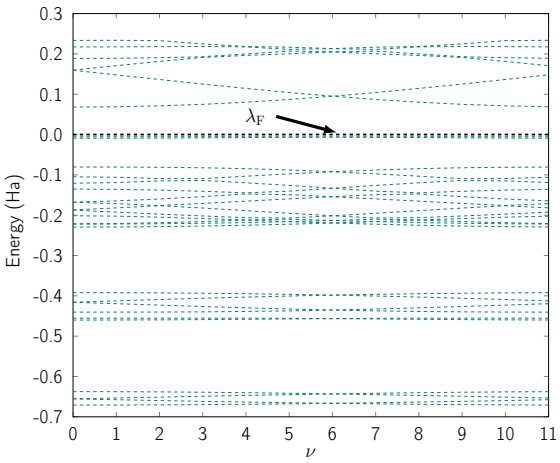

(b) Symmetry adapted band diagram in ν, along $\eta = 1/3$.

Figure 4.13: Symmetry adapted band diagrams of an undistorted armchair CKNT (radius 1.70 nm) obtained using Helical DFT (4; 5). λ_F denotes the Fermi level.

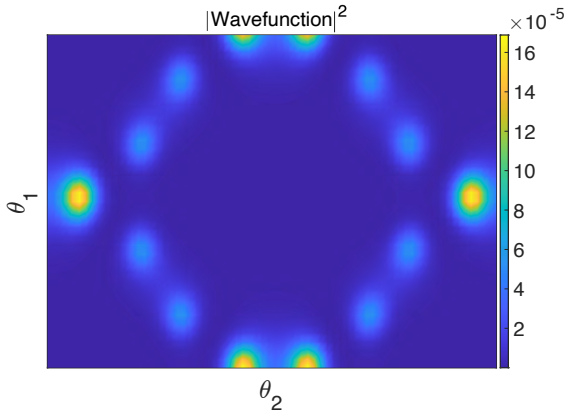

(a) VBM wavefunction

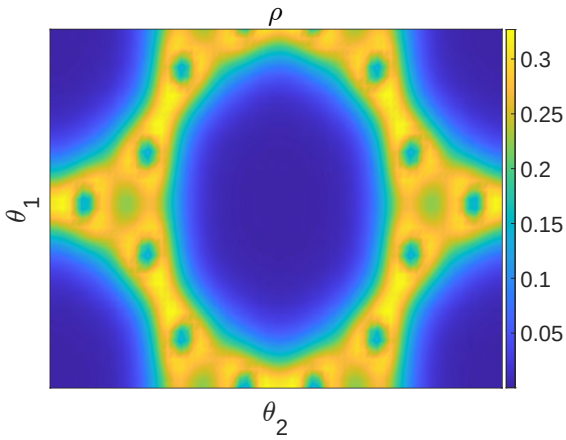

(b) Electron density

Figure 4.14: Valence Band Maximum (VBM) wavefunction and the electron density of an undeformed armchair $(12, 12)$ CKNT. A slice of the electronic fields at the average radial coordinate of the atoms in the computational domain (represented using helical coordinates (4)) is shown.

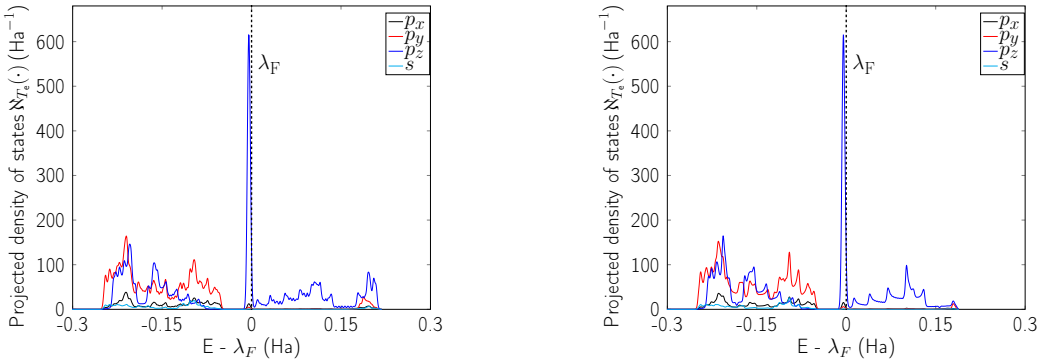

(a) Projected density of states for an armchair CKNT ($\mathfrak{N} = 6$)

(b) Projected density of states for a zigzag CKNT ($\mathfrak{N} = 9$)

Figure 4.15: Projected density of states (PDOS) for undistorted armchair and zigzag CKNTs. The largest contribution to the sharp peak near the Fermi level is seen to arise from p_z orbitals.

4.3.3.1 Electromechanical response of CKNTs: Effect of torsional and axial strains on electronic properties

We discuss the changes to electronic properties of CKNTs to applied deformations. First, we discuss the effect of torsional strains. We use the $(12, 12)$ armchair CKNT as a prototypical example; zigzag CKNTs are found to have similar behavior. As shown in Fig. 4.16a, application of twist to the CKNT destroys the in-plane C_6 symmetry of the underlying Kagome graphene lattice structure, while maintaining its C_2 symmetry. Consequently (311; 312; 313), the quadratic band crossing (QBC) point at $\eta = 0$ splits into a pair of Dirac points (Fig. 4.17a)[5]. Furthermore, the degeneracy in the $2\mathfrak{N}$ flat bands at the Fermi level appear to be lifted, and a number of dispersionless states appear to give way to bands that are only *partially flat*. The change of completely flat bands to ones which have some dispersion near $\eta = 0$ is also evidenced by the electronic density of states plot in Fig. 4.17b,

[5]The "tilted" nature of the linearly dispersive electronic bands near these Dirac points appears to suggest connections with (quasi-one-dimensional) Weyl semimetals (312; 314).

which shows that the sharp peak near the Fermi level decays as the rate of applied twist increases. Despite these twist induced changes, a number of dispersionless states survive (Fig. 4.16a) and spatially localized wavefunctions associated with such states continue to be hosted by the nanotube (Fig.4.16b). Notably, the application of twist results in energy dispersion relations that feature rather dramatic changes in the electronic effective mass as the Brillouin zone is traversed — from infinitely massive carriers near $\eta = 0$, to massless ones as the Dirac points are reached, and then re-appearance of infinitely massive ones as the edge of the Brillouin zone is approached (i.e., closer to $\eta = \pm\frac{1}{2}$). Overall, these observations suggest that torsional strains provide a way of controlling correlated electronic states in CKNTs. Moreover, twisted CKNTs, being chiral, are likely to show asymmetric transport properties (216; 217). Therefore, they provide an interesting, realistic material platform where the combined manifestations of anomalous transport phenomena (the Chiral Induced Spin Selectivity effect (315)) and flat band physics may be realized and studied.

Next, we discuss the case of axial strains. In general, such deformations also tend to introduce some degree of dispersion into the flat bands of CKNTs near $\eta = 0$, while lifting their degeneracies near the Fermi level. However, their influence appears to be less dramatic than the case of torsional deformations described above. Nevertheless, the axial compression case deserves particular mention. Considering the zigzag $(12, 0)$ CKNT for example, we observe (see Fig. 4.18a) that the dispersion introduced in the flat bands near $\eta = 0$ results in curvature of these states in a manner that is opposite (i.e., convex vs. concave) of the situation encountered while twist is applied (i.e., Fig. 4.17a). Thus, a scenario akin to the touching of a pair of parabolic bands (316; 313) emerges. Upon subjecting the tube to larger values of compression, we observed that the parabolic bands near $\eta = 0$ give way to linear dispersion, i.e., the emergence of Dirac points. Commensurate with these changes, the sharp peak in electronic the density of states (Fig. 4.18b) also diminishes with increasing magnitude of axial strain, although the decrease appears to be less dramatic than the situation encountered with torsion (i.e., Fig. 4.17b).

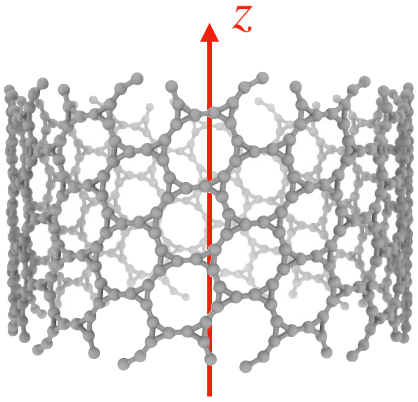

(a) Armchair $(12, 12)$ CKNT with $4.5°/\text{nm}$ twist

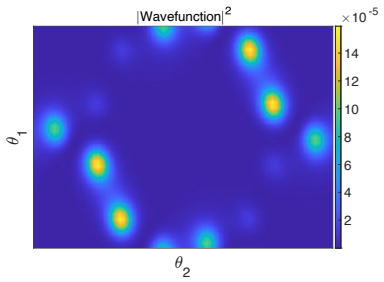

(b) VBM wavefunction

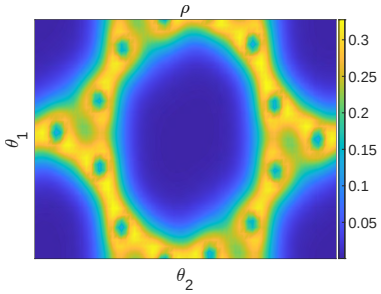

(c) Electron density

Figure 4.16: Atomic configuration, Valence Band Maximum (VBM) wavefunction and the electron density of an armchair $(12, 12)$ CKNT with $\beta = 4.5°/\text{nm}$ applied twist. A slice of the electronic fields at the average radial coordinate of the atoms in the computational domain (represented using helical coordinates (4)) is shown.

Overall, the above observations are consistent with literature that suggests that quadratic band crossing points are unstable with respect to strains (317; 318). It is also worthwhile at this point to contrast the electromechanical response of CKNTs to conventional CNTS. Zigzag CNTs with cyclic group order divisible by 3 and armchair CKNTs are both metallic (7), and they are known to be more sensitive to axial and torsional strains respectively. The effect of such deformations, at least for small strains, is to open up a gap at the Dirac points of these materials, resulting in metal-semiconductor transitions (3; 151; 1; 143; 5; 156). As described above, CKNTs appear to show more dramatic electronic transitions

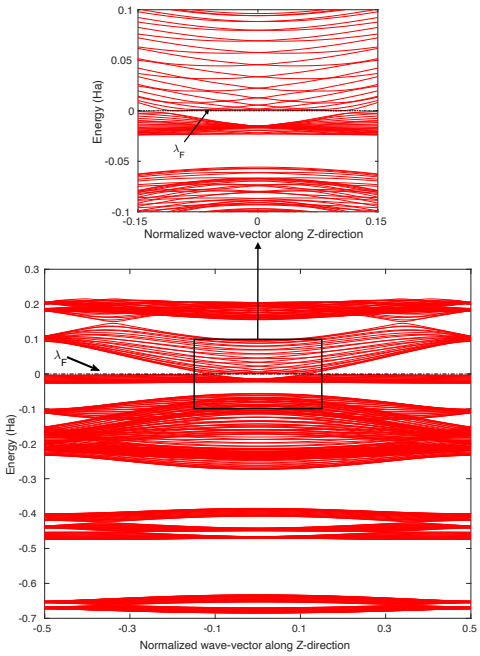

(a) Complete band diagram for a twisted armchair CKNT of radius 1.70 nm and a rate of twist of 4.20°/nm. Complete and partial flat bands, along with emergent Dirac points are featured.

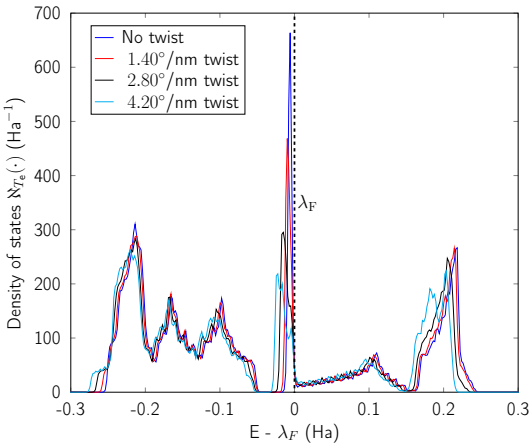

(b) Variation of the electronic density of states of the same material with twisting.

Figure 4.17: (a) Complete band diagram and (b) Electronic density of states near the Fermi level for the twisted armchair CKNT (radius 1.70 nm). λ_F denotes the Fermi level.

when subjected to such strains. At the same time, the simulations above suggest that at least some dispersionless states in CKNTs are robust and continue to be available when the tube is subjected to small torsional and axial strains.

4.3.4 Possible routes to the synthesis of CKNTs

Our calculations suggest that CKNTs are kinetically stable, which is often taken to be a promising sign of the synthesizability of carbon allotropes (207; 319). In the past, a wide variety of metastable carbon allotropes have been fabricated (320), often with significantly lower cohesive energies than other common stable counterparts. Examples of successful

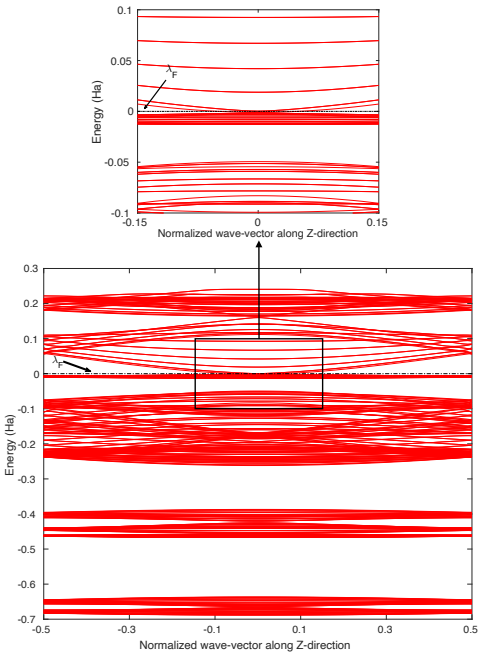

(a) Conventional band diagram for a stretched zigzag CKNT of radius 0.98 nm and an axial strain of -3.57%.

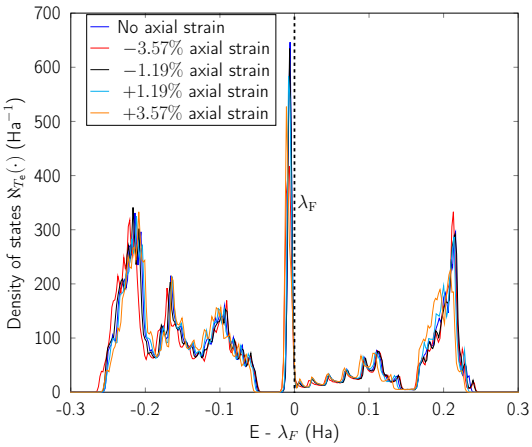

(b) Variation in electronic density of states of the same material with applied axial strains.

Figure 4.18: (a) Complete band diagram and (b) Electronic density of states near the Fermi level for the stretched Zigzag CKNT (radius 0.98 nm). λ_F denotes the Fermi level.

synthesis of such unusual carbon allotropes include γ-graphyne (291; 292; 293; 290) , T-carbon (236; 321) and nitrogen-doped Kagome graphene (257; 256). In particular, various methods of synthesis of conventional carbon nanotubes, including laser ablation and chemical vapor deposition have been explored (322; 323). Some of these techniques have also been successfully used in manufacturing other 1D carbon allotropes, e.g. T-carbon nanotubes, which can be created from conventional carbon nanotubes through a picosecond pulsed-laser irradiation induced first order phase transition. Such techniques provide additional routes for synthesizing CKNTs. Irrespective of the method, we anticipate that the analysis presented in this paper is likely to be instrumental in realizing CKNTs experimentally.

Since a variety of routes have been exploited for synthesizing different allotropes of carbon, multiple avenues also possibly exists for realizing CKNTs. We suggest two possibilities

here, both based on the organic synthesis of Kagome graphene and subsequent roll-up of this material to form CKNTs. One possibility is to use silver adatoms to transform tetrabromobocyclopropene to intermediate organometallic complex and to then form Kagome graphene on the surface of SiO_2 substrate with etchant sensitive gold layer in between (256), as represented in left panel of Fig. 4.19a. The second possibility is through the use of cyclopropane or bicyclopropane (207; 319), wherein tailoring of ligand chemistry can be used to form self-assembled kagome graphene on the surface of gold (111), deposited on a SiO_2 substrate (shown in right panel of Fig. 4.19a). This latter method is similar to recently demonstrated self-assembly procedures in metastable carbon nanowiggles (324; 325). After the synthesis of Kagome graphene, targeted etching of the gold layer (326) can result in the curling of the 2D material into CKNTs, as desired. The lower bending stiffness of kagome graphene in contrast to conventional graphene (Section 4.3.1) will likely assist in this step (Fig.4.19b).

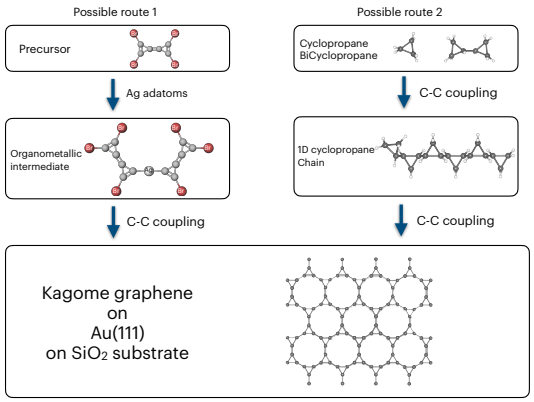

(a) Two possible ways to fabricate 2D flat sheet of Kagome graphene. Left panel: From tetrabromobicyclopropene to organometallic intermediate with Ag adatoms to the formation of final 2D sheet of carbon kagome lattice on Au(111) etchant material on SiO_2 substrate. Right Panel: From cyclopropane or bicycloprpane to 1D chain of cyclopropane to 2D sheet of carbon kagome lattice on Au(111) etchant material on SiO_2 substrate.

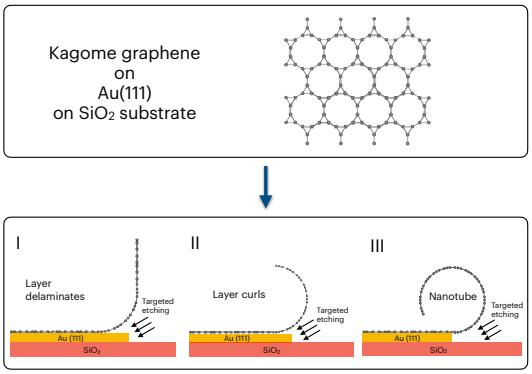

(b) Formation of Carbon kagome nanotube from Kagome graphene. After the target etching of Kagome graphene layer on Au etchant sensitive material on SiO_2 substrate surface the layer is curled up on to the sample surface where it can form bonds with itself.

Figure 4.19: Possible routes of synthesis of CKNTs. (a) Two possible routes to synthesis Kagome graphene. (b) Rolling up of a layer of Kagome graphene by target itching to form CKNTs.

CHAPTER 5

Nanotubes reimagined: Double Kagome P2C3 nanotubes

5.1 Introduction

A significant amount of research interests are currently directed towards nanomaterials and nanostructures because of their exotic electronic structure and diverse technological applications (327). The linearly dispersive Dirac cones crossing in graphene (135) and flat band touching quadratically the Dirac band in Kagome (328) are unconventional electronic bands. The former is associated with the massless fermions with very high mobility and exhibits unconventional electronic (329), transport (330), optical (331) and topological properties (332; 333). In latter electrons possess quenched kinetic energy and become spatially localized, thus existing in the strongly correlated regime. This phenomenon leads to fascinating collective electronic phases (173; 175) such as superconductivity(173; 177), ferromagnetism (334; 178), Wigner crystallization (179) and fractional quantum Hall effects (182; 183). While materials in kagome lattice can hosts both types of unorthodox bands, but the Dirac and flat bands do not appear simultaneously at the Fermi level. However, the lattices such as Lieb (335) and honeycomb-kagome (honeycomb split graph lattice) (336; 337; 338) possess flat bands with triply degenerate point at the Fermi level.

In this work, we introduce a quasi-one-dimenional P_2C_3 nanotubes (NTs) formed by mapping the optimized 2-dimensional lattice of P_2C_3 into seemless cylinders using the helical group of isometries as shown in the Fig. 5.1. It contains two sublattices comprising of gray carbon atoms which form kagome structure and orange phoshphorus atoms which link the carbon atoms occupy the hexagonal lattice sites. The nanotube can be classified by the non-negative

integers as chiral (n, m) and non-chiral - armchair (n, n) and zigzag $(n, 0)$ - depending on the direction of rolling. Here, we exclusively investigate armchair and zigzag nanotubes (see Fig. 5.1b & 5.1c) using first-principles calculations and also presented the second nearest neighbor tight-binding model. The nanotubes are not only kinetically stable but also show fascinating electronic structure properties.

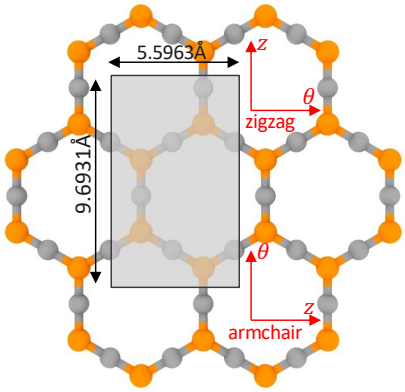

(a) Two-dimensional lattice of P_2C_3

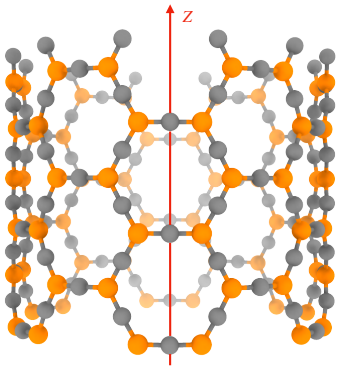

(b) Armchair (6,6) P_2C_3NT

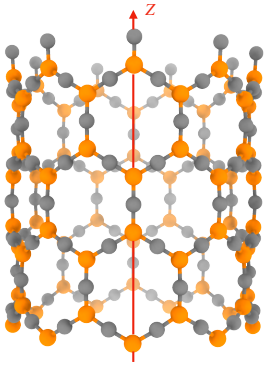

(c) Zigzag (9,0) P_2C_3NT

Figure 5.1: (a) Two dimensional lattice of P_2C_3 which is rolled up to form nanotubes. Two types of P_2C_3NTs is investigated in this work: (b) Armchair (n, n) and (c) Zigzag $(n, 0)$ nanotubes. The atoms in orange color are phosphorous and in grey color are carbon. The tube radii are 0.85 nm and 0.74 nm, respectively for the above examples. n is the cyclic symmetry group order about the tube axis.

5.2 Methodology

We employed specialized real-space based symmetry adapted Kohn Sham density functional theory (Helical DFT) (4; 5) for characterizing P_2C_3NTs. The plane-wave based codes - Quantum Espresso and Abinit are used to augment Helical DFT. The Helical DFT framework gives us an advantage to efficiently simulate quasi-one-dimensional materials such as nanotubes in pristine or deformed configuration by exploiting the global structural symmetries of the structure, which reduces the calculations to just a few atoms in the fundamental domain. In all the Helical DFT calculations we used 12^{th} order finite difference with vacuum distance of 10 bohr in the radial direction, 1 mili-Hartree of smearing using the Fermi–Dirac distribution and Perdew-Wang (PW) parametrization of the local density approximation (LDA) for the exchange correlation functional. To efficiently handle numerous electronic structure calculations for various P_2C_3NTs and investigate their electromechanical response to applied deformations, Helical DFT simulations were conducted in three successive phases. Initially, the atomic positions optimization is carried out, with mesh spacing $h = 0.3$ bohr and 15 η-point sampling, using limited memory Broyden–Fletcher–Goldfarb–Shanno (LBFGS) algorithm. These simulations are continued until the forces per atom are below 0.001 Ha/bohr. Subsequently, for ensuring precise calculation of energetics and stiffness parameters, we performed calculation on optimized structure with finer mesh of $h = 0.25$ bohr and 21 η-points. Finally, utilizing the self-consistent outcome from the previous step, we executed a singular Hamiltonian diagonalization step with 45 η-points. We used Abinit to optimize the geometry of two-dimensional (2D) hexagonal unit cell. To achieve this, we utilized norm-conserving Troullier–Martins pseudopotentials, PW-LDA exchange correlation functional, set an energy cutoff at 50 Ha, used $21 \times 21 \times 1$ k-point sampling, and applied Fermi–Dirac smearing with a value of 0.001 Ha. We also use Quantum Espresso code to calculate the projected density of states (pDOS) for undeformed nanotubes and to examine the thermal stability of the nanotubes we carried out *ab-inito* molecular dynamics (AIMD) simulations.

5.3 Properties of P_2C_3NTs

The conventional kagome-like structures has been observed as a central layer within bulk AB_3V_5 type materials. However, innate tendency of most elements to form a conventional 2D or even quasi -1D Kagome lattice is exceedingly limited. To achieve kaogme energy dispersion bands in nanotubes, we propose a P_2C_3NTs. Here, structurally relaxed single sheet of 2D P_2C_3 (339), with hexagonal lattice parameters (a = b = 5.69Å), is spontaneously rolled up into seemless cylinder. Specifically, the hexagonal unit cell comprises of two phosphorous and three carbon atoms which are strategically positioned at the corners of hexagonal lattice and the center of the hexagons' edges, respectively, thus stabilizing carbon atoms to exhibit kagome-like electronic structure. These nanotubes can be classified by the non-negative integers as chiral (n, m) and non-chiral - armchair (n, n) and zigzag $(n, 0)$ - depending on the direction of rolling. The natural number n in the achiral nanotubes denotes the cyclic group order, $\mathfrak{N}$, around the tube axis. In this letter, we exclusively investigate armchair and zigzag nanotubes (see Fig. 5.1b & 5.1c). We considered orthogonal unit cell (fundamental domain) which contains 10 representative atoms as shown in Fig. 5.1a. The parameter τ, which is associated with the pitch of screw transformation is 5.5963Å and 9.6931Å for undeformed armchair and zigzag nanotubes, respectively[1]. The angle of rotation of the cyclic symmetry group is defined as $\Theta = 2\pi/\mathfrak{N}$ accompanied by an additional scalar parameter α representing the applied or intrinsic twist in the structure. The amount of twist per unit length measured as $\beta = 2\pi\alpha/\tau$, where α varies from 0 to 1, with $\alpha = 0$ being untwisted nanotube.

We analysed various structural properties to assess the stability of the P_2C_3NTs. The cohesive energy depicted in Fig. 5.2a shows monotonically decreasing behavior from -5.350eV to -5.457eV as the radius of both zigzag and armchair nanotubes is increased from 5 Å to 35 Å . This suggests that tubes of larger radius are energetically more favourable due to the elastic bending energy of the 2D sheet. These values are intermediate between -4.22

[1]Changes in τ allow to examine the effects of uniaxial extensions and compressions on the electronic structure.(62)

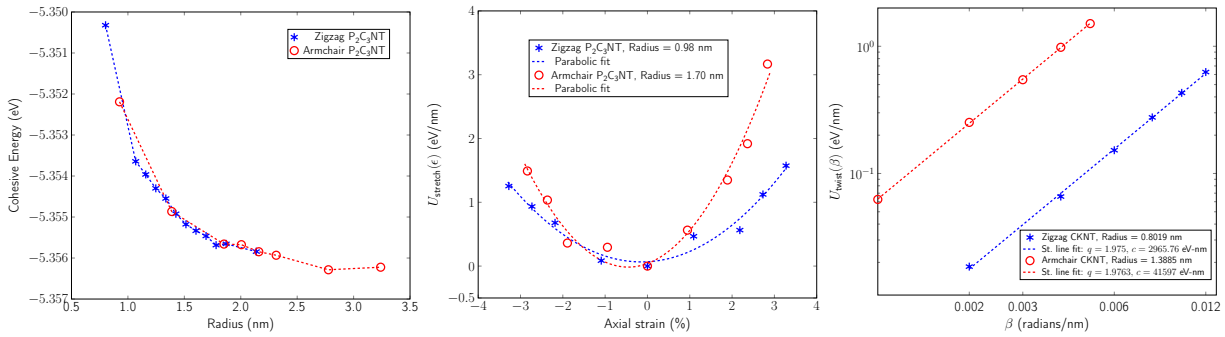

(a) (b) (c)

Figure 5.2: (a) Cohesive energy of zigzag and armchair P_2C_3 NTs. (b) Extensional energy per unit length as a function of axial strain for two representative P_2C_3 NTs. Dotted curves indicate parabolic fits of the data to an ansatz of the form $U_{\text{stretch}}(\epsilon) = c \times \epsilon^2$. (c) Twist energy per unit length as a function of angle of twist per unit length for two representative nanotubes (both axes logarithmic). Dotted lines indicate straight line fits of the data to an ansatz of the form $U_{\text{twist}}(\beta) = c \times \beta^q$. The exponent q is nearly 2 in both cases, suggesting linear elastic behavior.

eV of conventional phosphereneNTs and -8.80 eV of CNTs, suggesting thatP_2C_3NTs can be synthesized. The bending modulus of the P_2C_3 sheet comes out to be 0.1404 eV and 0.1520 eV when the sheet is bent in the armchair and zigzag directions, respectively. Notably, these findings indicate that the sheet bending modulus of P_2C_3 is approximately one-tenth of that observed for conventional graphene, estimated to be around 1.5 eV (7). Building upon the band-folding considerations of previous phonon stability calculations conducted on 2D sheets (339), we anticipate the structural integrity of P_2C_3NTs at zero temperature.

To understand the mechanical properties of P_2C_3 NTs, particularly their torsional and uniaxial strains response, we conducted HelicalDFT simulations by varying symmetry group parameters (τ and α) defining the nanotube. Particularly, we computed the torsional and stretching stiffness of the P_2C_3NTs which is defined as:

$$k = \left.\frac{\partial^2 U_{\text{deformed}}(x)}{\partial x^2}\right|_{x=0}, \tag{5.1}$$

where, U_{deformed} is the energy per unit length of the deformed system calculated as the difference between the ground state free energy of the relaxed deformed and pristine nanotubes:

$$U_{\text{deformed}} = \frac{\mathfrak{N}}{\tau_0}\left(\mathcal{F}_{\substack{\text{Ground}\\\text{State}}}(\mathcal{P}^{**},\mathcal{D},\mathcal{G}|_{\text{deformed}}) - \mathcal{F}_{\substack{\text{Ground}\\\text{State}}}(\mathcal{P}^{*},\mathcal{D},\mathcal{G}|_{\text{pristine}})\right). \tag{5.2}$$

Here, $\mathcal{G}|_{\text{deformed}}$ and $\mathcal{G}|_{\text{pristine}}$ represent the symmetry groups pertinent to the configurations under strain and without strain , correspondingly. Concurrently, $\mathfrak{N}$ signifies the order of the cyclic group, as stated previously and τ_0 represents the equilibrium undistorted pitch of helical group. $\mathcal{P}^{**}$ and $\mathcal{P}^{*}$ are utilized to denote the sets of equilibrium atomic positions within the fundamental domain in each scenarios, respectively. For torsional simulations, we systematically vary the parameter α in regular intervals, enforcing twists of up to about $\beta = 4.5°$ per nanometer—the acknowledged limit of linear response for conventional Carbon Nanotubes (CNTs). Our investigation shows that within the defined domain of torsional deformations, the $U_{\text{twist}}(\beta)$ shows quadratic behavior with respect to β, aligning with the expectations of linear elastic theory as depicted in Fig. 5.2. The torsional stiffness constant, k_{twist}, was estimated to attain values of 956.10 eV/nm for armchair configurations and 207.53 eV/nm for zigzag structures. This observation is in concordance with the predictions of continuum mechanics, which suggests cubic relationship between k_{twist} and the nanotube radius within the linear elastic regime. (5; 45) By use of this cubic relationship, we estimate that conventional CNTs with radii comparable to the P_2C_3NTs considered above are expected to be significantly more rigid with respect to twisting (with k_{twist} values equal to 15809 eV/nm and 3021.2 eV/nm for 1.39 nm and 0.82 nm radius conventional armchair and zigzag CNTs, respectively). Subsequently, our approach to simulate axial stretching and compression closely mirrors that employed in torsion simulations. Specifically, for a specified value of axial strain ε, we adjust the pitch of the helical symmetry group according to $\tau = \tau_0\,(1+\varepsilon)$. We constrained ε to a range spanning from +3.3% to -3.3% within our simulations. Within this specified interval, the dependence of $U_{\text{stretched}}(\varepsilon)$ exhibits a quadratic trend with ε, consistent with the anticipated linear elastic response, as depicted in Fig. **??**. Notably, for armchair (12,12) and zigzag (12,0) P_2C_3NTs, the estimated values of k_{stretch} are determined

to be 2711.3 eV/nm and 1257.4 eV/nm respectively. Utilizing scaling laws derived from continuum theory (165), we also estimated that conventional armchair and zigzag CNTs with the same radii as the P_2C_3NTs considered above would be noticeably stiffer to axial deformations (k_{stretch} values equal to 13318 eV/nm and 7678.1 eV/nm for 1.85 nm and 1.07 nm radius CNTs, respectively). In summary, our findings indicate a notable increase in the flexibility of P_2C_3NTs concerning both torsional and axial deformations when compared with conventional Carbon Nanotubes (CNTs). This heightened pliability aligns with the observed lower bending stiffness of P_2C_3 sheet relative to conventional graphene. Collectively, these observations imply a reduced value of the in-plane (thickness-normalized) Young's modulus and shear modulus for P_2C_3 sheet.

The electronic structure calculations reveals that all the P_2C_3NTs are metallic. The electronic band diagram of pristine armchair nanotube has a dispersion-less flat bands right below the Fermi level (denoted by λ_F) which touches a lower Dirac point near the $\eta = 0$ point and it is separated from the upper Dirac point with a small gap. Additionally, the other two sets of Dirac points at $\eta = \pm\frac{1}{3}$ close to λ_F along with the bunch of quasi-flatbands resembles Kagome energy bands produced by next-nearest neighbor tight binding model (Fig. 5.3a). Similarly, the zigzag P_2C_3NT also exhibits flat bands with Dirac points crossing near λ_F. Notably, the kagome-like Dirac points which appears in the armchair nanotube are folded to $\eta = 0$ point while rolling the sheet to form zigzag nanotube as shown in Fig. 5.4a. These arrangement of additional Dirac points has similarities in appearance with band structure of armchair and zigzag carbon nanotubes (CNTs), respectively. Remarkably, as noted in our previous study on carbon kagome nanotubes (CKNTs)(63), we also observe that the P_2C_3NT characterized by cyclic group order $\mathfrak{N}$ is discovered to possess $2\mathfrak{N}$ nearly degenerate flat bands with an associated peak in the electronic density of states (eDOS) plots as illustrated in Figs. 5.3b & 5.4b. These characteristics of P_2C_3NTs renders a noteworthy instance of another realistic quasi-one-dimensional materials that are inclined to display strongly correlated electronic states such as superconductivity, flat band ferromagnetism, and Wigner

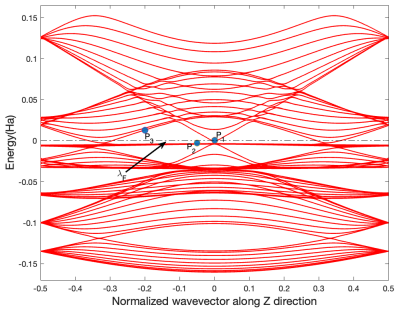

(a) Conventional band diagram for an pristine $(9, 9)$ armchair P_2C_3NT .

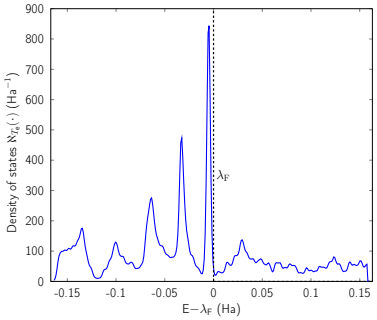

(b) Electronic density of states for untwisted armchair P_2C_3NT.

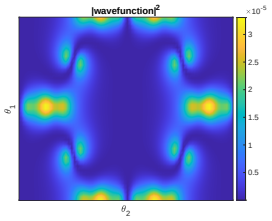

(c) Wavefunction distribution at point P_1

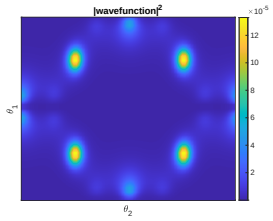

(d) Wavefunction distribution at point P_2

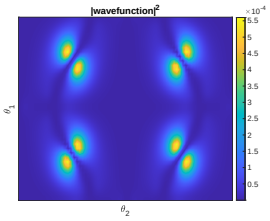

(e) Wavefunction distribution at point P_3

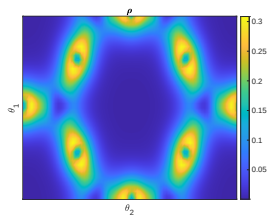

(f) Electron density

Figure 5.3: (a) Band diagram of $(9, 9)$ undeformed armchair P_2C_3NT. (b) Electronic density of states (eDOS) plot showing sharp peak near λ_F. From (c) to (e) shows the wavefunction square distribution of at P_1, P_2 and P_3 points shown in (a). (f) Electronic density. A slice of electronic fields at an average radial distance of atoms in computational domain is shown in terms of helical coordinates

crystallization.

In order to elucidate the orbital source of the electronic band structure of the two principle nanotubes studied, we illustrate the pDOS depicting different orbitals of P and C atoms (Fig. 5.5). It is evident that the intriguing electronic characteristics of the P_2C_3NTs predominantly originate from the participation of π electrons derived from radially oriented p_z $(l = 1, m_l = 0)$ orbitals of both C and P atoms. Specifically, the flat bands arise from

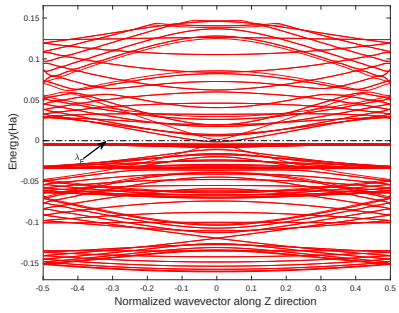

(a) Conventional band diagram for an pristine $(12, 0)$ zigzag P_2C_3NT .

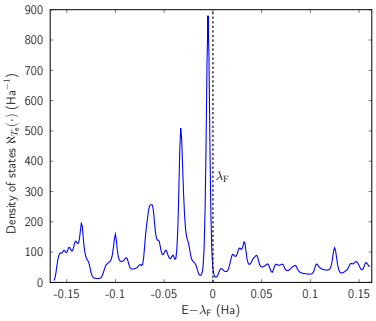

(b) Electronic density of states for untwisted zigzag P_2C_3NT.

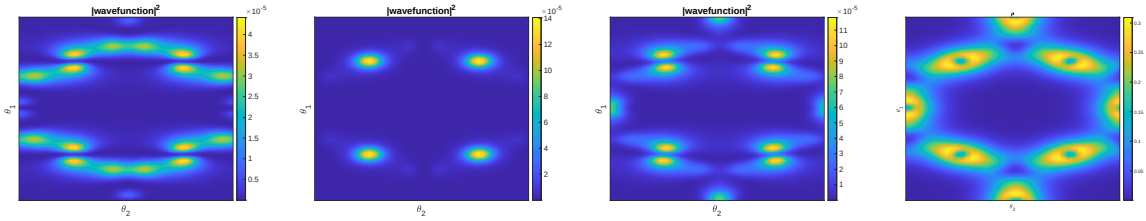

(c) Wavefunction distribution at point P_1

(d) Wavefunction distribution at point P_2

(e) Wavefunction distribution at point P_3

(f) Electron density

Figure 5.4: (a) Band diagram of $(12, 0)$ undeformed zigzag P_2C_3NT. (b) Electronic density of states (eDOS) plot showing sharp peak near λ_F. From (c) to (e) shows the wavefunction square distribution of at P_1, P_2 and P_3 points shown in (a). (f) Electronic density ρ. A slice of electronic fields at an average radial distance of atoms in computational domain is shown in terms of helical coordinates

the individual π-electrons of C atoms and the Dirac points situated at $\eta = 0$ in armchair and zigzag nanotubes are derived from the mixture of p_z orbitals of both P and C atoms (see Fig. 5.5). This can also be visualized in the wavefunction distribution represented in Fig. 5.3c, 5.3d, 5.4c & 5.4d at the points P_1 and P_2 in the band diagrams (Fig. 5.3a & 5.4a) showing electrons localized at p_z atomic orbitals. Hence, the p_z orbitals in this arrangement create a bipartite lattice, also recognized as a honeycomb split graph [2](338). On the other

[2]The split graph operation applied to the bipartite honeycomb lattice (graphene) introduces additional sites at the center of each edge, resulting in the lattice depicted in Fig. 5.1.

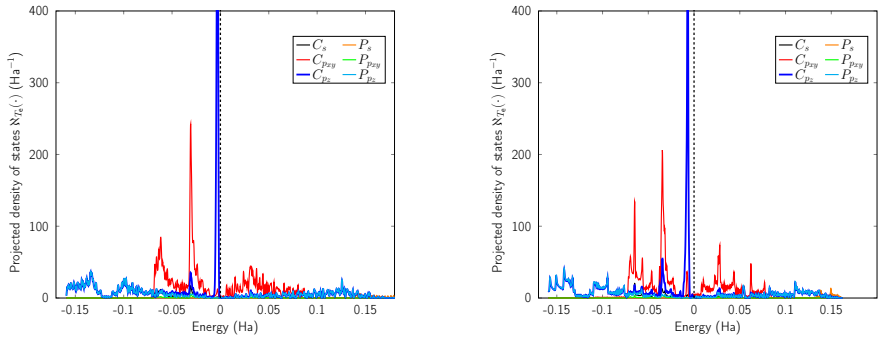

(a) Projected density of states for an $(9,9)$ armchair P_2C_3NTs of group order

(b) Projected density of states for a $(9,0)$ zigzag P_2C_3NTs

Figure 5.5: Projected density of states for undistorted armchair and zigzag P_2C_3NTs.

hand, in-plane p_{xy} orbitals of C atoms play a role in forming set of three kagome-like bands shown in Fig. 5.3e & 5.4e. These group of bands include distorted flat bands and Dirac bands positioned near the Fermi level at $\eta = \pm 1/3$ in armchair nanotube and at $\eta = 0$ in zigzag nanotubes.

On investigating the impact of external strain on the electronic structure, we observd that both torsion and axial deformation applied to the nanotubes disrupts the $2\mathfrak{N}$ degeneracy of the flat band below the Fermi level. Further increasing the applied strain leads to an increase in the energy width of the flat bands, accompanied by a decrease in the flatness, as demonstrated by the electronic density of states plots of twisted and uniaxially compressed nanotubes shown in Fig. 5.6c and Fig. 5.7b, respectively. The height of the sharp peak decreases and its width broadens near λ_F. Specifically, when torsional deformation applied to the armchair nanotube with group order $\mathfrak{N} = 9$, the flat bands become slightly dispersive close to the $\eta = 0$ point, exhibiting partial flatness (Fig. 5.6b). While the gap diminishes between the top Dirac point and the flat bands, a small gap emerges between the flat bands and the lower Dirac points situated at $\eta = 0$ and $\eta = \pm 1/3$. Interestingly, the wavefunction distribution at point $D1$ in Fig. 5.6d is now concentrated only at the p_z atomic orbital

of carbon atoms, at state D_2 in the flat band it is shifted to other set of carbon atoms (Fig. 5.6e). The uniaxial strain also induces some degree of dispersion in the flat bands. As illustrated in the band structure of $(12, 0)$ zigzag nanotube under longitudinal compression of 3.28%, the flat bands shows no drastic deformation near $\eta = 0$ point, comparatively, but a tiny gap opens (Fig. 5.7a). There is no significant effect of compression is observed on the electron cloud distribution in zigzag case (see Fig 5.7c to 5.7d) Overall, this suggests that the flat bands in both the principle nanotubes, although show some dispersion but they are more or less robust against the torsional and uniaxial strain, thus the P_2C_3 helical structure preserves the strongly correlated electronic states. This behavior is in contrast with CKNTs (63) where the quadratic band touching the flat band states protected by the local C_6 rotation symmetry of the unit cell evolves into tilted Dirac cones upon perturbing the system by external deformation. This makes P_2C_3NTs a realistic quasi-one dimensional material platform where stable strongly correlated physics can be studied.

Drawing insights from the pDOS calculations (Fig. 5.5), we constructed a next-nearest neighbor symmetry-adapted tight bindging (TB) model [3] to capture the salient feature of the electronic structure properties of P_2C_3NTs (see Fig. 5.8). The TB model considered here has contributions from the two sets of orthogonal orbitals, that are, three in-plane orbital p_{xy} of C atoms and three radially oriented orbitals p_z of C and two of that of P atoms. Since the interactions between the p_{xy} and p_z orbitals is negligible, the 8 bands TB Hamiltonian is written as direct product of p_{xy} kagome bands and p_z honeycomb split graph bands:

$$\mathbf{H} = \sum_{i,\gamma} \varepsilon_{i\gamma} \mathsf{a}^{\dagger}_{i\gamma} \mathsf{a}_{i\gamma} + \sum_{\gamma} \sum_{\langle i,j \rangle} t_{(i\gamma,j\gamma)} \mathsf{a}^{\dagger}_{i\gamma} \mathsf{a}_{j\gamma} + \sum_{\gamma} \sum_{\langle\langle i,j \rangle\rangle} \tilde{t}_{(i\gamma,j\gamma)} \mathsf{a}^{\dagger}_{i\gamma} \mathsf{a}_{j\gamma} + \text{h.c.}\,.$$

Here, the annhilation and creation operators are denoted by $\mathsf{a}_{i\gamma}$, $\mathsf{a}^{\dagger}_{i\gamma}$, respectively. The onsite energy of site i and orbital γ is $\varepsilon_{i\gamma}$, $t_{(i\gamma,j\gamma)}$ and $\tilde{t}_{(i\gamma,j\gamma)}$ are the hopping amplitudes between orbitals γ of the nearest-neighbors (NNs) $\langle i, j \rangle$ and the next-nearest-neighbors (NNNs) $\langle\langle i, j \rangle\rangle$,

[3] We utilize the Dresselhaus approach, which entails developing a TB formulation for the flat sheet of P_2C_3, followed by mapping the atoms of the two-dimensional lattice onto a cylinder to apply boundary conditions suitable for the nanotube.

respectively, and h.c. is the hermitian conjugate. The on-site energy of p_z orbitals of carbon and phosphorous atoms is $\varepsilon_{\mathrm{C}_{p_z}} = 0$ and $\varepsilon_{\mathrm{P}_{p_z}} = 0.05$eV, respectively. While, the NN hopping amplitude between p_z orbitals both the types of atoms is $t_{\mathrm{CP}_{p_z}} = -2.6$eV. The interactions between three p_{xy} orbitals for carbon is given by $t_{\mathrm{C}_{p_{xy}}} = 0.6$eV with the on-site energy $\varepsilon_{\mathrm{C}_{p_{xy}}} = -0.6$eV. The partially flat band of p_{xy} character is due to the consideration of NNN interaction of magnitude $\tilde{t}_{C_{p_{xy}}} = 0.1$eV between the p_{xy} electrons. To incorporate the influence of deformation on the nanotubes,we also considered the NNN hopping amplitudes for p_z honeycomb split graph bands, denoted as $\tilde{t}_{C_{p_z}} = 0.01$eV and $\tilde{t}_{P_{p_z}} = 0.001$eV, respectively. The outcomes of our TB calculations for pristine P_2C_3NTs are illustrated in Fig. 5.8a & 5.8b, and for twisted armchair nanotube and uniaxially compressed zigzag nanotube are showcased in Fig. 5.8c & 5.8d. It is evident from these figures that there is a remarkable qualitative agreement between these results and the first principles data presented.

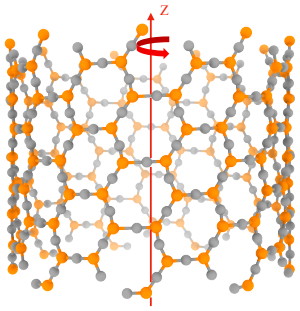

(a) Twisted armchair P_2C_3NT

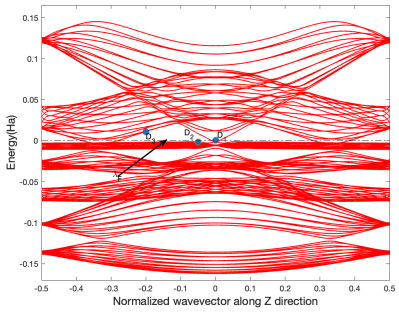

(b) Band diagram for twisted (9,0) armchair P_2C_3NT .

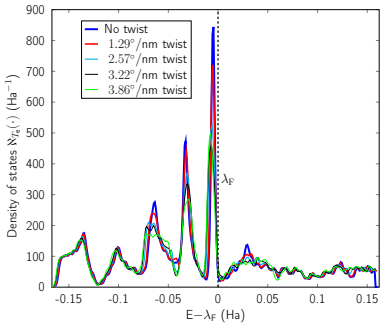

(c) Electronic density of states for twisted armchair P_2C_3NT.

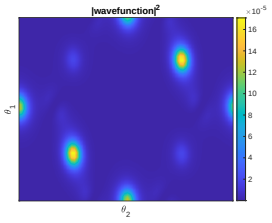

(d) wave function distribution at point D_1

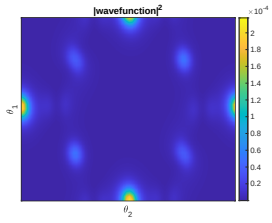

(e) wave function distribution at point D_2

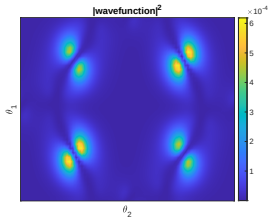

(f) wave function distribution at point D_3

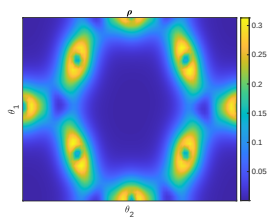

(g) Electron density

Figure 5.6: (a) Twisted armchair P_2C_3NT. (b) Band diagram of $(9, 9)$ twisted armchair P_2C_3NT at $3.86°/nm$. (c) Electronic density of states (eDOS) plot for different rate of twists. From (d) to (f) shows the wavefunction square distribution of at D_1, D_2 and D_3 points shown in (b). (g) Electronic density ρ. A slice of electronic fields at an average radial distance of atoms in computational domain is shown in terms of helical coordinates

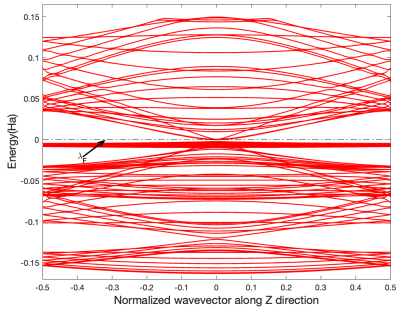

(a) Band diagram for an uniaxially compressed (12,0) zigzag P_2C_3NT .

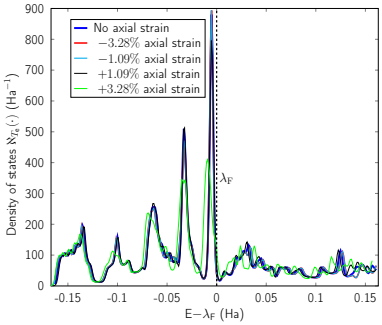

(b) Electronic density of states for uniaxially strained zigzagP_2C_3NT.

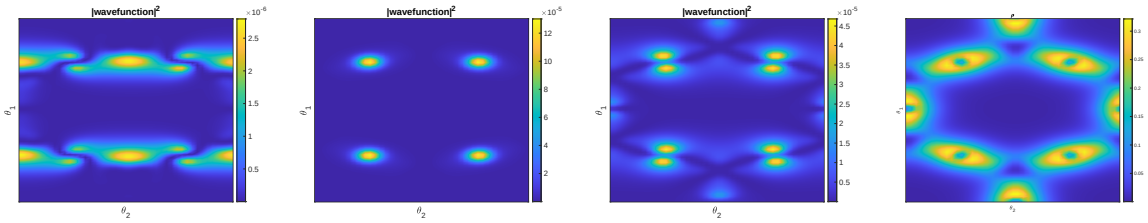

(c) (d) (e) (f) Electron density

Figure 5.7: (a) Band diagram of $(12, 0)$ compressed zigzag P_2C_3NT by 3.28%. (c) Electronic density of states (eDOS) plot for different rate of twists. From (d) to (f) shows the wavefunction square distribution of at D_1, D_2 and D_3 points shown in (b). (g) Electronic density ρ. A slice of electronic fields at an average radial distance of atoms in computational domain is shown in terms of helical coordinates

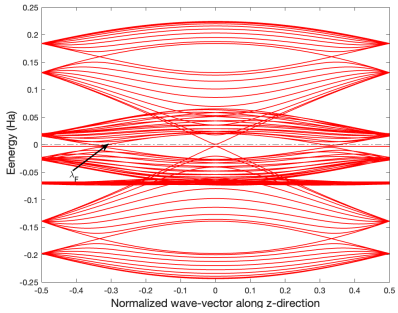

(a) Tight binding band diagram of (9,9) armchair P_2C_3NT .

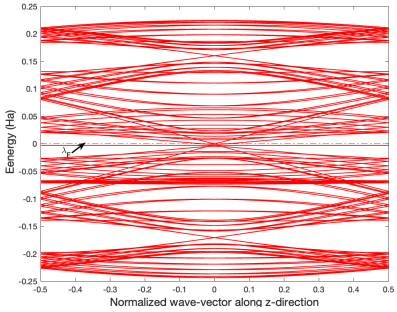

(b) Tight binding band diagram for (12,0) zigzag P_2C_3NT .

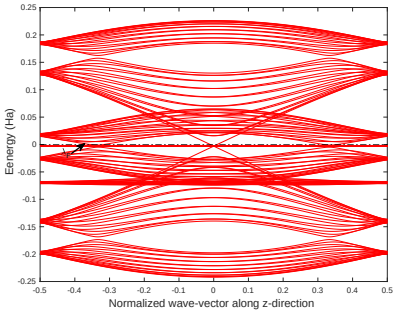

(c) Tight binding band diagram of twisted (9,9) armchair P_2C_3NT .

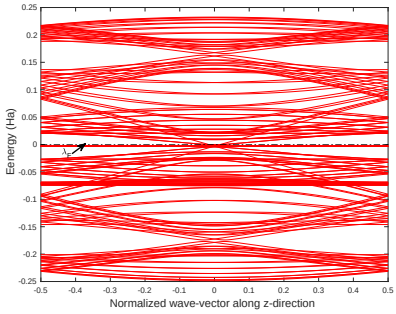

(d) Tight binding band diagram of uniaxially compressed (12,0) zigzag P_2C_3NT .

Figure 5.8: Tight binding band diagram of pristine and deformed armchair (a) and (c), and zigzag (b) and (d) P_2C_3NTs, respectively.

CHAPTER 6

Machine learning based prediction of the electronic structure of nanotubes under strain

6.1 Introduction

Over the last decade, machine learning (ML) models have percolated into all areas of science and engineering. Indeed, data-driven research is already an important part of the medical sciences (340; 341; 342), chemistry (343; 344), and engineering fields like manufacturing (345; 346), applied thermodynamics (347; 348), and miscellaneous others (see e.g. (349; 350; 351; 352)). The recent interest in these techniques has been driven by the improvement in the machine learning algorithms themselves, as well as an exponential growth in computation power, and the abundance of data. Additionally, data analysis tasks such as regression, classification and dimensionality reduction, which are commonly used across all areas of science, are easily handled by machine learning algorithms by their innate design (353; 354), and this has contributed to the wide applicability of machine learning techniques.

Machine learning methods have also shown great promise for various materials physics problems (355; 356; 357; 358; 359; 360; 361; 362). In particular, the use of high-throughput Density Functional Theory (DFT) (72; 363) calculations in conjunction with machine learning techniques, has attracted much attention as a powerful tool for materials discovery (364; 365; 366; 367; 368). A large section of the research in this direction so far, has been aimed at predicting specific material properties and screening novel materials for targeted applications such as energy storage. This includes electronic properties like the band gap,

chemical properties like adsorption and formation energies, and mechanical properties like Young's modulus and fracture toughness (369; 370; 371; 372; 373; 374; 375; 376; 350). A common feature of most of these predicted material properties is that they are *low–dimensional* — usually, simple scalars. An alternative to these approaches is to use machine learning to directly predict electronic fields such as the ground state electron density for atomic configurations of interest. This is appealing since such fields contain all the information for predicting various material properties — at least in principle, and the machine learning model provides a way to bypass expensive DFT calculations which can compute these fields. Recent work in this direction includes (377; 378; 379; 380; 381; 382; 383; 384; 385; 386; 387; 388; 389). The large majority of these contributions have focused on molecular systems (e.g. hydrocarbon chains and clusters), while a few have considered bulk materials. The current contribution can be viewed as an extension of the aforementioned efforts of machine learning based prediction of electronic fields to broader classes of nanomaterials — specifically, quasi-1D nanostructures. Notably, a separate strand of work has also explored improving Density Functional Theory predictions themselves, by trying to learn the elusive Hohenberg-Kohn functional (363) or by improving exchange correlation functionals used in Kohn-Sham theory (378; 390; 391; 392; 393). This latter class of developments will not have much bearing on the discussion that follows below.

Although machine learning based prediction of the electronic fields appears to be an attractive option for the aforementioned reasons, the high–dimensional nature of the fields usually makes it necessary to generate large amounts of data for model training and validation purposes. Additionally, since the models require a description of the atomic environments as input, it becomes necessary to choose a cutoff radius for limiting the size of the environments, or to focus on small sized systems, in order to make the models tractable. Furthermore, a careful choice of the atomic environment descriptors needs to be made to enforce symmetry and locality properties (384). From this perspective, the current contribution is quite distinct in that global structural symmetries in lieu of environmental descriptors are utilized here,

and strains are employed as model inputs. Our approach is related in spirit to (388) where the authors investigated machine learning models for the electronic fields in a hexagonal close packed crystalline material.

We present here a machine learning model that can predict the electronic structure of quasi-one-dimensional materials as they are subjected to strains commensurate with their geometries. One of the key motivations of our work is that the complex interplay of electronic fields and mechanical deformations in low–dimensional materials is an active area of investigation in the literature (394; 395; 23; 19; 24; 396; 20; 396), and therefore, it is desirable to have machine learning models where strain parameters can be mapped to electronic fields for such systems. Additionally, the techniques described here are likely to find use in the discovery of novel phases of low–dimensional chiral matter (33) and multiscale modeling (397). The data generation process for the ML model here is based on a recently formulated electronic structure calculation technique, that exploits the global symmetries of quasi-one-dimensional structures, and enables Kohn-Sham DFT calculations for such systems using a few representative atoms in a symmetry adapted unit cell (54; 4; 55; 398; 5; 171; 399). This computational method, called Helical Density Functional Theory (Helical DFT), solves the symmetry adapted Kohn-Sham equations in so-called helical coordinates to yield electronic fields of interest, and is able to accommodate deformation modes such as extension, compression and torsion, commonly associated with tubular or wire-like nanostructures. Atomic relaxation effects as a response to the applied strains are automatically included, by driving the Hellman-Feynman forces (273) to zero. In order to map strain parameters to resultant electronic fields, we utilize a two-step machine learning model, motivated by recently developed techniques used to predict the high–dimensional deformation fields of multi walled carbon nanotubes (400). Specifically, we use Principal Component Analysis (PCA) to perform dimensionality reduction of the electronic fields, and a neural network to learn in the reduced space. Using armchair single-wall carbon nanotubes as an example, we demonstrate that the ML model accurately predicts the ground-state electron density and the nuclear

pseudocharge fields when the radius of the nanotube, its axial stretch, and the twist per unit length are provided as inputs. We have also developed a novel technique based on clustering that allows us to determine the nuclear coordinates from the ML model predicted nuclear pseudocharge field, and we demonstrate the superior performance of this method when compared to alternatives. Other quantities of interest, including ground state energies and symmetry-adapted band diagrams can be readily computed from the ML model predicted fields through low-overhead postprocessing steps. The strategy of predicting smoothly varying ground state fields such as the electron density, and obtaining energies from this field, instead of predicting the latter directly, appears to work better in practice (378; 388). In a similar manner, computation of the electronic bands using a non-self-consistent calculation involving the machine-learning based Hamiltonian (i.e., diagonalization of a symmetry adapted Kohn-Sham Hamiltonian, with the effective potential arising from machine learning predicted fields) is more straightforward when compared to prediction of the band diagram directly, as a function of the inputs. This is due to the complexities in the structure of the latter (401; 402), including e.g., the appearance of band crossings associated with insulator-metal transitions.

In our example, only about 160 simulations were performed, out of which around 120 are used for training purposes. Yet, ground state energies could be typically predicted to chemical accuracy (i.e., to better than 1.6 milli-Hartree per atom, or 1-kcal/mol), band gap predictions were generally accurate to 0.02 eV, while the band gap location was predicted accurately every time. This suggests that the predictions of three-dimensional electronic fields themselves are rather accurate even with this limited training data, a fact also directly borne out by the low normalized root mean square errors in these quantities. The high accuracy of the present ML model is likely related to (i) the constraints imposed by symmetry in the problem setup, (ii) efficient exploration of the input space through quasi-random low-discrepancy sequences, and (iii) significant reduction in the dimensionality of the electronic fields. Indeed, only 7 and 15 principal component modes were found to be sufficient

to capture most of the variations in the ground state electron density and the nuclear pseudocharge fields, respectively, which reinforces points (i) and (iii) above. We also observed that the electronic fields and post-processed quantities are accurately predicted for inputs whose values were not used during training, thus suggesting that our model can predict anywhere in the input space, even beyond the training data. Notably, the machine learning surrogate model is much cheaper computationally — while the DFT calculation can take up to hundreds of CPU hours (in order to include atomic relaxation effects through ab initio geometry optimization), the machine learning model prediction can be done in a fraction of a second, and the subsequent post-processing steps (including prediction of band diagrams) can be typically performed in about 30 to 40 minutes of wall time.

6.2 Machine learning model methodology

This section describes the proposed Machine Learning (ML) model that aims to predict the electronic structure (high–dimensional) of quasi–one–dimensional materials under torsional and axial loads. The tubular structures considered in this work can be characterized by their radius — which is related to the degree of cyclic symmetry present in the structure, and the position of the atoms within the fundamental domain. Given strain parameters related to axial and torsional loads that the structure might be subject to, these atomic positions can be determined by minimizing the system's energy with respect to them. Thus, the trio of parameters R_{avg} — the nanotube radius (or equivalently, the average radial coordinate of the atoms in the fundamental domain), α — the twist parameter, and τ — the axial pitch parameter, serve to specify a particular nanotube, along with the imposed torsional and axial strains. Accordingly, we let $\mathcal{H}$ denote the map from the space consisting of system and loading parameters $(R_{\text{avg}}, \alpha, \tau)$ to the electronic fields ρ, b of the deformed nanotubes:

$$\mathcal{H} : \{R_{\text{avg}}, \alpha, \tau\} \to \{\rho, b\} \tag{6.1}$$

The objective of this work is to approximate this map $\mathcal{H}$ using a machine learning model. Inputs of this map R_{avg}, α and τ are scalars, while the outputs $\rho\left(r,\, \theta_1,\, \theta_2\right)$ and $b\left(r,\, \theta_1,\, \theta_2\right)$ are high–dimensional discretized scalar fields (expressed in helical coordinates).

Approximating the map $\mathcal{H}$ directly through a supervised machine learning algorithm (such as a Neural Network (NN)) is infeasible since the output quantities $\rho\left(r,\, \theta_1,\, \theta_2\right)$ and $b\left(r,\, \theta_1,\, \theta_2\right)$ are very high–dimensional. For instance, with the discretization choices adopted in this work, the field $\rho\left(r,\, \theta_1,\, \theta_2\right)$ is represented by a vector of dimension close to 60,000 (see Section **??**). The difficulty in predicting such high-dimensional outputs using machine learning models is referred to as curse of dimensionality. Specifically, the number of discrete cells required to discretize the output space grows exponentially with its dimensionality, and an exponentially large quantity of training data is then needed to ensure that the cells in the output space are accurately mapped from the input space (353).

In the present work, we circumvent this problem by using Principal Component Analysis (PCA) to reduce the dimensions of the electronic fields. Subsequently, the low–dimensional representation of the electronic fields is learned via neural networks in a supervised manner. This two-step approach, i.e., dimensionality reduction followed by learning in the reduced space, allows the prediction of the high-dimensional quantities such as electronic fields while reducing the data required for training. Schematic of the two-step ML model introduced above is given in Fig. 6.1. Recently, a similar approach has been found to have excellent accuracy in high-dimensional predictions related to purely mechanical problems (400; 403).

In the following sections, we detail various important aspects of the above ML model and also describe an auxiliary clustering based technique that allows us to determine the nuclear coordinates from the ML model predicted nuclear pseudocharge field.

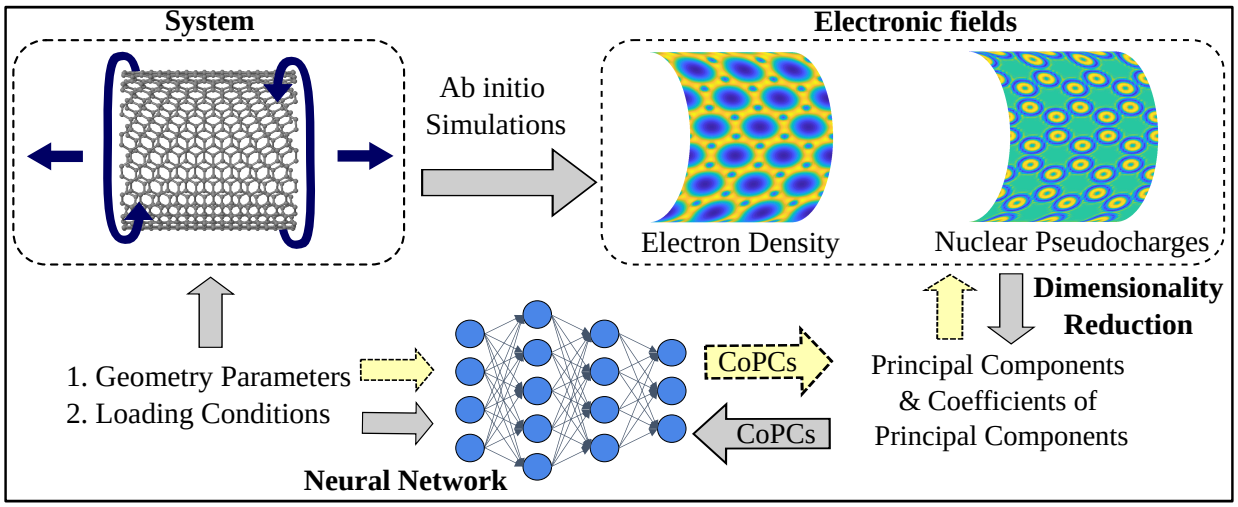

Figure 6.1: Schematic of the present Machine Learning (ML) model and the data generation process via DFT simulations. The firm arrows show the steps for data generation and training, and the dashed arrows show the steps for prediction via the ML model.

6.2.1 Design of experiments to explore the input space

We now describe the use of Design of Experiments (DoE) (404; 405) techniques for efficient sampling in the input space. As described above, the triplet of input parameters $\{R_{\text{avg}}, \alpha, \tau\}$ specify a particular nanotube and the applied strains. The number of possible combinations with these three input variables can be quite large even if finite bounds are emplaced for these variables. Given the relatively high cost of DFT simulations for the deformed nanotubes, it is infeasible to simulate nearly all possible combinations in the input space. Purely random sampling of the input space is not desirable either, since it may require a large number of sampling points to learn the pattern in the data accurately (406; 407; 408). To address this challenge, we generate sequences of quasi-random sampling points in the input space to reduce the number of simulations required for training an accurate ML model. Quasi-random sampling: Space-filling designs can be used to explore the input domain effectively since they sample the space uniformly without assuming any prior knowledge of the problem (409; 406). Commonly used space-filling designs include low dis-

crepancy sequences (410; 411), good lattice points (412), Latin Hypercube Sampling (413) and Orthogonal Latin Hypercube sampling (414). These methods are often evaluated based on their measure of uniformity (407; 415; 416), and such criteria suggest that Optimal Latin hypercube sampling (417) and Sobol sequences (418; 411) offer a great balance between uniform and random sampling. In this work, we have chosen Sobol sequences (low discrepancy quasirandom sequences), to sample the input space. The main advantage of this technique is that the samples generated via this procedure are spread out over the input variables space non-uniformly, but cover the space evenly (419), thus allowing efficient exploration of the input space. An additional benefit is that as the Sobol sequence progresses, the input variables space is refined successively. This latter feature allows us to add simulations to the training in a systematic manner, till the desired accuracy is achieved in the ML model.

6.2.2 Dimensionality reduction of the electronic fields and regression in the reduced dimension

Dimensionality Reduction of the Electronic Fields: We reduce the high dimensionality of the electronic fields using Principal Component Analysis (PCA) (420; 421; 422; 423). PCA reduces the dimensionality of the data in an unsupervised manner. PCA reduces the dimensionality of the data by projecting it onto a lower–dimensional space such that the maximum statistical information within the data is retained. From a geometric perspective, PCA can be viewed as finding a new coordinte system where the data is aligned along the directions of maximum variance. By projecting the original data onto these principal components, we effectively reduce the dimensionality of the data while preserving most of its variability. In other words, the principal components are ordered in such a way that the first few components capture the majority of the variability in the data, and dimensionality reduction can be done by neglecting the components that capture the least variability. The basis vectors for this low-dimensional space are uncorrelated with each other and are called the principal components. Thus, PCA enables dimensionality reduction while minimizing the informa-

tion loss. To elaborate further, given the data points, PCA allows one to obtain a lower dimensional approximation $\tilde{\mathbf{x}}_i \in \mathbb{R}^K$, such that, $K < d$, and:

$$\tilde{\mathbf{x}}_i = \sum_{j=1}^{K} c_{ij}\mathbf{v}_j + \boldsymbol{\mu}\,. \tag{6.2}$$

Here, $\boldsymbol{\mu} = \frac{1}{n}\sum_{i=1}^{n}\mathbf{x}_i$ is the sample mean, the orthonormal vectors $\mathbf{v}_j$ are the principal components (PCs) and the scalars c_{ij} are the coefficients of the principal components (CoPCs). Importantly, the PCs ($\mathbf{v}_j$) depend on the entire dataset rather than being associated with a particular data point; therefore, all the points in the original dataset can be defined in terms of distinct c_{ij} values, but the same $\mathbf{v}_j$. The value of K depends on the degree of variance of the data that needs to be captured. We perform PCA on the electronic field (ρ and b) – data generated by the DFT simulations. Specifically, in Helical DFT, the discretized grid of the fundamental domain of electronic fields has 89 points along the radial direction, 19 points along the θ_1 direction and 35 points along the θ_2 direction. Given this discretization, the total number of grid points in the fundamental domain is 59,185. The electronic fields are therefore represented as a nearly 60,000 dimensional vector by the DFT simulations. PCA enables us to represent these high-dimensional electronic fields in terms of a few CoPCS only (7 and 15 for ρ and b, respectively, as described in Section 6.4.1).

Regression for the Electronic Fields in the Reduced Dimension: We employ Neural Networks (NN) (353; 424) to perform regression for the electronic fields in the reduced dimension. The choice of NN is motivated by our previous work on the ML based modeling of complex rippling deformation fields of low-dimensional nanostructures (400). The NN architecture consists of the input layer, multiple hidden layers, and the output layer. The neurons of the hidden layers contain a weighted linear transform of neurons in the previous layer acted upon by a nonlinear activation function. During the training phase of the model, the neural network learns (in a supervised manner) the map between input and output spaces by finding the weights of these linear transforms such that it can accurately predict output for a given input. We use NNs to predict the coefficients of the principal components (CoPCs) of the

electronic fields for a given system and loading parameters. We deploy two different neural networks $\mathcal{N}_1$ and $\mathcal{N}_2$ to predict CoPCs for ρ and b respectively, which use the same input parameters. In the input layer, we have three neurons, for the input parameters (i) R_{avg}, (ii) α and (iii) τ. The neurons of the output layer correspond to the CoPCs (c_{ij}). Note that the number of CoPCs depends on the desired variance to be captured in the data. Inference via the trained ML model involves the following two steps. First, the CoPCs are predicted for a given input using the neural network. Second, the predicted CoPCs are used to obtain the higher dimensional electronic fields using the principal components following Eq. 6.2. These two steps inference procedure via the ML model are shown in Fig. 6.1.

6.2.3 Prediction of nuclear coordinates from pseudocharge fields

As mentioned earlier, calculation of the Kohn-Sham Hamiltonian arising from ML predicted fields requires knowledge of the nuclear coordinates so that the non-local part of the pseudopotential operator may be constructed. In this section we deal with the problem of obtaining these coordinates as a function of the tube geometry and loading parameters, i.e., $\{R_{\text{avg}}, \alpha, \tau\}$.

One possible approach (388) is to directly train a neural network with these parameters as inputs and the desired nuclear coordinates as outputs. In our experience, however, this approach does not appear to work particularly well, and the amount of training data that was found to be adequate for predicting the electronic fields ρ and b accurately, was found to result in unacceptable levels of error while predicting the nuclear coordinates. This led us to devise a new strategy for determining the nuclear coordinates from the ML predicted nuclear pseudocharge field $b(\mathbf{x})$, since this field is readily predicted with relatively high accuracy (Section 6.4.2), and it already contains the nuclear coordinate information in principle. Our proposed strategy to find nuclear coordinates is based on a clustering approach and identifies the nuclear coordinates from the nuclear pseudocharge field in an unsupervised manner.

We make the observation that the nuclear pseudocharge field over the fundamental do-

main is a superposition of the individual atomic pseudocharges i.e., $b(\mathbf{x}) = \sum_{i=1}^{M} b_i(\mathbf{x})$. Furthermore, each atomic pseudocharge field is spherically symmetric and atom centered (i.e. $b_i(\mathbf{x}) \equiv b_i(|\mathbf{x}-\mathbf{r}_i|)$), and under usual circumstances, also non-overlapping. This suggests that a clustering based approach that can identify agglomerations of positive charges arising from individual atoms might be fruitful, and the desired nuclear coordinates can then be determined as cluster centers. Clustering algorithms are widely employed to divide datasets into smaller subgroups in an unsupervised manner, such that the data points in each subgroup share some common attributes (353).

One of the most widely used and successful clustering algorithms is DBSCAN (Density-Based Spatial Clustering of Applications with Noise) (425; 426). This technique creates clusters for volumes with a high density of points, and treats the points which lie in very low-density volumes as outliers. DBSCAN offers advantages over other clustering algorithms like $k-$nearest neighbors, since it does not require prior knowledge of the number of clusters present in the data, it can find out any arbitrarily shaped clusters and it is robust against errors induced by the outliers. In the present case, this means that when applied to the nuclear pseudocharge data, DBSCAN should be able to form clusters around every nucleus in the fundamental domain, without the total number of nuclei being specified apriori. However, we found that a direct application of DBSCAN to the pseudocharge field fails to determine the nuclear coordinates accurately. In the following, we identify two reasons for this failure and develop procedures to overcome them.

First, the fundamental domain is effectively periodic in the θ_1 and θ_2 directions. However, clustering algorithms are not typically aware of domain boundary conditions, as a result of which, pseudocharges associated with atoms close to the domain edges may result in the identification of clusters for which the cluster centers are not at the nuclear coordinates. This issue is readily addressed by expanding the fundamental domain into a supercell, applying the clustering procedure to the periodically replicated pseudocharge field in the supercell,

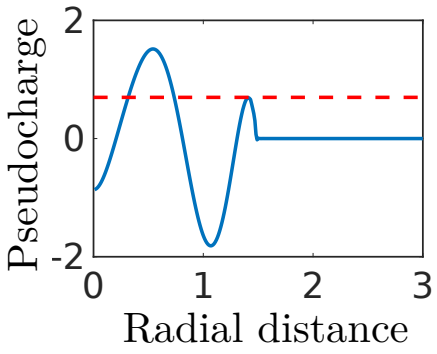

Figure 6.2: Atomic pseudocharge as a function of distance (in Bohr) from the atom for the Troullier-Martins pseudopotential for Carbon used in this chapter. The dashed red line indicates the truncation level employed before the DBSCAN procedure is used.

and finally, retaining the cluster centers found to lie within the fundamental domain. Second, some atomic pseudocharges (such as the one associated with the Troullier Martins pseudopotential for Carbon used in this chapter), while being radially symmetric, may exhibit multiple peaks, when plotted as a function of atom center distance (see Figure 6.2). This can cause the clustering algorithm to identify multiple clusters near a single nucleus and the centers of these clusters will not coincide with the nuclei. To overcome this challenge we propose a map ($\mathcal{T}$) that truncates the pseudocharge field b to retain only the data around the first peak (see Figure 6.2):

$$\mathcal{T} : b(r,\theta_1,\theta_2) \rightarrow \bar{b}(r,\theta_1,\theta_2), \quad \bar{b}(r,\theta_1,\theta_2) = \begin{cases} b(r,\theta_1,\theta_2), & \text{if } b(r,\theta_1,\theta_2) > c_t \\ 0, & \text{if } b(r,\theta_1,\theta_2) \leq c_t \end{cases} \tag{6.3}$$

The only quantitative information needed for implementing this map is the height of the second peak c_t, which is readily available for the pseudopotentials used to produce the training data. The DBSCAN procedure, when applied on the truncated field $\bar{b}$ can readily identify the nuclear pseudocharge density cluster around each nucleus. Nuclear coordinates are subsequently computed as centers of these clusters.

Together, the above set of strategies leads to a robust and efficient method for obtaining

the nuclear coordinates as a function of the ML model inputs. The entire procedure outlined above executes within a few seconds of wall time on a desktop and is able to determine the nuclear coordinates to acceptable levels of accuracy in every case (see Table 6.2).

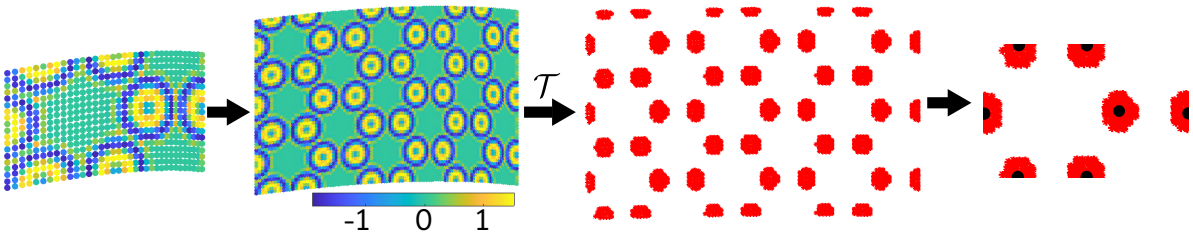

Figure 6.3: Cluster formation from nuclear pseudocharge field to determine nuclei position. A slice of the pseudocharge field at the average radial coordinate of the atoms in the fundamental domain is shown. Red clusters show the positive charge around the nucleus and the black dots are nuclei. The pseudocharge field on the fundamental domain is expanded to a supercell to avoid domain edge effects, a truncation is implemented to discard secondary peaks in the atomic pseudocharges, the DBSCAN procedure is then applied on the supercell and finally, the nuclear coordinates within the fundamental domain are identified.

6.3 Post-processing of ML predicted electronic fields

In this section, we describe the postprocessing steps used for computing quantities of interest from the machine learning model predicted fields and atomic coordinates. The machine learning model produces electronic fields $\rho^{\text{ML}}(\mathbf{x})$ and $b^{\text{ML}}(\mathbf{x})$ that includes self-consistency and atomic relaxation effects. Within the ML model, however, we do not explicitly enforce any constraints regarding the net charges associated with these fields. Although in practice these constraints seem to be automatically obeyed by the model — at least approximately (see Table 6.1 within the section on Results), we find it useful to scale the ML predicted

fields for postprocessing purposes (427), as shown below:

$$\rho^{\text{Scaled}}(\mathbf{x}) = \rho^{\text{ML}}(\mathbf{x}) \times \frac{N_{\text{e}}}{\int_{\mathcal{D}} \rho^{\text{ML}}(\mathbf{x})\, d\mathbf{x}}\,,$$
$$b^{\text{Scaled}}(\mathbf{x}) = b^{\text{ML}}(\mathbf{x}) \times \frac{-N_{\text{e}}}{\int_{\mathcal{D}} b^{\text{ML}}(\mathbf{x})\, d\mathbf{x}}\,. \tag{6.4}$$

Using these scaled fields, we compute the net electrostatic potential Φ via iterative solution of eq. **??** using preconditioned GMRES (95) iterations. The exchange correlation potential V_{xc} is directly computed from the electron density. Next, we use a clustering based unsupervised learning technique (see Section 6.2.3) to pick out the nuclear coordinates from the nuclear pseudocharge field and use it to set up the non-local pseudopotential operator $\mathcal{V}_{\text{nl}}$. Thereafter, we diagonalize the Kohn-Sham Hamiltonian (eq. **??**) resulting from these machine learning predicted quantities, to obtain the Kohn-Sham eigenstates. We use a combination of Generalized Preconditioned Locally Harmonic Residual (GPLHR) (102) and Arnoldi Iterations (428) to carry out the diagonalization, and initialize the calculations using random wavefunction vectors. The Fermi level of the system is subsequently determined from the Kohn-Sham eigenvalues by enforcing the constraint of having a fixed number of electrons within the fundamental domain. From all this information, band structure dependent quantities, such as the value of the band gap and its location in (η, ν) space, can be calculated.

Using the aforementioned post-processed quantities, the ground state free energy per unit fundamental domain may be calculated as (5):

$$\mathcal{F} = E_{\text{kin}} + E_{\text{xc}} + E_{\text{nl}} + E_{\text{el}} - T_{\text{e}} S\,, \tag{6.5}$$

with the terms on the right hand side denoting the electronic kinetic energy, the exchange correlation energy, the non-local pseudopotential energy, the electrostatic energy and the electronic entropy contribution at temperature T_{e}, respectively. Alternately, a more accurate estimate for the ground state free energy per unit fundamental domain may be obtained using

the Harris-Foulkes functional (79; 80):

$$\mathcal{F}^{\mathrm{HF}} = E_{\mathrm{band}} + E_{\mathrm{xc}} - \widetilde{E}_{\mathrm{xc}} + \widetilde{E}_{\mathrm{el}} + E_{\mathrm{sc}} - T_{\mathrm{e}}\, S\,. \tag{6.6}$$

In the above, the first term on the right hand side is the electronic band energy:

$$E_{\mathrm{band}} = 2\int_{-\frac{1}{2}}^{\frac{1}{2}} \frac{1}{\mathfrak{N}} \sum_{\nu=0}^{\mathfrak{N}-1} \sum_{j=1}^{\infty} \lambda_j(\eta,\nu)\, g_j(\eta,\nu)\, d\eta\,, \tag{6.7}$$

in which $g_j(\eta,\nu)$ denotes the electronic occupations. The term E_{xc} denotes the exchange correlation energy, while:

$$\widetilde{E}_{\mathrm{xc}} = \int_{\mathcal{D}} V_{\mathrm{xc}}(\rho(\mathbf{x}))\rho(\mathbf{x})\, d\mathbf{x}\,. \tag{6.8}$$

The term $\widetilde{E}_{\mathrm{el}}$ is related to electrostatic interactions and has the form:

$$\widetilde{E}_{\mathrm{el}} = \frac{1}{2}\int_{\mathcal{D}} \big(b(\mathbf{x}) - \rho(\mathbf{x})\big)\Phi(\mathbf{x})\, d\mathbf{x}\,. \tag{6.9}$$

Finally, E_{sc} accounts for nuclear pseudocharge self-interactions and overlap corrections (55), while the last term is related to the electronic entropy contribution. Notably, in the above breakdown for the Harris-Foulkes energy, E_{xc} and $\widetilde{E}_{\mathrm{xc}}$ depend solely on the electron density field, E_{sc} depends on the nuclear coordinates and the nuclear pseudocharge field, the electrostatic term $\widetilde{E}_{\mathrm{el}}$ depends on both the electron density and nuclear pseudocharge fields, while E_{band} depends on the Kohn-Sham operator eigenvalues (i.e., its dependence on ρ and b is implicit). Therefore, monitoring these terms in addition to $\mathcal{F}^{\mathrm{HF}}$ allows us to estimate the accuracy of the machine learning based predictions of ρ, b and other post-processed quantities (such as the eigenstates), in the energetic sense.

6.4 Machine learning predictions

We now present the predictions of the machine learning (ML) model for armchair carbon nanotubes under torsional and axial loading. These are compared against Helical DFT

simulations to quantify the ML model's accuracy and efficacy. Notably, the inference process from the trained ML model is orders of magnitude faster compared to the cost of the ab initio simulations using Helical DFT. While the ML model requires 0.003 seconds and 0.009 seconds to predict the ρ and b fields respectively (average times on a desktop with a 2.2 GHz Intel Xeon Gold processor), a typical ab initio structural relaxation calculation using Helical DFT can stretch into hundreds of CPU hours. Post-processing of the ML predicted electronic fields (to calculate band structures, energies, etc.) can be typically performed in about 30 to 40 minutes of wall time. Training of the neural networks for ρ and b requires about 12 and 15 minutes, respectively, measured using the same hardware setup.

6.4.1 Principal component analysis and neural networks

Principal Component Analysis Results: As the first step in our two-step ML model, we utilize PCA to obtain reduced dimensional representations for the outputs of the map $\mathcal{H}$. To reconstruct the original electronic fields with minimum reconstruction error, we capture 99.99% variance of the data. As shown later (Section 6.4.3), this is generally sufficient for obtaining electronic ground state energies to chemical accuracy and also adequate for reproducing band structures correctly. For capturing this level of variance in the data, we required only 7 PCs in case of ρ and 15 PCs in case of b (Figure 6.4).

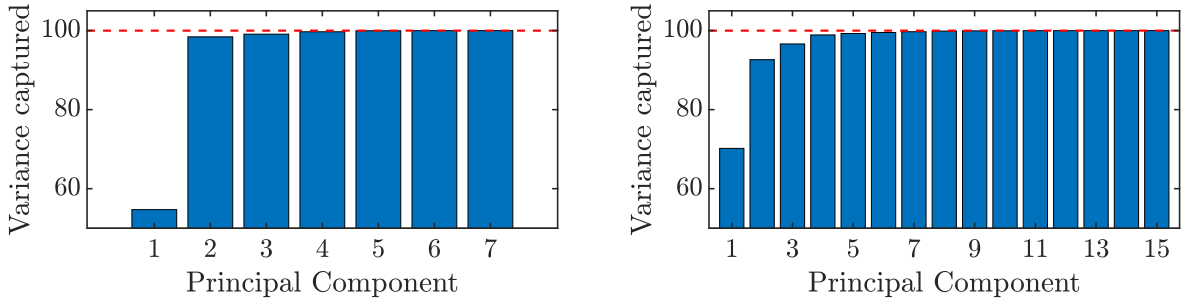

Figure 6.4: Cumulative percentage of variance vs Principal components for ρ (left) and b (right). The red dashed line shows 99.99% variance.

Neural Network: As the second step in our two-step ML model, two Neural Networks $\mathcal{N}_1$ and $\mathcal{N}_2$ are trained to predict CoPCs corresponding to ρ and b, respectively. Since 7 PCs in case of ρ and 15 PCs in case of b are required to capture 99.99% variance of the data, the number of neurons in output layers is 7 for $\mathcal{N}_1$ and 15 for $\mathcal{N}_2$. Following our architecture optimization strategy we choose 6 hidden layers of 150 neurons each for $\mathcal{N}_1$ and 2 hidden layers of 150 neurons each for $\mathcal{N}_2$. We use Rectified Linear Unit (ReLU) as an activation function for both networks. Mean Squared Error(MSE) is utilized as a loss function along with the elastic net regularization (429), and the Adam optimizer (430) with a learning rate of 0.001 was employed. Before the training phase, each input parameter column was scaled to zero mean and unit variance, thus standardizing the input features. 75% of the total data points were utilized for training (123 data points), 10% were utilized for validation (16 data points), and the remaining 15% were utilized for testing (25 data points).

6.4.2 Prediction of electronic fields by the ML model

We now discuss the overall performance of the machine learning model for the prediction of the electronic fields. The Pearson correlation coefficient (R) between the predicted and actual electronic fields at each point of the discretized domain for the test data was found to be 0.9949 and 0.9983 for ρ and b, respectively. In addition to the test data points described

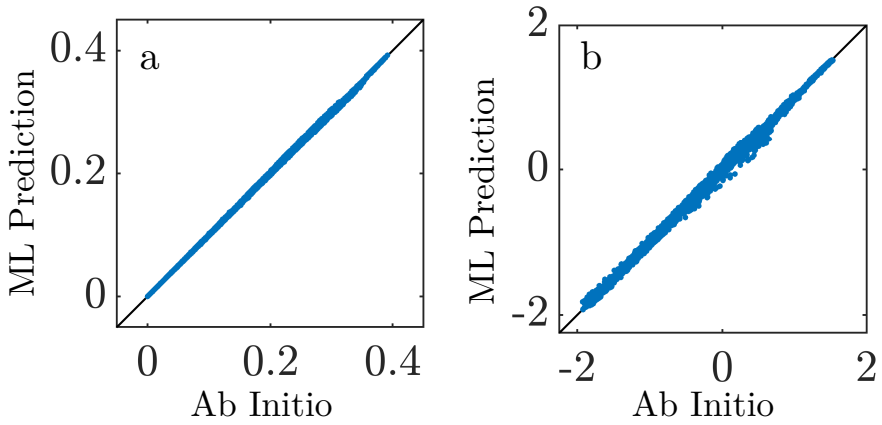

Figure 6.5: Parity plots for (a) test data of ρ ($R = 0.9949$), (b) test data of b ($R = 0.9983$).

above, we have chosen three additional test data points where the input parameters were partially unseen during the training (i. $R_{\text{avg}} = 49.51\,\text{Bohr}$, $\alpha = 0.002$, $\tau = 4.5052\,\text{Bohr}$; ii. $R_{\text{avg}} = 35.55\,\text{Bohr}$, $\alpha = 0.00125$, $\tau = 4.6052\,\text{Bohr}$; iii. $R_{\text{avg}} = 53.32\,\text{Bohr}$, $\alpha = 0.0015$, $\tau = 4.5552\,\text{Bohr}$). For each of these three test cases, there is one input variable whose value was not used in the training data (e.g. data point with τ and α values present in the training data but the value of R_{avg} not present in the training data).

Finally, we have randomly selected two additional test data points where none of the three input variables were seen by the ML model during training (i. $R_{\text{avg}} = 49.51\,\text{Bohr}$, $\alpha = 0.00125$, $\tau = 4.5552\,\text{Bohr}$; ii. $R_{\text{avg}} = 30.46\,\text{Bohr}$, $\alpha = 0.00075$, $\tau = 4.6552\,\text{Bohr}$). These additional test data points with partial or wholly unseen input parameters help assess the ML model's capability to generalize beyond training data. Machine Learning predicted and actual (DFT) electronic fields for one of the test data points with all unknown input parameters are compared in Fig. 6.6.

We quantify the error in the predicted electronic fields through the normalized root mean square error (NRMSE) (388):

$$\text{NRMSE} = \frac{\sqrt{\frac{1}{d}\sum_{i=1}^{d}\left(\rho_i^{\text{DFT}} - \rho_i^{\text{ML}}\right)^2}}{|\max(\rho^{\text{DFT}}) - \min(\rho^{\text{DFT}})|} \tag{6.10}$$

Here $\max(\cdot)$ and $\min(\cdot)$ denote maximum and minimum over the fundamental domain and d is the dimension of the data ($\sim 60,000$). NRMSE for b is calculated similarly. The NRMSE for various categories of test data points, including cases with partial or wholly unseen inputs, are presented in Table 6.1. The low NRMSE values on the test data are indicative of the general accuracy of the ML model. In particular, low NRMSE values for the input conditions beyond the training data establish the generalization capacity of the model.

In addition to evaluating the NRMSE values, we monitored the integrals of ρ^{ML} and b^{ML} over the fundamental domain. For a neutral system with N_{e} electrons within the computational unit cell, the electron density and the nuclear pseudocharge fields obey the normalization conditions $\int_{\mathcal{D}} \rho(\mathbf{x})\,\mathrm{d}\mathbf{x} = N_{\text{e}}$ and $\int_{\mathcal{D}} b(\mathbf{x})\,d\mathbf{x} = -N_{\text{e}}$ respectively. Since these constraints

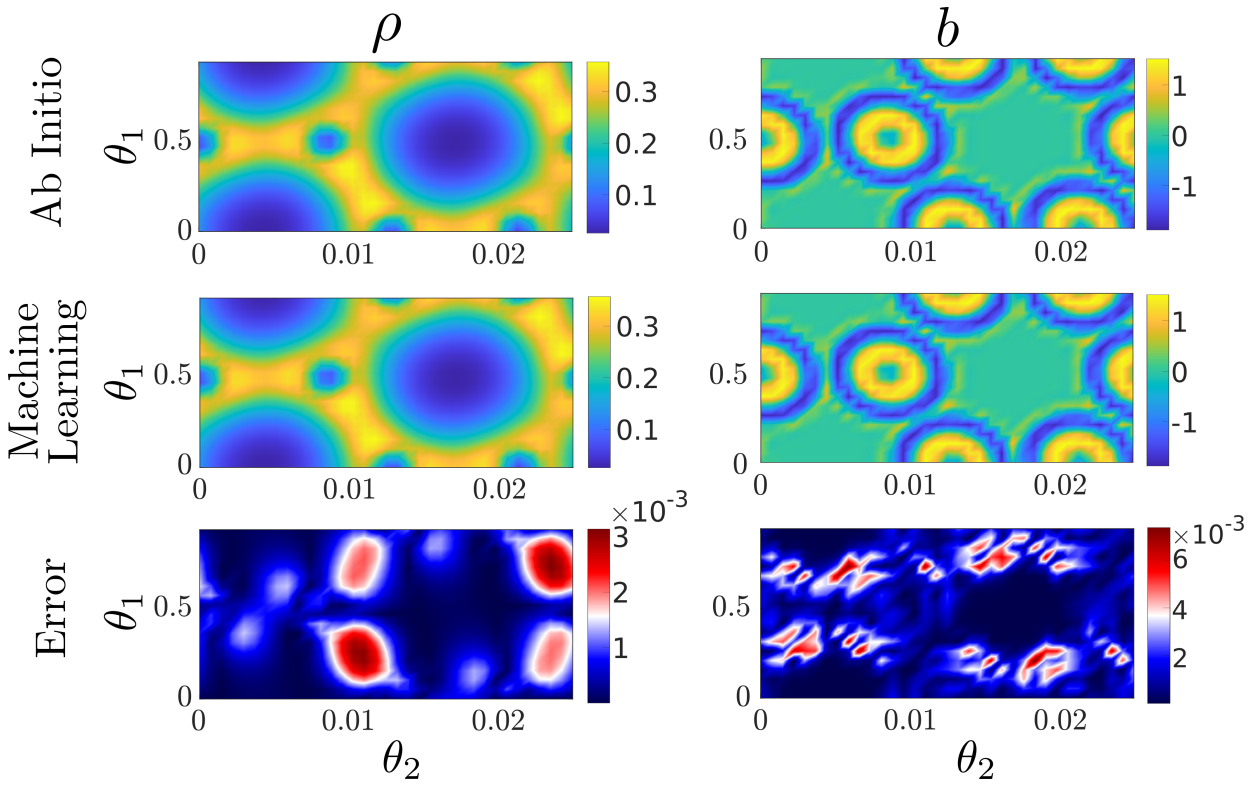

Figure 6.6: Comparison between ML predicted and DFT simulation obtained electronic fields for a test data point with all unknown input parameters ($R_{\text{avg}} = 49.51\,\text{Bohr}$, $\alpha = 0.00125$, $\tau = 4.5552\,\text{Bohr}$). A slice of the electronic fields at the average radial coordinate of the atoms in the fundamental domain is shown. The error is computed as $\frac{|\rho^{\text{DFT}} - \rho^{\text{ML}}|}{|\max(\rho^{\text{DFT}}) - \min(\rho^{\text{DFT}})|}$, similarly for b. Here, $\max(\cdot)$ and $\min(\cdot)$ denote maximum and minimum over the fundamental domain.

were not built into the ML model, they allow additional quality checks on the ML predicted fields to be performed. As shown in Table 6.1, the errors associated with deviations from these constraints are quite low (0.000625 particles or lower, per electron), indicating high quality predictions of the electronic fields by the ML model.

Case	NRMSE (ρ)	$\left\lvert N_\mathrm{e} - \int_\mathcal{D} \rho^\mathrm{ML}(\mathbf{x})\mathrm{d}\mathbf{x}\right\rvert$	NRMSE (b)	$\left\lvert(-N_\mathrm{e}) - \int_\mathcal{D} b^\mathrm{ML}(\mathbf{x})\mathrm{d}\mathbf{x}\right\rvert$
Average for test data set	2.8×10^{-4}	3.2×10^{-3}	5.6×10^{-4}	5.4×10^{-3}
Random test data point $R_\mathrm{avg} = 40.64\ , \alpha = 0.0015, \tau = 4.7052$	2.8×10^{-4}	9.2×10^{-3}	2.8×10^{-4}	8.6×10^{-3}
Test data point with unknown R_avg $R_\mathrm{avg} = 49.51\ , \alpha = 0.002, \tau = 4.5052$	1.3×10^{-4}	5.2×10^{-4}	2.1×10^{-4}	2.5×10^{-3}
Test data point with unknown α $R_\mathrm{avg} = 35.55\ , \alpha = 0.00125, \tau = 4.6052$	2.5×10^{-4}	1.2×10^{-3}	1.9×10^{-4}	5.6×10^{-3}
Test data point with unknown τ $R_\mathrm{avg} = 53.32\ , \alpha = 0.0015, \tau = 4.5552$	1.6×10^{-4}	4.2×10^{-3}	2.5×10^{-4}	8.6×10^{-3}
Test data point with unknown R_avg, α, τ $R_\mathrm{avg} = 49.51\ , \alpha = 0.00125, \tau = 4.5552$	2.1×10^{-4}	4.3×10^{-3}	4.8×10^{-4}	3.1×10^{-3}
Test data point with unknown R_avg, α, τ $R_\mathrm{avg} = 30.46\ , \alpha = 0.00075, \tau = 4.6552$	2.3×10^{-4}	3.0×10^{-3}	2.8×10^{-4}	2.8×10^{-3}

Table 6.1: Table showing NRMSE for ML predicted ρ and b for various test cases. Also shown are errors in the integrals of electronic fields over the fundamental domain. R_avg and τ values are in Bohr.

6.4.3 Prediction of nuclear coordinates, energies and band structure

Finally, we post-process the ML predicted electronic fields for various test data points to obtain nuclear coordinates, electronic properties and energy components of interest. We compute the errors in these quantities for a random test data point, as well as the aforementioned five test cases for which the inputs were partially or wholly unseen by the ML model during training (Table 6.2). In general, the errors in the total ground state energy, as computed through the Harris-Foulkes functional (eq. 6.6) are found to be appreciably smaller than the chemical accuracy threshold (1.6×10^{-3} Ha/atom), except for one of the cases which had an unseen value of α. Considering the various components of the Harris-Foulkes energy, we see that the highest accuracies in the ML predictions are associated with the exchange correlation term E_xc, possibly due to the sole dependence of this quantity on the electron density, which itself is predicted rather accurately. The energy component $\widetilde{E}_\mathrm{xc}$ (eq. 6.6) also

has a very similar behavior and is not shown in Table 6.2. The nuclear self-energy and correction terms which depend only on the nuclear pseudocharge field are also predicted with high accuracy. The electrostatic term which depends on both the nuclear pseudocharge field and the electron density, and the electronic band energy, which depends on the Kohn-Sham eigenvalues are seen to be associated with somewhat lower accuracy predictions, particularly for the test data points which had values of α and/or τ unseen by the ML model. However, even in these cases, the errors are less than 3.0×10^{-3} Ha/atom, and error cancellation leads to overall accurate ground state energy predictions. The ability to predict ground-state energies of deformed quasi-one-dimensional structures (while having atomic relaxation effects already included) with first principles accuracy, at a small computational cost is one of the great advantages of the proposed ML model, thus leading to its potential use in the multiscale modeling of low-dimensional systems (397).

The unsupervised learning procedure used for picking out nuclear coordinates is also found to be quite accurate, with typical errors (measured as the maximum error in the Cartesian coordinate components of all atoms in the fundamental domain) of the order of 0.02 to 0.03 Bohrs. The accuracy in the prediction of these coordinates is also reflected in the overall accuracy of the ML predicted Kohn-Sham Hamiltonian, which in turn, affects the quality of electronic band diagrams and other eigenstate-dependent quantities computed from the Hamiltonian. We found strikingly good agreement between ML predicted and Helical DFT band diagrams for the test data points considered here, with a typical case (associated with wholly unseen inputs) demonstrated in Fig 6.7. Undeformed armchair carbon nanotubes are metallic (7; 151) but develop an oscillatory band gap as a function of imposed twist (151; 5). The band gap (computed here as the difference between the smallest eigenvalue above the Fermi level and the largest eigenvalue below the Fermi level as the symmetry indices (η, ν) are varied) is particularly error prone since it is the difference of two quantities. Additionally, as the tube is deformed, the location and nature (i.e., direct vs. indirect) of the band gap is expected to change (5). However, the ML predicted

location of the band gap was correct for every test case and its value was correct to about 0.02 eV or better, in almost every test case. In this regard, our approach to predicting band structure dependent quantities by means of a post-processing step applied to the ML predicted electronic fields appears to be especially effective. Overall, the ability of our approach to accurately and efficiently predict the electronic structure of low-dimensional materials as a function of imposed deformation, opens up the use of such techniques for strain-engineering applications (394; 395; 396).

Case	Ground state energy $\mathcal{F}^{\text{HF}}$ (Ha/atom)	Exch. Corr. energy E_{xc} (Ha/atom)	Electrostatic term $\widetilde{E}_{\text{el}}$ (Ha/atom)	Nuclear self energy & correction term E_{sc} (Ha/atom)	Band Energy E_{band} (Ha/atom)	Band gap (eV)	Atomic coordinates $\mathbf{r}_i$ (Bohr)
Random test data point $R_{\text{avg}} = 40.64\,, \alpha = 0.0015, \tau = 4.7052$	9.0×10^{-4}	4.1×10^{-5}	7.1×10^{-5}	1.5×10^{-4}	9.9×10^{-4}	0.017	0.026
Test data point with unknown R_{avg}: $R_{\text{avg}} = 49.51\,, \alpha = 0.0020, \tau = 4.5052$	6.7×10^{-4}	1.9×10^{-5}	4.2×10^{-4}	4.3×10^{-4}	6.7×10^{-4}	0.018	0.028
Test data point with unknown α $R_{\text{avg}} = 35.55\,, \alpha = 0.00125, \tau = 4.6052$	3.6×10^{-3}	8.9×10^{-5}	2.1×10^{-3}	3.2×10^{-4}	1.2×10^{-3}	0.042	0.019
Test data point with unknown τ $R_{\text{avg}} = 53.32\,, \alpha = 0.0015, \tau = 4.5552$	2.2×10^{-4}	5.4×10^{-5}	2.7×10^{-3}	4.7×10^{-5}	2.9×10^{-3}	0.008	0.023
Test data point with unknown R_{avg}, α, τ $R_{\text{avg}} = 49.51\,, \alpha = 0.00125, \tau = 4.5552$	6.5×10^{-4}	7.4×10^{-5}	1.9×10^{-3}	1.8×10^{-4}	1.4×10^{-3}	0.008	0.022
Test data point with unknown R_{avg}, α, τ $R_{\text{avg}} = 30.46\,, \alpha = 0.00075, \tau = 4.6552$	1.35×10^{-4}	8.0×10^{-5}	1.8×10^{-3}	4.1×10^{-4}	1.3×10^{-3}	0.002	0.034

Table 6.2: Errors in various post-processed quantities. Refer to eq. 6.6 and related discussion for interpretation of the various energetic terms. R_{avg} and τ values are in Bohr.

We attribute the high accuracy of the model here to the accuracy in both dimensionality reduction and learning through NNs. The fact that during training, the model uses only about 120 data points and that chemical accuracy requirements are met during prediction even for unseen input test cases, are particularly noteworthy and prove the effectiveness and generalizability of our model. Also, as pointed out earlier, in addition to being accurate, the proposed ML model is significantly more computationally efficient than DFT simulations. We also anticpate that the approach described here, i.e., obtaining complex electronic structure

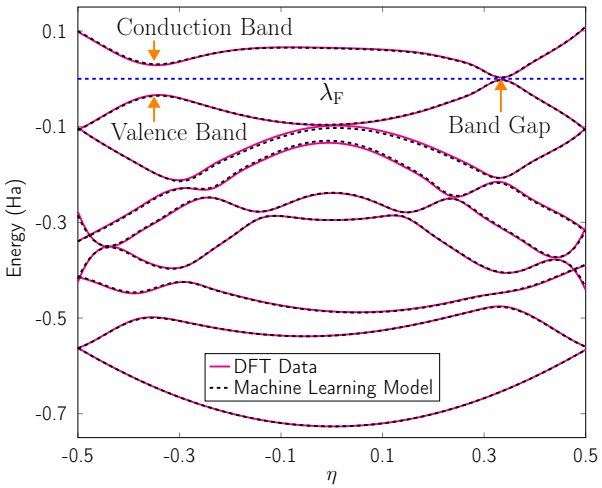

(a) Symmetry adapted band diagram in η, at $\nu = 2$.

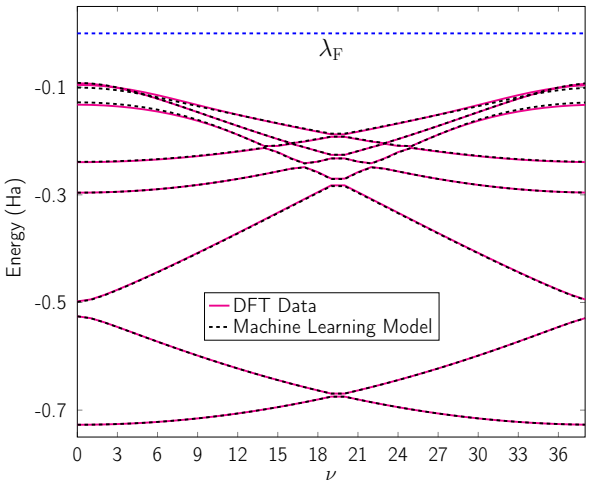

(b) Symmetry adapted band diagram in ν, at $\eta = 0$.

Figure 6.7: Comparison of symmetry adapted band diagrams produced by the original DFT method and the machine learning model (with post processing) for the unknown test data point with $R_{\text{avg}} = 49.51$ Bohr$, \alpha = 0.00125$ and $\tau = 4.5552$ Bohr. The agreement appears excellent and the post–processed ML model is also able to precisely predict the location of the band–gap (at $\eta = \frac{1}{3}, \nu = 2$) as well as its value (0.128 eV from Helical DFT) to about 6% accuracy in this case. Note that λ_F denotes the system's Fermi level.

dependent quanties through post-processing of ML predicted electronic fields, instead of predicting such quantities through ML directly, is going to find utility in computational studies related to the polarization and transport properties of low-dimensional systems.

6.4.4 Interpretation of PCA modes

The number of PCs required in this problem is significantly less than the original dimensions of the electronic fields data ($\sim$ 60,000), thus indicating that these quantities are mostly confined to subspaces of much lower–dimension. The presence of these hidden lower–dimensional features, and the significant reduction of dimensionality of the data through PCA, in turn, implies that just a few CoPCs have to be predicted as a function of the input parameters by the second step of the ML model. This helps account for the fact that such predictions can be made with relatively little training data, as discussed earlier. Remarkably, just the first couple of PCs appear sufficient to capture well over 90% of the variance in both ρ and b. Figure 6.8 shows these two PCA modes for each quantity visualized using helical coordinates, specifically in a $\theta_1 - \theta_2$ plane located at the center of the simulation domain. As expected, the PCs of ρ and b capture the most significant aspects of the variations in these quantities, with the modes of ρ reflecting changes in charge density along the carbon-carbon bonds, and those of b capturing shifts in the nuclear positions.

To elaborate on the above interpretations, we first recall that in the absence of relaxation effects, an atom within the fundamental domain has the same values of θ_1 and $\mathfrak{N}\,\theta_2$, regardless of the tube radius or the level of axial/torsional strain imposed (as before, $\mathfrak{N}$ denotes the cyclic symmetry group order). Consequently, for all values of the input parameters, the nuclei are expected to be located in the same relative positions in a $\theta_1 - \theta_2$ planar plot, if atomic relaxation effects can be ignored. In the practice, upon imposition of strain, the nuclei re-adjust their positions to minimize the system energy during the structural relaxation procedure, leading to somewhat different values of the helical coordinates associated with their pseudocharge centers, than would be suggested by purely geometrical considerations.

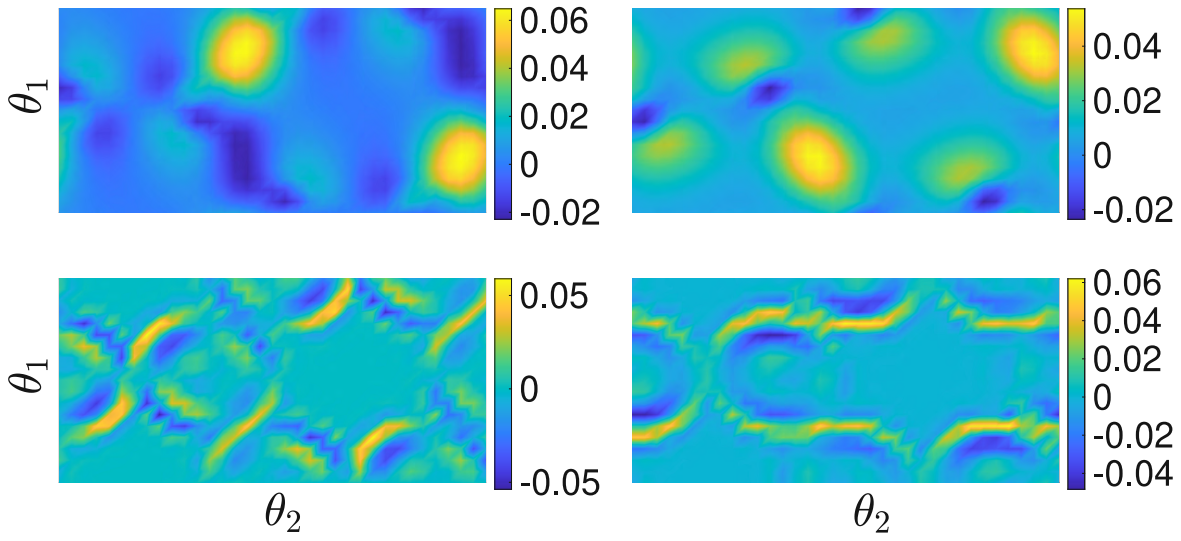

Figure 6.8: First two principal components for ρ (*top*) and b (*bottom*). A slice of the PCA modes at the average radial coordinate of the atoms in the fundamental domain is shown.

The PCA modes for b illustrated in Figure 6.8 appear to be capturing this "motion" of the pseudocharge centers (i.e., nuclear coordinates) associated with the relaxation procedure. Furthermore, due to the changes in the nuclear positions, the carbon-carbon bond lengths change, and the PCA modes for ρ appear to be capturing changes in the electron density along these bonds while they are stretched or compressed due to the imposed strains. Notably, these bonds are at angles with respect to the $\theta_1 - \theta_2$ axes, leading to the tilted appearance of the electron density lobes observable in Figure 6.8. Finally, the presence of more wiggles in the plots for the PCA modes for b, as compared to those for ρ can be explained by observing that at a discrete level, the latter is a smoother quantity. Specifically, the discretized b field can have sharper local jumps since it is the sum of individual atom centered pseudocharges, while ρ is more smeared out (also see top row of Figure 6.6). Indeed, this difference in relative degrees of smoothness at the discrete level probably contributes to the different number of PCA modes for these quantities needed to capture the same level of variance in the data (Figure 6.4).

CHAPTER 7

Beyond nanotubes: Gaussian curvature

7.0.1 Introduction

Gaussian curvature is a fundamental geometrical property that plays a crucial role in determining the behavior and characteristics of nano-scale materials and structures. The Gaussian curvature modulus, along with the mean curvature modulus, can govern the dominant deformation modes of two-dimensional (2D) materials such as graphene, nanotubes, fullerenes, and lipid bilayer membranes (431; 432). Some slected example of such geometry is shown in Fig.7.1 These curvature elastic moduli are intimately linked to important physical processes like pore formation, structural deformations, cellular transport, and topological changes accompanying events such as membrane fusion and fission.(433) Despite its significance, the Gaussian curvature modulus has proven remarkably difficult to evaluate accurately through experiments or computational simulations. (434; 435) Unlike the relatively straightforward mean curvature modulus, the Gaussian curvature modulus is not directly accessible from the well-established thermal fluctuation spectra analysis that has been successfully applied to extract the former property. The key challenge arises from the profound geometrical result known as the Gauss-Bonnet theorem (436), which states that the integral of the Gaussian curvature over a closed surface is an invariant, independent of any deformations that do not change the topology. To circumvent this longstanding obstacle, several approaches have been proposed, however often involve restrictive assumptions. (437; 438; 439) Common limitations include zero-temperature conditions, small system sizes susceptible to finite-size effects, or inherent inconsistencies between the underlying theoretical models and the simu-

lated systems at finite temperatures. Overcoming these challenges necessitates a more comprehensive and accurate first-principles approach capable of capturing the intricate interplay between geometry, temperature, and electronic interactions. In this work, we introduce a novel computational framework that amalgamates the power of DFT with the concept of ellipsoidal coordinate systems and symmetries. By adapting revised periodic boundary conditions tailored to ellipsoidal geometries within a real-space finite difference DFT formalism, our method enables efficient simulations of nanoscale systems exhibiting Gaussian curvature while the ellipsoidal symmetry elegantly circumvents the limitations imposed by the Gauss-Bonnet theorem, allowing for the direct evaluation of the Gaussian curvature modulus within a finite-sized simulation domain.

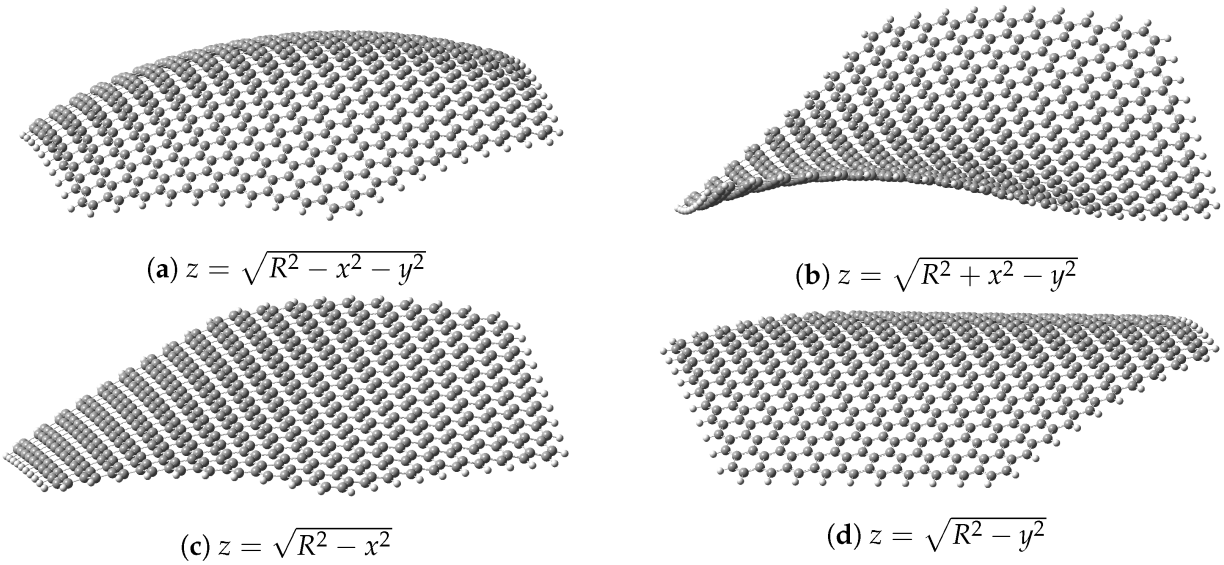

(**a**) $z = \sqrt{R^2 - x^2 - y^2}$

(**b**) $z = \sqrt{R^2 + x^2 - y^2}$

(**c**) $z = \sqrt{R^2 - x^2}$

(**d**) $z = \sqrt{R^2 - y^2}$

Figure 7.1: The four different geometries considered in this study for the graphene dot with $R = 50$ and their respective equations: (a) sphere; (b) one-sheet hyperboloid; (c) x-cylinder; (d); y-cylinder. Images generated with GaussView 6 and published in this paper (6)

7.0.2 Problem setup and simplification

To effectively model systems with Gaussian curvature within a finite-domain simulation, we employ the ellipsoidal coordinate system as the basis for our geometric reformulation. The ellipsoidal coordinates are a set of orthogonal curvilinear coordinates that naturally describe ellipsoidal geometries. In this system, a point in three-dimensional space is specified by the following relations (440):

$$\begin{aligned} x^2 &= \frac{(a^2+\lambda)(a^2+\mu)(a^2+\nu)}{(b^2-a^2)(c^2-a^2)} \\ y^2 &= \frac{(b^2+\lambda)(b^2+\mu)(b^2+\nu)}{(a^2-b^2)(c^2-b^2)} \\ z^2 &= \frac{(c^2+\lambda)(c^2+\mu)(c^2+\nu)}{(a^2-c^2)(b^2-c^2)} \end{aligned} \tag{7.1}$$

where a, b and c are scaling factor related to the semi-major axes of the ellipsoid, and $-\lambda < c^2 < -\mu < b^2 < -\nu < a^2$ are the ellipsoidal coordinates. The coordinate surfaces are confocal ellipsoids (λ = constant), hyperboloids of two sheets (ν = constant), and hyperboloids of one sheet (μ = constant).

By exploiting the separability of the ellipsoidal coordinate system, we can reformulate the geometric problem in terms of angular parametrizations (r, θ_1, θ_2) while constraining the radial coordinate r to a finite range. This approach allows us to effectively model a finite domain exhibiting Gaussian curvature within a computationally tractable framework:

$$\begin{aligned} x &= ar\sin\theta_1\cos\theta_2 \\ y &= br\sin\theta_1\sin\theta_2 \\ z &= cr\cos\theta_1 \end{aligned} \tag{7.2}$$

Note that the Helmholtz differential equation is separable in both approach here. We then define a finite simulation domain ω bounded by the following constraints:

$$
\begin{aligned}
r_{min} \leq r \leq r_{max} \\
0 \leq \theta_1 \leq \pi \\
0 \leq \theta_2 \leq 2\pi
\end{aligned}
\tag{7.3}
$$

where r_{min} and r_{max} represent the inner and outer radial boundaries of the ellipsoidal shell, respectively. By appropriately choosing these boundaries, we can capture the desired Gaussian curvature within the simulation domain while maintaining a finite system size. The angular parametrizations are then discretized using a finite-difference scheme, allowing for the numerical solution of the governing equations within the bounded ellipsoidal domain. Periodic boundary conditions are applied along the angular directions ($\theta 1$ and θ_2), effectively representing a toroidal topology that seamlessly wraps around the ellipsoidal geometry.

This reformulation of the geometric problem in terms of ellipsoidal coordinates and angular parametrizations is a key step in our approach, as it enables the efficient modeling of Gaussian curvature within a finite-domain simulation while circumventing the limitations imposed by the Gauss-Bonnet theorem. By exploiting the revised periodic boundary conditions tailored to the ellipsoidal geometry, we can directly evaluate the Gaussian curvature modulus and other curvature-dependent properties within the bounded simulation domain.

7.0.3 Ellipsoidal symmetry-adapted Laplacian operator

In the pursuit of understanding density functional theory within the framework of ellipsoidal coordinates, we embark on deriving the Laplacian coefficient, a crucial element for computing the kinetic energy of the electrons and more. Notably, the angular parametrization of ellipsoidal coordinates parallels that of the spherical system, albeit with an additional factor of a, b and c to accommodate the ellipsoidal geometry.

To proceed, we employ the separation of variables technique, assuming solutions to the Laplace equation in ellipsoidal coordinates can be represented as products of functions of

individual coordinates. By invoking the properties of ellipsoidal coordinates and employing appropriate transformations, we arrive at the expression for the Laplacian coefficient for the diagonal elements specific to our coordinate system:

$$
\begin{aligned}
c_1 &= \left[\left(\frac{1}{a^2}\right)\sin^2\theta_1\cos^2\theta_2 + \left(\frac{1}{b^2}\right)\sin^2\theta_1\sin^2\theta_2 + \left(\frac{1}{c^2}\right)\cos^2\theta_1\right]\frac{\partial^2 f}{\partial r^2} \\
c_2 &= \left[\frac{\cos^2\theta_1\cos^2\theta_2}{a^2r^2} + \frac{\cos^2\theta_1\sin^2\theta_2}{b^2r^2} + \frac{\sin^2\theta_1}{c^2r^2}\right]\frac{\partial^2 f}{\partial {\theta_1}^2} \\
c_3 &= \left[\frac{\left(\frac{1}{a^2}\right)\left[\sin^2\theta_2 - \sin\theta_2\cos\theta_2\right] + \left(\frac{1}{b^2}\right)\left[\cos^2\theta_2 - \cos\theta_2\sin\theta_2\right]}{r^2\sin^2\theta_1}\right]\frac{\partial^2 f}{\partial {\theta_2}^2}
\end{aligned}
\tag{7.4}
$$

Similarly, the off-diagonal elements and the cross-derivative terms are:

$$
\begin{aligned}
c_4 &= \left[\frac{\cos^2\theta_1\cos^2\theta_2 + \sin^2\theta_2}{a^2r} + \frac{\cos^2\theta_1\sin^2\theta_2 + \cos^2\theta_2}{b^2r} + \frac{\sin^2\theta_1}{c^2r}\right]\frac{\partial f}{\partial r} \\
c_5 &= \left[\frac{-2\sin\theta_1\cos\theta_1\cos^2\theta_2}{a^2r^2} + \frac{\cos\theta_1\sin^2\theta_2}{a^2r^2\sin\theta_1}\right. \\
&\quad \left. - \frac{2\sin\theta_1\cos\theta_1\sin^2\theta_2}{b^2r^2} + \frac{\cos\theta_1\cos^2\theta_2}{b^2r^2\sin\theta_1} + \frac{2\sin\theta_1\cos\theta_1}{c^2r^2}\right]\frac{\partial f}{\partial\theta_1} \\
c_6 &= \left[\frac{\sin\theta_2\cos\theta_2}{r^2} + \frac{\sin\theta_2\cos\theta_2\cos^2\theta_1 + \sin\theta_2\cos\theta_2}{r^2\sin^2\theta_1}\right]\left(\frac{1}{a^2} - \frac{1}{b^2}\right)\frac{\partial f}{\partial\theta_2} \\
c_7 &= \left[\frac{2\sin\theta_1\cos\theta_1\cos^2\theta_2}{a^2r^2} + \frac{2\sin\theta_1\cos\theta_1\sin^2\theta_2}{b^2r^2} - \frac{2\sin\theta_1\cos\theta_1}{c^2r^2}\right]\frac{\partial^2 f}{\partial r\partial\theta_1} \\
c_8 &= \left[\frac{(a^2-b^2)\cot\theta_1\sin 2\theta_2}{a^2b^2r^2}\right]\frac{\partial^2 f}{\partial\theta_1\partial\theta_2} \\
c_9 &= \left[\frac{(a^2-b^2)\sin\theta_2\cos\theta_2}{a^2b^2r}\right]\frac{\partial^2 f}{\partial r\partial\theta_2} \\
c_{10} &= \left[\frac{(a^2-b^2)\sin\theta_2\cos\theta_2}{a^2b^2r}\right]\frac{\partial^2 f}{\partial\theta_2\partial r}
\end{aligned}
\tag{7.5}
$$

The Laplacian operator then can be obtained by summing up all the terms:

$$
\nabla^2 f = \sum_{i=1}^{10} c_i f \tag{7.6}
$$

Drawing inspiration from the methodology employed in Helical DFT, we utilized finite difference techniques to accurately calculate the Laplacian in ellipsoidal coordinates. To validate the fidelity of our implementation, we conducted a rigorous accuracy assessment. As a benchmark test case, we computed the Laplacian of a function given by $\nabla^2 \left((r\sin(\theta_1)\cos(\theta_2))^2 \, r\sin(\theta_1)\sin(\theta_2) \right) = 2r\sin(\theta_1)sin(\theta_2)$ utilizing sixth-order finite difference with 20 grid points in each of the three directions. Dirichlet boundary conditions were applied in the radial direction, while periodic boundary conditions were enforced in θ_1 and θ_2. The obtained results, demonstrating the precision of our implementation, are presented in Figure XX. This validation not only ensures the correctness of our computational approach but also underscores its potential for applications in diverse fields reliant on accurate Laplacian calculations within ellipsoidal coordinate systems.

In Fig.7.2, our comprehensive analysis unveils a remarkable consistency between the numerical solution and the analytical counterpart across the radial (r), θ_1, and θ_2 directions. Notably, owing to the utilization of a sixth-order finite difference scheme coupled with Dirichlet boundary conditions in the radial direction, a discernible discrepancy is expected at the initial and final three grid points, as depicted in Figure 1b. Despite this, the discrepancy does not manifest in the θ_1 and θ_2 directions, owing to the imposition of periodic boundary conditions. Interestingly, an observed spike in error at $\theta_1 = 0$ stems from the singularity inherent at this point in equation 7.0.3. To address this singularity, a minute deviation from zero was integrated during the computation process, with the expectation that error reduction will be achieved with the adoption of higher-order finite difference techniques. This thorough examination underscores not only the efficacy of our computational methodology but also highlights the intricacies involved in mitigating singularities and ensuring accuracy in numerical simulations within ellipsoidal coordinate systems.

7.0.4 Bound states of a quantum dot in a spherical shell

Solving the eigenfunctions of the ellipsoidal Laplacian can be likened to solving the problem of a particle confined within a spherical shell, similar to particle in a box, albeit with certain distinct features owing to the ellipsoidal nature of the coordinate system. The eigenfunctions obtained from such solutions provide valuable insights into the behavior of bound states in physical systems, such as atomic nuclei or quantum dots.

In the realm of quantum dots, which are nanoscale semiconductor structures confining electrons in three dimensions, the eigenfunctions of the ellipsoidal Laplacian elucidate the quantum mechanical behavior of confined electrons. By characterizing the spatial distribution of electron wavefunctions and quantizing their energy levels, these eigenfunctions dictate the electronic properties of quantum dots, such as their optical and electrical behavior. Moreover, the shape anisotropy inherent in ellipsoidal confinement manifests in the distinct energy spectra and spatial distributions of electron states, influencing the optical and electronic properties of quantum dot devices. Utilizing the numerical framework in the previous section 7.0.3, we delve into solving the eigenfunctions of the ellipsoidal Laplacian, treating it akin to a particle confined within a spherical box. The implications of these eigenfunctions extend beyond theoretical elucidation, informing practical applications ranging from materials science to quantum computing. The results are shown in Fig.7.3.

As anticipated, owing to the imposition of an infinite "square" potential in the radial direction via Dirichlet boundary conditions that gives us the spherical shell, the ground state eigenfunction demonstrates a pronounced peak at the center of the confinement "box," as depicted in Fig.7.3a. This observation aligns seamlessly with the theoretical predictions derived from spherical Bessel functions. By extracting a cross-sectional view at the peak of the radial eigenfunction, an intuitive three-dimensional visualization of the eigenfunction is rendered feasible. Fig. 7.3 illustrates that while the ground state eigenfunction exhibits periodicity in the θ_2 direction, it attenuates near the two poles of the spherical confinement.

Notably, the second and third lowest eigenstates also manifest behaviors consistent with the expectations from spherical harmonics, characteristic of a spherically symmetric infinite "square" potential configuration.

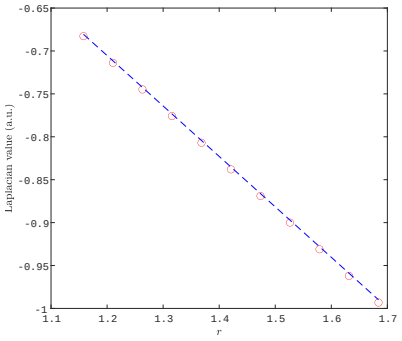

(a) Both numerical and analytical solutions are linear with respect to r, as expected.

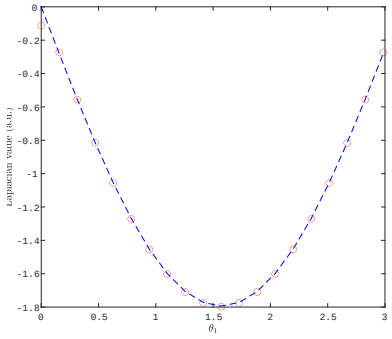

(b) Solution are sinusoidal in θ_1.

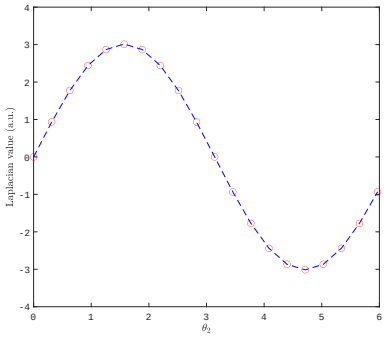

(c) Solution are sinusoidal in θ_2.

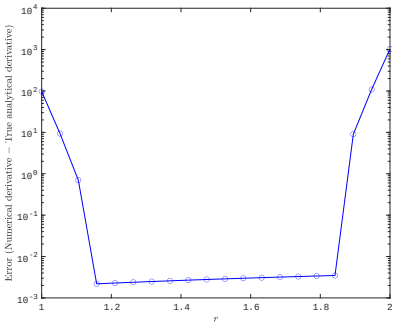

(d) Absolute error in radial direction.

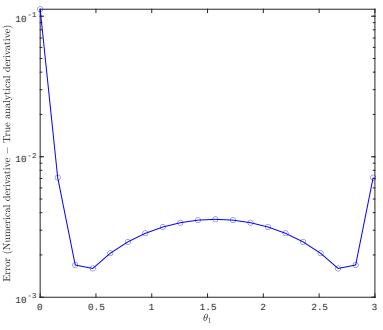

(e) Absolute error in θ_1 direction.

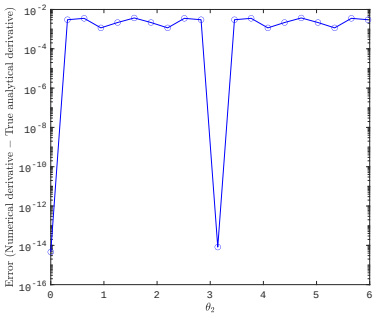

(f) Absolute error in θ_2 direction.

Figure 7.2: Benchmark test results (a-c) Comparisons between numerical and analytical solutions. The first and last 3 grid points in radial directions are neglected. (d-f) Absolute error between numerical and analytical solutions in r, θ_1, and θ_2 directions, respectively.

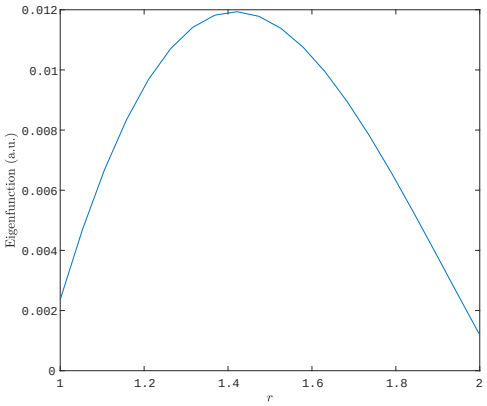

(a) Ground state eigenfunction in radial direction (r).

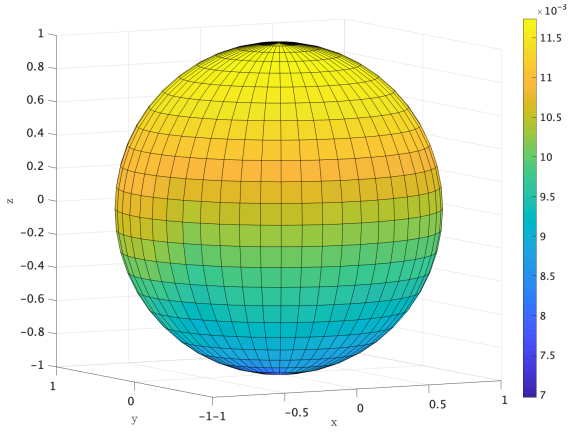

(b) Ground state eigenfunction.

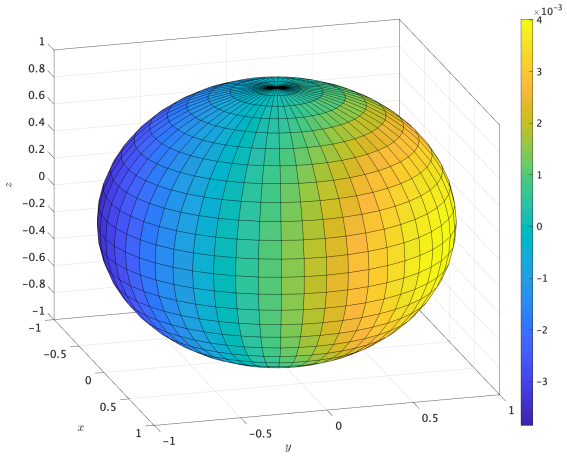

(c) Second lowest eigenfunction.

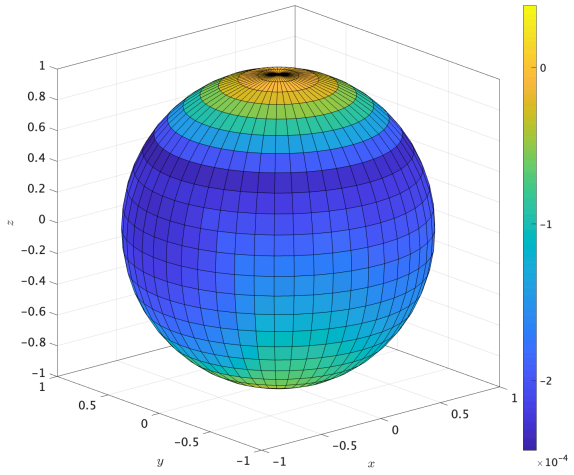

(d) Third lowest eigenfunction.

Figure 7.3: Eigenfunctions of the ellipsoidal laplacians as approximations of the bound states of a quantum dot restriced to a spherical shell.

CHAPTER 8

Conclusion and Future direction

8.0.1 Conclusion

In summary, we introduced a computational method for efficiently simulating systems with twisted geometries, employing symmetry-adapted equations, higher-order finite difference schemes in helical coordinates, and ab initio pseudopotentials. This technique facilitates simulations of quasi-one-dimensional systems, including their deformations, with minimal computational resources. We applied this method to study the mechanical and electronic properties of single-wall zigzag and armchair group-IV nanotubes, ranging from 1 to 3 nm in radius, as they undergo torsional deformation. Our extensive simulations not only extracted mechanical properties directly from first principles but also revealed variations in electronic properties due to torsional deformation, extending known electro-mechanical insights from carbon nanotubes to group IV nanotubes. The exploration of carbon Kagome nanotubes (CKNTs) and Double Kagome P_2C_3 nanotubes introduces two novel allotropes with unique electronic properties, such as flat bands and Dirac points, offering a new platform for studying strongly correlated electronic phenomena in nanomaterials. Extensive first-principles simulations suggest CKNTs nad P_2C_3NTs are stable and exhibit metallic behavior with significant pliability under torsional and extensional deformation. Parallelly, advancements in machine learning (ML) models for predicting electronic fields of quasi-one-dimensional materials under mechanical loads have demonstrated the potential for significantly accelerating computational investigations and enabling efficient strain engineering in low-dimensional systems. The specialized symmetry-adapted version of Kohn-Sham density

functional theory (DFT) used alongside ML models underscores the symbiotic relationship between computational efficiency and advanced material discovery. Wwe have introduced an innovative computational framework designed to simulate systems with Gaussian curvature efficiently and from first principles. By integrating the concepts of ellipsoidal coordinate systems with density functional theory (DFT), our method overcomes the traditional challenges associated with the Gauss-Bonnet theorem, enabling direct evaluation of the Gaussian curvature modulus within finite-sized domains. This approach, which employs high-order finite difference schemes and ab initio pseudopotentials, allows for the convenient simulation of quasi-one-dimensional systems and their deformations without demanding extensive computational resources. We applied this methodology to analyze the behavior of single-wall zigzag and armchair group-IV nanotubes, uncovering insights into their mechanical and electronic properties under torsional deformation. Our comprehensive numerical framework not only facilitates the modeling of systems exhibiting Gaussian curvature but also extends our understanding of curvature-dependent properties, paving the way for future investigations into nano-scale materials and structures.

8.0.2 Future Direction

Expanding on the groundwork established by the current studies, future efforts should aim to broaden our computational framework's application to include a diverse array of nanomaterials and intricate geometric shapes. The utilization of Gaussian curvature in both the development and examination of cutting-edge nanomaterials, especially those characterized by complex topological features and effects induced by curvature, offers a fertile ground for further research. This includes probing into the deformations of nanotubes within more elaborate geometrical configurations. Incorporating machine learning methods into our ellipsoidal coordinate-driven DFT strategy could significantly improve simulation efficiency and precision, aiding in the identification of materials with customized properties. With comprehensive simulation data, a universal principle governing nanotube deformations across

all types might emerge. Moreover, the experimental realization and validation of the novel nanotubes reimagined in this study are essential for translating computational theories into tangible technological advancements.

Bibliography

[1] D. Zhang, R. D. James, T. Dumitrica, Electromechanical characterization of carbon nanotubes in torsion via symmetry adapted tight-binding objective molecular dynamics, Physical Review B 80 (11) (2009) 115418.

[2] J. Correa, A. J. da Silva, M. Pacheco, Tight-binding model for carbon nanotubes from ab initio calculations, Journal of Physics: Condensed Matter 22 (27) (2010) 275503.

[3] L. Yang, M. Anantram, J. Han, J. Lu, Band-gap change of carbon nanotubes: Effect of small uniaxial and torsional strain, Physical Review B 60 (19) (1999) 13874.

[4] A. S. Banerjee, Ab initio framework for systems with helical symmetry: Theory, numerical implementation and applications to torsional deformations in nanostructures, Journal of the Mechanics and Physics of Solids 154 (2021) 104515. doi:https://doi.org/10.1016/j.jmps.2021.104515.
URL https://www.sciencedirect.com/science/article/pii/S0022509621001794

[5] H. M. Yu, A. S. Banerjee, Density functional theory method for twisted geometries with application to torsional deformations in group-iv nanotubes, Journal of Computational Physics 456 (2022) 111023.

[6] S. de-la Huerta-Sainz, A. Ballesteros, N. A. Cordero, Gaussian curvature effects on graphene quantum dots, Nanomaterials 13 (1) (2022) 95.

[7] S. Ghosh, A. S. Banerjee, P. Suryanarayana, Symmetry-adapted real-space density functional theory for cylindrical geometries: Application to large group-IV nanotubes, Physical Review B 100 (12) (2019) 125143.

[8] B. Sarikavak-Lisesivdin, S. B. Lisesivdin, E. Ozbay, F. Jelezko, Structural parameters and electronic properties of 2d carbon allotrope: Graphene with a kagome lattice structure, Chemical physics letters 760 (2020) 138006–138006. doi:10.1016/j.cplett.

2020.138006.

URL https://doi.org/10.1016/j.cplett.2020.138006

[9] Y. Chen, Y. Y. Sun, H. Wang, D. West, Y. Xie, J. Zhong, V. Meunier, M. L. Cohen, S. B. Zhang, Carbon kagome lattice and orbital-frustration-induced metal-insulator transition for optoelectronics, Phys. Rev. Lett. 113 (2014) 085501. doi:10.1103/PhysRevLett.113.085501.

URL https://link.aps.org/doi/10.1103/PhysRevLett.113.085501

[10] B. Bhushan, Springer handbook of nanotechnology, Springer, 2017.

[11] G. Cao, Nanostructures and nanomaterials: synthesis, properties and applications, World scientific, 2004.

[12] M. Fulekar, Nanotechnology: Importance and Applications, 1st Edition, I K International Publishing House, 2010.

[13] Nanotechnology and you: Benefits and applications, http://www.nano.gov/you/nanotechnology-benefits, official website of the United States National Nanotechnology Initiative.

[14] L. V. Zhigilei, A. N. Volkov, A. M. Dongare, Computational Study of Nanomaterials: From Large-Scale Atomistic Simulations to Mesoscopic Modeling, Springer Netherlands, 2012.

[15] S. M. Musa, Computational Nanotechnology: Modeling and Applications with MATLAB®, CRC Press, 2011.

[16] D. Marx, J. Hutter, Ab initio molecular dynamics: basic theory and advanced methods, 1st Edition, Cambridge University Press, 2009.

[17] J. R. Chelikowsky, Introductory Quantum Mechanics with MATLAB: For Atoms, Molecules, Clusters, and Nanocrystals, John Wiley & Sons, 2019.

[18] Computational modelling of nanomaterials, Vol. 17 of Frontiers of Nanoscience, Elsevier, 2020.

[19] V. M. Pereira, A. C. Neto, Strain engineering of graphene's electronic structure, Physical Review Letters 103 (4) (2009) 046801.

[20] H. M. Ghassemi, C. H. Lee, Y. K. Yap, R. S. Yassar, Field emission and strain engineering of electronic properties in boron nitride nanotubes, Nanotechnology 23 (10) (2012) 105702.

[21] R. Fei, L. Yang, Strain-engineering the anisotropic electrical conductance of few-layer black phosphorus, Nano letters 14 (5) (2014) 2884–2889.

[22] R. Roldán, A. Castellanos-Gomez, E. Cappelluti, F. Guinea, Strain engineering in semiconducting two-dimensional crystals, Journal of Physics: Condensed Matter 27 (31) (2015) 313201.

[23] D. G. Schlom, L.-Q. Chen, C. J. Fennie, V. Gopalan, D. A. Muller, X. Pan, R. Ramesh, R. Uecker, Elastic strain engineering of ferroic oxides, Mrs Bulletin 39 (2) (2014) 118–130.

[24] J. Li, Z. Shan, E. Ma, Elastic strain engineering for unprecedented materials properties, MRS Bulletin 39 (2) (2014) 108–114.

[25] A. Hall, L. An, J. Liu, L. Vicci, M. Falvo, R. Superfine, S. Washburn, Experimental measurement of single-wall carbon nanotube torsional properties, Physical review letters 96 (25) (2006) 256102.

[26] N. Wei, L. Xu, H.-Q. Wang, J.-C. Zheng, Strain engineering of thermal conductivity in graphene sheets and nanoribbons: a demonstration of magic flexibility, Nanotechnology 22 (10) (2011) 105705.

[27] M. R. Falvo, G. Clary, R. n. Taylor, V. Chi, F. Brooks, S. Washburn, R. Superfine, Bending and buckling of carbon nanotubes under large strain, Nature 389 (6651) (1997) 582–584.

[28] S. Yang, C. Wang, H. Sahin, H. Chen, Y. Li, S.-S. Li, A. Suslu, F. M. Peeters, Q. Liu, J. Li, et al., Tuning the optical, magnetic, and electrical properties of rese2 by nanoscale strain engineering, Nano letters 15 (3) (2015) 1660–1666.

[29] M. Endo, S. Iijima, M. S. Dresselhaus, Carbon nanotubes, Elsevier, 2013.

[30] X. Chen, S. Zhang, D. A. Dikin, W. Ding, R. S. Ruoff, L. Pan, Y. Nakayama, Mechanics of a carbon nanocoil, Nano Letters 3 (9) (2003) 1299–1304.

[31] W. Ma, L. Xu, A. F. de Moura, X. Wu, H. Kuang, C. Xu, N. A. Kotov, Chiral inorganic nanostructures, Chemical reviews 117 (12) (2017) 8041–8093.

[32] R. D. James, Objective structures, Journal of the Mechanics and Physics of Solids 54 (11) (2006) 2354–2390.

[33] C. D. Aiello, J. M. Abendroth, M. Abbas, A. Afanasev, S. Agarwal, A. S. Banerjee, D. N. Beratan, J. N. Belling, B. Berche, A. Botana, J. R. Caram, G. L. Celardo, G. Cuniberti, A. Garcia-Etxarri, A. Dianat, I. Diez-Perez, Y. Guo, R. Gutierrez, C. Herrmann, J. Hihath, S. Kale, P. Kurian, Y.-C. Lai, T. Liu, A. Lopez, E. Medina, V. Mujica, R. Naaman, M. Noormandipour, J. L. Palma, Y. Paltiel, W. Petuskey, J. C. Ribeiro-Silva, J. J. Saenz, E. J. G. Santos, M. Solyanik-Gorgone, V. J. Sorger, D. M. Stemer, J. M. Ugalde, A. Valdes-Curiel, S. Varela, D. H. Waldeck, M. R. Wasielewski, P. S. Weiss, H. Zacharias, Q. H. Wang, A chirality-based quantum leap, ACS Nano 0 (0), PMID: 35318848, arXiv: https://arxiv.org/abs/2009.00136 (2022). doi:10.1021/acsnano.1c01347.
URL https://doi.org/10.1021/acsnano.1c01347

[34] R. Bistritzer, A. H. MacDonald, Moiré bands in twisted double-layer graphene, Proceedings of the National Academy of Sciences 108 (30) (2011) 12233–12237.

[35] Y. Cao, V. Fatemi, S. Fang, K. Watanabe, T. Taniguchi, E. Kaxiras, P. Jarillo-Herrero, Unconventional superconductivity in magic-angle graphene superlattices, Nature 556 (7699) (2018) 43–50.

[36] Y. Cao, V. Fatemi, A. Demir, S. Fang, S. L. Tomarken, J. Y. Luo, J. D. Sanchez-Yamagishi, K. Watanabe, T. Taniguchi, E. Kaxiras, et al., Correlated insulator behaviour at half-filling in magic-angle graphene superlattices, Nature 556 (7699) (2018) 80–84.

[37] S. Carr, S. Fang, Z. Zhu, E. Kaxiras, Exact continuum model for low-energy electronic states of twisted bilayer graphene, Physical Review Research 1 (1) (2019) 013001.

[38] Y. Zhao, C. Zhang, D. D. Kohler, J. M. Scheeler, J. C. Wright, P. M. Voyles, S. Jin, Supertwisted spirals of layered materials enabled by growth on non-euclidean surfaces, Science 370 (6515) (2020) 442–445.

[39] M. J. Bierman, Y. A. Lau, A. V. Kvit, A. L. Schmitt, S. Jin, Dislocation-driven nanowire growth and eshelby twist, Science 320 (5879) (2008) 1060–1063.

[40] S. Jin, M. J. Bierman, S. A. Morin, A new twist on nanowire formation: Screw-dislocation-driven growth of nanowires and nanotubes, The Journal of Physical Chemistry Letters 1 (9) (2010) 1472–1480.

[41] G. Kresse, J. Furthmuller, Efficient iterative schemes for ab initio total-energy calculations using a plane-wave basis set, Physical Review B 54 (1996) 11169–11186.

[42] X. Gonze, J.-M. Beuken, R. Caracas, F. Detraux, M. Fuchs, G.-M. Rignanese, L. Sindic, M. Verstraete, G. Zerah, F. Jollet, M. Torrent, A. Roy, M. Mikami, P. Ghosez, J.-Y. Raty, D. Allan, First-principles computation of material properties:

the ABINIT software project, Computational Materials Science 25 (3) (2002) 478 – 492.

[43] P. Giannozzi, S. Baroni, N. Bonini, M. Calandra, R. Car, C. Cavazzoni, D. Ceresoli, G. L. Chiarotti, M. Cococcioni, I. Dabo, A. D. Corso, S. de Gironcoli, S. Fabris, G. Fratesi, R. Gebauer, U. Gerstmann, C. Gougoussis, A. Kokalj, M. Lazzeri, L. Martin-Samos, N. Marzari, F. Mauri, R. Mazzarello, S. Paolini, A. Pasquarello, L. Paulatto, C. Sbraccia, S. Scandolo, G. Sclauzero, A. P. Seitsonen, A. Smogunov, P. Umari, R. M. Wentzcovitch, QUANTUM ESPRESSO: a modular and open-source software project for quantum simulations of materials, Journal of Physics: Condensed Matter 21 (39) (2009) 395502.

[44] M. D. Segall, P. J. D. Lindan, M. J. Probert, C. J. Pickard, P. J. Hasnip, S. J. Clark, M. C. Payne, First-principles simulation: ideas, illustrations and the CASTEP code, Journal of Physics: Condensed Matter 14 (11) (2002) 2717.

[45] T. Dumitrica, R. D. James, Objective molecular dynamics, Journal of the Mechanics and Physics of Solids 55 (10) (2007) 2206 – 2236.

[46] D. Zhang, E. Akatyeva, T. Dumitrică, Bending ultrathin graphene at the margins of continuum mechanics, Phys. Rev. Lett. 106 (2011) 255503.

[47] T. Dumitrica, Computational nanomechanics of quasi-one-dimensional structures in a symmetry-adapted tight binding framework, in: V. Barsan, A. Aldea (Eds.), Trends in Nanophysics, Vol. 0 of Engineering Materials, Springer Berlin Heidelberg, 2010, pp. 29–55.

[48] J. Ma, Y. Ni, S. Volz, T. Dumitrică, Thermal transport in single-walled carbon nanotubes under pure bending, Physical Review Applied 3 (2) (2015) 024014.

[49] P. Koskinen, O. O. Kit, Efficient approach for simulating distorted materials, Physical review letters 105 (10) (2010) 106401.

[50] P. Koskinen, Electronic and optical properties of carbon nanotubes under pure bending, Phys. Rev. B 82 (2010) 193409.

[51] P. Koskinen, Graphene nanoribbons subject to gentle bends, Physical Review B 85 (20) (2012) 205429.

[52] O. O. Kit, L. Pastewka, P. Koskinen, Revised periodic boundary conditions: Fundamentals, electrostatics, and the tight-binding approximation, Physical Review B 84 (15) (2011) 155431.

[53] W. Cai, W. Fong, E. Elsen, C. R. Weinberger, Torsion and bending periodic boundary conditions for modeling the intrinsic strength of nanowires, Journal of the Mechanics and Physics of Solids 56 (11) (2008) 3242–3258.

[54] A. S. Banerjee, Density functional methods for Objective Structures: Theory and simulation schemes, Ph.D. thesis, University of Minnesota, Minneapolis (2013).

[55] A. S. Banerjee, P. Suryanarayana, Cyclic density functional theory: A route to the first principles simulation of bending in nanostructures, Journal of the Mechanics and Physics of Solids 96 (2016) 605–631.

[56] P. D'Arco, Y. Noel, R. Demichelis, R. Dovesi, Single-layered chrysotile nanotubes: A quantum mechanical ab initio simulation, The Journal of chemical physics 131 (20) (2009) 204701.

[57] R. Dovesi, V. Saunders, C. Roetti, R. Orlando, C. Zicovich-Wilson, F. Pascale, B. Civalleri, K. Doll, N. Harrison, I. Bush, et al., Crystal17 (2017).

[58] C. T. White, D. H. Robertson, J. W. Mintmire, Helical and rotational symmetries of nanoscale graphitic tubules, Physical Review B 47 (1993) 5485–5488.

[59] E. Chang, G. Bussi, A. Ruini, E. Molinari, First-principles approach for the calculation of optical properties of one-dimensional systems with helical symmetry: The case of carbon nanotubes, Physical Review B 72 (2005) 195423.

[60] Y. Noel, P. D'arco, R. Demichelis, C. M. Zicovich-Wilson, R. Dovesi, On the use of symmetry in the ab initio quantum mechanical simulation of nanotubes and related materials, Journal of Computational Chemistry 31 (4) (2010) 855–862.

[61] E. Chang, G. Bussi, A. Ruini, E. Molinari, Excitons in carbon nanotubes: An *Ab Initio* symmetry-based approach, Physical Review Letters 92 (2004) 196401.

[62] S. Pathrudkar, H. M. Yu, S. Ghosh, A. S. Banerjee, Machine learning based prediction of the electronic structure of quasi-one-dimensional materials under strain, Physical Review B 105 (2022) 195141. doi:10.1103/PhysRevB.105.195141.

[63] H. M. Yu, S. Sharma, S. Agarwal, O. Liebman, A. S. Banerjee, Carbon kagome nanotubes—quasi-one-dimensional nanostructures with flat bands, RSC advances 14 (2) (2024) 963–981.

[64] P. Koskinen, Quantum simulations of one-dimensional nanostructures under arbitrary deformations, Physical Review Applied 6 (3) (2016) 034014.

[65] M. Hammermesh, Group Theory and Its Application to Physical Problems, 1st Edition, Dover, 1989.

[66] R. McWeeny, Symmetry:An Introduction to Group Theory and Its Applications, 1st Edition, Dover, 2002.

[67] G. B. Folland, A Course in Abstract Harmonic Analysis, 1st Edition, Studies in Advanced Mathematics, Taylor & Francis, 1994.

[68] A. O. Barut, R. Raczka, Theory of Group Representations and Applications, second revised Edition, World Scientific Publishing Company, 1986.

[69] S. Ghosh, P. Suryanarayana, SPARC: Accurate and efficient finite-difference formulation and parallel implementation of density functional theory: Isolated clusters, Computer Physics Communications 212 (2017) 189–204.

[70] S. Ghosh, P. Suryanarayana, SPARC: Accurate and efficient finite-difference formulation and parallel implementation of density functional theory: Extended systems, Computer Physics Communications 216 (2017) 109–125.

[71] N. Troullier, J. L. Martins, Efficient pseudopotentials for plane-wave calculations, Physical review B 43 (3) (1991) 1993.

[72] W. Kohn, L. J. Sham, Self-consistent equations including exchange and correlation effects, Physical Review 140 (4A) (1965) 1133–1138.

[73] J. P. Perdew, K. Burke, M. Ernzerhof, Generalized gradient approximation made simple, Phys. Rev. Lett. 77 (1996) 3865–3868.

[74] L. Kleinman, D. Bylander, Efficacious form for model pseudopotentials, Physical Review Letters 48 (20) (1982) 1425.

[75] P. Suryanarayana, D. Phanish, Augmented lagrangian formulation of orbital-free density functional theory, Journal of Computational Physics 275 (2014) 524–538.

[76] J. E. Pask, P. A. Sterne, Real-space formulation of the electrostatic potential and total energy of solids, Phys. Rev. B 71 (2005) 113101.

[77] P. Motamarri, M. Iyer, J. Knap, V. Gavini, Higher-order adaptive finite-element methods for orbital-free density functional theory, Journal of Computational Physics 231 (20) (2012) 6596–6621.

[78] I. Nikiforov, B. Hourahine, B. Aradi, T. Frauenheim, T. Dumitrică, Ewald summation on a helix: A route to self-consistent charge density-functional based tight-binding objective molecular dynamics, The Journal of Chemical Physics 139 (9) (2013) 094110.

[79] J. Harris, Simplified method for calculating the energy of weakly interacting fragments, Physical Review B 31 (4) (1985) 1770.

[80] W. M. C. Foulkes, R. Haydock, Tight-binding models and density-functional theory, Physical review B 39 (17) (1989) 12520.

[81] M. Defranceschi, C. Le Bris, Computing a molecule: A mathematical viewpoint, Journal of Mathematical Chemistry 21 (1) (1997) 1–30.

[82] E. B. Tadmor, R. E. Miller, Modeling Materials: Continuum, Atomistic and Multiscale Techniques, Cambridge University Press, 2011.

[83] E. B. Tadmor, R. E. Miller, R. S. Elliott, Continuum mechanics and thermodynamics: from fundamental concepts to governing equations, Cambridge University Press, 2012.

[84] E. Prodan, W. Kohn, Nearsightedness of electronic matter, Proceedings of the National Academy of Sciences of the United States of America 102 (33) (2005) 11635–11638.

[85] P. Motamarri, M. Nowak, K. Leiter, J. Knap, V. Gavini, Higher-order adaptive finite-element methods for Kohn-Sham density functional theory, Journal of Computational Physics 253 (2013) 308–343.

[86] A. S. Banerjee, L. Lin, P. Suryanarayana, C. Yang, J. E. Pask, Two-level chebyshev filter based complementary subspace method: pushing the envelope of large-scale electronic structure calculations, Journal of chemical theory and computation 14 (6) (2018) 2930–2946.

[87] J. R. Chelikowsky, N. Troullier, Y. Saad, Finite-difference-pseudopotential method: Electronic structure calculations without a basis, Physical review letters 72 (8) (1994) 1240.

[88] J. R. Chelikowsky, N. Troullier, K. Wu, Y. Saad, Higher order finite difference pseudopotential method: An application to diatomic molecules, Phys. Rev. B 50 (1994) 11355–11364.

[89] X. Jing, N. Troullier, D. Dean, N. Binggeli, J. R. Chelikowsky, K. Wu, Y. Saad, Ab initio molecular-dynamics simulations of si clusters using the higher-order finite-difference-pseudopotential method, Physical Review B 50 (16) (1994) 12234–12237.

[90] H. Kikuji, O. Tomoya, F. Yoshitaka, T. Shigeru, First-principles calculations in real-space formalism: electronic configurations and transport properties of nanostructures, World Scientific, 2005.

[91] D. A. Mazziotti, Spectral difference methods for solving differential equations, Chemical physics letters 299 (5) (1999) 473–480.

[92] H. J. Monkhorst, J. D. Pack, Special points for brillouin-zone integrations, Physical review B 13 (12) (1976) 5188.

[93] I. I. Geru, Time-Reversal Symmetry, Springer, 2018.

[94] A. S. Banerjee, P. Suryanarayana, J. E. Pask, Periodic Pulay method for robust and efficient convergence acceleration of self-consistent field iterations, Chemical Physics Letters 647 (2016) 31–35.

[95] Y. Saad, M. H. Schultz, Gmres: A generalized minimal residual algorithm for solving nonsymmetric linear systems, SIAM Journal on scientific and statistical computing 7 (3) (1986) 856–869.

[96] Y. Saad, Iterative methods for sparse linear systems, 2nd Edition, SIAM, 2003.

[97] G. E. Forsythe, M. Malcolm, C. Moler, Computer methods for mathematical computations., Prentice-Hall series in automatic computation 259 (1977).

[98] F. Gygi, G. Galli, Real-space adaptive-coordinate electronic-structure calculations, Physical Review B 52 (4) (1995) R2229.

[99] Y. Zhou, J. R. Chelikowsky, Y. Saad, Chebyshev-filtered subspace iteration method free of sparse diagonalization for solving the kohn–sham equation, Journal of Computational Physics 274 (2014) 770–782.

[100] Y. Saad, A. Stathopoulos, J. Chelikowsky, K. Wu, S. Öğüt, Solution of large eigenvalue problems in electronic structure calculations, BIT Numerical Mathematics 36 (3) (1996) 563–578.

[101] Y. Saad, J. R. Chelikowsky, S. M. Shontz, Numerical methods for electronic structure calculations of materials, SIAM review 52 (1) (2010) 3–54.

[102] E. Vecharynski, C. Yang, F. Xue, Generalized preconditioned locally harmonic residual method for non-hermitian eigenproblems, SIAM Journal on Scientific Computing 38 (2015) A500—A527.

[103] Y. Zhou, Y. Saad, M. L. Tiago, J. R. Chelikowsky, Self-consistent-field calculations using Chebyshev-filtered subspace iteration, Journal of Computational Physics 219 (2006) 172–184.

[104] Y. Zhou, Y. Saad, M. L. Tiago, J. R. Chelikowsky, Parallel self-consistent-field calculations via Chebyshev-filtered subspace acceleration, Phys. Rev. E 74 (2006) 066704.

[105] MATLAB, 9.7.0.1190202 (R2019b), the MathWorks Inc., Natick, Massachusetts (2019).

[106] E. Bitzek, P. Koskinen, F. Gähler, M. Moseler, P. Gumbsch, Structural relaxation made simple, Physical Review Letters 97 (17) (2006) 170201.

[107] L. Verlet, Computer" experiments" on classical fluids. i. thermodynamical properties of lennard-jones molecules, Physical review 159 (1) (1967) 98.

[108] J. P. Perdew, Y. Wang, Accurate and simple analytic representation of the electron-gas correlation energy, Physical Review B 45 (1992) 13244–13249.

[109] G. W. Stewart, A krylov–schur algorithm for large eigenproblems, SIAM Journal on Matrix Analysis and Applications 23 (3) (2002) 601–614.

[110] R. A. Èvarestov, Theoretical modeling of inorganic nanostructures: Symmetry and ab-initio calculations of nanolayers, nanotubes and nanowires, Springer, 2015.

[111] A. Molle, J. Goldberger, M. Houssa, Y. Xu, S.-C. Zhang, D. Akinwande, Buckled two-dimensional xene sheets, Nature materials 16 (2) (2017) 163.

[112] Z. Ni, Q. Liu, K. Tang, J. Zheng, J. Zhou, R. Qin, Z. Gao, D. Yu, J. Lu, Tunable bandgap in silicene and germanene, Nano letters 12 (1) (2011) 113–118.

[113] N. Drummond, V. Zolyomi, V. Fal'Ko, Electrically tunable band gap in silicene, Physical Review B 85 (7) (2012) 075423.

[114] S. Balendhran, S. Walia, H. Nili, S. Sriram, M. Bhaskaran, Elemental analogues of graphene: silicene, germanene, stanene, and phosphorene, small 11 (6) (2015) 640–652.

[115] F.-f. Zhu, W.-j. Chen, Y. Xu, C.-l. Gao, D.-d. Guan, C.-h. Liu, D. Qian, S.-C. Zhang, J.-f. Jia, Epitaxial growth of two-dimensional stanene, Nature materials 14 (10) (2015) 1020.

[116] E. Scalise, Vibrational properties of silicene and germanene, in: Vibrational Properties of Defective Oxides and 2D Nanolattices, Springer, 2014, pp. 61–93.

[117] M. Dávila, L. Xian, S. Cahangirov, A. Rubio, G. Le Lay, Germanene: a novel two-dimensional germanium allotrope akin to graphene and silicene, New Journal of Physics 16 (9) (2014) 095002.

[118] A. Kara, H. Enriquez, A. P. Seitsonen, L. L. Y. Voon, S. Vizzini, B. Aufray, H. Oughaddou, A review on silicene—new candidate for electronics, Surface science reports 67 (1) (2012) 1–18.

[119] R. Martel, T. Schmidt, H. Shea, T. Hertel, P. Avouris, Single-and multi-wall carbon nanotube field-effect transistors, Applied physics letters 73 (17) (1998) 2447–2449.

[120] A. Javey, J. Guo, Q. Wang, M. Lundstrom, H. Dai, Ballistic carbon nanotube field-effect transistors, nature 424 (6949) (2003) 654–657.

[121] V. N. Popov, Carbon nanotubes: properties and application, Materials Science and Engineering: R: Reports 43 (3) (2004) 61–102.

[122] K. Gong, F. Du, Z. Xia, M. Durstock, L. Dai, Nitrogen-doped carbon nanotube arrays with high electrocatalytic activity for oxygen reduction, science 323 (5915) (2009) 760–764.

[123] M.-H. Park, M. G. Kim, J. Joo, K. Kim, J. Kim, S. Ahn, Y. Cui, J. Cho, Silicon nanotube battery anodes, Nano letters 9 (11) (2009) 3844–3847.

[124] H. Wu, G. Chan, J. W. Choi, I. Ryu, Y. Yao, M. T. McDowell, S. W. Lee, A. Jackson, Y. Yang, L. Hu, et al., Stable cycling of double-walled silicon nanotube battery anodes through solid–electrolyte interphase control, Nature nanotechnology 7 (5) (2012) 310–315.

[125] M.-H. Park, Y. Cho, K. Kim, J. Kim, M. Liu, J. Cho, Germanium nanotubes prepared by using the kirkendall effect as anodes for high-rate lithium batteries, Angewandte Chemie International Edition 50 (41) (2011) 9647–9650.

[126] X. Li, G. Meng, Q. Xu, M. Kong, X. Zhu, Z. Chu, A.-P. Li, Controlled synthesis of germanium nanowires and nanotubes with variable morphologies and sizes, Nano letters 11 (4) (2011) 1704–1709.

[127] L. Zhao, M. Yosef, M. Steinhart, P. Göring, H. Hofmeister, U. Gösele, S. Schlecht, Porous silicon and alumina as chemically reactive templates for the synthesis of tubes and wires of snse, sn, and sno2, Angewandte Chemie International Edition 45 (2) (2006) 311–315.

[128] M. Xu, T. Liang, M. Shi, H. Chen, Graphene-like two-dimensional materials, Chemical reviews 113 (5) (2013) 3766–3798.

[129] G. R. Bhimanapati, Z. Lin, V. Meunier, Y. Jung, J. Cha, S. Das, D. Xiao, Y. Son, M. S. Strano, V. R. Cooper, et al., Recent advances in two-dimensional materials beyond graphene, ACS nano 9 (12) (2015) 11509–11539.

[130] S. Z. Butler, S. M. Hollen, L. Cao, Y. Cui, J. A. Gupta, H. R. Gutiérrez, T. F. Heinz, S. S. Hong, J. Huang, A. F. Ismach, et al., Progress, challenges, and opportunities in two-dimensional materials beyond graphene, ACS nano 7 (4) (2013) 2898–2926.

[131] M. Naguib, V. N. Mochalin, M. W. Barsoum, Y. Gogotsi, 25th anniversary article: Mxenes: a new family of two-dimensional materials, Advanced materials 26 (7) (2014) 992–1005.

[132] G. Fiori, F. Bonaccorso, G. Iannaccone, T. Palacios, D. Neumaier, A. Seabaugh, S. K. Banerjee, L. Colombo, Electronics based on two-dimensional materials, Nature nanotechnology 9 (10) (2014) 768–779.

[133] F. Koppens, T. Mueller, P. Avouris, A. Ferrari, M. Vitiello, M. Polini, Photodetectors based on graphene, other two-dimensional materials and hybrid systems, Nature nanotechnology 9 (10) (2014) 780–793.

[134] K. S. Novoselov, A. K. Geim, S. V. Morozov, D. Jiang, Y. Zhang, S. V. Dubonos, I. V. Grigorieva, A. A. Firsov, Electric field effect in atomically thin carbon films, science 306 (5696) (2004) 666–669.

[135] K. Novoselov, D. Jiang, F. Schedin, T. Booth, V. Khotkevich, S. Morozov, A. Geim, Two dimensional atomic crystals, Proceedings of the National Academy of Sciences 102 (30) (2005) 10451–10453.

[136] A. K. Geim, Graphene: status and prospects, science 324 (5934) (2009) 1530–1534.

[137] S. Iijima, T. Ichihashi, Single-shell carbon nanotubes of 1-nm diameter, nature 363 (6430) (1993) 603.

[138] R. Saito, G. Dresselhaus, M. S. Dresselhaus, Physical properties of carbon nanotubes, World Scientific, 1998.

[139] J. Sha, J. Niu, X. Ma, J. Xu, X. Zhang, Q. Yang, D. Yang, Silicon nanotubes, Advanced Materials 14 (17) (2002) 1219–1221.

[140] C. Wang, X. Fu, Y. Guo, Z. Guo, C. Xia, Y. Jia, Band gap scaling laws in group iv nanotubes, Nanotechnology 28 (11) (2017) 115202.

[141] X. Blase, L. X. Benedict, E. L. Shirley, S. G. Louie, Hybridization effects and metallicity in small radius carbon nanotubes, Physical review letters 72 (12) (1994) 1878.

[142] C. D. Spataru, S. Ismail-Beigi, L. X. Benedict, S. G. Louie, Excitonic effects and optical spectra of single-walled carbon nanotubes, Physical Review Letters 92 (7) (2004) 077402.

[143] L. Yang, J. Han, Electronic structure of deformed carbon nanotubes, Physical review letters 85 (1) (2000) 154.

[144] S. B. Fagan, R. Baierle, R. Mota, A. J. da Silva, A. Fazzio, Ab initio calculations for a hypothetical material: Silicon nanotubes, Physical Review B 61 (15) (2000) 9994.

[145] L. X. Benedict, S. G. Louie, M. L. Cohen, Static polarizabilities of single-wall carbon nanotubes, Physical Review B 52 (11) (1995) 8541.

[146] M. e. Zhang, Y. Kan, Q. Zang, Z. Su, R. Wang, Why silicon nanotubes stably exist in armchair structure?, Chemical physics letters 379 (1-2) (2003) 81–86.

[147] X. Yang, J. Ni, Electronic properties of single-walled silicon nanotubes compared to carbon nanotubes, Physical Review B 72 (19) (2005) 195426.

[148] G. Giovannetti, P. A. Khomyakov, G. Brocks, V. v. Karpan, J. van den Brink, P. J. Kelly, Doping graphene with metal contacts, Physical review letters 101 (2) (2008) 026803.

[149] P. Vogt, P. De Padova, C. Quaresima, J. Avila, E. Frantzeskakis, M. C. Asensio, A. Resta, B. Ealet, G. Le Lay, Silicene: compelling experimental evidence for graphene-like two-dimensional silicon, Physical review letters 108 (15) (2012) 155501.

[150] G. Seifert, T. Köhler, Z. Hajnal, T. Frauenheim, Tubular structures of germanium, Solid state communications 119 (12) (2001) 653–657.

[151] J. Ding, X. Yan, J. Cao, Analytical relation of band gaps to both chirality and diameter of single-wall carbon nanotubes, Physical Review B 66 (7) (2002) 073401.

[152] Z. Najafi, A. Ahmadkhan Kordbacheh, M. Afshar, Analysis of cooperative effects between uniaxial and torsional strains in carbon nanotubes, Journal of Applied Physics 119 (24) (2016) 244303.

[153] J. Ding, X. Yan, J. Cao, D. Wang, Y. Tang, Q. Yang, Curvature and strain effects on electronic properties of single-wall carbon nanotubes, Journal of Physics: Condensed Matter 15 (27) (2003) L439.

[154] S. Sreekala, X.-H. Peng, P. Ajayan, S. Nayak, Effect of strain on the band gap and effective mass of zigzag single-wall carbon nanotubes: First-principles density-functional calculations, Physical Review B 77 (15) (2008) 155434.

[155] A. Rochefort, P. Avouris, F. Lesage, D. R. Salahub, Electrical and mechanical properties of distorted carbon nanotubes, Physical Review B 60 (19) (1999) 13824.

[156] R. Heyd, A. Charlier, E. McRae, Uniaxial-stress effects on the electronic properties of carbon nanotubes, Physical Review B 55 (11) (1997) 6820.

[157] C. L. Kane, E. Mele, Size, shape, and low energy electronic structure of carbon nanotubes, Physical Review Letters 78 (10) (1997) 1932.

[158] A. Abbasi, J. Jahanbin Sardroodi, Structural and electronic properties of group-iv tin nanotubes and their effects on the adsorption of so2 molecules: insights from dft computations, Journal of Applied Physics 124 (16) (2018) 165302.

[159] A. Abbasi, A. Khataee, Band gap tunability and structural stability of metal/nonmetal codoped group-iv tin nanotubes: effect of spin-orbit coupling, Physica E: Low-dimensional Systems and Nanostructures 114 (2019) 113644.

[160] A. Abbasi, J. J. Sardroodi, A. R. Ebrahimzadeh, M. Yaghoobi, Theoretical study of the structural and electronic properties of novel stanene-based buckled nanotubes and their adsorption behaviors, Applied Surface Science 435 (2018) 733–742.

[161] X. Gonze, F. Jollet, F. A. Araujo, D. Adams, B. Amadon, T. Applencourt, C. Audouze, J.-M. Beuken, J. Bieder, A. Bokhanchuk, et al., Recent developments in the abinit software package, Computer Physics Communications 205 (2016) 106–131.

[162] T. Minka, The lightspeed matlab toolbox, https://github.com/tminka/lightspeed.

[163] Intel Corporation, APP metrics for the Intel®microporcessors., https://www.intel.com/content/dam/support/us/en/documents/processors/APP-for-Intel-Xeon-Processors.pdf.

[164] William Gropp, Lecture 4: Modeling sparse matrix-vector multiply, https://wgropp.cs.illinois.edu/courses/cs598-s15/lectures/lecture04.pdf.

[165] S. Timoshenko, D. H. Young, Elements of strength of materials, Van Nostrand Princeton, NJ, 1968.

[166] J. Tersoff, New empirical approach for the structure and energy of covalent systems, Physical review B 37 (12) (1988) 6991.

[167] T. W. Odom, J.-L. Huang, P. Kim, C. M. Lieber, Structure and electronic properties of carbon nanotubes, The Journal of Physical Chemistry B 104 (13) (2000) 2794–2809.

[168] M. Ouyang, J.-L. Huang, C. M. Lieber, Fundamental electronic properties and applications of single-walled carbon nanotubes, Accounts of chemical research 35 (12) (2002) 1018–1025.

[169] M. Ouyang, J.-L. Huang, C. L. Cheung, C. M. Lieber, Energy gaps in" metallic" single-walled carbon nanotubes, Science 292 (5517) (2001) 702–705.

[170] S. Agarwal, A. S. Banerjee, Solution of the Schrödinger equation for quasi-one-dimensional materials using helical waves, (in preparation) (2021).

[171] S. Agarwal, A. Banerjee, A spectral scheme for kohn-sham density functional theory of helical structures, Bulletin of the American Physical Society (2021).

[172] K. Novoselov, A. Morozov, et. al., Two-dimensional gas of massless dirac fermions in graphene, Nature 438 (7065) (2005) 197–200.
URL https://doi.org/10.1038/nature04233

[173] L. Balents, C. R. Dean, D. K. Efetov, A. F. Young, Superconductivity and strong correlations in moiré flat bands, Nature Physics 16 (7) (2020) 725–733.

[174] J.-X. Yin, S. S. Zhang, G. Chang, Q. Wang, S. S. Tsirkin, Z. Guguchia, B. Lian, H. Zhou, K. Jiang, I. Belopolski, et al., Negative flat band magnetism in a spin–orbit-coupled correlated kagome magnet, Nature Physics 15 (5) (2019) 443–448.

[175] O. Derzhko, J. Richter, M. Maksymenko, Strongly correlated flat-band systems: The route from heisenberg spins to hubbard electrons, International Journal of Modern Physics B 29 (12) (2015) 1530007.

[176] C. Elias, G. Fugallo, P. Valvin, C. L'Henoret, J. Li, J. Edgar, F. Sottile, M. Lazzeri, A. Ouerghi, B. Gil, et al., Flat bands and giant light-matter interaction in hexagonal boron nitride, Physical Review Letters 127 (13) (2021) 137401.

[177] V. Iglovikov, F. Hébert, B. Grémaud, G. Batrouni, R. Scalettar, Superconducting transitions in flat-band systems, Physical Review B 90 (9) (2014) 094506.

[178] R. Pons, A. Mielke, T. Stauber, Flat-band ferromagnetism in twisted bilayer graphene, Physical Review B 102 (23) (2020) 235101.

[179] C. Wu, D. Bergman, L. Balents, S. D. Sarma, Flat bands and wigner crystallization in the honeycomb optical lattice, Physical review letters 99 (7) (2007) 070401.

[180] M. Shayegan, Wigner crystals in flat band 2d electron systems, Nature Reviews Physics 4 (4) (2022) 212–213.

[181] Y.-F. Wang, H. Yao, C.-D. Gong, D. Sheng, Fractional quantum hall effect in topological flat bands with chern number two, Physical Review B 86 (20) (2012) 201101.

[182] E. Tang, J.-W. Mei, X.-G. Wen, High-temperature fractional quantum hall states, Physical review letters 106 (23) (2011) 236802.

[183] K. Sun, Z. Gu, H. Katsura, S. D. Sarma, Nearly flatbands with nontrivial topology, Physical review letters 106 (23) (2011) 236803.

[184] T. Neupert, L. Santos, C. Chamon, C. Mudry, Fractional quantum hall states at zero magnetic field, Physical review letters 106 (23) (2011) 236804.

[185] E. Y. Andrei, D. K. Efetov, P. Jarillo-Herrero, A. H. MacDonald, K. F. Mak, T. Senthil, E. Tutuc, A. Yazdani, A. F. Young, The marvels of moiré materials, Nature Reviews Materials 6 (3) (2021) 201–206.

[186] L. Wang, E.-M. Shih, A. Ghiotto, L. Xian, D. A. Rhodes, C. Tan, M. Claassen, D. M. Kennes, Y. Bai, B. Kim, et al., Correlated electronic phases in twisted bilayer transition metal dichalcogenides, Nature materials 19 (8) (2020) 861–866.

[187] Y. Choi, H. Kim, Y. Peng, A. Thomson, C. Lewandowski, R. Polski, Y. Zhang, H. S. Arora, K. Watanabe, T. Taniguchi, et al., Correlation-driven topological phases in magic-angle twisted bilayer graphene, Nature 589 (7843) (2021) 536–541.

[188] D. Leykam, A. Andreanov, S. Flach, Artificial flat band systems: from lattice models to experiments, Advances in Physics: X 3 (1) (2018) 1473052. doi:10.1080/23746149.2018.1473052.
URL http://dx.doi.org/10.1080/23746149.2018.1473052

[189] M. N. Huda, S. Kezilebieke, P. Liljeroth, Designer flat bands in quasi-one-dimensional atomic lattices, Physical Review Research 2 (4) (2020) 043426. doi:10.1103/physrevresearch.2.043426.
URL http://dx.doi.org/10.1103/PhysRevResearch.2.043426

[190] X. Li, Q. Li, T. Ji, R. Yan, W. Fan, B. Miao, L. Sun, G. Chen, W. Zhang, H. Ding, Lieb lattices formed by real atoms on ag (111) and their lattice constant-dependent electronic properties, Chinese Physics Letters 39 (5) (2022) 057301.

[191] C. Barreteau, F. Ducastelle, T. Mallah, A bird's eye view on the flat and conic band world of the honeycomb and kagome lattices: towards an understanding of 2d metal-organic frameworks electronic structure, Journal of Physics: Condensed Matter 29 (46) (2017) 465302. doi:10.1088/1361-648x/aa8fec.
URL https://doi.org/10.1088/1361-648x/aa8fec

[192] G. Tarnopolsky, A. J. Kruchkov, A. Vishwanath, Origin of magic angles in twisted bilayer graphene, Physical review letters 122 (10) (2019) 106405.

[193] C. Naud, G. Faini, D. Mailly, Aharonov-bohm cages in 2d normal metal networks, Physical Review Letters 86 (22) (2001) 5104.

[194] J. Vidal, R. Mosseri, B. Douçot, Aharonov-bohm cages in two-dimensional structures, Physical review letters 81 (26) (1998) 5888.

[195] B. R. Ortiz, L. C. Gomes, J. R. Morey, M. Winiarski, M. Bordelon, J. S. Mangum, I. W. Oswald, J. A. Rodriguez-Rivera, J. R. Neilson, S. D. Wilson, et al., New kagome prototype materials: discovery of kv 3 sb 5, rbv 3 sb 5, and csv 3 sb 5, Physical Review Materials 3 (9) (2019) 094407.

[196] M. Li, Q. Wang, G. Wang, Z. Yuan, W. Song, R. Lou, Z. Liu, Y. Huang, Z. Liu, H. Lei, et al., Dirac cone, flat band and saddle point in kagome magnet ymn6sn6, Nature communications 12 (1) (2021) 1–8.

[197] M. Kang, L. Ye, S. Fang, J.-S. You, A. Levitan, M. Han, J. I. Facio, C. Jozwiak, A. Bostwick, E. Rotenberg, et al., Dirac fermions and flat bands in the ideal kagome metal fesn, Nature materials 19 (2) (2020) 163–169.

[198] E. Liu, Y. Sun, N. Kumar, L. Muechler, A. Sun, L. Jiao, S.-Y. Yang, D. Liu, A. Liang, Q. Xu, et al., Giant anomalous hall effect in a ferromagnetic kagome-lattice semimetal, Nature physics 14 (11) (2018) 1125–1131.

[199] D. Liu, A. Liang, E. Liu, Q. Xu, Y. Li, C. Chen, D. Pei, W. Shi, S. Mo, P. Dudin, et al., Magnetic weyl semimetal phase in a kagomé crystal, Science 365 (6459) (2019) 1282–1285.

[200] T. Neupert, M. M. Denner, J.-X. Yin, R. Thomale, M. Z. Hasan, Charge order and superconductivity in kagome materials, Nature Physics 18 (2) (2022) 137–143.

[201] Y.-X. Jiang, J.-X. Yin, M. M. Denner, N. Shumiya, B. R. Ortiz, G. Xu, Z. Guguchia, J. He, M. S. Hossain, X. Liu, et al., Unconventional chiral charge order in kagome superconductor kv3sb5, Nature Materials 20 (10) (2021) 1353–1357.

[202] T.-H. Han, M. Norman, J.-J. Wen, J. A. Rodriguez-Rivera, J. S. Helton, C. Broholm, Y. S. Lee, Correlated impurities and intrinsic spin-liquid physics in the kagome material herbertsmithite, Physical Review B 94 (6) (2016) 060409.

[203] H. Liu, S. Meng, F. Liu, Screening two-dimensional materials with topological flat bands, Physical Review Materials 5 (8) (2021) 084203.

[204] C. Zhong, Y. Xie, Y. Chen, S. Zhang, Coexistence of flat bands and dirac bands in a carbon-kagome-lattice family, Carbon 99 (2016) 65–70. doi:https://doi.org/10.1016/j.carbon.2015.11.073.
URL https://www.sciencedirect.com/science/article/pii/S0008622315304814

[205] C. Zhong, Y. Xie, Y. Chen, S. Zhang, Coexistence of flat bands and dirac bands in a carbon-kagome-lattice family, Carbon 99 (2016) 65–70.

[206] O. Leenaerts, B. Schoeters, B. Partoens, Stable kagome lattices from group IV elements, Phys. Rev. B 91 (2015) 115202. doi:10.1103/PhysRevB.91.115202.
URL https://link.aps.org/doi/10.1103/PhysRevB.91.115202

[207] Y. Chen, S. Xu, Y. Xie, C. Zhong, C. Wu, S. B. Zhang, Ferromagnetism and wigner crystallization in kagome graphene and related structures, Phys. Rev. B 98 (2018) 035135. doi:10.1103/PhysRevB.98.035135.

[208] D. M. Kennes, L. Xian, M. Claassen, A. Rubio, One-dimensional flat bands in twisted bilayer germanium selenide, Nature communications 11 (1) (2020) 1–8.

[209] Y. Li, Q. Yuan, D. Guo, C. Lou, X. Cui, G. Mei, H. Petek, L. Cao, W. Ji, M. Feng, One-

dimensional electronic flat bands in untwisted moiré superlattices, Advanced Materials (2023) 2300572.

[210] G. R. Schleder, M. Pizzochero, E. Kaxiras, One-dimensional moir\'e physics and chemistry in heterostrained bilayer graphene, arXiv preprint arXiv:2306.09799 (2023).

[211] P. C. Hohenberg, Existence of long-range order in one and two dimensions, Phys. Rev. 158 (1967) 383–386. doi:10.1103/PhysRev.158.383.
URL https://link.aps.org/doi/10.1103/PhysRev.158.383

[212] N. D. Mermin, H. Wagner, Absence of ferromagnetism or antiferromagnetism in one-or two-dimensional isotropic heisenberg models, Physical Review Letters 17 (22) (1966) 1133.

[213] K. Arutyunov, D. Golubev, A. Zaikin, Superconductivity in one dimension, Physics Reports 464 (1-2) (2008) 1–70. doi:10.1016/j.physrep.2008.04.009.
URL https://doi.org/10.1016%2Fj.physrep.2008.04.009

[214] R. Martin, L. Reining, D. Ceperly, Interacting Electrons: Theory and Computational Approaches, Cambridge University Press, 2016.

[215] J. M. Kim, M. F. Haque, E. Y. Hsieh, S. M. Nahid, I. Zarin, K.-Y. Jeong, J.-P. So, H.-G. Park, S. Nam, Strain engineering of low-dimensional materials for emerging quantum phenomena and functionalities, Advanced Materials (2022) 2107362.

[216] C. D. Aiello, M. Abbas, J. Abendroth, A. S. Banerjee, D. Beratan, J. Belling, B. Berche, A. Botana, J. R. Caram, L. Celardo, et al., A chirality-based quantum leap: A forward-looking review, arXiv preprint arXiv:2009.00136 (2020) 4989–5035.

[217] R. Naaman, D. H. Waldeck, Spintronics and chirality: Spin selectivity in electron transport through chiral molecules, Annual review of physical chemistry 66 (2015) 263–281.

[218] R. Nakajima, D. Hirobe, G. Kawaguchi, Y. Nabei, T. Sato, T. Narushima, H. Okamoto, H. Yamamoto, Giant spin polarization and a pair of antiparallel spins in a chiral superconductor, Nature 613 (7944) (2023) 479–484.

[219] J. Linder, J. W. Robinson, Superconducting spintronics, Nature Physics 11 (4) (2015) 307–315.

[220] A. Sidorenko, Functional nanostructures and metamaterials for superconducting spintronics, Cham, Switzerland: Springer International Publishing (2018).

[221] F. Qin, W. Shi, T. Ideue, M. Yoshida, A. Zak, R. Tenne, T. Kikitsu, D. Inoue, D. Hashizume, Y. Iwasa, Superconductivity in a chiral nanotube, Nature communications 8 (1) (2017) 1–6.

[222] A. Hirsch, The era of carbon allotropes, Nature materials 9 (11) (2010) 868–871.

[223] R.-S. Zhang, J.-W. Jiang, The art of designing carbon allotropes, Frontiers of Physics 14 (1) (2019) 1–17.

[224] R. Hoffmann, A. A. Kabanov, A. A. Golov, D. M. Proserpio, Homo citans and carbon allotropes: For an ethics of citation, Angewandte Chemie International Edition 55 (37) (2016) 10962–10976.

[225] Z. Li, Y. Xie, Y. Chen, Three-dimensional kagome graphene networks and their topological properties, Computational Materials Science 173 (2020) 109406.

[226] Z. Wang, X.-F. Zhou, X. Zhang, Q. Zhu, H. Dong, M. Zhao, A. R. Oganov, Phagraphene: a low-energy graphene allotrope composed of 5–6–7 carbon rings with distorted dirac cones, Nano letters 15 (9) (2015) 6182–6186.

[227] Y. Chen, Y. Xie, X. Yan, M. L. Cohen, S. Zhang, Topological carbon materials: A new perspective, Physics Reports 868 (2020) 1–32.

[228] P. Yan, T. Ouyang, C. He, J. Li, C. Zhang, C. Tang, J. Zhong, Newly discovered graphyne allotrope with rare and robust dirac node loop, Nanoscale 13 (6) (2021) 3564–3571.

[229] J.-Y. You, B. Gu, G. Su, Flat band and hole-induced ferromagnetism in a novel carbon monolayer, Scientific Reports 9 (1) (2019) 1–7. doi:https://doi.org/10.1038/s41598-019-56738-8.

[230] X. Shi, S. Li, J. Li, T. Ouyang, C. Zhang, C. Tang, C. He, J. Zhong, High-throughput screening of two-dimensional planar sp2 carbon space associated with a labeled quotient graph, The Journal of Physical Chemistry Letters 12 (47) (2021) 11511–11519.

[231] M. Zhou, Z. Liu, W. Ming, Z. Wang, F. Liu, s d 2 graphene: Kagome band in a hexagonal lattice, Physical review letters 113 (23) (2014) 236802.

[232] M. Maruyama, S. Okada, Interplay between the kagome flat band and the dirac cone in porous graphitic networks, Carbon 125 (2017) 530–535.

[233] K. Wakabayashi, M. Fujita, H. Ajiki, M. Sigrist, Electronic and magnetic properties of nanographite ribbons, Physical Review B 59 (12) (1999) 8271.

[234] Y.-W. Son, M. L. Cohen, S. G. Louie, Energy gaps in graphene nanoribbons, Physical review letters 97 (21) (2006) 216803.

[235] S. Yu, W. Zheng, Q. Wen, Q. Jiang, First principle calculations of the electronic properties of nitrogen-doped carbon nanoribbons with zigzag edges, Carbon 46 (3) (2008) 537–543.

[236] J. Zhang, R. Wang, X. Zhu, A. Pan, C. Han, X. Li, D. Zhao, C. Ma, W. Wang, H. Su, C. Niu, Pseudo-topotactic conversion of carbon nanotubes to t-carbon nanowires under picosecond laser irradiation in methanol, Nature Communications 8 (1) (2017) 683.

doi:10.1038/s41467-017-00817-9.
URL https://doi.org/10.1038/s41467-017-00817-9

[237] V. R. Coluci, S. F. Braga, S. B. Legoas, D. S. Galvão, R. H. Baughman, Families of carbon nanotubes: Graphyne-based nanotubes, Phys. Rev. B 68 (2003) 035430. doi:10.1103/PhysRevB.68.035430.
URL https://link.aps.org/doi/10.1103/PhysRevB.68.035430

[238] V. Coluci, S. Braga, S. Legoas, D. Galvao, R. Baughman, New families of carbon nanotubes based on graphyne motifs, Nanotechnology 15 (4) (2004) S142.

[239] B. Kang, J. Y. Lee, Electronic properties of alpha-graphyne nanotubes, Carbon 84 (2015) 246–253. doi:https://doi.org/10.1016/j.carbon.2014.12.002.
URL https://www.sciencedirect.com/science/article/pii/S000862231401152X

[240] V. Coluci, D. Galvao, R. Baughman, Theoretical investigation of electromechanical effects for graphyne carbon nanotubes, The Journal of chemical physics 121 (7) (2004) 3228–3237.

[241] B. Kang, J. H. Moon, J. Y. Lee, Size dependent electronic band structures of beta- and gamma-graphyne nanotubes, RSC Adv. 5 (2015) 80118–80121. doi:10.1039/C5RA12188D.
URL http://dx.doi.org/10.1039/C5RA12188D

[242] D.-C. Yang, R. Jia, Y. Wang, C.-P. Kong, J. Wang, Y. Ma, R. I. Eglitis, H.-X. Zhang, Novel carbon nanotubes rolled from 6, 6, 12-graphyne: Double dirac points in 1d material, The Journal of Physical Chemistry C 121 (27) (2017) 14835–14844.

[243] K. Wakabayashi, Y. Takane, M. Yamamoto, M. Sigrist, Electronic transport properties of graphene nanoribbons, New Journal of Physics 11 (9) (2009) 095016.

[244] X. Yang, G. Wu, Itinerant flat-band magnetism in hydrogenated carbon nanotubes, ACS nano 3 (7) (2009) 1646–1650.

[245] O. Arroyo-Gascón, R. Fernández-Perea, E. Suárez Morell, C. Cabrillo, L. Chico, One-dimensional moiré superlattices and flat bands in collapsed chiral carbon nanotubes, Nano Letters 20 (10) (2020) 7588–7593, pMID: 32870695. arXiv:https://doi.org/10.1021/acs.nanolett.0c03091, doi:10.1021/acs.nanolett.0c03091.
URL https://doi.org/10.1021/acs.nanolett.0c03091

[246] O. Arroyo-Gascón, R. Fernández-Perea, E. S. Morell, C. Cabrillo, L. Chico, Universality of moiré physics in collapsed chiral carbon nanotubes, Carbon 205 (2023) 394–401.

[247] M. Koshino, P. Moon, Y.-W. Son, Incommensurate double-walled carbon nanotubes as one-dimensional moiré crystals, Physical Review B 91 (3) (2015) 035405.

[248] Z. Liu, F. Liu, Y.-S. Wu, Exotic electronic states in the world of flat bands: From theory to material, Chinese Physics B 23 (7) (2014) 077308. doi:10.1088/1674-1056/23/7/077308.
URL https://doi.org/10.1088/1674-1056/23/7/077308

[249] T. Wavrunek, Q. Peng, N. Abu-Zahra, Mechanical properties and buckling of kagome graphene under tension: A molecular dynamics study, Crystals 12 (2) (2022) 292.

[250] A. Rüegg, J. Wen, G. A. Fiete, Topological insulators on the decorated honeycomb lattice, Physical Review B 81 (20) (2010) 205115.

[251] M. F. López, J. Merino, Magnetism and topological phases in an interacting decorated honeycomb lattice with spin-orbit coupling, Physical Review B 102 (3) (2020) 035157.

[252] M. F. López, B. J. Powell, J. Merino, Topological superconductivity from doping a triplet quantum spin liquid in a flat-band system, Physical Review B 106 (23) (2022) 235129.

[253] J. Merino, M. F. López, B. J. Powell, Unconventional superconductivity near a flat band in organic and organometallic materials, Physical Review B 103 (9) (2021) 094517.

[254] M. Chen, H.-Y. Hui, S. Tewari, V. Scarola, Quantum anomalous hall state from spatially decaying interactions on the decorated honeycomb lattice, Physical Review B 97 (3) (2018) 035114.

[255] J.-W. Rhim, K. Kim, B.-J. Yang, Quantum distance and anomalous landau levels of flat bands, Nature 584 (7819) (2020) 59–63.

[256] R. Pawlak, X. Liu, S. Ninova, P. D'astolfo, C. Drechsel, J.-C. Liu, R. Häner, S. Decurtins, U. Aschauer, S.-X. Liu, et al., On-surface synthesis of nitrogen-doped kagome graphene, Angewandte Chemie 133 (15) (2021) 8451–8456.

[257] X. Li, D. Han, T. Qin, J. Xiong, J. Huang, T. Wang, H. Ding, J. Hu, Q. Xu, J. Zhu, Selective synthesis of kagome nanoporous graphene on ag (111) via an organometallic template, Nanoscale 14 (16) (2022) 6239–6247.

[258] A. Korde, B. Min, E. Kapaca, O. Knio, I. Nezam, Z. Wang, J. Leisen, X. Yin, X. Zhang, D. S. Sholl, et al., Single-walled zeolitic nanotubes, Science 375 (6576) (2022) 62–66.

[259] Y. Wang, K. Wan, F. Pan, X. Zhu, Y. Jiang, H. Wang, Y. Chen, X. Shi, M. Liu, Bamboo-like π-nanotubes with tunable helicity and circularly polarized luminescence, Angewandte Chemie 133 (30) (2021) 16751–16757.

[260] S. Agarwal, A. S. Banerjee, Solution of the schrodinger equation for quasi-one-dimensional materials using helical waves, arXiv preprint arXiv:2210.12252 (2022).

[261] G. Dresselhaus, M. S. Dresselhaus, S. Riichiro, Physical Properties of Carbon Nanotubes, World Scientific, 1998.

[262] A. H. Romero, D. C. Allan, B. Amadon, G. Antonius, T. Applencourt, L. Baguet, J. Bieder, F. Bottin, J. Bouchet, E. Bousquet, et al., Abinit: Overview and focus on selected capabilities, The Journal of chemical physics 152 (12) (2020) 124102.

[263] N. Troullier, J. L. Martins, Efficient pseudopotentials for plane-wave calculations, Physical Review B 43 (3) (1991) 1993.

[264] J. P. Perdew, K. Burke, M. Ernzerhof, Generalized gradient approximation made simple, Physical review letters 77 (18) (1996) 3865.

[265] A. Van de Walle, G. Ceder, Correcting overbinding in local-density-approximation calculations, Physical Review B 59 (23) (1999) 14992.

[266] N. Hamada, S.-i. Sawada, A. Oshiyama, New one-dimensional conductors: Graphitic microtubules, Phys. Rev. Lett. 68 (1992) 1579–1581. doi:10.1103/PhysRevLett.68.1579.
URL https://link.aps.org/doi/10.1103/PhysRevLett.68.1579

[267] S. B. Sinnott, R. Andrews, Carbon nanotubes: Synthesis, properties, and applications, Critical Reviews in Solid State and Materials Sciences 26 (3) (2001) 145–249. arXiv:https://doi.org/10.1080/20014091104189, doi:10.1080/20014091104189.
URL https://doi.org/10.1080/20014091104189

[268] S. Roy, V. Jain, R. Bajpai, P. Ghosh, A. Pente, B. Singh, D. Misra, Formation of carbon nanotube bucky paper and feasibility study for filtration at the nano and molecular scale, The Journal of Physical Chemistry C 116 (35) (2012) 19025–19031.

[269] B. Corry, Designing carbon nanotube membranes for efficient water desalination, The Journal of Physical Chemistry B 112 (5) (2008) 1427–1434.

[270] E. Frackowiak, F. Beguin, Electrochemical storage of energy in carbon nanotubes and nanostructured carbons, Carbon 40 (10) (2002) 1775–1787.

[271] E. Frackowiak, S. Gautier, H. Gaucher, S. Bonnamy, F. Beguin, Electrochemical storage of lithium in multiwalled carbon nanotubes, Carbon 37 (1) (1999) 61–69.

[272] C. Nützenadel, A. Züttel, D. Chartouni, L. Schlapbach, Electrochemical storage of hydrogen in nanotube materials, Electrochemical and solid-state letters 2 (1) (1998) 30.

[273] R. M. Martin, Electronic Structure: Basic Theory and Practical Methods, 1st Edition, Cambridge University Press, 2004.

[274] W. Hu, L. Lin, C. Yang, Dgdft: A massively parallel method for large scale density functional theory calculations, The Journal of chemical physics 143 (12) (2015) 124110.

[275] L. Lin, J. Lu, L. Ying, E. Weinan, Adaptive local basis set for kohn–sham density functional theory in a discontinuous galerkin framework i: Total energy calculation, Journal of Computational Physics 231 (4) (2012) 2140–2154.

[276] W. Jia, L.-W. Wang, L. Lin, Parallel transport time-dependent density functional theory calculations with hybrid functional on summit, in: Proceedings of the International Conference for High Performance Computing, Networking, Storage and Analysis, 2019, pp. 1–23.

[277] W. Hu, L. Lin, A. S. Banerjee, E. Vecharynski, C. Yang, Adaptively compressed exchange operator for large-scale hybrid density functional calculations with applications to the adsorption of water on silicene, Journal of chemical theory and computation 13 (3) (2017) 1188–1198.

[278] D. Hamann, Optimized norm-conserving vanderbilt pseudopotentials, Physical Review B 88 (8) (2013) 085117.

[279] M. Schlipf, F. Gygi, Optimization algorithm for the generation of oncv pseudopotentials, Computer Physics Communications 196 (2015) 36–44.

[280] D. C. Liu, J. Nocedal, On the limited memory bfgs method for large scale optimization, Mathematical programming 45 (1) (1989) 503–528.

[281] D. J. Evans, B. L. Holian, The nose–hoover thermostat, The Journal of chemical physics 83 (8) (1985) 4069–4074.

[282] G. J. Martyna, M. L. Klein, M. Tuckerman, Nosé–hoover chains: The canonical ensemble via continuous dynamics, The Journal of chemical physics 97 (4) (1992) 2635–2643.

[283] P. Giannozzi, O. Andreussi, T. Brumme, O. Bunau, M. B. Nardelli, M. Calandra, R. Car, C. Cavazzoni, D. Ceresoli, M. Cococcioni, et al., Advanced capabilities for materials modelling with quantum espresso, Journal of physics: Condensed matter 29 (46) (2017) 465901.

[284] P. Giannozzi, O. Baseggio, P. Bonfà, D. Brunato, R. Car, I. Carnimeo, C. Cavazzoni, S. De Gironcoli, P. Delugas, F. Ferrari Ruffino, et al., Quantum espresso toward the exascale, The Journal of chemical physics 152 (15) (2020) 154105.

[285] G. Prandini, A. Marrazzo, I. E. Castelli, N. Mounet, N. Marzari, A standard solid state pseudopotentials (SSSP) library optimized for precision and efficiency, materials Cloud Archive 2021.76, https://doi.org/10.24435/materialscloud:rz-77 (2021).

[286] G. Prandini, A. Marrazzo, I. E. Castelli, N. Mounet, N. Marzari, Precision and efficiency in solid-state pseudopotential calculations, npj Computational Materials 4 (1) (2018) 1–13.

[287] M. S. Dresselhaus, G. Dresselhaus, P. C. Eklund, Science of fullerenes and carbon nanotubes: their properties and applications, Elsevier, 1996.

[288] M. Dresselhaus, G. Dresselhaus, R. Saito, Physics of carbon nanotubes, Carbon 33 (7) (1995) 883–891.

[289] L. V. Liu, W. Q. Tian, Y. A. Wang, Ab initio studies of vacancy-defected fullerenes and single-walled carbon nanotubes, International Journal of Quantum Chemistry 109 (14) (2009) 3441–3456.

[290] H. Shin, S. Kang, J. Koo, H. Lee, J. Kim, Y. Kwon, Cohesion energetics of carbon allotropes: Quantum monte carlo study, The Journal of chemical physics 140 (11) (2014) 114702.

[291] Y. Hu, C. Wu, Q. Pan, Y. Jin, R. Lyu, V. Martinez, S. Huang, J. Wu, L. J. Wayment, N. A. Clark, et al., Synthesis of γ-graphyne using dynamic covalent chemistry, Nature Synthesis (2022) 1–6.

[292] V. G. Desyatkin, W. B. Martin, A. E. Aliev, N. E. Chapman, A. F. Fonseca, D. S. Galvão, E. R. Miller, K. H. Stone, Z. Wang, D. Zakhidov, et al., Scalable synthesis and characterization of multilayer γ-graphyne, new carbon crystals with a small direct band gap, Journal of the American Chemical Society (2022) 17999–18008.

[293] Q. Li, Y. Li, Y. Chen, L. Wu, C. Yang, X. Cui, Synthesis of γ-graphyne by mechanochemistry and its electronic structure, Carbon 136 (2018) 248–254.

[294] H. Zhang, Z. Yao, J. Wang, W. Zhong, Phonon dispersion analysis of carbon nanotubes based on inter-belt model and symplectic solution method, International Journal of Solids and Structures 44 (20) (2007) 6428–6449.

[295] R. Jishi, L. Venkataraman, M. Dresselhaus, G. Dresselhaus, Phonon modes in carbon nanotubules, Chemical Physics Letters 209 (1-2) (1993) 77–82.

[296] R. Saito, T. Takeya, T. Kimura, G. Dresselhaus, M. Dresselhaus, Raman intensity of single-wall carbon nanotubes, Physical Review B 57 (7) (1998) 4145.

[297] J. Kürti, G. Kresse, H. Kuzmany, First-principles calculations of the radial breathing mode of single-wall carbon nanotubes, Physical Review B 58 (14) (1998) R8869.

[298] Z. Yao, C.-C. Zhu, M. Cheng, J. Liu, Mechanical properties of carbon nanotube by molecular dynamics simulation, Computational Materials Science 22 (3-4) (2001) 180–184.

[299] T. Tang, A. Jagota, C.-Y. Hui, N. J. Glassmaker, Collapse of single-walled carbon nanotubes, Journal of Applied Physics 97 (7) (2005) 074310.

[300] J. Xiao, B. Liu, Y. Huang, J. Zuo, K. Hwang, M. Yu, Collapse and stability of single- and multi-wall carbon nanotubes, Nanotechnology 18 (39) (2007) 395703.

[301] J. A. Elliott, J. K. Sandler, A. H. Windle, R. J. Young, M. S. Shaffer, Collapse of single-wall carbon nanotubes is diameter dependent, Physical Review Letters 92 (9) (2004) 095501.

[302] E. B. Barros, A. Jorio, G. G. Samsonidze, R. B. Capaz, A. G. S. Filho, J. M. Filho, G. Dresselhaus, M. S. Dresselhaus, Review on the symmetry-related properties of carbon nanotubes, Physics Reports 431 (6) (2006) 261 – 302.

[303] T. T. Heikkilä, N. B. Kopnin, G. E. Volovik, Flat bands in topological media, JETP Letters 94 (3) (2011) 233–239. doi:10.1134/s0021364011150045.
URL https://doi.org/10.1134%2Fs0021364011150045

[304] B. Dóra, I. F. Herbut, R. Moessner, Occurrence of nematic, topological, and berry phases when a flat and a parabolic band touch, Physical Review B 90 (4) (2014) 045310.

[305] H.-M. Guo, M. Franz, Topological insulator on the kagome lattice, Phys. Rev. B 80 (2009) 113102. doi:10.1103/PhysRevB.80.113102.
URL https://link.aps.org/doi/10.1103/PhysRevB.80.113102

[306] E. Tang, J.-W. Mei, X.-G. Wen, High-temperature fractional quantum hall states,

Phys. Rev. Lett. 106 (2011) 236802. doi:10.1103/PhysRevLett.106.236802.
URL https://link.aps.org/doi/10.1103/PhysRevLett.106.236802

[307] D. Yudin, D. Hirschmeier, H. Hafermann, O. Eriksson, A. I. Lichtenstein, M. I. Katsnelson, Fermi condensation near van hove singularities within the hubbard model on the triangular lattice, Phys. Rev. Lett. 112 (2014) 070403. doi:10.1103/PhysRevLett.112.070403.
URL https://link.aps.org/doi/10.1103/PhysRevLett.112.070403

[308] M. Cutler, N. F. Mott, Observation of anderson localization in an electron gas, Physical Review 181 (3) (1969) 1336.

[309] A. Lagendijk, B. Van Tiggelen, D. S. Wiersma, Fifty years of anderson localization, Phys. today 62 (8) (2009) 24–29.

[310] L. Van Hove, The occurrence of singularities in the elastic frequency distribution of a crystal, Physical Review 89 (6) (1953) 1189.

[311] K. Sun, H. Yao, E. Fradkin, S. A. Kivelson, Topological insulators and nematic phases from spontaneous symmetry breaking in 2d fermi systems with a quadratic band crossing, Physical Review Letters 103 (4) (2009) 046811.

[312] M. Milićević, G. Montambaux, T. Ozawa, O. Jamadi, B. Real, I. Sagnes, A. Lemaître, L. Le Gratiet, A. Harouri, J. Bloch, et al., Type-iii and tilted dirac cones emerging from flat bands in photonic orbital graphene, Physical Review X 9 (3) (2019) 031010.

[313] J.-W. Rhim, B.-J. Yang, Classification of flat bands according to the band-crossing singularity of bloch wave functions, Physical Review B 99 (4) (2019) 045107.

[314] Y. Gomes, R. O. Ramos, Tilted dirac cone effects and chiral symmetry breaking in a planar four-fermion model, Physical Review B 104 (24) (2021) 245111.

[315] R. Naaman, D. H. Waldeck, Chiral-induced spin selectivity effect, The journal of physical chemistry letters 3 (16) (2012) 2178–2187.

[316] J. M. Murray, O. Vafek, Renormalization group study of interaction-driven quantum anomalous hall and quantum spin hall phases in quadratic band crossing systems, Physical Review B 89 (20) (2014) 201110.

[317] S. Uebelacker, C. Honerkamp, Instabilities of quadratic band crossing points, Physical Review B 84 (20) (2011) 205122.

[318] Y. Chong, X.-G. Wen, M. Soljačić, Effective theory of quadratic degeneracies, Physical Review B 77 (23) (2008) 235125.

[319] Y. Chen, Y. Sun, H. Wang, D. West, Y. Xie, J. Zhong, V. Meunier, M. L. Cohen, S. Zhang, Carbon kagome lattice and orbital-frustration-induced metal-insulator transition for optoelectronics, Physical review letters 113 (8) (2014) 085501.

[320] A. Tyagi, R. S. Ningthoujam, Handbook on Synthesis Strategies for Advanced Materials: Volume-III: Materials Specific Synthesis Strategies, Springer, 2021.

[321] G. Qin, K.-R. Hao, Q.-B. Yan, M. Hu, G. Su, Exploring t-carbon for energy applications, Nanoscale 11 (13) (2019) 5798–5806.

[322] T. Guo, P. Nikolaev, A. Thess, D. T. Colbert, R. E. Smalley, Catalytic growth of single-walled manotubes by laser vaporization, Chemical physics letters 243 (1-2) (1995) 49–54.

[323] M. Kumar, Y. Ando, Chemical vapor deposition of carbon nanotubes: a review on growth mechanism and mass production, Journal of nanoscience and nanotechnology 10 (6) (2010) 3739–3758.

[324] E. Costa Girão, L. Liang, E. Cruz-Silva, A. G. S. Filho, V. Meunier, Emergence of atypical properties in assembled graphene nanoribbons, Phys. Rev. Lett. 107 (2011)

135501. doi:10.1103/PhysRevLett.107.135501.
URL https://link.aps.org/doi/10.1103/PhysRevLett.107.135501

[325] P. Han, K. Akagi, F. Federici Canova, R. Shimizu, H. Oguchi, S. Shiraki, P. S. Weiss, N. Asao, T. Hitosugi, Self-assembly strategy for fabricating connected graphene nanoribbons, ACS nano 9 (12) (2015) 12035–12044.

[326] O. G. Schmidt, K. Eberl, Thin solid films roll up into nanotubes, Nature 410 (6825) (2001) 168–168.

[327] R. Mas-Balleste, C. Gomez-Navarro, J. Gomez-Herrero, F. Zamora, 2d materials: to graphene and beyond, Nanoscale 3 (1) (2011) 20–30.

[328] S. Nishimoto, M. Nakamura, A. O'Brien, P. Fulde, Metal-insulator transition of fermions on a kagome lattice at 1/3 filling, Physical Review Letters 104 (19) (2010) 196401.

[329] A. C. Neto, F. Guinea, N. M. Peres, K. S. Novoselov, A. K. Geim, The electronic properties of graphene, Reviews of modern physics 81 (1) (2009) 109.

[330] N. M. Peres, Colloquium: The transport properties of graphene: An introduction, Reviews of modern physics 82 (3) (2010) 2673.

[331] L. A. Falkovsky, Optical properties of graphene, in: Journal of Physics: conference series, Vol. 129, IOP Publishing, 2008, p. 012004.

[332] K. K. Gomes, W. Mar, W. Ko, F. Guinea, H. C. Manoharan, Designer dirac fermions and topological phases in molecular graphene, Nature 483 (7389) (2012) 306–310.

[333] C.-C. Liu, W. Feng, Y. Yao, Quantum spin hall effect in silicene and two-dimensional germanium, Physical review letters 107 (7) (2011) 076802.

[334] F. Pollmann, P. Fulde, K. Shtengel, Kinetic ferromagnetism on a kagome lattice, Physical review letters 100 (13) (2008) 136404.

[335] W. Jiang, M. Kang, H. Huang, H. Xu, T. Low, F. Liu, Topological band evolution between lieb and kagome lattices, Physical Review B 99 (12) (2019) 125131.

[336] T. Mizoguchi, Y. Kuno, Y. Hatsugai, Square-root higher-order topological insulator on a decorated honeycomb lattice, Physical Review A 102 (3) (2020) 033527.

[337] T. Mizoguchi, T. Yoshida, Y. Hatsugai, Square-root topological semimetals, Physical Review B 103 (4) (2021) 045136.

[338] D.-S. Ma, Y. Xu, C. S. Chiu, N. Regnault, A. A. Houck, Z. Song, B. A. Bernevig, Spin-orbit-induced topological flat bands in line and split graphs of bipartite lattices, Physical review letters 125 (26) (2020) 266403.

[339] S. Huang, Y. Xie, C. Zhong, Y. Chen, Double kagome bands in a two-dimensional phosphorus carbide p2c3., The journal of physical chemistry letters 9 11 (2018) 2751–2756.
URL https://api.semanticscholar.org/CorpusID:13704390

[340] T. Ching, D. S. Himmelstein, B. K. Beaulieu-Jones, A. A. Kalinin, B. T. Do, G. P. Way, E. Ferrero, P.-M. Agapow, M. Zietz, M. M. Hoffman, et al., Opportunities and obstacles for deep learning in biology and medicine, Journal of The Royal Society Interface 15 (141) (2018) 20170387.

[341] P. Mamoshina, A. Vieira, E. Putin, A. Zhavoronkov, Applications of deep learning in biomedicine, Molecular pharmaceutics 13 (5) (2016) 1445–1454.

[342] P. Thiagarajan, P. Khairnar, S. Ghosh, Explanation and use of uncertainty quantified by bayesian neural network classifiers for breast histopathology images, IEEE Transactions on Medical Imaging 41 (4) (2022) 815–825. doi:10.1109/TMI.2021.3123300.

[343] O. V. Prezhdo, Advancing physical chemistry with machine learning (2020).

[344] A. Richardson, B. M. Signor, B. A. Lidbury, T. Badrick, Clinical chemistry in higher dimensions: machine-learning and enhanced prediction from routine clinical chemistry data, Clinical biochemistry 49 (16-17) (2016) 1213–1220.

[345] T. Wuest, D. Weimer, C. Irgens, K.-D. Thoben, Machine learning in manufacturing: advantages, challenges, and applications, Production & Manufacturing Research 4 (1) (2016) 23–45.

[346] D. T. Pham, A. A. Afify, Machine-learning techniques and their applications in manufacturing, Proceedings of the Institution of Mechanical Engineers, Part B: Journal of Engineering Manufacture 219 (5) (2005) 395–412.

[347] J. Chen, R. Randall, B. Peeters, W. Desmet, H. Van der Auweraer, Artificial neural network based fault diagnosis of ic engines, in: Key Engineering Materials, Vol. 518, Trans Tech Publ, 2012, pp. 47–56.

[348] F. Wang, S. Ma, H. Wang, Y. Li, J. Zhang, Prediction of nox emission for coal-fired boilers based on deep belief network, Control Engineering Practice 80 (2018) 26–35.

[349] M. Raissi, P. Perdikaris, G. E. Karniadakis, Physics-informed neural networks: A deep learning framework for solving forward and inverse problems involving nonlinear partial differential equations, Journal of Computational Physics 378 (2019) 686–707.

[350] X. Liu, C. E. Athanasiou, N. P. Padture, B. W. Sheldon, H. Gao, A machine learning approach to fracture mechanics problems, Acta Materialia 190 (2020) 105–112.

[351] S. L. Brunton, B. R. Noack, P. Koumoutsakos, Machine learning for fluid mechanics, Annual Review of Fluid Mechanics 52 (2020) 477–508.

[352] R. Mattey, S. Ghosh, A novel sequential method to train physics informed neural networks for allen cahn and cahn hilliard equations, Computer Methods in Applied Mechanics and Engineering 390 (2022) 114474.

[353] C. M. Bishop, Pattern recognition, Machine learning 128 (9) (2006).

[354] B. Efron, T. Hastie, Computer age statistical inference, Vol. 5, Cambridge University Press, 2016.

[355] K. Rajan, Materials informatics: The materials "gene" and big data, Annual Review of Materials Research 45 (2015) 153–169.

[356] J.-P. Correa-Baena, K. Hippalgaonkar, J. van Duren, S. Jaffer, V. R. Chandrasekhar, V. Stevanovic, C. Wadia, S. Guha, T. Buonassisi, Accelerating materials development via automation, machine learning, and high-performance computing, Joule 2 (8) (2018) 1410–1420.

[357] Y. Liu, T. Zhao, W. Ju, S. Shi, Materials discovery and design using machine learning, Journal of Materiomics 3 (3) (2017) 159–177.

[358] J. Schmidt, M. R. Marques, S. Botti, M. A. Marques, Recent advances and applications of machine learning in solid-state materials science, npj Computational Materials 5 (1) (2019) 1–36.

[359] K. T. Butler, D. W. Davies, H. Cartwright, O. Isayev, A. Walsh, Machine learning for molecular and materials science, Nature 559 (7715) (2018) 547–555.

[360] G. S. Na, S. Jang, Y.-L. Lee, H. Chang, Tuplewise material representation based machine learning for accurate band gap prediction, The Journal of Physical Chemistry A 124 (50) (2020) 10616–10623.

[361] J. Wei, X. Chu, X.-Y. Sun, K. Xu, H.-X. Deng, J. Chen, Z. Wei, M. Lei, Machine learning in materials science, InfoMat 1 (3) (2019) 338–358.

[362] G. R. Schleder, A. C. Padilha, C. M. Acosta, M. Costa, A. Fazzio, From dft to machine learning: recent approaches to materials science–a review, Journal of Physics: Materials 2 (3) (2019) 032001.

[363] P. C. Hohenberg, W. Kohn, Inhomogenous electron gas, Physical Review 136 (3B) (1964) 864–871.

[364] K. Kim, L. Ward, J. He, A. Krishna, A. Agrawal, C. Wolverton, Machine-learning-accelerated high-throughput materials screening: Discovery of novel quaternary heusler compounds, Physical Review Materials 2 (12) (2018) 123801.

[365] S. P. Ong, Accelerating materials science with high-throughput computations and machine learning, Computational Materials Science 161 (2019) 143–150.

[366] C. Kim, G. Pilania, R. Ramprasad, From organized high-throughput data to phenomenological theory using machine learning: the example of dielectric breakdown, Chemistry of Materials 28 (5) (2016) 1304–1311.

[367] Z. Li, Q. Xu, Q. Sun, Z. Hou, W.-J. Yin, Thermodynamic stability landscape of halide double perovskites via high-throughput computing and machine learning, Advanced Functional Materials 29 (9) (2019) 1807280.

[368] P. De Luna, J. Wei, Y. Bengio, A. Aspuru-Guzik, E. Sargent, Use machine learning to find energy materials (2017).

[369] G. Pilania, A. Mannodi-Kanakkithodi, B. Uberuaga, R. Ramprasad, J. Gubernatis, T. Lookman, Machine learning bandgaps of double perovskites, Scientific reports 6 (1) (2016) 1–10.

[370] A. C. Rajan, A. Mishra, S. Satsangi, R. Vaish, H. Mizuseki, K.-R. Lee, A. K. Singh, Machine-learning-assisted accurate band gap predictions of functionalized mxene, Chemistry of Materials 30 (12) (2018) 4031–4038.

[371] S. Chibani, F.-X. Coudert, Machine learning approaches for the prediction of materials properties, APL Materials 8 (8) (2020) 080701.

[372] T. Toyao, K. Suzuki, S. Kikuchi, S. Takakusagi, K.-i. Shimizu, I. Takigawa, Toward effective utilization of methane: machine learning prediction of adsorption energies on metal alloys, The Journal of Physical Chemistry C 122 (15) (2018) 8315–8326.

[373] K. Takahashi, I. Miyazato, Rapid estimation of activation energy in heterogeneous catalytic reactions via machine learning, Journal of computational chemistry 39 (28) (2018) 2405–2408.

[374] M. De Jong, W. Chen, R. Notestine, K. Persson, G. Ceder, A. Jain, M. Asta, A. Gamst, A statistical learning framework for materials science: application to elastic moduli of k-nary inorganic polycrystalline compounds, Scientific reports 6 (1) (2016) 1–11.

[375] J. D. Evans, F.-X. Coudert, Predicting the mechanical properties of zeolite frameworks by machine learning, Chemistry of Materials 29 (18) (2017) 7833–7839.

[376] B. A. Calfa, J. R. Kitchin, Property prediction of crystalline solids from composition and crystal structure, AIChE Journal 62 (8) (2016) 2605–2613.

[377] J. R. Moreno, G. Carleo, A. Georges, Deep learning the hohenberg-kohn maps of density functional theory, Physical Review Letters 125 (7) (2020) 076402.

[378] F. Brockherde, L. Vogt, L. Li, M. E. Tuckerman, K. Burke, K.-R. Müller, Bypassing the kohn-sham equations with machine learning, Nature communications 8 (1) (2017) 1–10.

[379] A. Grisafi, A. Fabrizio, B. Meyer, D. M. Wilkins, C. Corminboeuf, M. Ceriotti, Transferable machine-learning model of the electron density, ACS central science 5 (1) (2018) 57–64.

[380] A. Chandrasekaran, D. Kamal, R. Batra, C. Kim, L. Chen, R. Ramprasad, Solving the electronic structure problem with machine learning, npj Computational Materials 5 (1) (2019) 1–7.

[381] D. Kamal, A. Chandrasekaran, R. Batra, R. Ramprasad, A charge density prediction model for hydrocarbons using deep neural networks, Machine Learning: Science and Technology 1 (2) (2020) 025003.

[382] M. Bogojeski, F. Brockherde, L. Vogt-Maranto, L. Li, M. E. Tuckerman, K. Burke, K.-R. Müller, Efficient prediction of 3d electron densities using machine learning, arXiv preprint arXiv:1811.06255 (2018).

[383] A. Fabrizio, A. Grisafi, B. Meyer, M. Ceriotti, C. Corminboeuf, Electron density learning of non-covalent systems, Chemical science 10 (41) (2019) 9424–9432.

[384] L. Zepeda-Núñez, Y. Chen, J. Zhang, W. Jia, L. Zhang, L. Lin, Deep density: circumventing the kohn-sham equations via symmetry preserving neural networks, Journal of Computational Physics 443 (2021) 110523.

[385] M. Tsubaki, T. Mizoguchi, Quantum deep field: Data-driven wave function, electron density generation, and atomization energy prediction and extrapolation with machine learning, Physical Review Letters 125 (20) (2020) 206401.

[386] J. M. Alred, K. V. Bets, Y. Xie, B. I. Yakobson, Machine learning electron density in sulfur crosslinked carbon nanotubes, Composites Science and Technology 166 (2018) 3–9.

[387] S. Gong, T. Xie, T. Zhu, S. Wang, E. R. Fadel, Y. Li, J. C. Grossman, Predicting charge density distribution of materials using a local-environment-based graph convolutional network, Physical Review B 100 (18) (2019) 184103.

[388] Y. S. Teh, S. Ghosh, K. Bhattacharya, Machine-learned prediction of the electronic fields in a crystal, Mechanics of Materials 163 (2021) 104070.

[389] J. A. Ellis, L. Fiedler, G. A. Popoola, N. A. Modine, J. A. Stephens, A. P. Thomp-

son, A. Cangi, S. Rajamanickam, Accelerating finite-temperature kohn-sham density functional theory with deep neural networks, Physical Review B 104 (3) (2021) 035120.

[390] R. Nagai, R. Akashi, S. Sasaki, S. Tsuneyuki, Neural-network kohn-sham exchange-correlation potential and its out-of-training transferability, The Journal of chemical physics 148 (24) (2018) 241737.

[391] B. Kanungo, P. M. Zimmerman, V. Gavini, Exact exchange-correlation potentials from ground-state electron densities, Nature communications 10 (1) (2019) 1–9.

[392] J. Schmidt, C. L. Benavides-Riveros, M. A. Marques, Machine learning the physical nonlocal exchange–correlation functional of density-functional theory, The journal of physical chemistry letters 10 (20) (2019) 6425–6431.

[393] B. Kanungo, P. M. Zimmerman, V. Gavini, A comparison of exact and model exchange–correlation potentials for molecules, The Journal of Physical Chemistry Letters 12 (2021) 12012–12019.

[394] Z. Dai, L. Liu, Z. Zhang, Strain engineering of 2d materials: issues and opportunities at the interface, Advanced Materials 31 (45) (2019) 1805417.

[395] C. Si, Z. Sun, F. Liu, Strain engineering of graphene: a review, Nanoscale 8 (6) (2016) 3207–3217.

[396] J.-W. Jiang, Strain engineering for thermal conductivity of single-walled carbon nanotube forests, Carbon 81 (2015) 688–693.

[397] Y. Hakobyan, E. Tadmor, R. James, Objective quasicontinuum approach for rod problems, Physical Review B 86 (24) (2012) 245435.

[398] S. Ghosh, A. S. Banerjee, P. Suryanarayana, Symmetry-adapted real-space density functional theory for cylindrical geometries: Application to large group-iv nanotubes,

Phys. Rev. B 100 (2019) 125143. doi:10.1103/PhysRevB.100.125143.
URL https://link.aps.org/doi/10.1103/PhysRevB.100.125143

[399] S. Agarwal, A. Banerjee, Solution of the schrödinger equation for quasi-one-dimensional materials using helical waves, (In preparation) (2022).

[400] U. Yadav, S. Pathrudkar, S. Ghosh, Interpretable machine learning model for the deformation of multiwalled carbon nanotubes, Physical Review B 103 (3) (2021) 035407.

[401] A. Damle, A. Levitt, L. Lin, Variational formulation for wannier functions with entangled band structure, Multiscale Modeling & Simulation 17 (1) (2019) 167–191.

[402] N. Marzari, D. Vanderbilt, Maximally localized generalized wannier functions for composite energy bands, Physical review B 56 (20) (1997) 12847.

[403] S. Pathrudkar, Deformation manifold learning model for multi walled carbon nanotubes, Master's thesis, Michigan Technological University (2021).

[404] H. Robbins, Some aspects of the sequential design of experiments, Bulletin of the American Mathematical Society 58 (5) (1952) 527–535.

[405] S. L. Lohr, Sampling: design and analysis, Chapman and Hall/CRC, 2019.

[406] K.-T. Fang, R. Li, A. Sudjianto, Design and modeling for computer experiments, Chapman and Hall/CRC, 2005.

[407] J. Santiago, M. Claeys-Bruno, M. Sergent, Construction of space-filling designs using wsp algorithm for high dimensional spaces, Chemometrics and Intelligent Laboratory Systems 113 (2012) 26–31.

[408] T. W. Simpson, J. Poplinski, P. N. Koch, J. K. Allen, Metamodels for computer-based engineering design: survey and recommendations, Engineering with computers 17 (2) (2001) 129–150.

[409] D. K. Lin, T. W. Simpson, W. Chen, Sampling strategies for computer experiments: design and analysis, International Journal of Reliability and applications 2 (3) (2001) 209–240.

[410] J. M. Hammersley, Monte carlo methods for solving multivariable problems, Annals of the New York Academy of Sciences 86 (3) (1960) 844–874.

[411] I. Sobol', On the distribution of points in a cube and the approximate evaluation of integrals, USSR Computational Mathematics and Mathematical Physics 7 (4) (1967) 86–112. doi:https://doi.org/10.1016/0041-5553(67)90144-9.
URL https://www.sciencedirect.com/science/article/pii/0041555367901449

[412] M. D. McKay, R. J. Beckman, W. J. Conover, A comparison of three methods for selecting values of input variables in the analysis of output from a computer code, Technometrics 42 (1) (2000) 55–61.

[413] R. Jin, W. Chen, A. Sudjianto, An efficient algorithm for constructing optimal design of computer experiments, in: International Design Engineering Technical Conferences and Computers and Information in Engineering Conference, Vol. 37009, 2003, pp. 545–554.

[414] A. B. Owen, Orthogonal arrays for computer experiments, integration and visualization, Statistica Sinica (1992) 439–452.

[415] M. E. Johnson, L. M. Moore, D. Ylvisaker, Minimax and maximin distance designs, Journal of statistical planning and inference 26 (2) (1990) 131–148.

[416] M. Gunzburger, J. Burkardt, Uniformity measures for point sample in hypercubes, Rapp. tech. Florida State University (cf. p. 73) (2004).

[417] J.-S. Park, Optimal latin-hypercube designs for computer experiments, Journal of statistical planning and inference 39 (1) (1994) 95–111.

[418] H. Niederreiter, Low-discrepancy and low-dispersion sequences, Journal of number theory 30 (1) (1988) 51–70.

[419] M. A. Bessa, R. Bostanabad, Z. Liu, A. Hu, D. W. Apley, C. Brinson, W. Chen, W. K. Liu, A framework for data-driven analysis of materials under uncertainty: Countering the curse of dimensionality, Computer Methods in Applied Mechanics and Engineering 320 (2017) 633–667.

[420] S. Wold, K. Esbensen, P. Geladi, Principal component analysis, Chemometrics and intelligent laboratory systems 2 (1-3) (1987) 37–52.

[421] I. T. Jolliffe, Springer series in statistics, Principal component analysis 29 (2002).

[422] J. A. Lee, M. Verleysen, Nonlinear dimensionality reduction, Springer Science & Business Media, 2007.

[423] I. T. Jolliffe, J. Cadima, Principal component analysis: a review and recent developments, Philosophical Transactions of the Royal Society A: Mathematical, Physical and Engineering Sciences 374 (2065) (2016) 20150202.

[424] S.-C. Wang, Artificial neural network, in: Interdisciplinary computing in java programming, Springer, 2003, pp. 81–100.

[425] M. Ester, H.-P. Kriegel, J. Sander, X. Xu, et al., A density-based algorithm for discovering clusters in large spatial databases with noise., in: kdd, Vol. 96,34, 1996, pp. 226–231.

[426] E. Schubert, J. Sander, M. Ester, H. P. Kriegel, X. Xu, Dbscan revisited, revisited: why and how you should (still) use dbscan, ACM Transactions on Database Systems (TODS) 42 (3) (2017) 1–21.

[427] J. M. Alred, K. V. Bets, Y. Xie, B. I. Yakobson, Machine learning electron density in sulfur crosslinked carbon nanotubes, Composites Science and Technology 166 (2018)

3–9, carbon nanotube composites for structural applications. doi:https://doi.org/10.1016/j.compscitech.2018.03.035.
URL https://www.sciencedirect.com/science/article/pii/S0266353817330300

[428] Y. Saad, Numerical Methods for Large Eigenvalue Problems, Revised Edition, SIAM, 2011.

[429] H. Zou, T. Hastie, Journal of the Royal Statistical Society: series B (statistical methodology) 67 (2) (2005) 301–320.

[430] D. P. Kingma, J. Ba, arXiv preprint arXiv:1412.6980 (2014).

[431] V. Shenoy, C. Reddy, A. Ramasubramaniam, Y. Zhang, Edge-stress-induced warping of graphene sheets and nanoribbons, Physical review letters 101 (24) (2008) 245501.

[432] H. W. Kroto, J. R. Heath, S. C. O'Brien, R. F. Curl, R. E. Smalley, C60: Buckminsterfullerene, nature 318 (6042) (1985) 162–163.

[433] D. P. Siegel, The gaussian curvature elastic energy of intermediates in membrane fusion, Biophysical journal 95 (11) (2008) 5200–5215.

[434] M. Zelisko, F. Ahmadpoor, H. Gao, P. Sharma, Determining the gaussian modulus and edge properties of 2d materials: From graphene to lipid bilayers, Physical Review Letters 119 (6) (2017) 068002.

[435] P. Koskinen, O. O. Kit, Approximate modeling of spherical membranes, Physical Review B 82 (23) (2010) 235420.

[436] E. Abbena, S. Salamon, A. Gray, Modern differential geometry of curves and surfaces with Mathematica, Chapman and Hall/CRC, 2017.

[437] Y. Wei, B. Wang, J. Wu, R. Yang, M. L. Dunn, Bending rigidity and gaussian bending stiffness of single-layered graphene, Nano letters 13 (1) (2013) 26–30.

[438] C. Davini, A. Favata, R. Paroni, The gaussian stiffness of graphene deduced from a continuum model based on molecular dynamics potentials, Journal of the Mechanics and Physics of Solids 104 (2017) 96–114.

[439] M. Hu, J. J. Briguglio, M. Deserno, Determining the gaussian curvature modulus of lipid membranes in simulations, Biophysical journal 102 (6) (2012) 1403–1410.

[440] P. Moon, D. E. Spencer, Field theory handbook: including coordinate systems, differential equations and their solutions, Springer, 2012.